Exploration of the Ionic Conduction Properties of Porous MOF Materials

Kiran Taksande

▶ **To cite this version:**

Kiran Taksande. Exploration of the Ionic Conduction Properties of Porous MOF Materials. Material chemistry. Université de Montpellier, 2022. English. NNT : 2022UMONS010 . tel-03789646

HAL Id: tel-03789646

https://theses.hal.science/tel-03789646

Submitted on 27 Sep 2022

HAL is a multi-disciplinary open access archive for the deposit and dissemination of scientific research documents, whether they are published or not. The documents may come from teaching and research institutions in France or abroad, or from public or private research centers.

L'archive ouverte pluridisciplinaire **HAL**, est destinée au dépôt et à la diffusion de documents scientifiques de niveau recherche, publiés ou non, émanant des établissements d'enseignement et de recherche français ou étrangers, des laboratoires publics ou privés.

THÈSE POUR OBTENIR LE GRADE DE DOCTEUR DE L'UNIVERSITÉ DE MONTPELLIER

En Chimie et Physico-chimie des Matériaux

École doctorale Sciences Chimiques Balard

Unité de recherche Institut Charles Gerhardt Montpellier (ICGM) - Equipe D3

Exploration of the Ionic Conduction Properties of Porous MOF Materials

Présentée par Kiran Narayan Taksande

Le 23 Mars 2022

Sous la direction de Sabine Devautour-Vinot Directrice de thèse
Et de Guillaume Maurin Co-Directeur de thèse

Devant le jury composé de

Dr. Georgeta POSTOLE, Maître de Conférences, IRCELYON Université de Lyon	Rapporteure
Dr. Michael BADAWI, Maître de Conférences, LPCT, Université de Lorraine	Rapporteur
Prof Isabelle BEURROIES, Professeur, ENAP Madirel, Aix Marseille Université	Examinatrice
Prof. Marc CRETIN, Professeur, IEM, Université de Montpellier	Examinateur
Dr. Sabine DEVAUTOUR-VINOT, Maître de Conférences, ICGM, Université de Montpellier	Directrice de thèse
Prof.Guillaume MAURIN, Professeur, ICGM, Université de Montpellier	Co-Directeur de thèse

UNIVERSITÉ DE MONTPELLIER

Acknowledgements

I would have not been possible to write this doctoral thesis without the help and support of kind people around me, to only some of whom it is possible to give particular mention here.

Foremost, I express my sincere gratitude to Pioneers of India education and social reforms, Mrs. Savitribai Phule and Dr. Babasheb Ambedkar because of whom many like me could complete the formal education.

Above all, I am indebted to Prof Guillaume Maurin for his patience, support and motivation throughout the course from my first introductory email to him, till this date of my defence. It was very kind of him to agree to host me in his laboratory and provide me with this opportunity. I am also very grateful to him for introducing me to my advisor Dr. Sabine Devautour-Vinot and agreeing to cosupervise me.

I am short of words to express my gratitude to Dr. Sabine Devautour-Vinot for ther constant support, hard-work, motivation, enthusiasm and immense knowledge. Her guidance helped me throughout my research and writing of the thesis. I could have never imagined a better advisor and mentor for my Ph D studies.

Indeed, without the help, support and guidance of Dr. Sabine and Prof. Maurin this journey would not have been realized.

My sincere appreciation to the jury members, Dr. Georgeta Postole and Dr. Michael Badawi for having agreed to read this manuscript as reviewers as well as Prof. Isabelle Beurroies and Prof. Marc Cretin for agreeing to be part of my doctoral thesis committee.

Furthermore, I express my deep gratitude to my employer Government of Maharashtra, my college, my colleagues of chemistry department and our Principal Prof. Swati Wahval for allocating and allowing me the study leave to complete PhD.

I also thank my present and former labmates of the ICGM, D3 group Dr. Shyama, Dr. Rocio, Dr. Wahid, Dr. Carla, Dr. Anusha, Dr. Paul, Mr. Pierre, Dr. Salva, Mr. Patrick, Mr. Ruben, Ms. Hanae, Dr. Linda, Dr. Amine, Mr. Robin, Dr. Kamal, Dr. Karim, Dr. Amandine for the simulating discussions, support, sleepless nights, parties and all the fun we had during these years. I express my special thanks to Dr. Renjith Pillai for his support and my best friend Shweta Sharma for her encouragement and care.

I would also like to give special thanks to my husband Dr. Ranjit Hawaldar for his love and care, my father Mr. Narayan Taksande, mother-in-law Mrs. Ranjana Hawaldar, sister-in-law Dr. Padmaja Hawaldar and my family as a whole for their continuous support and understanding.

Lastly, I also extend my gratitude towards all those who directly and indirectly facilitated in my degree and my stay in Montpellier, whom I could not mention herein.

Finally, I would like to dedicate this thesis to my late lovely and affectionate mother late. Prabhavati Taksande.

Table of Content

General Introduction

Since the dawn of the industrial revolution mankind's hunger for energy has increased with each passing day. Rapid industrialization globally accompanied by enrichment in standard of living has further fuelled global energy consumption to a record level. All the energy drawn today comes mostly from fossil fuels such as oil and natural gas. Over the last few centuries uncontrolled burning of fossil fuels has led to not only depletion of fossil fuels but also to environmental damage. To circumvent these issues, concerted efforts are being made to harness clean energy sources or alternative energy storage/conversion devices like fuel cells, electrolysers, supercapacitors and batteries.

In this context, proton exchange membrane fuel cells (PEMFC) have attracted great deal of attention owing to their advantages of zero-emission, efficient energy conversion among others advantages.[1,2] The key component in a PEMFC is the electrolyte through the proton exchange membrane, which allows the flow of protons generated at the anode towards the cathode. Till date, Nafion^{TM} series perfluorinated sulfonic acid membrane is the most preferred candidate. Nafion^{TM} is favoured owing to its high proton conductivity and good chemical stability when compared to its counterparts. However, Nafion^{TM} has certain disadvantages: (1) optimal operational temperature for Nafion^{TM} is 343–363 K. Beyond 363 K there is drastic deterioration in the performance owing to evaporation of H_2O; (2) Carbon fuels like methanol have high permeability with Nafion^{TM} and hence Nafion^{TM} is not suitable for use in direct methanol fuel cells (DMFC); (3) Lack of high crystalline order makes it hard to deeply study and analyse proton conductivity mechanisms; (4) Film formation is difficult because synthesis and sulfonation of perfluorinated compounds is a herculean task, thereby adding to the cost.[3,4] Hence, the development of new inexpensive proton-conducting materials with outstanding performance has been a subject of intensive research. The application of crystalline solid-state proton conductive materials in fuel cells, proton sieving, electrochemical sensing and biochemistry are in the foreground, among which proton conducting metal–organic frameworks (MOFs) are potentially attractive candidates.[5,6]

MOFs are porous hybrid crystalline compounds made from an infinite array of repeating small building units. These units comprise of polydentate organic ligands connected to metal ions or clusters thereby forming multidimensional networks. They possess large accessible regularly shaped cages with remarkably high surface area and pore volume, which makes them capable of

trapping different molecules within these cavities. This makes them suitable for a wide range of applications including gas storage, separation, catalysis, magnetism, photoluminescence, sensing, drug delivery and many more. Propitiously, MOFs are attractive candidates for proton conduction owing to their unique structural features like crystallinity, tailorable porosity, dynamic behaviour and regular arrangement of voids.[5] Furthermore, their ability to form thin films and mixed-matrix membranes has increased their viability for industrial applications.[5,6]

Regarding solid-state ionic conducting solids dedicated to batteries purposes, a large panel of solids have been identified, while many efforts are still being devoted to the development of new materials. In this field, molecular crystals are rather underexplored versatile materials from the standpoint of water-assisted ionic conduction similar to zeolites and MOFs. Molecular crystals offer an extensive opportunity to create a wide range of functional materials due to appropriate flexibility of component units combined with structural and chemical versatility. They offer finer control at molecular level thereby giving high degree of freedom to design conduction paths in their 3D ordered structures for rapid ion diffusion. Till date, only a very few molecular crystals have been investigated as ionic conductors.[7–11]

In this thesis, the conductivity performances of a new series of chemically stable proton conducting MOFs as well as a superionic molecular crystal were explored. The selection of the materials results from a collaboration between our research team and three groups expert in the synthesis of porous materials: IMAP Paris -Dr. C. Serre & Dr. S. Wang-, ILV-Versailles -N. Steunou- and Hanyang University -Dr. H. Chun-. Our contribution was to (i) select a variety of architectures and functionalities of robust MOFs/superionic molecular solids and (ii) characterize and rationalize their conducting performances over various temperature/humidity conditions. Noteworthy, quantum- and force-field based simulations carried out in the group were combined with our experimental conclusions to elucidate the microscopic mechanisms at the origin of the ionic conducting properties of the studied materials. This fundamental knowledge will further serve to create novel robust superionic conductors with outstanding performances that will pave the way towards appealing societal applications for clean energy production.

Chapter 1 describes the main solid-state proton conductor technologies, including a glance of typical devices like fuel cells, redox-flow batteries as well as the main categories of benchmark

solid-state proton conductors. Subsequently, detailed insights into MOFs, including their chemical and structural description and their applications in diverse fields, is provided. The state of the art regarding their identified key-features that drive their proton conducting performances encloses this chapter.

Chapter 2 gives a description of basic concepts related to ionic conduction and diffusion in solids. The various experimental and computational techniques used to characterize this process in MOFs are enumerated. Afterwards, the fundamental of Complex Impedance Spectroscopy (CIS) and the experimental set-up employed in the frame of this work are thoroughly detailed.

Chapters 3 and 4 present the exploration of two series of MOFs we designed to achieve promising proton-conducting performances, using distinct approaches to modulate the concentration of Brønsted acidic sites and charge carriers and further boost the conductivity properties. First, a multicomponent ligand replacement strategy was successfully employed to elaborate a series of multivariate sulfonic-based solids MIP-207-$(SO_3H\text{-IPA})_x$-$(BTC)_{1-x}$ which combine structural integrity with high proton conductivity values (*e.g.*, $\sigma = 2.6 \times 10^{-2}$ S.cm^{-1} at 363 K/95% Relative Humidity -RH-). Secondly, a proton conducting composite was prepared through the impregnation of an ionic liquid (1-Ethyl-3-methylimidazolium chloride, EMIMCl) in the mesoporous MIL-101(Cr)-SO_3H. The composite displaying high thermal and chemical stability, exhibits outstanding proton conductivity not only at the anhydrous state ($\sigma_{473\ K} = 1.5 \times 10^{-3}$ S.cm^{-1}) but also under humidity ($\sigma_{(343\ K/60\%\text{-}80\%RH)} \geq 0.10$ S.cm^{-1}) conditions.

Chapter 5 explores the ionic conducting properties of another class of porous solids, considering a zirconium-formate molecular solid containing KCl ion pairs (ZF-3). ZF-3 switches from an insulator ($\sigma = 5.1 \times 10^{-10}$ S.cm^{-1} at 363 K/0% RH) to a superionic conductor upon hydration ($\sigma = 5.2 \times 10^{-2}$ S.cm^{-1} at 363 K/95% RH), in relation with the boost of Cl^- dynamics upon water adsorption.

Finally, the last section of this manuscript assembles the main conclusions of this work along with the perspectives it delivers.

REFERENCES

[1] V.F. Valdés-López, T. Mason, P.R. Shearing, D.J.L. Brett, Carbon monoxide poisoning and mitigation strategies for polymer electrolyte membrane fuel cells – A review, Prog. Energy Combust. Sci. 79 (2020) 100842. https://doi.org/10.1016/j.pecs.2020.100842.

[2] M. Shabani, H. Younesi, M. Pontié, A. Rahimpour, M. Rahimnejad, A.A. Zinatizadeh, A critical review on recent proton exchange membranes applied in microbial fuel cells for renewable energy recovery, J. Clean. Prod. 264 (2020) 121446. https://doi.org/10.1016/j.jclepro.2020.121446.

[3] K.A. Mauritz, R.B. Moore, State of Understanding of Nafion, Chem. Rev. 104 (2004) 4535–4586. https://doi.org/10.1021/cr0207123.

[4] L. Zanchet, L.G. da Trindade, W. Bariviera, K.M. Nobre Borba, R.D.M. Santos, V.A. Paganin, C.P. de Oliveira, E.A. Ticianelli, E.M.A. Martini, M.O. de Souza, 3-Triethylammonium propane sulfonate ionic liquids for Nafion-based composite membranes for PEM fuel cells, J. Mater. Sci. 55 (2020) 6928–6941. https://doi.org/10.1007/s10853-020-04454-4.

[5] P. Ramaswamy, N.E. Wong, G.K.H. Shimizu, MOFs as proton conductors – challenges and opportunities, Chem. Soc. Rev. 43 (2014) 5913–5932. https://doi.org/10.1039/C4CS00093E.

[6] X. Chen, G. Li, Proton conductive Zr-based MOFs, Inorg. Chem. Front. 7 (2020) 3765–3784. https://doi.org/10.1039/d0qi00883d.

[7] T. Nakamura, T. Akutagawa, K. Honda, A.E. Underhill, A.T. Coomber, R.H. Friend, A molecular metal with ion-conducting channels, Nature. 394 (1998) 159–162. https://doi.org/10.1038/28128.

[8] M. Moriya, D. Kato, W. Sakamoto, T. Yogo, Structural Design of Ionic Conduction Paths in Molecular Crystals for Selective and Enhanced Lithium Ion Conduction, Chem. - A Eur. J. 19 (2013) 13554–13560. https://doi.org/10.1002/chem.201300106.

[9] M. Moriya, K. Nomura, W. Sakamoto, T. Yogo, Precisely controlled supramolecular ionic conduction paths and their structure–conductivity relationships for lithium ion transport, CrystEngComm. 16 (2014) 10512–10518. https://doi.org/10.1039/C4CE01417K.

[10] M. Moriya, Construction of nanostructures for selective lithium ion conduction using self-assembled molecular arrays in supramolecular solids, Sci. Technol. Adv. Mater. 18 (2017) 634–643. https://doi.org/10.1080/14686996.2017.1366816.

[11] H. Zhu, D.R. MacFarlane, J.M. Pringle, M. Forsyth, Organic Ionic Plastic Crystals as Solid-State Electrolytes, Trends Chem. 1 (2019) 126–140. https://doi.org/10.1016/j.trechm.2019.01.002.

Chapter 1

Overview on the metal organic frameworks as solid-state proton electrolytes

1.1. Introduction

The objective of this chapter is to introduce the reader to the main concepts of solid-state proton electrolytes, a brief description of Metal-Organic Frameworks and their ability to act as proton conductors.

The first part of this chapter deals with the general description of solid-state proton electrolytes followed by their use for fuel cells, redox flow batteries and resistivity-based humidity sensors applications. Different classes of proton-electrolytes materials are then listed and described, including oxo acids, water containing systems, perovskite-like solids and hybrid materials, depending on their typical operating conditions and their driving forces involved in the proton conduction process.

The second part of the chapter is devoted to the description of a new class of hybrid porous materials, namely Metal-Organic Frameworks (MOFs). Even though these materials have been discovered quite recently, due to their vast diversity of compositions, topologies and pore sizes, some of pure and composite superprotonic MOF materials have been discovered, with promising proton conducting performances.

1.2. Solid-state proton electrolytes

1.2.1. Solid-state proton conductors-based technology

The investigation of solid-state proton conductors was initiated early 1900's when ice was found as an electrical conductor,[1] and continued specially in the 1950's with a focus on defective solids. At this stage, the proton conduction phenomenon was mostly explored from a fundamental perspective. In the 1960's NASA began developing Proton Exchange Membrane Fuel Cells (PEMFCs) in the context of the Gemini and Apollo space programs,[2] which boosted the research on solid-state proton conductors, further amplified by the discovery of Nafion^{TM}, the first commercial proton conducting material. Thereafter, proton conductors have been envisaged for several applications including the energy production and storage with the use of ***fuel cells*** [3,4] and ***redox-flow batteries***,[5,6] as well as microionic devices such as ***humidity sensors*** [7,8] or in a less extend as proton pumps in biological systems or in selective catalysis. The following section is dedicated to a brief description of the three first applications.

(a) Fuel Cells

An electrochemical cell that converts the chemical energy of a fuel, often hydrogen, and an oxidizing agent, often oxygen from air, into electricity through a pair of redox reaction is commonly termed as a fuel cell. It efficiently converts oxidant and chemical energy accumulated in the fuel directly into electrical energy, with heat and water as by-products. These electrochemical converters generate electricity without involving any moving mechanical part. Differently from batteries, fuel cells can provide electrical power continuously as long as a fuel (hydrogen, methanol or light hydrocarbons) and oxygen are supplied. In general, fuel cells encompass PEMFC, protonic ceramic fuel cell (PCFC), solid acid fuel cell (SAFC), direct methanol fuel cell (DMFC), alkaline fuel cell (AFC), molten carbonate fuel cell (MCFC) and solid oxide fuel cell (SOFC). Fuel cells are majorly distinguished into two categories depending on their operating temperatures, namely those operating i) at temperature higher than 523 K (SOFCs, MCFC, PCFC) mainly for stationary power application and ii) at temperature lower than 523 K (phosphoric acid fuel cell (PAFC), PEMFC, DMFC, AFC) for transportation and stationary power [9–12] applications. Noteworthy, Hydrogen is the most common encountered fuel, involved in PCFCs, SAFCs, DMFCs and PEMFCs.

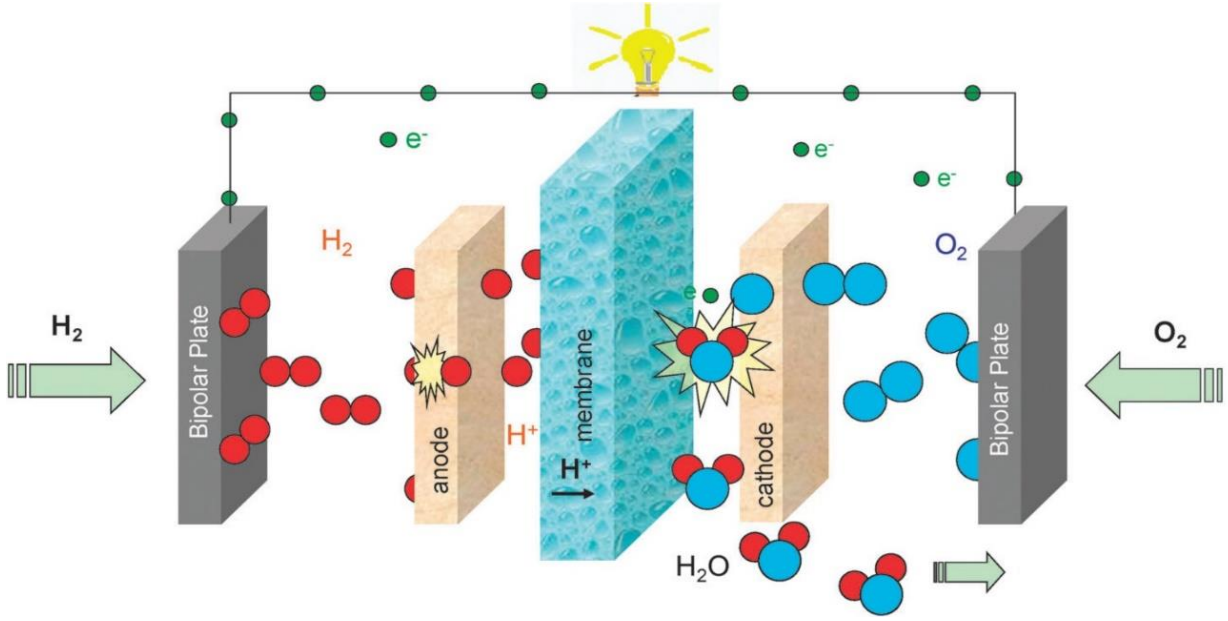

Figure 1.1 – Schematic representation of the electrochemical conversion of hydrogen in a PEMFC. Adapted from ref [9].

As illustrated in Figure 1.1, a fuel cell consists of main components, i.e., an anode, a cathode, an electrolyte and structural components (e.g., end plates). In PEMFCs, the fuel undergoes oxidation reaction at the catalyst loaded anode to generate protons and electrons (equation 1.1). Protons move from the anode to the cathode through the electrolyte. Simultaneously, electrons flow from the anode to the cathode through the external circuit. At the cathode, the electrons from the circuit and the protons from the electrolyte membrane promote the reduction of O_2 into H_2O molecules according to equation 1.2. Thus, a PEMFC responds to the global equation 1.3.

$$Anode: 2H_{2(g)} \rightarrow 4H^{+}_{(aq)} + 4e^{-} \quad \text{Eq.1.1}$$

$$Cathode: O_{2(g)} + 4\,H^{+}_{(aq)} + 4e^{-} \rightarrow 2\,H_2O_{(l)} \quad \text{Eq.1.2}$$

$$Global\ reaction: 2H_{2(g)} + O_{2(g)} \rightarrow 2H_2O_{(l)} \quad \text{Eq.1.3}$$

One of the most important parts of the proton-based fuel cell systems is the solid electrolyte through which the important process of proton transport takes place. Apart from being mechanically and chemically stable, it should be able to efficiently transfer the proton from the anode to the cathode, while being electronically insulating to prevent electron transfer. It should also be thermally robust as well as resistant to the direct passage of gases from one electrode to the other (cross-over process).

Initially in the 1960's, polystyrene sulfonic acid-based proton-conducting solid polymer electrolyte membrane emerged,[13] but suffered from a lack of long-term performance due to poor chemical stability. Walther Grot of the E.I. Dupont Corporation then developed and patented a perfluorocarbon sulfonic acid polymer under the tradename Nafion^{TM}.[14,15] Despite being invented in the 1970's, Nafion^{TM} is still nowadays considered as the benchmark material used at low temperature (T < 373 K), owing to its high chemical stability and high proton conductivity of 0.1 S.cm^{-1}.[16] It consists of a fluorinated hydrophobic backbone side-attached with hydrophilic sulfonic groups, forming channels (Figure 1.2a).[17,18] The proton conductivity performance is driven by the hydration level of these channels. At low water content, two hydrophobic and hydrophilic domains are separated and the material behaves as an insulator. In these conditions, the water molecules are located only at the vicinity of the sulfonic groups. However, when saturated with water, well-developed percolated sulfonic-water networks, comprising channels

filled with free water molecules, are formed. This results in proton conductivity values approaching that of bulk aqueous electrolytes, i.e. ~1 x 10^{-1} S.cm^{-1} at 353 K (Figure 1.2b).[18,19] Undeniably, Nafion™ exhibits both a high conductivity and a reasonable chemical stability at low temperatures.

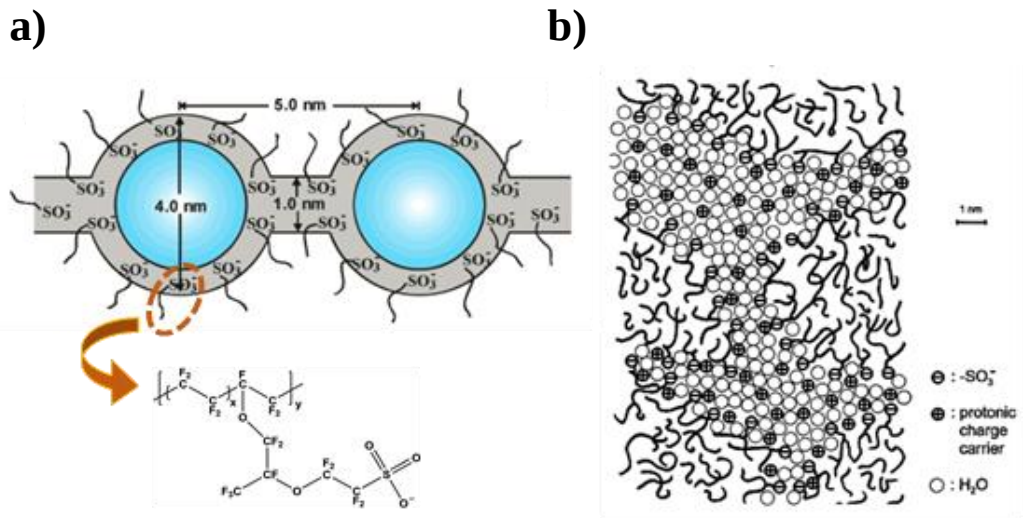

Figure 1.2 - Morphology description of Nafion™ as cluster channels, evidencing the hydrophobic backbone connected to hydrophilic **a)** chains and **b)** clusters. Adapted from ref.[17].

Though Nafion™ is an excellent proton conductor, it is not free from drawbacks. The strong dependence of the proton conductivity on its hydration state does not meet the requirements for its use at temperature significantly over 373 K. Moreover, due to a glass transition, this material displays poor mechanical stability at T > 398 K.[20] Nafion™ also does not tolerate other cations than H^+, which are known to catalyze the polymer chain decomposition.[21] In addition, the incorporation of Nafion™ in methanol fuel cells is hampered, because of insufficient resistance to methanol cross-over.[18] Lastly, the complex manufacturing process makes Nafion™ ridiculously expensive.

To address the short-comings of Nafion™, typically the poor mechanical and chemical stability, a number of studies have been reported in the literature to improve the properties of Nafion™ type membranes through the incorporation of inorganic fillers,[22] or to develop new partially fluorinated and non-fluorinated acid membranes. In this context, aromatic-based and acid-base polymers blends and/or composites, including sulfonated poly (ether-ethyl ketone) (SPEEK)

[23] or poly(benzimidazole) (PBI) [24] membranes, have gathered a lot of attention. However, these alternatives still show limitations, such as lower conductivity performance than Nafion™ or long-term durability issues due to the leaching of the acid molecules in the case of composites.

Alternatively, to Proton Exchange Membranes (PEMs), pure inorganic conductors have attracted great attention as solid-state proton electrolytes. In this context, polyoxometalates showed moderate to high levels of conductivity at low temperature ($\sigma = 10^{-4}$ to 10^{-1} S.cm^{-1} at 293 K),[25] while solid acids, as exemplified by $CsHSO_4$, display a dramatic jump in conductivity to reach attractive performances ($\sigma > 10^{-2}$ S.cm^{-1}) above a critical temperature depending on the system (~413 K).[26] However most of these inorganic compounds are highly soluble in water and suffer from unstability under normal fuel cell operating conditions.[26–28] On the other hand, ceramic-based proton electrolytes are also mentioned in the literature, while their use is restricted to PCFCs, as they operate at much higher temperature than the conditions considered for PEMFCs. Table 1.1 summarizes the main types of fuel cells using solid-state proton electrolytes, depending on the operating conditions as well as their applicable properties.

Table 1.1 – Summary of the main types of solid-state fuel cells based on proton conducting electrolytes, their respective most common employed electrolytes, operating temperature and applications.[29–31]

Type of fuel cell	Common electrolyte	Operating temperature (K)	Application
PEMFC or DMFC	Nafion™	353 363-393	Mobile & transportation power
SAFC	$CsHPO_4$	503-553	Transportation & stationary power
PCFC	BCY[a], BCZY[b]	673-973	Stationary power

[a] BCY = yttrium-doped barium cerates. [b] BCZY = yttrium-doped barium cerates zirconates.

(b) Redox Flow Batteries (RFBs)

RFBs are attractive candidates for electrical energy storage as they can effectively stabilize the fluctuating power generation from renewable energy sources. They promise energy storage in

the range of several kW/kWh up to tens of MW/MWh for stationary applications.[5,6,32] Moreover, they work at room temperature as the system involves use of liquid solutions to either store or produce energy according to their operating modes. The reactions involved in the process are listed in equations 1.4 and 1.5, considering the charging and the inverse discharging modes, respectively. In these equations, A and B species are placed at the anode and the cathode respectively.

$$A^{n+} + xe^{-} \rightleftharpoons A^{(n-x)+} \qquad \text{Eq.1.4}$$

$$B^{m+} - ye^{-} \rightleftharpoons B^{(m+y)+} \qquad \text{Eq.1.5}$$

The four main RFB technologies are the Fe/Cr,[33] the all-vanadium,[34,35] the V-Br [36] and the V-O_2 [37] cells. The representation of the components of each technology is expressed in terms of A^{n+}/B^{m+} pairs incorporated in equations 1.4 and 1.5. They correspond to Cr^{3+}/Fe^{2+}, V^{3+}/VO^{2+}, VBr_3/Br^- and V^{3+}/H_2O respectively.[38] In particular, vanadium redox flow batteries (VRFBs) are promising owing to their long service life, scalability, safety and high output. Using vanadium as the redox-active material in aqueous solution, the battery generates electricity based on the potential differences of the VO^{2+}/VO_2 and V^{2+}/V^{3+} redox couples separated by a membrane. Charge carriers are transported through the membrane electrode assembly to maintain the electrical neutrality of the electrolyte solutions. The membrane itself needs to be mechanically robust and chemically stable under strongly oxidizing and acidic conditions, while it should prevent the water transfer and consequent flooding of the half cells and facilitate the crossing of charge equilibrium species, like protons (H^+).[39] Tremendous efforts have been dedicated to develop sustainable and affordable ion exchange membranes for RFBs.[39] By now, numerous flow battery targeted membranes for the VRFB exist. Similarly, to PEMs, perfluorinated proton exchange membranes are popular in view of their high proton conductivity and good chemical stability. In addition to face the issues encountered by Nafion™ listed in the previous section and to increase the ion selectivity, the membranes have been modified with inorganic (e.g. SiO_2,[40] TiO_2 [22]) and organic (e.g. polyethylenimine,[41] polypyrrole [42]) components. Other non-fluorinated membranes were also employed in RFBs,[43–46] such as (i) pore filled composites, consisting in ion-exchange resins (e.g., Amberlite CG 400 [47]) or polyelectrolytes (e.g., polystyrene sulfonate

[48]) introduced in a polymeric matrix, (ii) sulfonated polymers,[49] and (iii) inorganic materials (e.g., zeolites [50]). Despite being intrinsically more susceptible to oxidation, hydrocarbon-based membranes have recently been investigated in efforts to lower cost and improve permselectivity [18,51–53]. Finally, more than 200 membrane samples are sorted into fluoro-carbons, hydrocarbons or N-heterocycles according to the basic polymer used. Most developments show improved VRFB performance when compared to VRFB equipped with reference Nafion^{TM}-based membranes. To maximize VRFB effectiveness, it is critical to promote ion selectivity for proton over vanadium ions, by suppressing vanadium crossover. Because they are all positively charged ion species, achieving high permselectivity without degrading the proton conductivity is still challenging.[52]

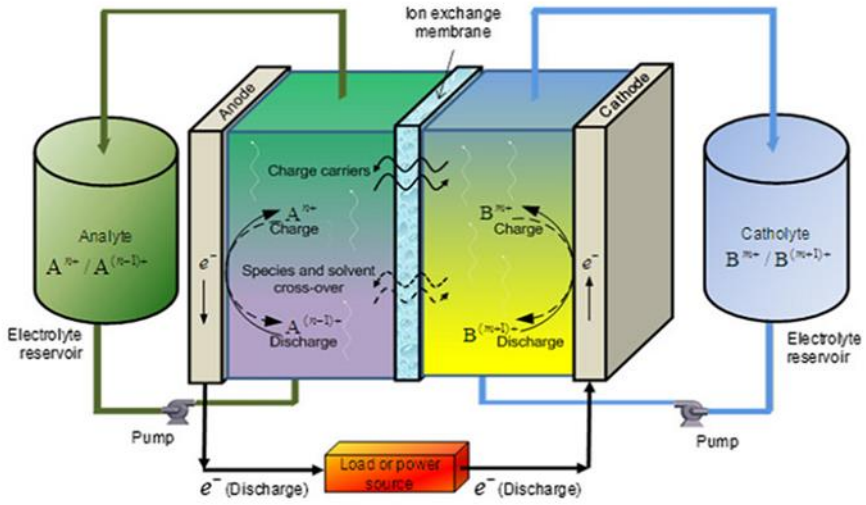

Figure 1.3 – Diagram scheme of a redox-flow battery taken from ref.[54] Cylinders represent the reservoirs where the catholyte and analyte solutions are stored. The width of the space membrane/cathode and membrane/anode where the charge and discharge reaction that place are exaggerated for clarity. Usually many of these anode/membranes/cathodes are stacked adjacently in order to enhance the RFB power density.

(c) Humidity sensors

Sensors that detect the amount of water vapour present in the environment are of profound importance. Humidity sensors are capable of providing accurate measurements of absolute humidity by mixing measurements of temperature and relative humidity (RH). Humidity sensors

are involved in a wide range of domestic and industrial applications, e.g. building and construction, food processing, medical and health monitoring, agriculture, fuel, aerospace, automobile and human comfort.[8,55–60] Depending on the detection mechanism, these sensors are categorized into capacitive, resistive, piezoresistive, optical, gravimetric or magnetoelastic types.[8,61] In the case of electrical-based mechanism, humidity sensing is achieved by converting the change in proton conductivity of a solid electrolyte upon water exposure to an electrical response via ac impedance spectroscopy measurements. The later yields the electrical capacitance or impedance of the sample, further transformed as conductivity, as a function of humidity at a given temperature. Notably, materials suitable for sensor development should meet the following criteria: exhibit large impedance change with relatively small changes of humidity, wide range of humidity response, quick response time, reproducibility, selectivity (i.e., minimal response to gases other than water vapor), chemical resistance to dirt or other gases, stability and long-life time.

For applications below T < 473 K, various oxide hydrates/hydroxides with two-dimensional (2D) layered and three-dimensional (3D) network structures, e.g. α-$Zr(HPO_4)_2.H_2O$, have been investigated,[62,63] while it is well established that the conductivity in such hydrates occurs via conductivity of protons in presence of water. Perovskite oxides are also promising candidates for high temperature (above 573 K) sensing.[64] Some Cerium-based perovskites are known for humidity sensing above 973 K.[65]

Figure 1.4 presents a schematic representation of a resistivity-based humidity sensor, resulting from the film deposition of an active porous solid in interdigit electrode support.

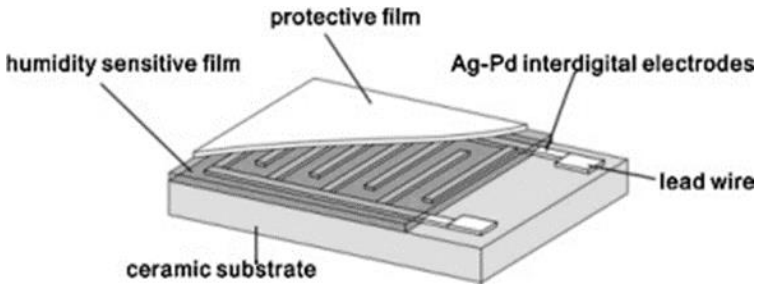

Figure 1.4 – Schematic representation of a humidity resistive-sensor (from ref [66]).

1.2.2. Classification of solid-state proton conductors

A common thread that connects all the proton-based conducting technologies described above is the quest to improve their performances. It is therefore of paramount interest to explore the proton conduction properties of the materials that are foreseen as potential solid-state electrolytes.

Based on their electrical properties, proton conducting materials can broadly be divided into three groups:[67] (i) those with residual conductivity lower than 10^{-10} $S.cm^{-1}$, termed as insulators, (ii) those with conductivity between 10^{-5} and 10^{-10} $S.cm^{-1}$ and (iii) conductors that possess proton conductivity higher than 10^{-4} $S.cm^{-1}$, termed as superprotonic conductors.[67]

Proton conductivity occurs in materials via different proton conduction mechanisms like proton transfer, structural reorganization and diffusional motion of extended moieties. Based on the specific conduction mechanism, Kreuer [68] has identified four main groups of compounds as fast proton conductors of technological and engineering significance. These four categories are listed as follows:

(a) Hydrated or water-containing systems

Diverse standard materials such as inorganic layered solids,[69,70] oxide hydrates,[71,72] heteropoly acid,[73] protonic β-aluminas,[74,75] acidic phosphates and phosphonates,[62,69,76–82] and hydrated acidic polymers [83,84] come under this category. Nafion^{TM} is the most well-known member of this family, displaying the highest proton conductivity. In these materials, the water molecules play a prominent role in the proton conduction mechanism, by dissociating and delocalizing protons from their active sites and by acting as a mediator for the proton transfer throughout the solid, as described in the following section.

(b) Oxo-acid salts

This group includes the range of salts and acids pertaining to the heteroatom oxo-anions of sulphate, selenate, phosphate, arsenate, nitrate, etc. In the anhydrous state, these compounds are able to conduct protons due to self-dissociation and the hopping or jumping mechanism of protons among hetero-oxo ions (e.g., NO_3^-, SeO_4^{2-}, SO_4^{2-}, PO_4^{3-}, AsO_4^{3-}…) through the rotation of hetero-oxo ions from one group to the next.[26] Alkali and alkaline earth oxoacid salts with sizeable

cations (e.g. $CsHSO_4$, $RbHSO_4$) received great attention as superprotonic conductors, due to the formation of an orientationally disordered phase called as superprotonic phase transition, at moderate temperatures – usually above 413 K.[85,86] To enhance their thermal and chemical susceptibilities, oxo-anion systems based on phosphates or complex hetero-polyacids are more likely to be of practical interest,[87,88] while their use in tandem with intergranular oxides (e.g., SiO_2, Al_2O_3, Fe_2O_3, etc.), allows to improve their mechanical properties.[89]

(c) Densely packed oxides

This group of proton conductors is extremely large and encompasses a series of different classes of perovskite and pyrochlore materials,[90–92] while their specificity relies on their high thermal stability, allowing their use at much higher temperature than the other classes of proton conductors. They show a specific proton conduction process by vacancies, either intrinsic or introduced by the involvement of dopants or chemical treatment.[89] The perovskites such as the yttria-doped Ba (Ce, Zr)O_3 (BCY and BCZY) [93,94] oxides are typical examples of this family, displaying superprotonic behaviour at high temperatures, while efforts are also continually being made to develop oxides that conduct protons at intermediate temperature ranges (573-973 K).

(d) Organic/Inorganic composites

The fourth category refers to the association of organic and inorganic systems to form composites with a synergetic effect resulting from both components. As an example, acids like H_2SO_4 or H_3PO_4 are combined to organic systems incorporating basic functions, such as triethylenediamine or polyacrylamide, or incorporated with various polymers, e.g. polyacrylamide.[95,96] Acids can be replaced by others protic solvents, such as heterocyclic bases, pyrazoles, imidazoles and alkyls or ammonium salts, and further immobilized in meso/microporous materials, including polymers, silica, zeolites, phosphates/phosphonates among others.[97–99] In this category, the driving force for the proton conduction is the synergy between the rich source of protons and a structure matrix for the proton transmission provided by the solvent and the porous material, respectively.[100–102]

Proton conductors can also be classified based on the operating conditions i.e., low, medium and high temperature, as listed in Table 1.1. Materials that belong to the low temperature

category operate at T < 373 K. Their proton conductivity is a function of the RH, the higher RH allowing to ensure a high-water concentration to assist the proton migration. Materials with coordinated water (e.g., zirconium sulfoaryl phosphonates,[103] SPEEK,[23] acid-enriched poly diallyl dimethylammonium (PAMA),[104] and PBI [105] maintained at high pressure (e.g. 6 atm)) and porous solids with protic solvents (e.g. imidazole, triazole [97,106]) fall into the second category, operating at intermediate temperature range, i.e. between 373 and 473 K. Finally, lanthanum tungstates (LWO [107,108]) or perovskite-like oxides (e.g., $SrCeO_3$, $SrTiO_3$ [109]) belong to the third set of materials, as they display efficient proton conductivity at high temperature, i.e. usually above 673 K. Figure 1.5 displays the temperature dependence of the proton conductivity for the four categories of proton conducting materials, as classified by Kreuer.

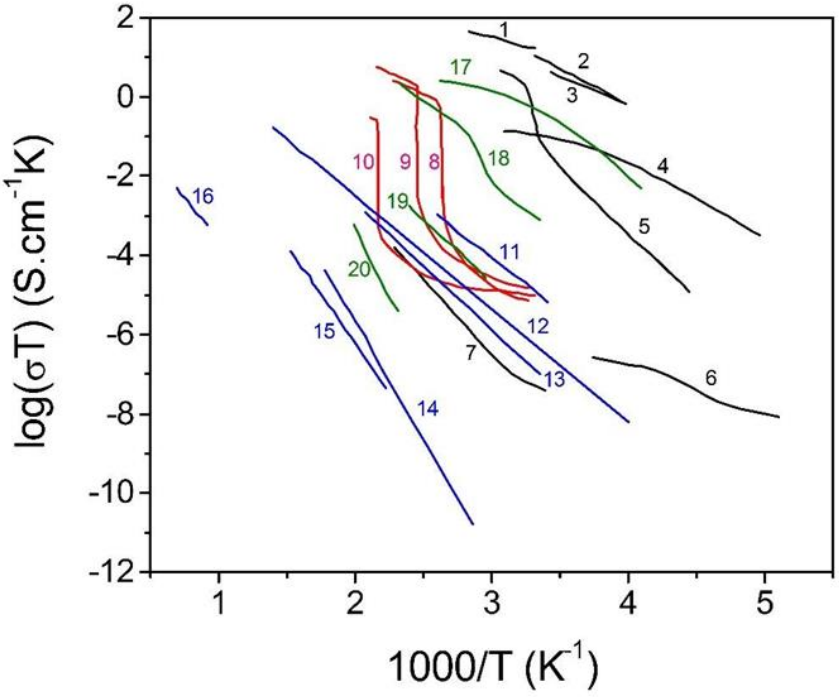

Figure 1.5 – Temperature dependence of the proton conductivity for the 4 different classes of proton conducting materials (adapted from ref.[68]). In black, water containing systems; in red, oxo-acids; in blue, densely packed oxides and in green inorganic/organic systems. The materials considered in this plot are the **1)** Nafion^{TM}, **2)** $H_4SiW_{12}O_{40}\cdot 28H_2O$, **3)** γ-Zr sulfophosphonates, **4)** $SnO_2\cdot nH_2O$, **5)** $H_3UO_2AsO_4\cdot 3H_2O$, **6)** ice, **7)** H_2O – β-alumina, **8)** $(Cs,Tl)HSO_4$, **9)** $CsHSO_4$, **10)** $RbHSO_4$, **11)** Nd:$BaCeO_3$, **12)** Y:ZrO_3, **13)** Y:$SrCeO_3$, **14)** $FeLiNbO_3$, **15)** Ni:$KTaO_3$, **16)** Y_2O_3, **17)** polyacrylamide$\cdot 1.2H_2SO_4$, **18)** poly(ethylene oxide) – NH_4ClO_4 blend, **19)** α-$Zr(HPO_4)_2$/0.75 pyrazole and **20)** $Zr(PO_3(CH_2)_5COOH)_2$.

1.3. Metal Organic frameworks

1.3.1. Metal organic frameworks (MOFs)

Metal Organic Framework, abbreviated as MOFs, are a relatively new class of crystalline and hybrid porous solids originating from the assembly of inorganic and organic molecular building blocks by coordination bonds into crystalline frameworks with inherent porosity. According to IUPAC, a MOF is also defined as "a Coordination Polymer" or alternatively "Coordination Network", with an open framework containing potential voids.[110] The inorganic sub-units, usually termed as Secondary Building Units (SBU), are constituted by metallic nodes of polyhedrals, clusters, chains or layers. They can be constructed using all the elements of the periodic table, ranging from alkaline earth metals (Ca, Mg...), p block elements (Al, Ga, In...), transition metals (Sc, Ti, V…) to lanthanides (Figure 1.6). Similarly, a large variety of multidentate organic moieties are considered to form MOFs linkers, including aliphatic or aromatic compounds with anionic or neutral complexing groups such as O and N donors, e.g. polycarboxylates, polyphosphonates, polysulfonates, imidazolates, polypyrazolates, polytetrazolates (Figure 1.7)… Therewith, the almost infinite possible organic-inorganic combinations generate crystalline mono, di or three-dimensional frameworks with a large variety of topologies and compositions (Figure 1.8).[111–114] The abundance of available molecular building blocks in combination with different topologies gives rise to huge number of possible structures, as exemplified by discovery of more than 90,000 MOFs and over 500,000 MOFs-based structures predicted.[115,116] As an illustration, the most famous MOFs are depicted in Figure 1.9.

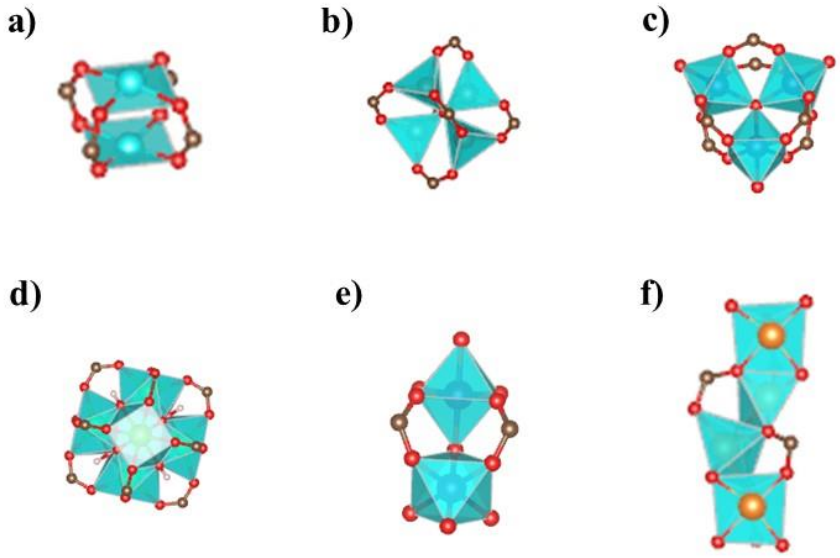

Figure 1.6 – Examples of inorganic secondary building units (SBU) commonly occurring in MOFs **a)** $M_2(CO_2)_4$ (M = Cu, Zn, Fe, Mo, Cr, Co, Ru), **b)** $Zn_4O(CO_2)_6$, **c)** $M_3O(CO_2)_6$ (M = Zn, Cr, In, Ga), **d)** $Zr_6O_8(OH)_4(CO_2)_{12}$, **e)** $M_3O_3(CO_2)_3$ (M = Zn, Mg, Co, Ni, Mn, Fe, Cu), **f)** $Al(OH)(CO_2)_2$.

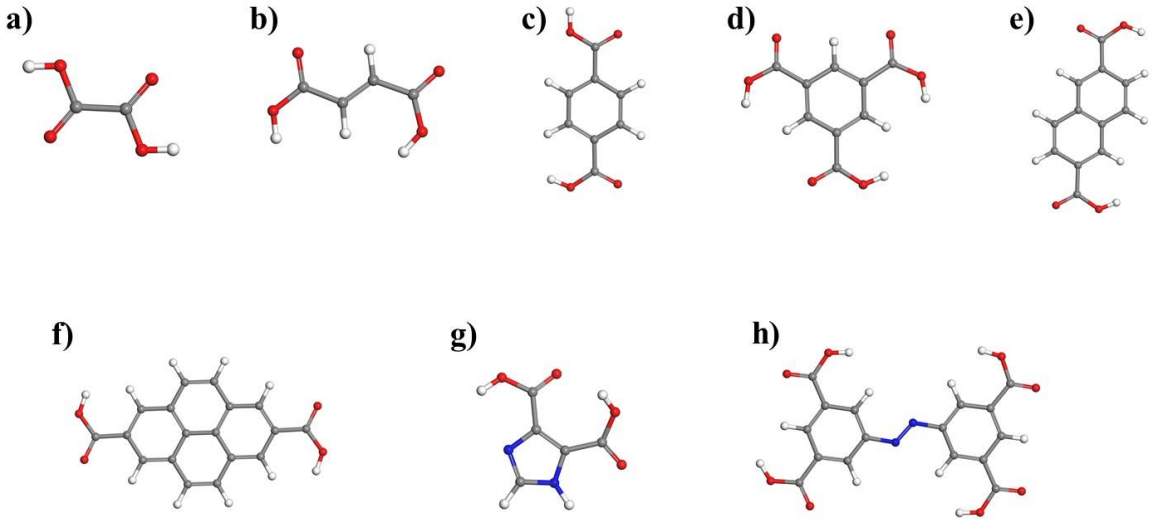

Figure 1.7 – Examples of organic linkers encountered in MOFs. **a)** oxalic acid, **b)** fumaric acid, **c)** 1,4-benzene dicarboxylic acid, **d)** 1,3,5-benzene tricarboxylic acid, **e)** 2,6-naphthalene dicarboxylic acid, **f)** 2,7-pyrene dicarboxylic acid, **g)** 1H-imidazole-4,5-dicarboxylic acid **h)** 3,3',5,5'-azobenzene tetracarboxylic acid. Carbon (grey), hydrogen (white), oxygen (red) and nitrogen (blue).

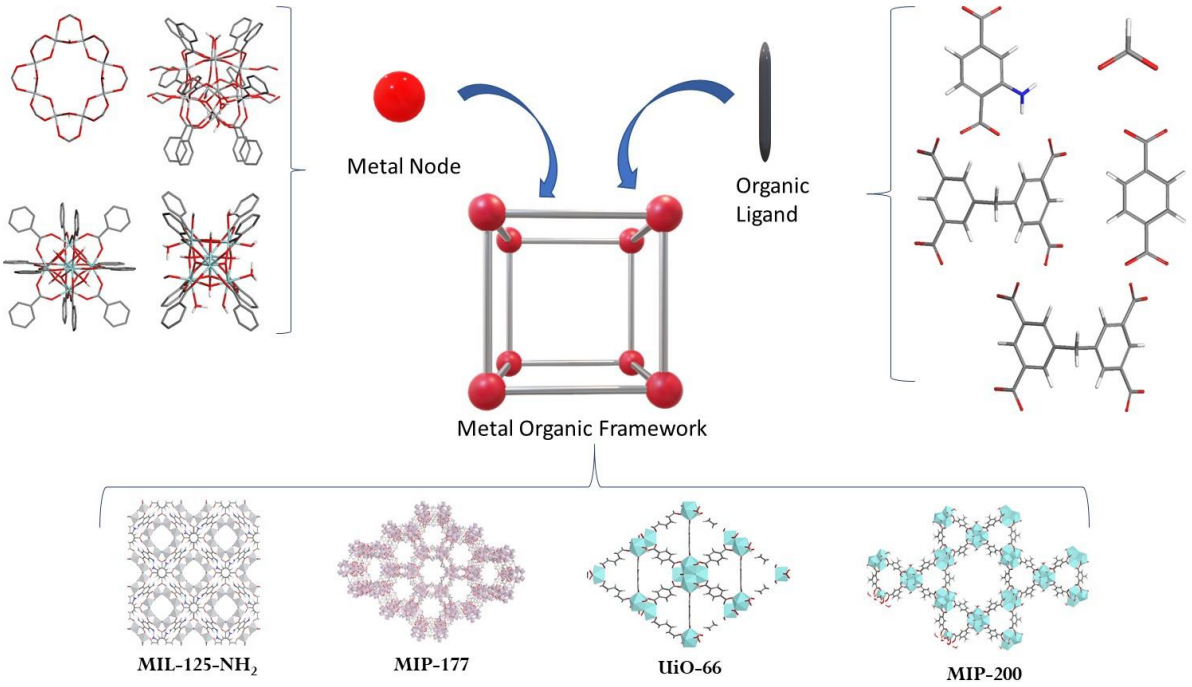

Figure 1.8 – Examples of inorganic secondary building units (SBU) and organic ligands combination commonly occurring in MOFs.

From a synthesis point of view, MOFs are prepared using different routes, including the conventional hydro/solvothermal synthesis method, resulting in the combination of the organic ligands and the cationic sources in a polar solvent.[117] In addition to room temperature synthesis, conventional electric heating, microwave heating and complementary routes including electrochemistry, mechanochemistry and ultrasonic methods have been employed.[118] After activation, one obtains porous hybrid materials stable up to 673 K for some of them, and showing exceptional textural and structural features: highly regularized pores with very high porosity (up to surface areas and pore volume of 7000 $m^2.g^{-1}$ (BET) and 4.4 $cm^3.g^{-1}$ respectively) [119] and diameters ranging from microporous (a few Å) to mesoporous (20-500 Å) scales,[120] in combination with modular structures (rigid and flexible) and high crystallinity with tailorable topologies and chemical functionalities.[114,120–127] Due to these unique features, MOFs are very attractive for diverse industrial and societal applications.

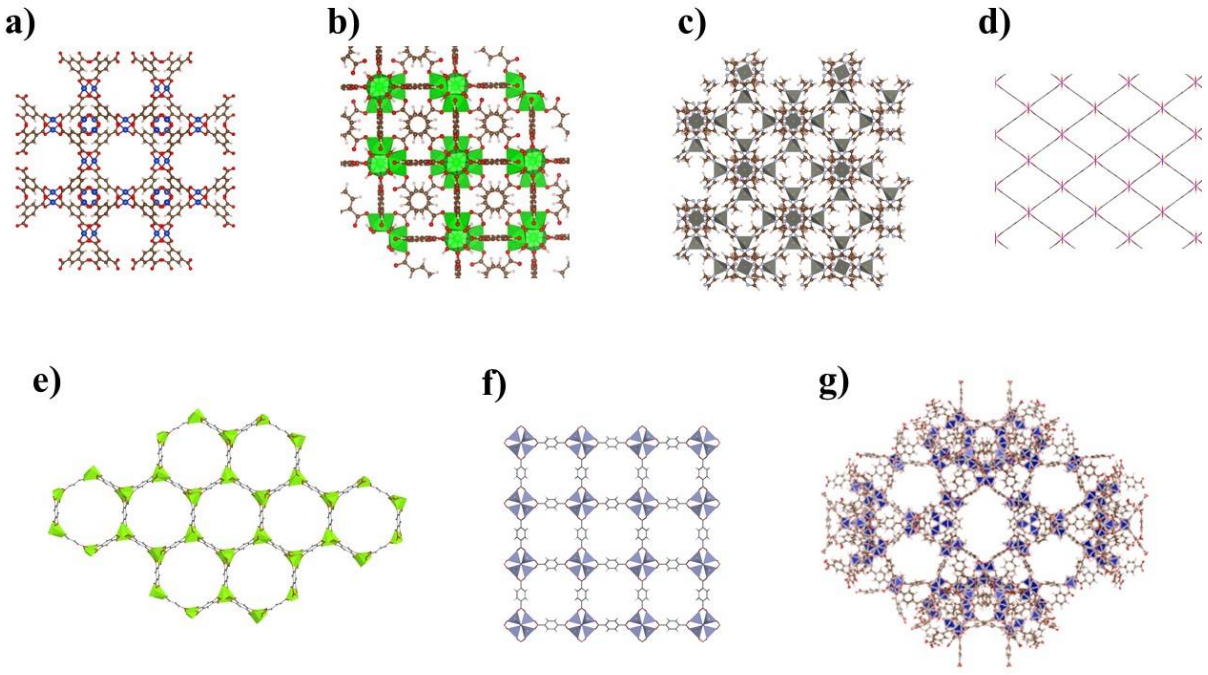

Figure 1.9 - Most iconic MOFs structures **a)** HKUST-1,[128] **b)** UiO-66,[129] **c)** ZIF-8,[130] **d)** MIL-53,[131] **e)** MOF-74,[132] **f)** MOF-5 [133] and **g)** MIL-101.[134]

1.3.2. Applications of Metal organic frameworks

In the past three decades, MOFs have emerged as promising candidates versus conventional porous solids, i.e. zeolites, mesoporous silica or activated carbons, for a wide range of environmental, health or energy applications.[135] A non-exhausted list of potential applications is given below:

(a) Gas storage and separation

Significant progress has been made in enhancing the affinity of MOFs for a specific adsorbate through ligand modification or the design of imperfect structure with open metal sites. These led to remarkable milestones in the field of H_2, CO_2 and CH_4 storage, CO_2 capture, acetylene/ethylene and propylene separation or toxic gas separation such as CO, NO_x, NH_3, SO_2 and H_2S.[136–138] In the same way, Volatile Organic Compounds (VOCs) were also considered in this field, as exemplified with the separation of xylene isomers.[139,140]

(b) Catalysis

MOFs are commonly employed as heterogeneous catalysts considering pristine solids or post-synthetic modified ones, bearing open coordination sites on the metal nodes or organic linkers as catalytic sites.[141–144] MOFs can also be considered as hosts to immobilize metal nanoparticles as catalytic species. In this context, electro- and photo-catalytic reactions were envisaged. Among the large collection of catalytic reactions using MOFs have used for the hydrogenation of olefins, oxidation of alcohols, CO oxidation among, CO2 reduction, water splitting among others…[59,142]

(c) Biomedical applications

MOFs have been successfully proposed for different bio-applications,[145–147] more specifically as cargos encapsulating agents (drugs, nucleic acids, proteins and dyes) for drug delivery with a controlled release of therapeutically active molecules (drugs, cosmetics, biological gases) but also as contrast agents for different imaging techniques, such as magnetic resonance imaging or tomography. In addition, MOFs were also considered for diverse therapeutic strategies, e.g., photodynamic therapy and radiotherapy, as they can absorb exogenous energy, light or X-rays, and convert it into local therapeutic effects.

(d) Chemical sensing

Based on the great promises of MOFs for adsorption and separation applications, they were envisaged as sensitive and selective chemical sensors, using various sensing approaches including optical, electromechanical, electrochemical, chemoresistive, chemocapacitive sensors, considering bulk MOFs or as a film coated on various supports (QCM, SAW, IDE…).[148–156] In this context, MOFs were explored as gas and vapour sensors. The intensive research efforts in recent years have highlighted their wide applicability range, from oxygen and humidity sensors, to toxic gases (NH_3, H_2S, NO_x, SO_x and CO_x), VOCs (aromatic and aliphatic hydrocarbons, ketones, alcohols, aldehydes, BTEX, polycyclic aromatic hydrocarbon), chemical warfare agents and explosives just to name a few.

(e) Electronic and ionic conduction

In the past two decades, MOFs have proven to be excellent candidates in electrochemical devices [157–159] dedicated to i) energy conversion, as solar cells, fuel cells, white light emitting diiodes and ii) energy storage, as supercapacitors or as metal (Zn/Al)-air and metal (Li/Na)-ion batteries, that require some combination of electronic and ionic conductivity.[160,161] Since MOFs are typically considered as poor conductors, efforts have been dedicated to induce electronic conductivity via "through-bond" and "through-space" approaches.[162] Promote electron delocalization can be achieved by considering conjugated 2D MOFs, redox-active moieties to provide charge hopping pathways, conductive molecular-scale bridges or guest molecules that can be engaged in donor-acceptor charge transfer interactions with the MOF.[163]

Regarding ion-conductive MOFs as electrolytes for fuel cells and secondary batteries applications, porous or channel structures of MOFs are fundamentally suitable for ion-conducting pathways.[164,165] Various ionic carriers were considered, such as proton (H^+), hydroxide ion (OH^-), lithium ion (Li^+), sodium ion (Na^+), magnesium ion (Mg^{2+}), zinc (Zn^{2+}) and aluminium (Al^{3+}). For H^+ and OH^- species, MOFs can provide both ions and conducting media, while the other ion carriers are incorporated considering the counter ions of the framework having opposite charges or using inclusion with counter ions as its salt. Remarkably, protons are the most widely investigated ionic carrier, as evidenced by the discovery of a large panel of proton-conducting MOFs. The following section is dedicated to this field.

1.3.3. Features for creating proton conductivity in MOFs

Over the past decade, the exploration of MOFs as proton conductors have attracted wide attention.[166–173] Compared with conventional materials, MOFs offer great opportunities to control the conductivity at the molecular level and tune the proton transport, owing to their tailorable structure, crystallinity, high porosity, rich chemistry and chemical/thermal stability. These inherent features allow to load in MOFs a variety of guest molecules as proton carriers and to systemically modify the proton concentration and mobility within the available space. Beyond the generation of super-protonic conduction, the crystalline nature of MOFs is also beneficial for understanding the proton conducting pathway and the corresponding mechanism to control the structural-conductivity relationships and further design outstanding materials. In order to improve

proton conductivity of MOFs, efforts have been pushed to increase the concentration and mobility of the proton carriers. While the overall acidity of the proton sources governs the proton carrier concentration, the mobility of protons can be promoted by a continuous H-bond network comprising protic sites, hydrophilic guests, a framework with optimal pore connectivity and also by creating ordered defects through which proton transfer takes place. Accordingly, different strategies have been envisaged to promote proton conductivity in MOFs,[174–178] depending on the operating conditions, i.e. anhydrous or hydrated conditions. The main approaches, illustrated in Figure 1.10 consist in i) generating proton carriers as counter ions of anionic framework of MOFs, ii) incorporating acidic functional groups into the host framework, iii) creating open metal sites to create defects or coordinate functional molecules, iv) loading protic species as proton carriers into the voids of MOFs, v) inducing structure phase transformations. These strategies are further detailed below.

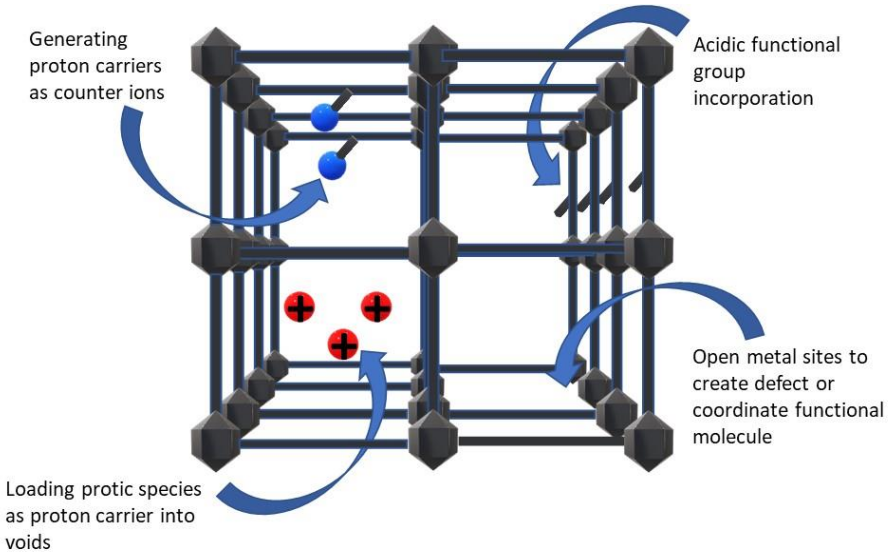

Figure 1.10 – Features for creating proton conductivity in MOFs, as detailed in the text.

1.3.3.1. Inherent proton carriers as counter ions into the pores of MOFs

There are several MOFs reported where metal coordination creates anionic framework, neutralized by various cationic molecules, e.g. NH_4^+, H_3O^+, $Me_2NH_2^+$ and $Et_2NH_2^+$ trapped inside the framework.[12,179,180] These trapped cations behave as proton transfer sites and initiate the

conduction process under humid conditions. The pioneer investigation was reported by Kitagawa *et al*.,[181] considering the zinc oxalate-based framework $(NH_4)_2$(adp)-$[Zn_2(ox)_2].3H_2O$. The proton conductivity of this MOF (σ = 8 x 10^{-3} S.cm^{-1} at 298 K under 98% RH) is due to the extended hydrogen-bonded network between ammonium (NH_4^+) cations, adipic (adp) acids and water (H_2O) molecules inside the interlayer space of the MOF 2D network. This strategy was also efficient for designing proton conducting MOFs at the anhydrous state,[182] as illustrated by an anionic Europium based MOF neutralized by $(Me_2NH_2)^+$ species, which shows anhydrous conductivity of 1.25 x 10^{-3} S.cm^{-1} at 423 K, and water-assisted proton conductivity of 3.76 x 10^{-3} S.cm^{-1} at 373 K and 98% RH.

1.3.3.2. Inherent water assisted proton conducting MOFs

The proton conduction can be efficiency achieved by inherent water molecules inside the MOF backbone, i.e., H_2O coordinated to the metal centre and those trapped inside the open space of the pore area. The first example relies on a ferrous oxalate dihydrate MOF, which shows proton conductivity of 1.3 x 10^{-3} S.cm^{-1} at 298 K under 98% RH.[183] The H_2O coordinated to Fe^{2+} species, i.e. a Lewis acid site, is more acidic with easier proton donation than free H_2O molecules. The proton is then substracted from the coordinated water molecules in presence of humidity, while the one-dimensional (1D) ordered array of the coordinated water combined with the self-organization of the adsorbed water facilitates the formation of the H-bonded network for transporting protons through the pores. Interestingly, a similar proton transfer mechanism was further demonstrated by ICGM using a combined experimental/computational strategy [184] applied on the 2D KAUST-7' MOF (σ = 2.0 x 10^{-2} S.cm^{-1} at 363 K and 95% RH). As reported, the adsorbed H_2O serves as a bridge, connecting species coordinated to the metallic node, i.e., water molecules and fluorine atoms, resulting in a continuous cleavage/formation of H-bond interactions between the adsorbed H_2O, F^- and the coordinated H_2O.

1.3.3.3. Organic linker modification

Intrinsic proton sources can be achieved by attracting hydrophilic and acidic functional groups to the organic ligand of MOFs by predesigned or post-synthetic chemical reactions. This approach was largely explored to improve the proton concentration and mobility within the pores.

Shigematsu *et al*.,[185] reported the first representative example of the acidic group-dependent proton conductivity, by investigating MIL-53(Al) analogues, whose ligand was functionalized by $-NH_2$, -OH or $–(COOH)_2$ groups. They demonstrated that the nature of the attached group affects the proton transport performances, in correlation with the acidity (pKa) of the framework. A similar trend was observed by Li *et al*., in the case of UiO-66(Zr) derivatives.[186] To further increase the charge carrier density, stronger proton donors than the previous ones were envisaged, using post-synthetic functionalization of the MOFs backbone by $-PO_3H$ and $-SO_3H$ groups. It results in the development of proton conductivity surpassing 10^{-2} $S.cm^{-1}$ under hydrous conditions.[187–190] As a further step, Das *et al*., demonstrated that the conductivity can be even more improved up to 1.00×10^{-1} $S.cm^{-1}$ at 353 K and under 95% RH, by enlarging the alkyl chain attached to the ligand and bearing acidic group at its tail, due to a better accessibility of the Brønsted acid sited to the adsorbed water molecules.[191]

As an alternative, a multicomponent approach was considered by Shimizu *et al*., based on the isomorphous ligand replacement of β-PCMOF-2 to form the mixed ligand MOF β-PCMOF-2½, via partial substitution of 1,3,5-benzene-trisulfonate by 1,3,5-benzene-triphosphonate moieties of comparable size and shape.[192] The proton conductivity value of the parent MOF was improved by 1.5 orders of magnitude to reach 2.1×10^{-2} $S.cm^{-1}$ at 358 K and 90% RH, due to the increase of the number of freely available acidic protons from the backbone. This successful strategy was then extended to other series of organic linkers, considering naphthalene core units instead of benzene moieties, as exemplified for VNU-15(Fe) [193] and Cu-SAT.[194]

1.3.3.4. Metal node modification

Metal unit manipulations, including the metal ion replacement, the coordinative insert of functional molecules and the metal-centre missing as a defect site, were explored to generate proton-conductive MOFs. Accordingly, the impact of metal size, Lewis acidity, electronegativity, ability to provide unsaturated coordinative site and thermal stability was investigated.

Metal site replacement was firstly documented.[195] As an example, Demadis *et al*., investigated a series of alkali (Li, Na, K and Cs) metal phosphonocarboxylated, and observed a gradual increase in the dimensionality of the network, from 1D (Li) to 2D pillared-layered (Na)

and 3D (K, Cs), with the ionic radius of the alkali.[196] The resulting conductivity value is in the range 3.50 x 10^{-5} S.cm^{-1} for Cs to 5.60 x 10^{-3} S.cm^{-1} for Na, while the relationship between the ionic radius of the metal ion and the conductivity is not straight forward, due to structural changes.

Liu *et al*., proposed a combined strategy applied on MIL-88B, by the replacement in the Fe^{3+} based metallic nodes by Cr^{3+} analogous to enhance the structural stability of the parent solid, followed by the subsequent coordinative insertion of 3-pyridine sulfonic acid (PSA) and 2-(4-pyridyl) ethane sulfonic acid (PESA) as proton sources.[197] At 363 K and 85% RH, Cr-MIL-88B shows conductivity of 6.00 x 10^{-3} S.cm^{-1}, while for Cr-MIL-88B-PESA and Cr-MIL-88B σ = 4.50 x 10^{-2} and 1.58 x 10^{-1} S.cm^{-1}, respectively. Alternative species were coordinated to the metal nodes of various MOFs to create super-protonic conductors, as exemplified by the hydrogen-sulphate decorated titanium-based MIP-177-SO_4-LT,[198] Im-Fe-MOF displaying coordinated imidazole molecules at the metal centre [100] or more surprisingly by the coordinative urea insertion MOF-74 without any acidic moiety.[199] In the later case, the highly polarized urea bound to open metal sites is attractive for the guest H_2O molecules, resulting in the formation of an efficient hydrogen bond network.

Finally, missing metal centre was used to provide local defects and dangling linkers, expected to act as favourable proton conduction pathways. Intrinsic and extrinsic defects can be produced by using additive during the MOF synthesis or induced by metal or ligand replacement after MOF synthesis, respectively. As reported, missing metal linker connectivity in TMOF-2 induces unsaturated metal sites, resulting in an enhanced affinity of the MOF to water molecules, and consequently an improved proton conductivity by two orders of magnitude compared to its structural analogue TMOF-1 [200] ((σ = 1.23 × 10^{-4} S.cm^{-1} and 1.62 × 10^{-6} S.cm^{-1} at 363 K and 98% RH for TMOF-2 and TMOF-1, respectively). However, the control of the proton conductivity properties by introducing defective metal nodes is not straightforward, as evidenced by the detrimental proton-trapping effect in the case of Zr-based MOFs: the partial defects indeed decrease the mobile proton concentration, playing the role of an intrinsic buffer.[201]

1.3.3.5. Framework topology or structure change

The network topology and degree of interpenetration was demonstrated to play a key role for tuning the properties of water-assisted conductive MOFs, by impacting the solvent loading. As

reported by Xiang and co-workers, the In-based anionic FJU-17 displays higher conductivity (σ = 1.08 x 10^{-2} S.cm^{-1} at 373 K under anhydrous conditions) than the iso-structural FJU-16, in relation with the lower degree of interpenetration, i.e. two-fold and four-fold interpenetration respectively, which favors the accessibility of adsorbed water.[202]

On the other hand, humidity-induced insulator-to-proton-conductor transition was evidenced in a few series of MOFs, resulting from a structural transition towards a less dense MOF phase with water uptake.[184,203] When the abrupt change of conductivity is reversible, potential applications of such MOFs as humidity sensors were suggested.[203] As demonstrated by Kitagawa *et al*., the layered MOF, $(NH_4)_2(adp)[Zn_2(ox)_3]\cdot nH_2O$ (n = 0, 2, and 3) displays a huge insulator to superprotonic conductor transition ($\sigma \sim 10^{-12}$ to $\sim 10^{-2}$ S.cm^{-1} at room temperature) with the atmospheric humidity, resulting from the reversible structural transformations among the anhydrated and trihydrated phases.[204] These structural transformations modify the hydrogen-bonding networks consisting of ammonium ions, water molecules and carboxylic acid groups of the adipic acids inside the 2D interlayer space in the hydrated MOFs, according to the water content. Interestingly, single-crystal to single crystal (SCSC) transformations can also be induced by ligand substitution or temperature increase.[182,203–207] As an example, Bao *et al*., reported a layered 3d-4f phosphonate based MOF able to undergo a solid state phase transformation at 318 K/93% RH, accompanied by the release of protons from the intralayer phosphonate groups towards the interlayer space occupied by lattice water molecule.[205] This results in the formation of hydronium species, responsible for the 10-fold increase of the MOF proton conductivity. This insulator to proton conductor transition induced by SCSC transformations was also evidenced for denser MOFs, as illustrated in the case of the 3D $((CH_3)_2NH_2)_2[Li_2Zr(C_2O_4)_4]$.[203]

Similarly, the phase transition of MOFs from crystal to glass was considered to enhance proton conductivity, in order to overcome the detrimental effect of grain boundaries among the crystallites sometimes causing additional resistance, as discussed in chapter 2. In this context, Horike *et al*., demonstrated that the glassy state of a phosphonate-based MOF displays better proton conductivity than the crystalline analogue.[208,209] Owing to the isotropic disordered nature of the glassy state combined with the less rigid glassy structure, H^+ dynamics is enhanced and provides interesting σ value at the anhydrous conditions (σ = 8.00 x 10^{-3} S.cm^{-1} at 393 K).

1.3.3.6. Guest loading into the pores

Owing to their high porosity, MOFs were filled by charge-neutral proton carriers and functional guest molecules, such as non-volatile acidic molecules, protic heterocyclic organic molecules, polyoxometalate (POM) or metal-organic polyhedral (MOP) molecules and ionic liquids, to get high proton conductivity by increasing proton source and/or carrier concentrations.

For acid guest incorporation, e.g. H_3PO_4, H_2SO_4, CF_3SO_3H, TfOH, the mesoporous and highly stable MIL-101 structure was privileged.[11,210] Excellent proton conducting performances were recorded under both humid ($\sigma = 4.00 \times 10^{-2}$ S.cm^{-1} at 353 K and 90% RH) and anhydrous ($\sigma = 3.00 \times 10^{-3}$ S.cm^{-1} at 323 K) conditions. Furthermore, the synergic effect of H_2SO_4 impregnation combined with the sulfonic functionalization of ligands on the proton conductivity of MIL-101 was also established,[211,212] with σ value exceeding 1.00 S.cm^{-1} at 343 K and 90% RH.

Regarding the incorporation of N-heterocyclic compounds into MOFs voids, a large panel of protic organic molecules was explored, including imidazole, triazole, pyrazole, histamine, benzimidazole etc.[192,213,214] The resulting composites display a superprotonic behaviour under anhydrous conditions ($\sigma > 10^{-2}$ S.cm^{-1} at T > 373 K), resulting from a better control of the carrier mobility in confined nanospaces of MOFs compared to their motion in the bulk state.

In addition, proton conductive MOP [215] and POM [216,217] have recently attracted a few attention as alternative functional material inclusions in MOFs. The later acts as a stabilizing matrix of the guest, promoting the temperature range for recording the proton conducting performances in a larger extended, while a judicious choice of the MOP, such as bearing sulfonate functional groups, was demonstrated to modulate the hydrophilicity of the MOF hosting framework, with beneficial advantages on the proton conductivity performances.[218] Up to now, the resulting proton conductivity properties of these composites (in the order of 10^{-3} S.cm^{-1} at 353 K and 98% RH) are lower compared to those of other MOF-based composites, which calls for further improvements to satisfy the criteria for applying this category of composites as a solid-state proton electrolytes. Accordingly, some efforts have been dedicated to fabricate hybrid membranes by mixing these composites with polymers, even if the proton conductivity gain is still very small, i.e., only 3-fold increase of the properties.

As a promising alternative, microporous and mesoporous MOFs were also investigated as a porous support for the incorporation of various ionic liquids, to tune the intermolecular interactions of the ions constituting the ionic liquid for a better control of its phase behaviour and its corresponding conductivity.[219–221] Binary ionic liquids were also envisaged resulting in Brønsted acid-base buffers with the synergetic introduction of both H^+ -source and H^+-defect sites promoting the transport hopping process.[222–224] In comparison with the behaviour of the bulk ionic liquid, the proton transport properties of the confined species were found to be enhanced, as a result of its optimal spatial distribution within the MOF pores. Noteworthy, these composites were mostly investigated under anhydrous conditions with proton conductivity reaching 1.00×10^{-2} $S.cm^{-1}$ at 343 K,[225] while a few of them were studied under humid conditions, showing promising performances around 4.40×10^{-2} $S.cm^{-1}$ at 323 K under 23% RH.[226]

Appendix 1.1 & 1.2 reports the full list of MOFs showing proton conductivity exceeding 10^{-3} $S.cm^{-1}$. These MOFs are classified as anhydrous and water-mediated proton conductors.

1.3.4. MOFs-based crystalline composite membranes for PEMs applications

In the context of MOF-based electrolytes for PEMFCs applications, MOFs processing and formulation are required. Regarding the difficulties to process MOFs in their as-synthesized microcrystalline form and the lack of their ability to form thick films, some efforts were devoted to the preparation of MOFs-based mixed-matrix membranes (MMMs), by the incorporation of MOFs into polymeric matrix to create composites. The later combine the advantages of both fillers and polymer membranes, such as good reproducibility, high chemical and thermal resistance and relatively economical processing. Generally, the polymer stabilizes the mechanical properties of the system and fill the MOF grain boundaries (cf chapter 2), while the MOFs fillers act to raise proton conductivity, which is transferred to the composite membranes through MOF/polymer interfaces. Successful hybridization of MOFs and polymers thus requires i) good compatibility between the MOF fillers and the polymer matrix to avoid interfacial defects, ii) judicious selection of MOFs with functional groups able to form H-bonding chains to insure proton transfer in the polymeric matrix and iii) excellent distribution of the MOF particles inside the polymer to prevent irregular voids and membrane fragility.[24,227,228] Various proton conducting hybrid membranes are documented with well-known MOFs e.g., MIL-101s, UiOs, ZIFs…, incorporated

in polymers basically employed for PEMs applications, including Nafion^{TM} series, polyvinylpyrrolidone (PVP), poly(4-styrenesulfonate) PSS, polyvinylidene fluoride (PVDF), SPEEK, PBI, chitosan (CS) among others. The following section gives a brief overview of the main strategies developed to get promising MOF/polymer proton conductors. A more complete list of the best composites, along with their proton conducting performances, is available in appendix 1.3.

The first MOF/polymer composite was reported by Zhu *et al*., in 2013 using PVP as the polymer matrix and a chiral 2D MOF material, bearing protonated tertiary amines as intrinsic proton carriers and H-bonding chains as proton-conducting pathways.[227] Despite the unsatisfactory proton conductivity performances of the composited, this study has the merit of proposing a straightforward and universal strategy for practical utilization of MOF materials as PEMs for fuel cells applications. Since then, a large series of Nafion^{TM} blended composites were investigated considering various hydrophilic MOFs, i.e. CPO-27,[229] MIL-53(Al),[229] MIL-101s,[230] UiO-66s,[231] Zr-MOF-808,[232] resulting in materials exhibiting a better conductivity than that of the pristine Nafion^{TM} under high humidity conditions (RH = 95%). Many efforts were firstly dedicated to the elaboration of MMMs by the incorporation of MOFs showing inherent proton conductivity. As an example, sulphated functionalized MOFs, e.g. Zr-MOF-808 (SZM) [232] was considered PVP as a filler in Nafion^{TM}: the Brønsted acidic sites significantly retain water inside the composite and also serve as additional proton source, leading to good membrane performers. The gain in proton conductivity for MOF-based composites versus that of the pure polymer is not restrictive to Nafion^{TM} based membranes. Similarly, proton conductivity recorded at 348 K / 100% RH for the sulfonated MIL-101(Cr)/SPEEK composite ($\sigma = 3.06 \times 10^{-1}$ S.cm^{-1}) is about double to that of the pristine SPEEK membrane ($\sigma = 1.56 \times 10^{-1}$ S.cm^{-1}).[233] Alternatively, to acidic fuctionalized MOFs, amino based MOFs were equally demonstrated as efficient fillers to boost the hydrous proton conductivity to values exceeding that of the pure polymer, as reported for MIL-101(Fe)-NH_2/SPPO (sulfonated poly (2, 6-dimethyl-1, 4-phenylene oxide).[234]

As an alterrnative approach, Wu *et al*., Proposed to incorporate simultaneously inside a Nafion^{TM} matrix two functionalized MOFs, UiO-66-SO_3H and UiO-66-NH_2.[231] The corresponding membrane shows exceptional conductivity (2.56×10^{-1} S.cm^{-1} at 363 K/95% RH),

which is higher compared to that of Nafion^{TM} and of the single dopped composite. This results from the synergistic action of the two hydrophilic functionalized MOFs, displaying high water adsorption capacity: the denser hydrophilic channels of the fillers facilitate the proton migration, through the interaction between the two UiO-66-SO_3H and UiO-66-NH_2 MOFs with minor particle size and the ionic clusters in the membrane. Interestingly, the replacement of the two MOFs by a single amino-sulfo-bifunctionalized filler was demonstrated to have the same beneficial impact on the proton conducting performances.[235]

Another strategy to improve the proton conduction performances of MOF/polymer composites, consists in controlling the shape and morphology of the MOF filler. This was achieved by incorporating graphene oxide (GO) as a third component.[236–238] The resulting performances, exceeding 10^{-1} S.cm^{-1} at 353 K/95% RH, were attributed to the well-oriented pore channels and morphology of the MOF in interaction with GO: the homogeneous anchoring MOF on the GO surface creates a continuous proton transport channel, resulting in the formation of a very efficient H-bond network in the presence of water. Similarly, Wu *et al*., proposed to tune the proton conductivity of MOF/polymer composites via creating more complex architectures of MOFs at the mesoscopic/macroscopic scale: MOF nanocrystals are used as building units to construct higher-order superstructures.[239] ZIF-8 was grown on Carbon Nano Tubes (CNT) to form a hybrid cross-linked network ZIF/CNT, further blended to SPEEK matrix. The resulting composite corresponds to a 2D cross-linked network constructed from curved nanowires composed by internal CNT cores and outer ZIF-8 shells. Its proton conductivity is significantly improved under various conditions as compared to that of the recast SPEEK. It was suggested that the imidazole-based (Hmim) units issued from ZIF-8 shells acts as proton donors (sharing protons on N-H) and proton acceptors (through noncoordinated N atoms). Their interaction with the -SO_3H groups of SPEEK via electrostatic interaction, creates efficient sulfonic acid-Hmim pairs at the filler-SPEEK interfaces. The good compatibility between the MOF and the polymer is then favoured by the morphology of the system characterized by the interlaced cylindrical nanochannels of ZIF/CNT.

As mentioned in the previous section, a promising way to alter the chemical composition of MOFs for improving proton conduction consists in immobilizing inside their pores various proton carriers to form guest@MOFs. A handful of guest@MOF/polymer composites were then

designed with very attractive proton conducting performances under high, medium and low humidity conditions as well. In this context, the conductivity for phytic@MIL-101/Nafion^{TM}, at 353 K is 0.23, 6.08 x 10^{-2} and 7.63 x 10^{-4} S.cm^{-1} at 100% RH, 57% RH and 10% RH respectively.[230] The phytic acid trapped inside the porosity of the mesoporous MOF is able to retain large quantity of water: it shows high density of phosphate groups participating to the hydrogen-bond network with water molecules and sulfuric acid functions of Nafion^{TM}. The σ values cited above are 0.5 times, 2.8 times and 11.0 times higher than those of the pristine membrane, while the mechanical and thermal properties of Nafion^{TM} are maintained. The same strategy was successfully considered to prepare efficient proton conducting CS based composites: various acidic molecules (H_2SO_4, H_3PO_4, CF_3SO_3H) were immobilized inside MIL-101 and MIL-101-SO_3H, before their incorporation to CS.[228] In the same way, ionic liquids and imidazole were also demonstrated as efficient guest molecules to replace non-volatile acid molecules in guest@MOFs/polymer composites.[240–242] Finally, the DNA biomolecule also showed great promises as a guest, as it is a proton-rich linear biomolecule with large number of suitable proton carriers groups.[243] The high conductivity of DNA@ZIF-8/PSS (σ = 0.17 S.cm^{-1} under 97% RH at 348 K) illustrates the fast proton transfer resulting from the H-bonded networks formed by water molecules and phosphate groups of DNA which are optimally oriented once located inside the ZIF-8 nano channels.

Examples cited above refer to composites with attractive proton conducting performances under humid atmosphere. However, under anhydrous conditions or at temperature exceeding 373 K, the situation is much rarely satisfactory. To overcome this challenge, Zhang *et al*., extended the co-doping strategy developed by Wu's group, to fabricated dual MOF-cofilled hybrid membranes using CS as polymer.[244] They created proton conducting membranes able to work under hydrated conditions as in the case of the Nafion^{TM} based composite,[231] but also at the anhydrous state, due to the synergistic "acid-base pair" effect of the acidic (UiO-66-SO_3H) and alkaline (UiO-66-NH_2) MOFs with isomorphous structures on proton conductivity. As reported, the composite exhibits the highest anhydrous conductivity value: σ = 3.78 x 10^{-3} S.cm^{-1} at 393 K, i.e. a value 29.1 times higher than that of pure CS membrane. The -SO_3H and -NH_2 units of UiO-66-based MOFs were evidenced to interact with -OH and -NH_3 or -NH_2 moities of CS to establish efficient H-bonded networks inside the membrane without the help of water. In addtion, -SO_3H and -NH_2

groups of adjacent MOFs particles are able to form acid-base pairs: protons issued from -SO_3H groups can be transfered to NH_2 units used at transport sites, improving the proton conductivity under anhydrous conditions. In the meantime, the co-doped strategy was also applied on other systems to form ZIF-8/ZIF-67/PBI composites, showing exceptional proton conductivity under anhydrous conditions ($\sigma = 9.1 \times 10^{-2}$ S.cm^{-1} at 473 K).[245]

1.4. Conclusion

A handful of reviews has comprehensively enumerated the main proton conducting MOFs reported in literature.[166,169,249–254,171–173,176,178,246–248] We updated this listing with the inclusion of novel MOFs recently evidenced. Appendix 1.1 & 1.2 lists the MOFs that display a superprotonic behavior with σ exceeding 10^{-3} S.cm^{-1}. We deliberatively made the choice to classify the pure MOFs materials as anhydrous and water-mediated proton conductors, separately from the MOFs/polymer composites. We can notice that a large series of the reported materials reach the threshold value of 10^{-2} S.cm^{-1} at low temperature and under humidity conditions, making them very attractive as an alternative solution to the benchmark material (Nafion^{TM}), while some other materials are very promising for applications at the intermediate temperatures.

REFERENCES

[1] W.E. Ayrton, J. Perby, Ice as an Electrolyte. - Second Communication, Proc. Phys. Soc. London. 2 (1875) 199–201. https://doi.org/10.1088/1478-7814/2/1/320.

[2] M. Warshay, P.R. Prokopius, The fuel cell in space: yesterday, today and tomorrow, J. Power Sources. 29 (1990) 193–200. https://doi.org/10.1016/0378-7753(90)80019-A.

[3] M. Winter, R.J. Brodd, What Are Batteries, Fuel Cells, and Supercapacitors?, Chem. Rev. 104 (2004) 4245–4270. https://doi.org/10.1021/cr020730k.

[4] P. Knauth, M.L. Di Vona, Solid state proton conductors : properties and applications in fuel cells, Wiley Subscription Services, Inc., A Wiley Company, Sussex, 2012.

[5] P. Leung, X. Li, C. Ponce De León, L. Berlouis, C.T.J. Low, F.C. Walsh, Progress in redox flow batteries, remaining challenges and their applications in energy storage, RSC Adv. 2 (2012) 10125–10156. https://doi.org/10.1039/c2ra21342g.

[6] C. Ponce de León, A. Frías-Ferrer, J. González-García, D.A. Szánto, F.C. Walsh, Redox flow cells for energy conversion, J. Power Sources. 160 (2006) 716–732. https://doi.org/10.1016/j.jpowsour.2006.02.095.

[7] Y. Gao, P. Jing, N. Yan, M. Hilbers, H. Zhang, G. Rothenberg, S. Tanase, Dual-mode humidity detection using a lanthanide-based metal–organic framework: towards multifunctional humidity sensors, Chem. Commun. 53 (2017) 4465–4468. https://doi.org/10.1039/C7CC01122A.

[8] N. Yamazoe, Y. Shimizu, Humidity sensors: Principles and applications, Sensors and Actuators. 10 (1986) 379–398. https://doi.org/10.1016/0250-6874(86)80055-5.

[9] C. Laberty-Robert, K. Vallé, F. Pereira, C. Sanchez, Design and properties of functional hybrid organic–inorganic membranes for fuel cells, Chem. Soc. Rev. 40 (2011) 961. https://doi.org/10.1039/c0cs00144a.

[10] D. Umeyama, S. Horike, M. Inukai, T. Itakura, S. Kitagawa, Inherent Proton Conduction in a 2D Coordination Framework, J. Am. Chem. Soc. 134 (2012) 12780–12785. https://doi.org/10.1021/ja304693r.

[11] V.G. Ponomareva, K.A. Kovalenko, A.P. Chupakhin, D.N. Dybtsev, E.S. Shutova, V.P. Fedin, Imparting high proton conductivity to a metal-organic framework material by controlled acid impregnation, J. Am. Chem. Soc. 134 (2012) 15640–15643. https://doi.org/10.1021/ja305587n.

[12] S.S. Nagarkar, S.M. Unni, A. Sharma, S. Kurungot, S.K. Ghosh, Two-in-One: Inherent Anhydrous and Water-Assisted High Proton Conduction in a 3D Metal-Organic Framework, Angew. Chemie Int. Ed. 53 (2014) 2638–2642. https://doi.org/10.1002/anie.201309077.

[13] W.T. Grubb, L.W. Niedrach, Batteries with Solid Ion-Exchange Membrane Electrolytes, J. Electrochem. Soc. 107 (1960) 131. https://doi.org/10.1149/1.2427622.

[14] W. Grot, Perfluorierte Ionenaustauscher-Membrane von hoher chemischer und thermischer Stabilität, Chemie Ing. Tech. 44 (1972) 167–169. https://doi.org/10.1002/cite.330440408.

[15] W. Grot, Use of Nafion Perfluorosulfonic Acid Products as Separators in Electrolytic Cells, Chemie Ing. Tech. 50 (1978) 299–301. https://doi.org/10.1002/cite.330500415.

[16] M. Casciola, G. Alberti, M. Sganappa, R. Narducci, On the decay of Nafion proton conductivity at high temperature and relative humidity, J. Power Sources. 162 (2006) 141–145. https://doi.org/10.1016/j.jpowsour.2006.06.023.

[17] K.A. Mauritz, R.B. Moore, State of Understanding of Nafion, Chem. Rev. 104 (2004) 4535–4586. https://doi.org/10.1021/cr0207123.

[18] A. Kraytsberg, Y. Ein-Eli, Review of Advanced Materials for Proton Exchange Membrane Fuel Cells, Energy & Fuels. 28 (2014) 7303–7330. https://doi.org/10.1021/ef501977k.

[19] M. Casciola, G. Alberti, M. Sganappa, R. Narducci, On the decay of Nafion proton conductivity at high temperature and relative humidity, J. Power Sources. 162 (2006) 141–145. https://doi.org/10.1016/j.jpowsour.2006.06.023.

[20] H.-Y. Jung, J.W. Kim, Role of the glass transition temperature of Nafion 117 membrane in the preparation of the membrane electrode assembly in a direct methanol fuel cell (DMFC), Int. J. Hydrogen Energy. 37 (2012) 12580–12585. https://doi.org/10.1016/j.ijhydene.2012.05.121.

[21] N. Zamel, X. Li, Effect of contaminants on polymer electrolyte membrane fuel cells, Prog. Energy Combust. Sci. 37 (2011) 292–329. https://doi.org/10.1016/j.pecs.2010.06.003.

[22] X. Teng, Y. Zhao, J. Xi, Z. Wu, X. Qiu, L. Chen, Nafion/organic silica modified TiO2 composite membrane for vanadium redox flow battery via in situ sol–gel reactions, J. Memb. Sci. 341 (2009) 149–154. https://doi.org/10.1016/j.memsci.2009.05.051.

[23] Amir-Al-Ahmed, A.S. Sultan, S.M.J. Zaidi, Sulfonated Poly(Ether Ether Ketone) (SPEEK): A Promising Membrane Material for Polymer Electrolyte Fuel Cell, in: Ion Exch. Technol. I, Springer Netherlands, Dordrecht, 2012: pp. 437–451. https://doi.org/10.1007/978-94-007-1700-8_12.

[24] S. Mukhopadhyay, A. Das, T. Jana, S.K. Das, Fabricating a MOF Material with Polybenzimidazole into an Efficient Proton Exchange Membrane, ACS Appl. Energy Mater. 3 (2020) 7964–7977. https://doi.org/10.1021/acsaem.0c01322.

[25] J. Miao, Y. Liu, Q. Tang, D. He, G. Yang, Z. Shi, S. Liu, Q. Wu, Proton conductive watery channels constructed by Anderson polyanions and lanthanide coordination cations, Dalt. Trans. 43 (2014) 14749–14755. https://doi.org/10.1039/C4DT01715C.

[26] S.M. Haile, D.A. Boysen, C.R.I. Chisholm, R.B. Merle, Solid acids as fuel cell electrolytes, Nature. 410 (2001) 910–913. https://doi.org/10.1038/35073536.

[27] O. Nakamura, T. Kodama, I. Ogino, Y. Miyake, HIGH-CONDUCTIVITY SOLID PROTON CONDUCTORS: DODECAMOLYBDOPHOSPHORIC ACID AND DODECATUNGSTOPHOSPHORIC ACID CRYSTALS, Chem. Lett. 8 (1979) 17–18. https://doi.org/10.1246/cl.1979.17.

[28] R.C.T. Slade, J. Barker, H.A. Pressman, Studies of protonic self-diffusion and conductivity in 12-tungstophosphoric acid hydrates by pulsed field gradient 1H NMR and ac conductivity, Solid State Ionics. 28–30 (1988) 594–600. https://doi.org/10.1016/S0167-2738(88)80108-5.

[29] S.J. Peighambardoust, S. Rowshanzamir, M. Amjadi, Review of the proton exchange membranes for fuel cell applications, Int. J. Hydrogen Energy. 35 (2010) 9349–9384. https://doi.org/10.1016/j.ijhydene.2010.05.017.

[30] V. Evoen, Electrocatalysis in Solid Acid Fuel Cell Electrodes, 2016.

[31] M. Marrony, Proton-Conducting Ceramics, Jenny Stanford Publishing, 2015. https://doi.org/10.1201/b18921.

[32] P. Leung, A.A. Shah, L. Sanz, C. Flox, J.R. Morante, Q. Xu, M.R. Mohamed, C. Ponce de León, F.C. Walsh, Recent developments in organic redox flow batteries: A critical review, J. Power Sources. 360 (2017) 243–283. https://doi.org/10.1016/j.jpowsour.2017.05.057.

[33] M. Skyllas-Kazacos, M.H. Chakrabarti, S.A. Hajimolana, F.S. Mjalli, M. Saleem, Progress in Flow Battery Research and Development, J. Electrochem. Soc. 158 (2011) R55. https://doi.org/10.1149/1.3599565.

[34] Z. He, Z. Li, Z. Zhou, F. Tu, Y. Jiang, C. Pan, S. Liu, Improved performance of vanadium redox battery using methylsulfonic acid solution as supporting electrolyte, J. Renew. Sustain. Energy. 5 (2013) 023130. https://doi.org/10.1063/1.4800202.

[35] E. Sum, M. Rychcik, M. Skyllas-kazacos, Investigation of the V(V)/V(IV) system for use in the positive half-cell of a redox battery, J. Power Sources. 16 (1985) 85–95. https://doi.org/10.1016/0378-7753(85)80082-3.

[36] H. Vafiadis, M. Skyllas-Kazacos, Evaluation of membranes for the novel vanadium bromine redox flow cell, J. Memb. Sci. 279 (2006) 394–402. https://doi.org/10.1016/j.memsci.2005.12.028.

[37] C. Menictas, M. Skyllas-Kazacos, Performance of vanadium-oxygen redox fuel cell, J. Appl. Electrochem. 41 (2011) 1223–1232. https://doi.org/10.1007/s10800-011-0342-8.

[38] P. Alotto, M. Guarnieri, F. Moro, Redox flow batteries for the storage of renewable energy: A review, Renew. Sustain. Energy Rev. 29 (2014) 325–335. https://doi.org/10.1016/j.rser.2013.08.001.

[39] H. Prifti, A. Parasuraman, S. Winardi, T.M. Lim, M. Skyllas-Kazacos, Membranes for Redox Flow Battery Applications, Membranes (Basel). 2 (2012) 275–306. https://doi.org/10.3390/membranes2020275.

[40] J. Xi, Z. Wu, X. Qiu, L. Chen, Nafion/SiO2 hybrid membrane for vanadium redox flow battery, J. Power Sources. 166 (2007) 531–536. https://doi.org/10.1016/j.jpowsour.2007.01.069.

[41] Q. Luo, H. Zhang, J. Chen, P. Qian, Y. Zhai, Modification of Nafion membrane using interfacial polymerization for vanadium redox flow battery applications, J. Memb. Sci. 311 (2008) 98–103. https://doi.org/10.1016/j.memsci.2007.11.055.

[42] J. Zeng, C. Jiang, Y. Wang, J. Chen, S. Zhu, B. Zhao, R. Wang, Studies on polypyrrole modified nafion membrane for vanadium redox flow battery, Electrochem. Commun. 10 (2008) 372–375. https://doi.org/10.1016/j.elecom.2007.12.025.

[43] C.-H. Bae, E.P.. Roberts, R.A.. Dryfe, Chromium redox couples for application to redox flow batteries, Electrochim. Acta. 48 (2002) 279–287. https://doi.org/10.1016/S0013-4686(02)00649-7.

[44] M. Skyllas-Kazacos, Novel vanadium chloride/polyhalide redox flow battery, J. Power Sources. 124 (2003) 299–302. https://doi.org/10.1016/S0378-7753(03)00621-9.

[45] M. Skyllas-Kazacos, G. Kazacos, G. Poon, H. Verseema, Recent advances with UNSW vanadium-based redox flow batteries, Int. J. Energy Res. 34 (2010) 182–189. https://doi.org/10.1002/er.1658.

[46] F.-Q. Xue, Y.-L. Wang, W.-H. Wang, X.-D. Wang, Investigation on the electrode process of the Mn(II)/Mn(III) couple in redox flow battery, Electrochim. Acta. 53 (2008) 6636–6642. https://doi.org/10.1016/j.electacta.2008.04.040.

[47] S.C. Chieng, M. Kazacos, M. Skyllas-Kazacos, Modification of Daramic, microporous separator, for redox flow battery applications, J. Memb. Sci. 75 (1992) 81–91. https://doi.org/10.1016/0376-7388(92)80008-8.

[48] X. Li, H. Zhang, Z. Mai, H. Zhang, I. Vankelecom, Ion exchange membranes for vanadium redox flow battery (VRB) applications, Energy Environ. Sci. 4 (2011) 1147. https://doi.org/10.1039/c0ee00770f.

[49] D. Chen, S. Wang, M. Xiao, Y. Meng, Synthesis and characterization of novel sulfonated poly(arylene thioether) ionomers for vanadiumredox flow battery applications, Energy Environ. Sci. 3 (2010) 622–628. https://doi.org/10.1039/B917117G.

[50] Z. Xu, I. Michos, X. Wang, R. Yang, X. Gu, J. Dong, A zeolite ion exchange membrane for redox flow batteries, Chem. Commun. 50 (2014) 2416. https://doi.org/10.1039/c3cc47214k.

[51] M.A. Hickner, H. Ghassemi, Y.S. Kim, B.R. Einsla, J.E. McGrath, Alternative Polymer Systems for Proton Exchange Membranes (PEMs), Chem. Rev. 104 (2004) 4587–4612. https://doi.org/10.1021/cr020711a.

[52] C. Jeon, C. Choi, H.-T. Kim, M. Seo, Achieving Fast Proton Transport and High Vanadium Ion Rejection with Uniformly Mesoporous Composite Membranes for High-Efficiency Vanadium Redox Flow Batteries, ACS Appl. Energy Mater. 3 (2020) 5874–5881. https://doi.org/10.1021/acsaem.0c00804.

[53] C. Sun, J. Chen, H. Zhang, X. Han, Q. Luo, Investigations on transfer of water and vanadium ions across Nafion membrane in an operating vanadium redox flow battery, J. Power Sources. 195 (2010) 890–897. https://doi.org/10.1016/j.jpowsour.2009.08.041.

[54] A.Z. Weber, M.M. Mench, J.P. Meyers, P.N. Ross, J.T. Gostick, Q. Liu, Redox flow batteries: a review, J. Appl. Electrochem. 41 (2011) 1137–1164. https://doi.org/10.1007/s10800-011-0348-2.

[55] J. Li, X. Wang, G. Zhao, C. Chen, Z. Chai, A. Alsaedi, T. Hayat, X. Wang, Metal–organic framework-based materials: superior adsorbents for the capture of toxic and radioactive metal ions, Chem. Soc. Rev. 47 (2018) 2322–2356. https://doi.org/10.1039/C7CS00543A.

[56] J.-R. Li, R.J. Kuppler, H.-C. Zhou, Selective gas adsorption and separation in metal–organic frameworks, Chem. Soc. Rev. 38 (2009) 1477. https://doi.org/10.1039/b802426j.

[57] X. Zhao, Y. Wang, D. Li, X. Bu, P. Feng, Metal–Organic Frameworks for Separation, Adv. Mater. 30 (2018) 1705189. https://doi.org/10.1002/adma.201705189.

[58] Y. Xu, Q. Li, H. Xue, H. Pang, Metal-organic frameworks for direct electrochemical applications, Coord. Chem. Rev. 376 (2018) 292–318. https://doi.org/10.1016/j.ccr.2018.08.010.

[59] L. Jiao, Y. Wang, H.-L. Jiang, Q. Xu, Metal-Organic Frameworks as Platforms for Catalytic Applications, Adv. Mater. 30 (2018) 1703663. https://doi.org/10.1002/adma.201703663.

[60] J. Gascon, A. Corma, F. Kapteijn, F.X. Llabrés i Xamena, Metal Organic Framework Catalysis: Quo vadis ?, ACS Catal. 4 (2014) 361–378. https://doi.org/10.1021/cs400959k.

[61] Z. Chen, C. Lu, Humidity Sensors: A Review of Materials and Mechanisms, Sens. Lett. 3 (2005) 274–295. https://doi.org/10.1166/sl.2005.045.

[62] J.M. Troup, A. Clearfield, On the Mechanism of Ion Exchange in Zirconium Phosphates. 20. Refinement of the Crystal Structure of β-Zirconium Phosphate, Inorg. Chem. 16 (1977) 3311–3314. https://doi.org/10.1021/ic50178a065.

[63] G. Alberti, U. Costantino, J.S. Gill, Crystalline insoluble acid salts of tetravalent metals—XXIII, J. Inorg. Nucl. Chem. 38 (1976) 1733–1738. https://doi.org/10.1016/0022-1902(76)80670-7.

[64] H. Farahani, R. Wagiran, M.N. Hamidon, Humidity sensors principle, mechanism, and fabrication technologies: A comprehensive review, 2014. https://doi.org/10.3390/s140507881.

[65] H. Iwahara, H. Uchida, K. Ono, K. Ogaki, Proton Conduction in Sintered Oxides Based on BaCeO3, J. Electrochem. Soc. 135 (1988) 529–533. https://doi.org/10.1149/1.2095649.

[66] T.A. Blank, L.P. Eksperiandova, K.N. Belikov, Recent trends of ceramic humidity sensors development: A review, Sensors Actuators B Chem. 228 (2016) 416–442. https://doi.org/10.1016/j.snb.2016.01.015.

[67] P. Colomban, A. Novak, Proton transfer and superionic conductivity in solids and gels, J. Mol. Struct. 177 (1988) 277–308. https://doi.org/10.1016/0022-2860(88)80094-2.

[68] K.D. Kreuer, Proton conductivity: Materials and applications, Chem. Mater. 8 (1996) 610–641. https://doi.org/10.1021/cm950192a.

[69] A. Donnadio, M. Nocchetti, F. Costantino, M. Taddei, M. Casciola, F. da Silva Lisboa, R. Vivani, A Layered Mixed Zirconium Phosphate/Phosphonate with Exposed Carboxylic and Phosphonic Groups: X-ray Powder Structure and Proton Conductivity Properties, Inorg. Chem. 53 (2014) 13220–13226. https://doi.org/10.1021/ic502473w.

[70] J.C. Badot, A. Fourrier-Lamer, N. Baffier, P. Colomban, Phase transitions and dielectric relaxations in superionic protonic conductor HUP (H3OUO2PO4.3H2O) in the broad frequency range (10-2-1010 Hz), J. Phys. 48 (1987) 1325–1336. https://doi.org/10.1051/jphys:019870048080132500.

[71] S. Hara, S. Takano, M. Miyayama, Proton-conducting properties and microstructure of hydrated tin dioxide and hydrated

zirconia, J. Phys. Chem. B. 108 (2004) 5634–5639. https://doi.org/10.1021/jp0370369.

[72] J. Bielecki, S.F. Parker, D. Ekanayake, S.M.H. Rahman, L. Börjesson, M. Karlsson, Short-range structure of the brownmillerite-type oxide Ba2In2O5 and its hydrated proton-conducting form BaInO3H, J. Mater. Chem. A. 2 (2014) 16915–16924. https://doi.org/10.1039/c4ta03213f.

[73] S. Sachdeva, J.A. Turner, J.L. Horan, A.M. Herring, The use of heteropoly acids in proton exchange fuel cells, Struct. Bond. 141 (2011) 115–168. https://doi.org/10.1007/430_2011_45.

[74] K.G. Frase, G.C. Farrington, J.O. Thomas, Proton Transport in the β/β" -Aluminas , Annu. Rev. Mater. Sci. 14 (1984) 279–295. https://doi.org/10.1146/annurev.ms.14.080184.001431.

[75] G.C. Farrington, J.L. Briant, Hydronium beta″ alumina: A fast proton conductor, Mater. Res. Bull. 13 (1978) 763–773. https://doi.org/10.1016/0025-5408(78)90038-7.

[76] W.H.J. Hogarth, S.S. Muir, A.K. Whittaker, J.C. Diniz da Costa, J. Drennan, G.Q. (Max. Lu, Proton conduction mechanism and the stability of sol-gel titanium phosphates, Solid State Ionics. 177 (2007) 3389–3394. https://doi.org/10.1016/j.ssi.2006.10.015.

[77] E. Rodríguez-Castellón, J. Jiménez-Jiménez, A. Jiménez-López, P. Maireles-Torres, J.R. Ramos-Barrado, D.J. Jones, J. Rozière., Proton conductivity of mesoporous MCM type of zirconium and titanium phosphates, Solid State Ionics. 125 (1999) 407–410. https://doi.org/10.1016/S0167-2738(99)00202-7.

[78] G. Alberti, M. Bracardi, M. Casciola, Ionic conduction of γ-titanium phosphate in hydrogen and alkali metal salt forms, Solid State Ionics. 7 (1982) 243–247. https://doi.org/10.1016/0167-2738(82)90055-8.

[79] G. Alberti, M. Casciola, Layered metalIV phosphonates, a large class of inorgano-organic proton conductors, Solid State Ionics. 97 (1997) 177–186. https://doi.org/10.1016/s0167-2738(97)00070-2.

[80] G. Alberti, U. Costantino, M. Casciola, S. Ferroni, L. Massinelli, P. Staiti, Preparation, characterization and proton conductivity of titanium phosphate sulfophenylphosphonate, Solid State Ionics. 145 (2001) 249–255. https://doi.org/10.1016/S0167-2738(01)00948-1.

[81] G. Alberti, M. Casciola, S. Cavalaglio, R. Vivani, Proton conductivity of mesoporous zirconium phosphate pyrophosphate, Solid State Ionics. 125 (1999) 91–97. https://doi.org/10.1016/S0167-2738(99)00162-9.

[82] W.H.J. Hogarth, J.C.D. Da Costa, J. Drennan, G.Q. Lu, Proton conductivity of mesoporous sol-gel zirconium phosphates for fuel cell applications, J. Mater. Chem. 15 (2005) 754–758. https://doi.org/10.1039/b413413n.

[83] A.E.C. Palmqvist, Synthesis of ordered mesoporous materials using surfactant liquid crystals or micellar solutions, Curr. Opin. Colloid Interface Sci. 8 (2003) 145–155. https://doi.org/10.1016/S1359-0294(03)00020-7.

[84] P. Knauth, M.L. Di Vona, Proton Mobility in Hydrated Acidic Polymers: Consequences for Optimization of Proton Conductivity, ECS Trans. 50 (2013) 1037–1044. https://doi.org/10.1149/05002.1037ecst.

[85] a I. Baranov, L. a Shuvalov, N.M. Shchagina, Superion conductivity and phase transitions in CsHSO4 and CsHSeO4 crystals, JETP Lett. 36 (1982) 459–462.

[86] B.C. Wood, N. Marzari, Proton dynamics in superprotonic CsHSO4, Phys. Rev. B. 76 (2007) 134301. https://doi.org/10.1103/PhysRevB.76.134301.

[87] T. Matsui, S. Takeshita, Y. Iriyama, T. Abe, Z. Ogumi, Proton-Conductive Electrolyte Consisting of NH[sub 4]PO[sub 3]/TiP[sub 2]O[sub 7] for Intermediate-Temperature Fuel Cells, J. Electrochem. Soc. 152 (2005) A167. https://doi.org/10.1149/1.1829414.

[88] T. Uma, H.Y. Tu, S. Warth, D. Schneider, D. Freude, U. Stimming, Synthesis and characterization of proton conducting poly phosphate composites, J. Mater. Sci. 40 (2005) 2059–2063. https://doi.org/10.1007/s10853-005-1233-3.

[89] J.W. Phair, S.P.S. Badwal, Review of proton conductors for hydrogen separation, Ionics (Kiel). 12 (2006) 103–115. https://doi.org/10.1007/s11581-006-0016-4.

[90] K.E.J. Eurenius, E. Ahlberg, C.S. Knee, Proton conductivity in Sm2Sn2O7 pyrochlores, Solid State Ionics. 181 (2010) 1577–1585. https://doi.org/10.1016/j.ssi.2010.09.008.

[91] I. AHMED, S. ERIKSSON, E. AHLBERG, C. KNEE, P. BERASTEGUI, L. JOHANSSON, H. RUNDLOF, M. KARLSSON, A. MATIC, L. BORJESSON, Synthesis and structural characterization of perovskite type proton conducting

BaZr1−xInxO3−δ (0.0≤x≤0.75), Solid State Ionics. 177 (2006) 1395–1403. https://doi.org/10.1016/j.ssi.2006.07.009.

[92] J. LIU, A. NOWICK, The incorporation and migration of protons in Nd-doped BaCeO3, Solid State Ionics. 50 (1992) 131–138. https://doi.org/10.1016/0167-2738(92)90045-Q.

[93] J. Dailly, M. Marrony, BCY-based proton conducting ceramic cell: 1000 h of long term testing in fuel cell application, J. Power Sources. 240 (2013) 323–327. https://doi.org/10.1016/j.jpowsour.2013.04.028.

[94] Y. Yoo, N. Lim, Performance and stability of proton conducting solid oxide fuel cells based on yttrium-doped barium cerate-zirconate thin-film electrolyte, J. Power Sources. 229 (2013) 48–57. https://doi.org/10.1016/j.jpowsour.2012.11.094.

[95] H. Li, C. Han, Y. Huang, Y. Huang, M. Zhu, Z. Pei, Q. Xue, Z. Wang, Z. Liu, Z. Tang, Y. Wang, F. Kang, B. Li, C. Zhi, An extremely safe and wearable solid-state zinc ion battery based on a hierarchical structured polymer electrolyte, Energy Environ. Sci. 11 (2018) 941–951. https://doi.org/10.1039/C7EE03232C.

[96] T. Takahashi, S. Tanase, O. Yamamoto, S. Yamauchi, Proton conduction in triethylenediamine- and hexamethylenetetramine-sulfate, J. Solid State Chem. 17 (1976) 353–361. https://doi.org/10.1016/S0022-4596(76)80003-5.

[97] A. Jankowska, A. Zalewska, A. Skalska, A. Ostrowski, S. Kowalak, Proton conductivity of imidazole entrapped in microporous molecular sieves, Chem. Commun. 53 (2017) 2475–2478. https://doi.org/10.1039/C7CC00690J.

[98] K. Wang, X. Qi, Z. Wang, R. Wang, J. Sun, Q. Zhang, In Situ Encapsulation of Imidazolium Proton Carriers in Anionic Open Frameworks Leads the Way to Proton-Conducting Materials, Eur. J. Inorg. Chem. 2017 (2017) 2295–2300. https://doi.org/10.1002/ejic.201700157.

[99] Y. Ye, L. Zhang, Q. Peng, G.-E. Wang, Y. Shen, Z. Li, L. Wang, X. Ma, Q.-H. Chen, Z. Zhang, S. Xiang, High Anhydrous Proton Conductivity of Imidazole-Loaded Mesoporous Polyimides over a Wide Range from Subzero to Moderate Temperature, J. Am. Chem. Soc. 137 (2015) 913–918. https://doi.org/10.1021/ja511389q.

[100] F.-M. Zhang, L.-Z. Dong, J.-S. Qin, W. Guan, J. Liu, S.-L. Li, M. Lu, Y.-Q. Lan, Z.-M. Su, H.-C. Zhou, Effect of Imidazole Arrangements on Proton-Conductivity in Metal–Organic Frameworks, J. Am. Chem. Soc. 139 (2017) 6183–6189. https://doi.org/10.1021/jacs.7b01559.

[101] J. Tritt-Goc, I. Jankowska, K. Pogorzelec-Glaser, R. Pankiewicz, P. Ławniczak, Imidazole-doped nanocrystalline cellulose solid proton conductor: synthesis, thermal properties, and conductivity, Cellulose. 25 (2018) 281–291. https://doi.org/10.1007/s10570-017-1555-8.

[102] G. Scharfenberger, W.H. Meyer, G. Wegner, M. Schuster, K.D. Kreuer, J. Maier, Anhydrous polymeric proton conductors based on imidazole functionalized polysiloxane, Fuel Cells. 6 (2006) 237–250. https://doi.org/10.1002/fuce.200500210.

[103] G. Alberti, L. Boccali, M. Casciola, L. Massinelli, E. Montoneri, Protonic conductivity of layered zirconium phosphonates containing -SO3H groups. III. Preparation and characterization of γ-zirconium sulfoaryl phosphonates, Solid State Ionics. 84 (1996) 97–104. https://doi.org/10.1016/S0167-2738(96)83011-6.

[104] A. Bozkurt, M. Ise, K.D. Kreuer, W.H. Meyer, G. Wegner, Proton-conducting polymer electrolytes based on phosphoric acid, Solid State Ionics. 125 (1999) 225–233. https://doi.org/10.1016/S0167-2738(99)00179-4.

[105] R. He, Proton conductivity of phosphoric acid doped polybenzimidazole and its composites with inorganic proton conductors, J. Memb. Sci. 226 (2003) 169–184. https://doi.org/10.1016/j.memsci.2003.09.002.

[106] S.T. Günday, A. Bozkurt, W.H. Meyer, G. Wegner, Effects of different acid functional groups on proton conductivity of polymer-1,2,4-triazole blends, J. Polym. Sci. Part B Polym. Phys. 44 (2006) 3315–3322. https://doi.org/10.1002/polb.20956.

[107] A. Magrasó, Transport number measurements and fuel cell testing of undoped and Mo-substituted lanthanum tungstate, J. Power Sources. 240 (2013) 583–588. https://doi.org/10.1016/j.jpowsour.2013.04.087.

[108] C. Solís, V.B. Vert, M. Balaguer, S. Escolástico, S. Roitsch, J.M. Serra, Mixed Proton-Electron Conducting Chromite Electrocatalysts as Anode Materials for LWO-Based Solid Oxide Fuel Cells, ChemSusChem. 5 (2012) 2155–2158. https://doi.org/10.1002/cssc.201200446.

[109] T. Norby, Proton Conductivity in Perovskite Oxides, in: 2009: pp. 217–241. https://doi.org/10.1007/978-0-387-77708-5_11.

[110] S.R. Batten, N.R. Champness, X.-M. Chen, J. Garcia-Martinez, S. Kitagawa, L. Öhrström, M. O'Keeffe, M.P. Suh, J. Reedijk, Coordination polymers, metal–organic frameworks and the need for terminology guidelines, CrystEngComm. 14 (2012) 3001. https://doi.org/10.1039/c2ce06488j.

[111] T. Devic, C. Serre, Porous Metal Organic Frameworks, in: Ordered Porous Solids, Elsevier, 2009: pp. 77–99. https://doi.org/10.1016/B978-0-444-53189-6.00004-4.

[112] H. Furukawa, K.E. Cordova, M. O'Keeffe, O.M. Yaghi, M. O'Keeffe, O.M. Yaghi, The chemistry and applications of metal-organic frameworks, Science (80-.). 341 (2013) 1230444. https://doi.org/10.1126/science.1230444.

[113] O.M. Yaghi, M. O'Keeffe, N.W. Ockwig, H.K. Chae, M. Eddaoudi, J. Kim, Reticular synthesis and the design of new materials, Nature. 423 (2003) 705–714. https://doi.org/10.1038/nature01650.

[114] G. Férey, Hybrid porous solids: past, present, future, Chem. Soc. Rev. 37 (2008) 191–214. https://doi.org/10.1039/B618320B.

[115] P.Z. Moghadam, A. Li, S.B. Wiggin, A. Tao, A.G.P. Maloney, P.A. Wood, S.C. Ward, D. Fairen-Jimenez, Development of a Cambridge Structural Database Subset: A Collection of Metal-Organic Frameworks for Past, Present, and Future, Chem. Mater. 29 (2017) 2618–2625. https://doi.org/10.1021/acs.chemmater.7b00441.

[116] S.M. Moosavi, A. Nandy, K.M. Jablonka, D. Ongari, J.P. Janet, P.G. Boyd, Y. Lee, B. Smit, H.J. Kulik, Understanding the diversity of the metal-organic framework ecosystem, Nat. Commun. 11 (2020) 4068. https://doi.org/10.1038/s41467-020-17755-8.

[117] J.L.C. Rowsell, O.M. Yaghi, Metal–organic frameworks: a new class of porous materials, Microporous Mesoporous Mater. 73 (2004) 3–14. https://doi.org/10.1016/j.micromeso.2004.03.034.

[118] N. Stock, S. Biswas, Synthesis of Metal-Organic Frameworks (MOFs): Routes to Various MOF Topologies, Morphologies, and Composites, Chem. Rev. 112 (2012) 933–969. https://doi.org/10.1021/cr200304e.

[119] O.K. Farha, I. Eryazici, N.C. Jeong, B.G. Hauser, C.E. Wilmer, A.A. Sarjeant, R.Q. Snurr, S.T. Nguyen, A.Ö. Yazaydın, J.T. Hupp, Metal–Organic Framework Materials with Ultrahigh Surface Areas: Is the Sky the Limit?, J. Am. Chem. Soc. 134 (2012) 15016–15021. https://doi.org/10.1021/ja3055639.

[120] R.J. Kuppler, D.J. Timmons, Q.-R. Fang, J.-R. Li, T.A. Makal, M.D. Young, D. Yuan, D. Zhao, W. Zhuang, H.-C. Zhou, Potential applications of metal-organic frameworks, Coord. Chem. Rev. 253 (2009) 3042–3066. https://doi.org/10.1016/j.ccr.2009.05.019.

[121] G. Férey, C. Serre, T. Devic, G. Maurin, H. Jobic, P.L. Llewellyn, G. De Weireld, A. Vimont, M. Daturi, J.-S. Chang, Why hybrid porous solids capture greenhouse gases?, Chem. Soc. Rev. 40 (2011) 550–562. https://doi.org/10.1039/C0CS00040J.

[122] H.-C. "Joe" Zhou, S. Kitagawa, Metal–Organic Frameworks (MOFs), Chem. Soc. Rev. 43 (2014) 5415–5418. https://doi.org/10.1039/C4CS90059F.

[123] O.M. Yaghi, H. Li, Hydrothermal Synthesis of a Metal-Organic Framework Containing Large Rectangular Channels, J. Am. Chem. Soc. 117 (1995) 10401–10402. https://doi.org/10.1021/ja00146a033.

[124] B.F. Hoskins, R. Robson, Infinite polymeric frameworks consisting of three dimensionally linked rod-like segments, J. Am. Chem. Soc. 111 (1989) 5962–5964. https://doi.org/10.1021/ja00197a079.

[125] M. Kondo, T. Yoshitomi, H. Matsuzaka, S. Kitagawa, K. Seki, Three-Dimensional Framework with Channeling Cavities for Small Molecules:{[M2(4, 4′-bpy)3(NO3)4]·xH2O}n(M Co, Ni, Zn), Angew. Chemie Int. Ed. English. 36 (1997) 1725–1727. https://doi.org/10.1002/anie.199717251.

[126] G. Maurin, C. Serre, A. Cooper, G. Férey, The new age of MOFs and of their porous-related solids, Chem. Soc. Rev. 46 (2017) 3104–3107. https://doi.org/10.1039/C7CS90049J.

[127] W. Lu, Z. Wei, Z.-Y. Gu, T.-F. Liu, J. Park, J. Park, J. Tian, M. Zhang, Q. Zhang, T. Gentle III, M. Bosch, H.-C. Zhou, Tuning the structure and function of metal–organic frameworks via linker design, Chem. Soc. Rev. 43 (2014) 5561–5593. https://doi.org/10.1039/C4CS00003J.

[128] S.S. Chui, A Chemically Functionalizable Nanoporous Material [Cu3(TMA)2(H2O)3]n, Science (80-.). 283 (1999) 1148–1150. https://doi.org/10.1126/science.283.5405.1148.

[129] J.H. Cavka, S. Jakobsen, U. Olsbye, N. Guillou, C. Lamberti, S. Bordiga, K.P. Lillerud, A New Zirconium Inorganic Building Brick Forming Metal Organic Frameworks with Exceptional Stability, J. Am. Chem. Soc. 130 (2008) 13850–13851. https://doi.org/10.1021/ja8057953.

[130] K.S. Park, Z. Ni, A.P. Cote, J.Y. Choi, R. Huang, F.J. Uribe-Romo, H.K. Chae, M. O'Keeffe, O.M. Yaghi, Exceptional chemical and thermal stability of zeolitic imidazolate frameworks, Proc. Natl. Acad. Sci. 103 (2006) 10186–10191. https://doi.org/10.1073/pnas.0602439103.

[131] C. Serre, F. Millange, C. Thouvenot, M. Noguès, G. Marsolier, D. Louër, G. Férey, Very Large Breathing Effect in the First Nanoporous Chromium(III)-Based Solids: MIL-53 or Cr III (OH)· {O 2 C−C 6 H 4 −CO 2 }· {HO 2 C−C 6 H 4 −CO 2 H} x ·H 2 O y, J. Am. Chem. Soc. 124 (2002) 13519–13526. https://doi.org/10.1021/ja0276974.

[132] N.L. Rosi, J. Kim, M. Eddaoudi, B. Chen, M. O'Keeffe, O.M. Yaghi, Rod Packings and Metal−Organic Frameworks Constructed from Rod-Shaped Secondary Building Units, J. Am. Chem. Soc. 127 (2005) 1504–1518. https://doi.org/10.1021/ja045123o.

[133] H. Li, M. Eddaoudi, M. O'Keeffe, O.M. Yaghi, Design and synthesis of an exceptionally stable and highly porous metal-organic framework, Nature. 402 (1999) 276–279. https://doi.org/10.1038/46248.

[134] G. Ferey, A Chromium Terephthalate-Based Solid with Unusually Large Pore Volumes and Surface Area, Science (80-.). 309 (2005) 2040–2042. https://doi.org/10.1126/science.1116275.

[135] R. Freund, O. Zaremba, G. Arnauts, R. Ameloot, G. Skorupskii, M. Dincă, A. Bavykina, J. Gascon, A. Ejsmont, J. Goscianska, M. Kalmutzki, U. Lächelt, E. Ploetz, C.S. Diercks, S. Wuttke, The Current Status of MOF and COF Applications, Angew. Chemie Int. Ed. 60 (2021) 23975–24001. https://doi.org/10.1002/anie.202106259.

[136] H. Li, K. Wang, Y. Sun, C.T. Lollar, J. Li, H.-C. Zhou, Recent advances in gas storage and separation using metal–organic frameworks, Mater. Today. 21 (2018) 108–121. https://doi.org/10.1016/j.mattod.2017.07.006.

[137] Q. Qian, P.A. Asinger, M.J. Lee, G. Han, K. Mizrahi Rodriguez, S. Lin, F.M. Benedetti, A.X. Wu, W.S. Chi, Z.P. Smith, MOF-Based Membranes for Gas Separations, Chem. Rev. 120 (2020) 8161–8266. https://doi.org/10.1021/acs.chemrev.0c00119.

[138] R.-B. Lin, S. Xiang, W. Zhou, B. Chen, Microporous Metal-Organic Framework Materials for Gas Separation, Chem. 6 (2020) 337–363. https://doi.org/10.1016/j.chempr.2019.10.012.

[139] B. Van De Voorde, B. Bueken, J. Denayer, D. De Vos, Adsorptive separation on metal-organic frameworks in the liquid phase, Chem. Soc. Rev. 43 (2014) 5766–5788. https://doi.org/10.1039/c4cs00006d.

[140] K. Huang, X. Dong, R. Ren, W. Jin, Fabrication of homochiral metal-organic framework membrane for enantioseparation of racemic diols, AIChE J. 59 (2013) 4364–4372. https://doi.org/10.1002/aic.14194.

[141] A. Bavykina, N. Kolobov, I.S. Khan, J.A. Bau, A. Ramirez, J. Gascon, Metal–Organic Frameworks in Heterogeneous Catalysis: Recent Progress, New Trends, and Future Perspectives, Chem. Rev. 120 (2020) 8468–8535. https://doi.org/10.1021/acs.chemrev.9b00685.

[142] D. Yang, B.C. Gates, Catalysis by Metal Organic Frameworks: Perspective and Suggestions for Future Research, ACS Catal. 9 (2019) 1779–1798. https://doi.org/10.1021/acscatal.8b04515.

[143] J.N. Hall, P. Bollini, Structure, characterization, and catalytic properties of open-metal sites in metal organic frameworks, React. Chem. Eng. 4 (2019) 207–222. https://doi.org/10.1039/C8RE00228B.

[144] A. Dhakshinamoorthy, Z. Li, H. Garcia, Catalysis and photocatalysis by metal organic frameworks, Chem. Soc. Rev. 47 (2018) 8134–8172. https://doi.org/10.1039/C8CS00256H.

[145] M. Giménez-Marqués, T. Hidalgo, C. Serre, P. Horcajada, Nanostructured metal–organic frameworks and their bio-related applications, Coord. Chem. Rev. 307 (2016) 342–360. https://doi.org/10.1016/j.ccr.2015.08.008.

[146] H.-S. Wang, Y.-H. Wang, Y. Ding, Development of biological metal–organic frameworks designed for biomedical applications: from bio-sensing/bio-imaging to disease treatment, Nanoscale Adv. 2 (2020) 3788–3797. https://doi.org/10.1039/D0NA00557F.

[147] J. Yang, Y. Yang, Metal–Organic Frameworks for Biomedical Applications, Small. 16 (2020) 1906846. https://doi.org/10.1002/smll.201906846.

[148] M.D. Allendorf, R. Dong, X. Feng, S. Kaskel, D. Matoga, V. Stavila, Electronic Devices Using Open Framework Materials, Chem. Rev. 120 (2020) 8581–8640. https://doi.org/10.1021/acs.chemrev.0c00033.

[149] L.E. Kreno, K. Leong, O.K. Farha, M. Allendorf, R.P. Van Duyne, J.T. Hupp, Metal-organic framework materials as chemical sensors, Chem. Rev. 112 (2012) 1105–1125. https://doi.org/10.1021/cr200324t.

[150] A. Chidambaram, K.C. Stylianou, Electronic metal–organic framework sensors, Inorg. Chem. Front. 5 (2018) 979–998. https://doi.org/10.1039/C7QI00815E.

[151] Y. Li, A.-S. Xiao, B. Zou, H.-X. Zhang, K.-L. Yan, Y. Lin, Advances of metal–organic frameworks for gas sensing, Polyhedron. 154 (2018) 83–97. https://doi.org/10.1016/j.poly.2018.07.028.

[152] P. Kumar, A. Deep, K.-H. Kim, R.J.C. Brown, Coordination polymers: Opportunities and challenges for monitoring volatile organic compounds, Prog. Polym. Sci. 45 (2015) 102–118. https://doi.org/10.1016/j.progpolymsci.2015.01.002.

[153] W.-T. Koo, J.-S. Jang, I.-D. Kim, Metal-Organic Frameworks for Chemiresistive Sensors, Chem. 5 (2019) 1938–1963. https://doi.org/10.1016/j.chempr.2019.04.013.

[154] H.-Y. Li, S.-N. Zhao, S.-Q. Zang, J. Li, Functional metal–organic frameworks as effective sensors of gases and volatile compounds, Chem. Soc. Rev. 49 (2020) 6364–6401. https://doi.org/10.1039/C9CS00778D.

[155] P. Kumar, K.-H. Kim, P.K. Mehta, L. Ge, G. Lisak, Progress and challenges in electrochemical sensing of volatile organic compounds using metal-organic frameworks, Crit. Rev. Environ. Sci. Technol. 49 (2019) 2016–2048. https://doi.org/10.1080/10643389.2019.1601489.

[156] C. Lai, Z. Wang, L. Qin, Y. Fu, B. Li, M. Zhang, S. Liu, L. Li, H. Yi, X. Liu, X. Zhou, N. An, Z. An, X. Shi, C. Feng, Metal-organic frameworks as burgeoning materials for the capture and sensing of indoor VOCs and radon gases, Coord. Chem. Rev. 427 (2021) 213565. https://doi.org/10.1016/j.ccr.2020.213565.

[157] S. Chuhadiya, Himanshu, D. Suthar, S.L. Patel, M.S. Dhaka, Metal organic frameworks as hybrid porous materials for energy storage and conversion devices: A review, Coord. Chem. Rev. 446 (2021) 214115. https://doi.org/10.1016/j.ccr.2021.214115.

[158] B. Xu, H. Zhang, H. Mei, D. Sun, Recent progress in metal-organic framework-based supercapacitor electrode materials, Coord. Chem. Rev. 420 (2020) 213438. https://doi.org/10.1016/j.ccr.2020.213438.

[159] L. Kong, M. Zhong, W. Shuang, Y. Xu, X.-H.H. Bu, Electrochemically active sites inside crystalline porous materials for energy storage and conversion, Chem. Soc. Rev. 49 (2020) 2378–2407. https://doi.org/10.1039/C9CS00880B.

[160] G. Zhang, L. Jin, R. Zhang, Y. Bai, R. Zhu, H. Pang, Recent advances in the development of electronically and ionically conductive metal-organic frameworks, Coord. Chem. Rev. 439 (2021) 213915. https://doi.org/10.1016/j.ccr.2021.213915.

[161] H.-N.N. Wang, X. Meng, L.-Z.Z. Dong, Y. Chen, S.-L.L. Li, Y.-Q.Q. Lan, Coordination polymer-based conductive materials: Ionic conductivity: Vs. electronic conductivity, J. Mater. Chem. A. 7 (2019) 24059–24091. https://doi.org/10.1039/c9ta08253k.

[162] P. Thanasekaran, C.-H. Su, Y.-H. Liu, K.-L. Lu, Weak interactions in conducting metal–organic frameworks, Coord. Chem. Rev. 442 (2021) 213987. https://doi.org/10.1016/j.ccr.2021.213987.

[163] C.W. Kung, C.W. Kung, S. Goswami, I. Hod, T.C. Wang, J. Duan, O.K. Farha, J.T. Hupp, Charge Transport in Zirconium-Based Metal-Organic Frameworks, Acc. Chem. Res. 53 (2020) 1187–1195. https://doi.org/10.1021/acs.accounts.0c00106.

[164] M. Sadakiyo, H. Kitagawa, Ion-conductive metal-organic frameworks, Dalt. Trans. 50 (2021) 5385–5397. https://doi.org/10.1039/d0dt04384b.

[165] R. Zhao, Y. Wu, Z. Liang, L. Gao, W. Xia, Y. Zhao, R. Zou, Metal–organic frameworks for solid-state electrolytes, Energy Environ. Sci. 13 (2020) 2386–2403. https://doi.org/10.1039/D0EE00153H.

[166] P. Ramaswamy, N.E. Wong, G.K.H. Shimizu, MOFs as proton conductors – challenges and opportunities, Chem. Soc. Rev. 43 (2014) 5913–5932. https://doi.org/10.1039/C4CS00093E.

[167] X. Meng, H.N. Wang, S.Y. Song, H.J. Zhang, Proton-conducting crystalline porous materials, Chem. Soc. Rev. 46 (2017). https://doi.org/10.1039/c6cs00528d.

[168] A.L. Li, Q. Gao, J. Xu, X.H. Bu, Proton-conductive metal-organic frameworks: Recent advances and perspectives, Coord. Chem. Rev. 344 (2017) 54–82. https://doi.org/10.1016/j.ccr.2017.03.027.

[169] S. Chand, S.M. Elahi, A. Pal, M.C. Das, Metal–Organic Frameworks and Other Crystalline Materials for Ultrahigh Superprotonic Conductivities of 10 −2 S cm −1 or Higher, Chem. - A Eur. J. 25 (2019) 6259–6269. https://doi.org/10.1002/chem.201806126.

[170] X.X. Xie, Y.C. Yang, B.H. Dou, Z.F. Li, G. Li, Proton conductive carboxylate-based metal–organic frameworks, Coord. Chem. Rev. (2020). https://doi.org/10.1016/j.ccr.2019.213100.

[171] Y. Ye, L. Gong, S. Xiang, Z. Zhang, B. Chen, Metal–Organic Frameworks as a Versatile Platform for Proton Conductors, Adv. Mater. 32 (2020) 1907090. https://doi.org/10.1002/adma.201907090.

[172] D.-W. Lim, H. Kitagawa, Proton Transport in Metal–Organic Frameworks, Chem. Rev. 120 (2020) 8416–8467. https://doi.org/10.1021/acs.chemrev.9b00842.

[173] S.C. Pal, M.C. Das, Superprotonic Conductivity of MOFs and Other Crystalline Platforms Beyond 10 −1 S cm −1, Adv. Funct. Mater. 31 (2021) 2101584. https://doi.org/10.1002/adfm.202101584.

[174] D.W. Kang, M. Kang, C.S. Hong, Post-synthetic modification of porous materials: Superprotonic conductivities and membrane applications in fuel cells, J. Mater. Chem. A. 8 (2020) 7474–7494. https://doi.org/10.1039/d0ta01733g.

[175] T. Panda, P. Jhariat, P. Kumari, Structural features of Proton Conducting Metal Organic and Covalent Organic Frameworks, CrystEngComm. (2020). https://doi.org/10.1039/d0ce00902d.

[176] D.-W. Lim, H. Kitagawa, Rational strategies for proton-conductive metal–organic frameworks, Chem. Soc. Rev. 50 (2021) 6349–6368. https://doi.org/10.1039/D1CS00004G.

[177] M.K. Sarango-Ramírez, J. Park, J. Kim, Y. Yoshida, D. Lim, H. Kitagawa, Void Space versus Surface Functionalization for Proton Conduction in Metal–Organic Frameworks, Angew. Chemie Int. Ed. 60 (2021) 20173–20177. https://doi.org/10.1002/anie.202106181.

[178] K. Biradha, A. Goswami, R. Moi, S. Saha, Metal–organic frameworks as proton conductors: strategies for improved proton conductivity, Dalt. Trans. 50 (2021) 10655–10673. https://doi.org/10.1039/D1DT01116B.

[179] X.S. Xing, Z.H. Fu, N.N. Zhang, X.Q. Yu, M.S. Wang, G.C. Guo, High proton conduction in an excellent water-stable gadolinium metal-organic framework, Chem. Commun. 55 (2019) 1241–1244. https://doi.org/10.1039/c8cc08700h.

[180] N.T.T. Nguyen, H. Furukawa, F. Gándara, C.A. Trickett, H.M. Jeong, K.E. Cordova, O.M. Yaghi, Three-Dimensional Metal-Catecholate Frameworks and Their Ultrahigh Proton Conductivity, J. Am. Chem. Soc. 137 (2015) 15394–15397. https://doi.org/10.1021/jacs.5b10999.

[181] M. Sadakiyo, T. Yamada, H. Kitagawa, Rational Designs for Highly Proton-Conductive Metal−Organic Frameworks, J. Am. Chem. Soc. 131 (2009) 9906–9907. https://doi.org/10.1021/ja9040016.

[182] Y.-S. Wei, X.-P. Hu, Z. Han, X.-Y. Dong, S.-Q. Zang, T.C.W. Mak, Unique Proton Dynamics in an Efficient MOF-Based Proton Conductor, J. Am. Chem. Soc. 139 (2017) 3505–3512. https://doi.org/10.1021/jacs.6b12847.

[183] T. Yamada, M. Sadakiyo, H. Kitagawa, High Proton Conductivity of One-Dimensional Ferrous Oxalate Dihydrate, J. Am. Chem. Soc. 131 (2009) 3144–3145. https://doi.org/10.1021/ja808681m.

[184] P.G.M. Mileo, K. Adil, L. Davis, A. Cadiau, Y. Belmabkhout, H. Aggarwal, G. Maurin, M. Eddaoudi, S. Devautour-Vinot, Achieving Superprotonic Conduction with a 2D Fluorinated Metal–Organic Framework, J. Am. Chem. Soc. 140 (2018) 13156–13160. https://doi.org/10.1021/jacs.8b06582.

[185] A. Shigematsu, T. Yamada, H. Kitagawa, Wide Control of Proton Conductivity in Porous Coordination Polymers, J. Am. Chem. Soc. 133 (2011) 2034–2036. https://doi.org/10.1021/ja109810w.

[186] F. Yang, H. Huang, X. Wang, F. Li, Y. Gong, C. Zhong, J.-R. Li, Proton Conductivities in Functionalized UiO-66: Tuned Properties, Thermogravimetry Mass, and Molecular Simulation Analyses, Cryst. Growth Des. 15 (2015) 5827–5833. https://doi.org/10.1021/acs.cgd.5b01190.

[187] W.J. Phang, H. Jo, W.R. Lee, J.H. Song, K. Yoo, B. Kim, C.S. Hong, Superprotonic conductivity of a uio-66 framework functionalized with sulfonic acid groups by facile postsynthetic oxidation, Angew. Chemie Int. Ed. 54 (2015) 5142–5146. https://doi.org/10.1002/anie.201411703.

[188] F. Yang, G. Xu, Y. Dou, B. Wang, H. Zhang, H. Wu, W. Zhou, J.-R. Li, B. Chen, A flexible metal–organic framework with a high density of sulfonic acid sites for proton conduction, Nat. Energy. 2 (2017) 877–883.

https://doi.org/10.1038/s41560-017-0018-7.

[189] J.M. Taylor, K.W. Dawson, G.K.H. Shimizu, A Water-Stable Metal–Organic Framework with Highly Acidic Pores for Proton-Conducting Applications, J. Am. Chem. Soc. 135 (2013) 1193–1196. https://doi.org/10.1021/ja310435e.

[190] M. Bazaga-García, R.M.P. Colodrero, M. Papadaki, P. Garczarek, J. Zoń, P. Olivera-Pastor, E.R. Losilla, L. León-Reina, M.A.G. Aranda, D. Choquesillo-Lazarte, K.D. Demadis, A. Cabeza, Guest Molecule-Responsive Functional Calcium Phosphonate Frameworks for Tuned Proton Conductivity, J. Am. Chem. Soc. 136 (2014) 5731–5739. https://doi.org/10.1021/ja500356z.

[191] S. Mukhopadhyay, J. Debgupta, C. Singh, R. Sarkar, O. Basu, S.K. Das, Designing UiO-66-Based Superprotonic Conductor with the Highest Metal–Organic Framework Based Proton Conductivity, ACS Appl. Mater. Interfaces. 11 (2019) 13423–13432. https://doi.org/10.1021/acsami.9b01121.

[192] S. Kim, B. Joarder, J.A. Hurd, J. Zhang, K.W. Dawson, B.S. Gelfand, N.E. Wong, G.K.H.H. Shimizu, Achieving Superprotonic Conduction in Metal-Organic Frameworks through Iterative Design Advances, J. Am. Chem. Soc. 140 (2018) 1077–1082. https://doi.org/10.1021/jacs.7b11364.

[193] T.N. Tu, N.Q. Phan, T.T. Vu, H.L. Nguyen, K.E. Cordova, H. Furukawa, High proton conductivity at low relative humidity in an anionic Fe-based metal-organic framework, J. Mater. Chem. A. 4 (2016) 3638–3641. https://doi.org/10.1039/c5ta10467j.

[194] R. Moi, A. Ghorai, S. Banerjee, K. Biradha, Amino- and Sulfonate-Functionalized Metal–Organic Framework for Fabrication of Proton Exchange Membranes with Improved Proton Conductivity, Cryst. Growth Des. 20 (2020) 5557–5563. https://doi.org/10.1021/acs.cgd.0c00732.

[195] T. Kundu, S.C. Sahoo, R. Banerjee, Alkali earth metal (Ca, Sr, Ba) based thermostable metal–organic frameworks (MOFs) for proton conduction, Chem. Commun. 48 (2012) 4998. https://doi.org/10.1039/c2cc31135f.

[196] M. Bazaga-García, M. Papadaki, R.M.P. Colodrero, P. Olivera-Pastor, E.R. Losilla, B. Nieto-Ortega, M.Á.G. Aranda, D. Choquesillo-Lazarte, A. Cabeza, K.D. Demadis, Tuning Proton Conductivity in Alkali Metal Phosphonocarboxylates by Cation Size-Induced and Water-Facilitated Proton Transfer Pathways, Chem. Mater. 27 (2015) 424–435. https://doi.org/10.1021/cm502716e.

[197] S.-S. Liu, Z. Han, J.-S. Yang, S.-Z. Huang, X.-Y. Dong, S.-Q. Zang, Sulfonic Groups Lined along Channels of Metal–Organic Frameworks (MOFs) for Super-Proton Conductor, Inorg. Chem. 59 (2020) 396–402. https://doi.org/10.1021/acs.inorgchem.9b02649.

[198] M. Wahiduzzaman, S. Wang, J. Schnee, A. Vimont, V. Ortiz, P.G. Yot, R. Retoux, M. Daturi, J.S. Lee, J.-S.S. Chang, C. Serre, G. Maurin, S. Devautour-Vinot, A High Proton Conductive Hydrogen-Sulfate Decorated Titanium Carboxylate Metal-Organic Framework, ACS Sustain. Chem. Eng. 7 (2019) 5776–5783. https://doi.org/10.1021/acssuschemeng.8b05306.

[199] M.K. Sarango-Ramírez, D.-W.W. Lim, D.I. Kolokolov, A.E. Khudozhitkov, A.G. Stepanov, H. Kitagawa, Superprotonic Conductivity in Metal-Organic Framework via Solvent-Free Coordinative Urea Insertion., J. Am. Chem. Soc. 142 (2020) 6861–6865. https://doi.org/10.1021/jacs.0c00303.

[200] G. Zhang, H. Fei, Missing metal-linker connectivities in a 3-D robust sulfonate-based metal-organic framework for enhanced proton conductivity, Chem. Commun. 53 (2017) 4156–4159. https://doi.org/10.1039/c7cc01461a.

[201] J.M. Taylor, T. Komatsu, S. Dekura, K. Otsubo, M. Takata, H. Kitagawa, The Role of a Three Dimensionally Ordered Defect Sublattice on the Acidity of a Sulfonated Metal–Organic Framework, J. Am. Chem. Soc. 137 (2015) 11498–11506. https://doi.org/10.1021/jacs.5b07267.

[202] L. Liu, Z. Yao, Y. Ye, Q. Lin, S. Chen, Z. Zhang, S. Xiang, Enhanced Intrinsic Proton Conductivity of Metal–Organic Frameworks by Tuning the Degree of Interpenetration, Cryst. Growth Des. 18 (2018) 3724–3728. https://doi.org/10.1021/acs.cgd.8b00545.

[203] S. Tominaka, F.-X. Coudert, T.D. Dao, T. Nagao, A.K. Cheetham, Insulator-to-Proton-Conductor Transition in a Dense Metal–Organic Framework, J. Am. Chem. Soc. 137 (2015) 6428–6431. https://doi.org/10.1021/jacs.5b02777.

[204] M. Sadakiyo, T. Yamada, K. Honda, H. Matsui, H. Kitagawa, Control of crystalline proton-conducting pathways by water-induced transformations of hydrogen-bonding networks in a metal-organic framework, J. Am. Chem. Soc. 136 (2014) 7701–7707. https://doi.org/10.1021/ja5022014.

[205] S.-S. Bao, N.-Z. Li, J.M. Taylor, Y. Shen, H. Kitagawa, L.-M. Zheng, Co–Ca Phosphonate Showing Humidity-Sensitive Single Crystal to Single Crystal Structural Transformation and Tunable Proton Conduction Properties, Chem. Mater. 27 (2015) 8116–8125. https://doi.org/10.1021/acs.chemmater.5b03897.

[206] S. Nakatsuka, Y. Watanabe, Y. Kamakura, S. Horike, D. Tanaka, T. Hatakeyama, Solvent-Vapor-Induced Reversible Single-Crystal-to-Single-Crystal Transformation of a Triphosphaazatriangulene-Based Metal–Organic Framework, Angew. Chemie Int. Ed. 59 (2020) 1435–1439. https://doi.org/10.1002/anie.201912195.

[207] X. Chen, Z. Zhang, J. Chen, S. Sapchenko, X. Han, I. Da-Silva, M. Li, I.J. Vitorica-Yrezabal, G. Whitehead, C.C. Tang, K. Awaga, S. Yang, M. Schröder, Enhanced proton conductivity in a flexible metal–organic framework promoted by single-crystal-to-single-crystal transformation, Chem. Commun. 57 (2021) 65–68. https://doi.org/10.1039/D0CC05270A.

[208] W. Chen, S. Horike, D. Umeyama, N. Ogiwara, T. Itakura, C. Tassel, Y. Goto, H. Kageyama, S. Kitagawa, Glass Formation of a Coordination Polymer Crystal for Enhanced Proton Conductivity and Material Flexibility, Angew. Chemie Int. Ed. 55 (2016) 5195–5200. https://doi.org/10.1002/anie.201600123.

[209] N. Ma, S. Kosasang, A. Yoshida, S. Horike, Proton-conductive coordination polymer glass for solid-state anhydrous proton batteries, Chem. Sci. 12 (2021) 5818–5824. https://doi.org/10.1039/D1SC00392E.

[210] D.N. Dybtsev, V.G. Ponomareva, S.B. Aliev, A.P. Chupakhin, M.R. Gallyamov, N.K. Moroz, B.A. Kolesov, K.A. Kovalenko, E.S. Shutova, V.P. Fedin, High Proton Conductivity and Spectroscopic Investigations of Metal–Organic Framework Materials Impregnated by Strong Acids, ACS Appl. Mater. Interfaces. 6 (2014) 5161–5167. https://doi.org/10.1021/am500438a.

[211] S. Devautour-Vinot, E.S. Sanil, A. Geneste, V. Ortiz, P.G. Yot, J.S. Chang, G. Maurin, Guest-Assisted Proton Conduction in the Sulfonic Mesoporous MIL-101 MOF, Chem. - An Asian J. 14 (2019) 3561–3565. https://doi.org/10.1002/asia.201900608.

[212] X.-M. Li, L.-Z. Dong, S.-L. Li, G. Xu, J. Liu, F.-M. Zhang, L.-S. Lu, Y.-Q. Lan, Synergistic Conductivity Effect in a Proton Sources-Coupled Metal–Organic Framework, ACS Energy Lett. 2 (2017) 2313–2318. https://doi.org/10.1021/acsenergylett.7b00560.

[213] S. Bureekaew, S. Horike, M. Higuchi, M. Mizuno, T. Kawamura, D. Tanaka, N. Yanai, S. Kitagawa, One-dimensional imidazole aggregate in aluminium porous coordination polymers with high proton conductivity, Nat. Mater. 8 (2009) 831–836. https://doi.org/10.1038/nmat2526.

[214] M. V. Nguyen, T.H.N. Lo, L.C. Luu, H.T.T. Nguyen, T.N. Tu, Enhancing proton conductivity in a metal–organic framework at T > 80 °C by an anchoring strategy, J. Mater. Chem. A. 6 (2018) 1816–1821. https://doi.org/10.1039/C7TA10148A.

[215] B. Wang, Z. Feng, B. Hao, C. Zhang, Q. Wang, Promotion of Proton Conductivity by Encapsulation of Metal-Organic Polyhedra in Metal-Organic Frameworks, Chem. – A Eur. J. 27 (2021) 12137–12143. https://doi.org/10.1002/chem.202101213.

[216] F. Wang, C. Liang, J. Tang, F. Zhang, F. Qu, The promotion of proton conductivity by immobilizing molybdovanadophosphoric acids in metal–organic frameworks, New J. Chem. 44 (2020) 1912–1920. https://doi.org/10.1039/C9NJ05572J.

[217] X. Lai, Y. Liu, G. Yang, S.S. Liu, Z. Shi, Y. Lu, F. Luo, S.S. Liu, Controllable proton-conducting pathways via situating polyoxometalates in targeting pores of a metal–organic framework, J. Mater. Chem. A. 5 (2017) 9611–9617. https://doi.org/10.1039/C6TA10958F.

[218] J. Lee, D.-W. Lim, S. Dekura, H. Kitagawa, W. Choe, MOP × MOF: Collaborative Combination of Metal–Organic Polyhedra and Metal–Organic Framework for Proton Conductivity, ACS Appl. Mater. Interfaces. 11 (2019) 12639–12646. https://doi.org/10.1021/acsami.9b01026.

[219] K. Fujie, H. Kitagawa, Ionic liquid transported into metal-organic frameworks, Coord. Chem. Rev. 307 (2016) 382–390. https://doi.org/10.1016/j.ccr.2015.09.003.

[220] L.-H. Chen, B.-B. Wu, H.-X. Zhao, L.-S. Long, L.-S. Zheng, High temperature ionic conduction mediated by ionic liquid incorporated within the metal-organic framework UiO-67(Zr), Inorg. Chem. Commun. 81 (2017) 1–4. https://doi.org/10.1016/j.inoche.2017.04.019.

[221] K. Fujie, K. Otsubo, R. Ikeda, T. Yamada, H. Kitagawa, Low temperature ionic conductor: Ionic liquid incorporated within a metal-organic framework, Chem. Sci. 6 (2015) 4306–4310. https://doi.org/10.1039/c5sc01398d.

[222] W.L. Xue, W.H. Deng, H. Chen, R.H. Liu, J.M. Taylor, Y. kun Li, L. Wang, Y.H. Deng, W.H. Li, Y.Y. Wen, G.E. Wang, C.Q. Wan, G. Xu, MOF-Directed Synthesis of Crystalline Ionic Liquids with Enhanced Proton Conduction, Angew. Chemie - Int. Ed. 60 (2021) 1290–1297. https://doi.org/10.1002/anie.202010783.

[223] X.-L.L. Sun, W.-H.H. Deng, H. Chen, H.-L.L. Han, J.M. Taylor, C.-Q.Q. Wan, G. Xu, A Metal–Organic Framework Impregnated with a Binary Ionic Liquid for Safe Proton Conduction above 100 °C, Chem. - A Eur. J. 23 (2017) 1248–1252. https://doi.org/10.1002/chem.201605215.

[224] H. Chen, S.-Y.Y. Han, R.-H.H. Liu, T.-F.F. Chen, K.-L.L. Bi, J.-B.B. Liang, Y.-H.H. Deng, C.-Q.Q. Wan, High conductive, long-term durable, anhydrous proton conductive solid-state electrolyte based on a metal-organic framework impregnated with binary ionic liquids: Synthesis, characteristic and effect of anion, J. Power Sources. 376 (2018) 168–176. https://doi.org/10.1016/j.jpowsour.2017.11.089.

[225] Y. Yoshida, K. Fujie, D.W. Lim, R. Ikeda, H. Kitagawa, Superionic Conduction over a Wide Temperature Range in a Metal–Organic Framework Impregnated with Ionic Liquids, Angew. Chemie - Int. Ed. 58 (2019) 10909–10913. https://doi.org/10.1002/anie.201903980.

[226] J. Du, G. Yu, H. Lin, P. Jie, F. Zhang, F. Qu, C. Wen, L. Feng, X. Liang, Enhanced proton conductivity of metal organic framework at low humidity by improvement in water retention, J. Colloid Interface Sci. 573 (2020) 360–369. https://doi.org/10.1016/j.jcis.2020.04.023.

[227] X. Liang, F. Zhang, W. Feng, X. Zou, C. Zhao, H. Na, C. Liu, F. Sun, G. Zhu, From metal–organic framework (MOF) to MOF–polymer composite membrane: enhancement of low-humidity proton conductivity, Chem. Sci. 4 (2013) 983–992. https://doi.org/10.1039/C2SC21927A.

[228] X.Y. Dong, J.J. Li, Z. Han, P.G. Duan, L.K. Li, S.Q. Zang, Tuning the functional substituent group and guest of metal-organic frameworks in hybrid membranes for improved interface compatibility and proton conduction, J. Mater. Chem. A. 5 (2017) 3464–3474. https://doi.org/10.1039/c6ta07761g.

[229] C.-H. Tsai, C.-C. Wang, C.-Y. Chang, C.-H. Lin, Y.W. Chen-Yang, Enhancing performance of Nafion ® -based PEMFC by 1-D channel metal-organic frameworks as PEM filler, Int. J. Hydrogen Energy. 39 (2014) 15696–15705. https://doi.org/10.1016/j.ijhydene.2014.07.134.

[230] Z. Li, G. He, B. Zhang, Y. Cao, H. Wu, Z. Jiang, Z. Tiantian, Enhanced Proton Conductivity of Nafion Hybrid Membrane under Different Humidities by Incorporating Metal–Organic Frameworks With High Phytic Acid Loading, ACS Appl. Mater. Interfaces. 6 (2014) 9799–9807. https://doi.org/10.1021/am502236v.

[231] Z. Rao, B. Tang, P. Wu, Proton Conductivity of Proton Exchange Membrane Synergistically Promoted by Different Functionalized Metal–Organic Frameworks, ACS Appl. Mater. Interfaces. 9 (2017) 22597–22603. https://doi.org/10.1021/acsami.7b05969.

[232] H.A. Patel, N. Mansor, S. Gadipelli, D.J.L. Brett, Z. Guo, Superacidity in Nafion/MOF Hybrid Membranes Retains Water at Low Humidity to Enhance Proton Conduction for Fuel Cells, ACS Appl. Mater. Interfaces. 8 (2016) 30687–30691. https://doi.org/10.1021/acsami.6b12240.

[233] Z. Li, G. He, Y. Zhao, Y. Cao, H. Wu, Y. Li, Z. Jiang, Enhanced proton conductivity of proton exchange membranes by incorporating sulfonated metal-organic frameworks, J. Power Sources. 262 (2014) 372–379. https://doi.org/10.1016/j.jpowsour.2014.03.123.

[234] N. Anahidzade, A. Abdolmaleki, M. Dinari, K. Firouz Tadavani, M. Zhiani, Metal-organic framework anchored sulfonated poly(ether sulfone) as a high temperature proton exchange membrane for fuel cells, J. Memb. Sci. 565 (2018) 281–292. https://doi.org/10.1016/j.memsci.2018.08.037.

[235] C. Ru, Z. Li, C. Zhao, Y. Duan, Z. Zhuang, F. Bu, H. Na, Enhanced Proton Conductivity of Sulfonated Hybrid Poly(arylene ether ketone) Membranes by Incorporating an Amino–Sulfo Bifunctionalized Metal–Organic Framework for Direct Methanol Fuel Cells, ACS Appl. Mater. Interfaces. 10 (2018) 7963–7973. https://doi.org/10.1021/acsami.7b17299.

[236] Y.Y. Cai, J.J. Wang, Z.H. Cai, Q.G. Zhang, A.M. Zhu, Q.L. Liu, Enhanced Performance of Sulfonated Poly(ether ether Ketone) Hybrid Membranes by Introducing Sulfated MOF-808/Graphene Oxide Composites, ACS Appl. Energy Mater. 4 (2021) 9664–9672. https://doi.org/10.1021/acsaem.1c01789.

[237] Z. Rao, K. Feng, B. Tang, P. Wu, Construction of well interconnected metal-organic framework structure for effectively promoting proton conductivity of proton exchange membrane, J. Memb. Sci. 533 (2017) 160–170. https://doi.org/10.1016/j.memsci.2017.03.031.

[238] H. Sun, B. Tang, P. Wu, Rational Design of S-UiO-66@GO Hybrid Nanosheets for Proton Exchange Membranes with Significantly Enhanced Transport Performance, ACS Appl. Mater. Interfaces. 9 (2017) 26077–26087. https://doi.org/10.1021/acsami.7b07651.

[239] H. Sun, B. Tang, P. Wu, Two-Dimensional Zeolitic Imidazolate Framework/Carbon Nanotube Hybrid Networks Modified Proton Exchange Membranes for Improving Transport Properties, ACS Appl. Mater. Interfaces. 9 (2017) 35075–35085. https://doi.org/10.1021/acsami.7b13013.

[240] Z. Zhang, J. Ren, J. Xu, Z. Wang, W. He, S. Wang, X. Yang, X. Du, L. Meng, P. Zhao, Adjust the arrangement of imidazole on the metal-organic framework to obtain hybrid proton exchange membrane with long-term stable high proton conductivity, J. Memb. Sci. 607 (2020) 118194. https://doi.org/10.1016/j.memsci.2020.118194.

[241] P. Chen, S. Liu, Z. Bai, Y. Liu, Enhanced ionic conductivity of ionic liquid confined in UiO-67 membrane at low humidity, Microporous Mesoporous Mater. 305 (2020) 110369. https://doi.org/10.1016/j.micromeso.2020.110369.

[242] C. Liu, S. Feng, Z. Zhuang, D. Qi, G. Li, C. Zhao, X. Li, H. Na, Towards basic ionic liquid-based hybrid membranes as hydroxide-conducting electrolytes under low humidity conditions, Chem. Commun. 51 (2015) 12629–12632. https://doi.org/10.1039/c5cc03462k.

[243] Y. Guo, Z. Jiang, W. Ying, L. Chen, Y. Liu, X. Wang, Z.-J. Jiang, B. Chen, X. Peng, A DNA-Threaded ZIF-8 Membrane with High Proton Conductivity and Low Methanol Permeability, Adv. Mater. 30 (2018) 1705155. https://doi.org/10.1002/adma.201705155.

[244] X.-Y. Dong, J.-H. Wang, S.-S. Liu, Z. Han, Q.-J. Tang, F.-F. Li, S.-Q. Zang, Synergy between Isomorphous Acid and Basic Metal–Organic Frameworks for Anhydrous Proton Conduction of Low-Cost Hybrid Membranes at High Temperatures, ACS Appl. Mater. Interfaces. 10 (2018) 38209–38216. https://doi.org/10.1021/acsami.8b12846.

[245] J. Escorihuela, Ó. Sahuquillo, A. García-Bernabé, E. Giménez, V. Compañ, Phosphoric Acid Doped Polybenzimidazole (PBI)/Zeolitic Imidazolate Framework Composite Membranes with Significantly Enhanced Proton Conductivity under Low Humidity Conditions, Nanomaterials. 8 (2018) 775. https://doi.org/10.3390/nano8100775.

[246] D.W. Kang, M. Kang, C.S. Hong, Post-synthetic modification of porous materials: superprotonic conductivities and membrane applications in fuel cells, J. Mater. Chem. A. 8 (2020) 7474–7494. https://doi.org/10.1039/D0TA01733G.

[247] X. Chen, G. Li, Proton conductive Zr-based MOFs, Inorg. Chem. Front. (2020). https://doi.org/10.1039/d0qi00883d.

[248] A.L. Li, Q. Gao, J. Xu, X.H. Bu, Proton-conductive metal-organic frameworks: Recent advances and perspectives, Coord. Chem. Rev. 344 (2017) 54–82. https://doi.org/10.1016/j.ccr.2017.03.027.

[249] X. Meng, H.-N.N. Wang, S.-Y.Y. Song, H.-J.J. Zhang, Proton-conducting crystalline porous materials, Chem. Soc. Rev. 46 (2017) 464–480. https://doi.org/10.1039/c6cs00528d.

[250] P. Jhariat, P. Kumari, T. Panda, Structural features of proton-conducting metal organic and covalent organic frameworks, CrystEngComm. 22 (2020) 6425–6443. https://doi.org/10.1039/d0ce00902d.

[251] M. Yoon, K. Suh, S. Natarajan, K. Kim, Proton conduction in metal-organic frameworks and related modularly built porous solids, Angew. Chemie - Int. Ed. 52 (2013) 2688–2700. https://doi.org/10.1002/anie.201206410.

[252] X. Deng, J.-Y. Hu, J. Luo, W.-M. Liao, J. He, Conductive Metal–Organic Frameworks: Mechanisms, Design Strategies and Recent Advances, Top. Curr. Chem. 378 (2020) 27. https://doi.org/10.1007/s41061-020-0289-5.

[253] B.-X. Han, Y.-F. Jiang, X.-R. Sun, Z.-F. Li, G. Li, Proton conductive N-heterocyclic metal–organic frameworks, Coord. Chem. Rev. 432 (2021) 213754. https://doi.org/10.1016/j.ccr.2020.213754.

[254] C. Wang, X. Liu, N. Keser Demir, J.P. Chen, K. Li, Applications of water stable metal-organic frameworks, Chem. Soc. Rev. 45 (2016) 5107–5134. https://doi.org/10.1039/c6cs00362a.

Chapter 2

Characterization proton dynamics in MOFs

2.1. Introduction

The ionic transport in crystalline solids, in particular proton transport in MOFs, can be evidenced using different techniques coupled with the structural analysis obtained from X-ray diffraction experiments. These techniques include experimental tools, i.e., complex impedance spectroscopy, solid state nuclear magnetic resonance or neutron scattering methods, as well as computational approaches. Combined all together, these complementary techniques were demonstrated as very efficient to explore proton motions in MOFs over a broad range of length scale from atomistic to molecular levels.

This chapter is dedicated to a brief description of these techniques, with a peculiar attention given to the electrical measurements used in the frame of this work. As a starting point, the basic concepts of ionic conduction and ionic diffusion are firstly discussed.

2.2. Ionic conduction in solids

From a microscopic point of view, ionic conduction is driven by a diffusion mechanism, which is described by ions hopping, due to local defects.[1–3] In an ideal crystal, all ions are arranged in regular periodic fashion with too little space for ions to diffuse. As a consequence, they are only subjected to vibrations around their equilibrium position. However, at any non-zero temperature, defects are created, due to the increase of entropy to minimize the free energy of the system. Two main types of positional disorders crucial for ion mobility in crystals are ‘Schottky’ and ‘Frenkel’ defects. These belong to the class of ‘point defects’ in crystals. Schottky defect refers to the crystal imperfection in which a pair of ions disappears leaving their positions vacant. The Frenkel defect results from the missing of a single ion from its regular position towards an interstitial site. Both Frenkel and Schottky defects result in vacant sites in the crystal and any ion in the immediate vicinity can jump to one of these vacant sites. Similarly, the ion that moves to the interstitial site, giving rise to a Frenkel defect, can subsequently jump to a neighbouring interstitial site and so on, resulting in long distance motion of the ion. These processes can lead to transport of ions across the solid giving rise to conductivity. Apart from these two mechanisms, cooperative movements of two or more ions can also be involved in the conduction mechanism.

2.2.1. Ionic diffusion

As discussed above, in ionic conducting solids, the electrical current is transported by the movement or diffusion of ions of the crystal lattice, either as interstial or lattice ions though a hopping process. Long-range macroscopic transport of ions is then a consequence of microscopic ion diffusion, which requires accessible sites, i.e., a concentration gradient. Concentration gradient leads to the particle current (J_{diff}) and for particles with charge q, automatically to an electrical current, $J_{elect} = q \cdot J_{diff}$, given by Ficks laws. Considering a flux over one direction, it is proportional to the concentration gradient along this direction according to:

$$J_{diff} = -D\frac{\partial C}{\partial x} \qquad \text{Eq. 2.1}$$

With,

J_{diff} = atomic flux per surface area and time units

x = direction along with the diffusion occurs

C = concentration of the diffusing ion

D = coefficient of diffusion

Sign minus deals with the fact that diffusion occurs between areas from high towards low concentration of ions. When flux and gradient are time dependent, we have:

$$\frac{\partial C}{\partial t} = -\frac{\partial J_{diff}}{\partial x} \qquad \text{Eq. 2.2}$$

Combining Eq. 2.1 and 2.2 and assuming D is independent on C, we got the second Fick law:

$$\frac{\partial C}{\partial t} = D\frac{\partial^2 C}{\partial x^2} \qquad \text{Eq. 2.3}$$

The diffusion coefficient (D) characterizes the ion mobility (μ) through the Einstein-Smoluchowski relation:

$$D = \frac{kT\mu}{q} \qquad \text{Eq. 2.4}$$

It obeys to the Arrhenius law:

$$D = D_o\ exp(-\frac{E_a}{kT}) \quad \text{Eq. 2.5}$$

With,

D_o = frequency factor

E_a = activation energy of diffusion

K = Boltzmann constant

T = absolute temperature

The ionic conductivity of a charge q is defined as follows:

$$\sigma = Cq\mu \quad \text{Eq. 2.6}$$

When both ionic conductivity and ionic diffusion follow a random-walk mechanism, the Nernst-Einstein relation thus gives:

$$D = \frac{\sigma . kT}{q^{\,2} C} \quad \text{Eq. 2.7}$$

2.2.2. Ionic conduction

Within a statistical thermodynamic treatment of rate theory,[4,5] the probability of successful jumps (p) in which an ion can move from one stable site to the adjacent site is given by:

$$p = \exp\,(-\frac{\Delta G_m}{kT}) \quad \text{Eq. 2.8}$$

Where, ΔG_{m} is the height of the energy barrier of the jump, which is the rate-determining process (i.e., Gibbs free energy difference between a saddle point and a stable position). Ions vibrate within their lattice site and attempt to overcome the barrier with an attempt frequency (ν) close to 10^{13} s^{-1}. The ion hopping process is randomly distributed, resulting to a Brownian motion. The probability for the reverse jump is equal to that of the forward jump. When an electrical field E is applied to the material of interest, the energy landscape of the system is changed through the modification of the energy barrier in the forward and backward directions of the field. One demonstrates that the net velocity of the migrating ions (ν_{m}) in the direction of the field becomes:

$$\nu_m = \frac{\nu q a_0^2 E}{kT} \exp\left(-\frac{\Delta G_m}{kT}\right) \quad \text{Eq. 2.9}$$

Where, q is the charge of the ion, and a_0 is the jump distance.[6] Since the drift mobility of an ion (μ) and the ionic conductivity (σ) are defined as $\mu = \nu_m/E_v$ and Eq. 2.6 respectively, σ becomes:

$$\sigma = \frac{\gamma C \nu q^2 a_o^2}{kT} \exp\left(-\frac{\Delta G_m}{kT}\right) \quad \text{Eq. 2.10}$$

where, γ is a geometric factor linked to the dimensionality of the conduction pathway. The free energy consumption for the ion migration ΔG_m is separated into the enthalpy (ΔH_m) and entropy (ΔS_m) of migration ($\Delta G_m = \Delta H_m - T\Delta S_m$), because temperature-dependent conductivity measurements only provide an enthalpy for the jump:

$$\sigma = \frac{\gamma C \nu q^2 a_o^2}{kT} \exp\left(\frac{\Delta S_m}{k}\right) \exp\left(-\frac{\Delta H_m}{kT}\right) \quad \text{Eq. 2.11}$$

Noteworthy, a defect formation is also involved for the ion migration and the term of ΔG_F, the formation energy per defect, needs to be taken into account. As σ is usually measured temperature-dependent, an Arrhenius relation gives the activation barrier and the temperature-independent pre-exponential factor σ_0 as:

$$\sigma = \frac{\sigma_0}{T} \exp\left(-\frac{\Delta H_m}{kT}\right) \quad \text{Eq. 2.12}$$

The enthalpy of migration ΔH_m is often generalized with an activation energy E_a (unit of kJ.mol^{-1} or eV). According the Eq. 2.7, σ_0 is defined as follows:

$$\sigma_0 = \frac{D_0 q^2 C}{k} \exp\left(\frac{\Delta S_m}{k}\right) \quad \text{Eq. 2.13}$$

Where, D_0 is the frequency factor and ΔS_m corresponds to the entropy of the ion motion.

It is then concluded that fast ion transport requires high carrier densities (C) and a low barrier for migration (ΔH_m), which is dependent on structural features, i.e., the transport mechanism and pathway.

2.3. Microscopic mechanisms of proton conductivity

Proton is the only ion without an electron shell, which makes it a special case among all the other cations. As it is small and light, proton is highly mobile and able to polarize its surrounding environment. Proton possess 36.2 x 10^{-8} $m^2.S^{-1}.V^{-1}$ mobility in an aqueous medium, which is 9 times higher than lithium ion (4.0 x 10^{-8} $m^2.S^{-1}.V^{-1}$) and 7 times higher than sodium ion (5.2 x 10^{-8} $m^2.S^{-1}.V^{-1}$).[7,8] This is the reason behind its unusual ability to move in condensed water.

As discussed in the next section, performance studies on proton-conducting materials are mainly carried out using electrical measurements, among other techniques. The ionic conductivity (σ) deduced from electrical measurements, is a variable that evaluates the transfer of an ion from one site to others, through defects or assisted molecule creating a pathway in the solids. During its pathway, proton moves through condensed matter with help of a charge carrier at the microscopic level. Variety of charge carriers were extensively studied for their participation through hydrogen bond formation during the proton conduction mechanism such as water, oxoacid anions,[9,10] oxo-acids, [11] oxide ions,[7] amine-based molecules (NH_3,[12] dimethylammonium (DMA)[13]), and heterocycles (imidazole family compounds [14,15]). The hydrogen bond refers to the interaction of a hydrogen atom with light and polarizable atoms, especially N, F, and O. These interatomic forces mutually organize as three components: a donor (D), hydrogen (H) and an acceptor (A). A hydrogen bond is highly directional, with the angle D–H–A (Figure 2.1) normally exceeding 150° in the case of water molecules (Figure 2.1).[16] It is characterized by an intermediate energy between dispersive and covalent interactions. In the case of water in liquid state, this energy is 6.3 $kJ.mol^{-1}$,[17] whereas the energy of London and covalent interactions lies around a few $kJ.mol^{-1}$ and about 100 $kJ.mol^{-1}$, respectively. The dynamic nature, strength and number of H-bonds over time are significant features of the typical hydrogen bonds.[18] All these characteristics help to understand the proton transfer mechanism in homogenous or heterogeneous systems.

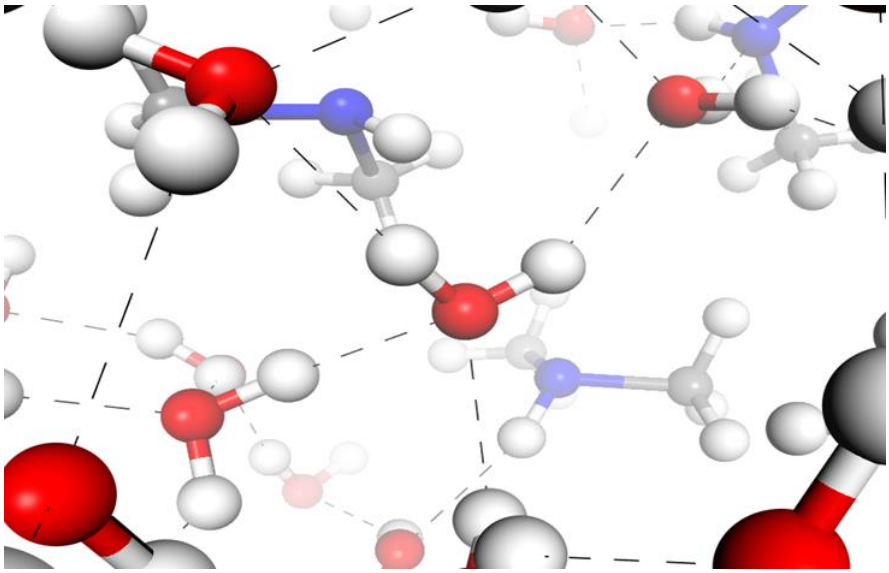

Figure 2.1 – Representation of the hydrogen bonds (dashed lines) in a system containing water and dimethylamine (DMA). Oxygen, nitrogen, carbon and hydrogen are identified with red, blue, gray and white colors, respectively. In blue light, atoms that participate to the hydrogen bond as donor (D), hydrogen (H), and acceptor (A) and the angle (θ) they establish.[19]

The proton transport mechanism depends on the nature of the proton charge carriers and the media via which they travel. The proton conduction mechanism is mainly characterized by two types of processes: the Grotthuss and the Vehicular mechanisms.[10] In the vehicular mechanism, a proton is bonded to a small vehicle molecule such as water, ammonia, etc. acting as Brønsted base and further travels through the media by molecular diffusion.[20] In the Grotthuss mechanism encountered in aqueous media, the proton transfer occurs from one water molecule to another one, while the oxygen of water receives and passes the extra proton to the neighboring molecule.[21] This mechanism was suggested by von Grotthuss in the 19th century while postulating series of observations for a galvanic cell.[22] A schematic representation of the Grotthuss and the vehicular mechanisms is shown in Figure 2.2.

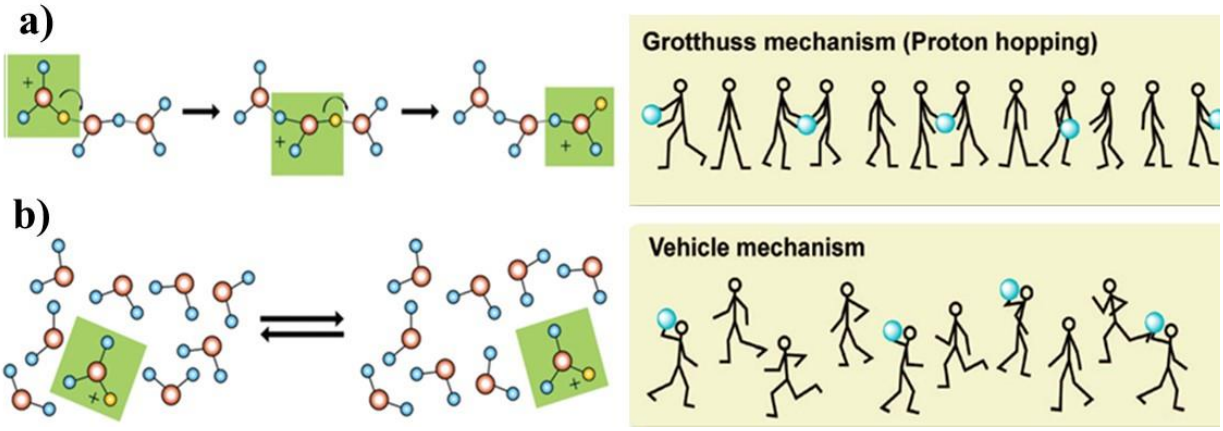

Figure 2.2 - Schematic representation of **a)** the Grotthuss and **b)** vehicular mechanism (taken from ref [23,24]).

The Grotthuss mechanism further gained a deeper understanding, due to advances in experimental and theoretical techniques. In contrast to initially proposed, the proton transfer cannot occur through a proton hopping mechanism from one molecule to the other in a subsequential hydrogen-bonded molecular chain,[25–29] because of critical electrostatic polarization of the chain. In aqueous media, the proton transport process is rather based on the concept of "structure diffusion". According to Figure 2.3, the solvated excess proton is discussed in terms of 2 limiting structures, the Eigen cation, a triply solvated hydronium ion ($H_3O^+.3H_2O$ or $H_9O_4^+$),[30] and the Zundel ion, a proton equally shared between 2 water molecules ($H_2O.H.OH_2^+$ or $H_5O_2^+$).[31] The very small difference in energy between both configurations allows their interconvection very easily,[32,33] so that the proton rapidly rattles between the oxygen atoms of two neighbouring water molecules, leading to the proton displacement without moving the protonic mass. The dynamic between the Eigen ion and a surrounding water molecule, forming the subsequent Zunder ion is assigned to the "special pair dance" terminology while the global mechanism is termed as Eigen-Zundel-Eigen (EZE) mechanism. In the EZE model, the excess charge does not actually move in large extent as its movements are just from the centre of an elongated bond to a more compact bond, while the centre of charge or "structure" is dislocated by a much longer distance. The resulting displacement of the protonic charge without moving the protonic mass, as referred in the Grotthuss mechanism, involves lower activation energy ($Ea < 0.4$ eV) than that characterizing the vehicular mechanism ($Ea > 0.4$ eV), which follows the displacement of bulkier ionic species like H_3O^+ or NH_4^+ with inevitably higher activation energy.

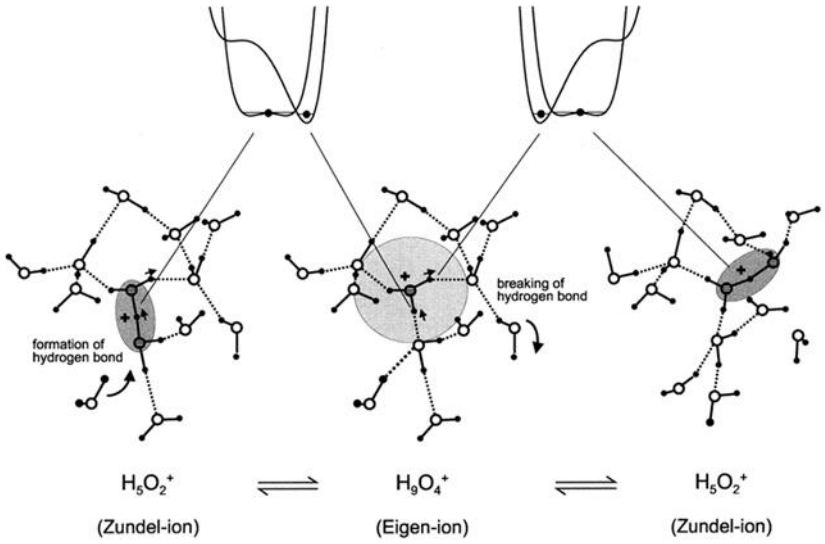

Figure 2.3 – Microscopic conduction mechanism of a proton in water.[7] The "structure diffusion" is highlighted in grey, with Zundel and Eigen ions shown respectively in dark and light grey. A schematic energy barrier assigned to the excess proton between two neighboring water molecules is also assigned and it shows the adiabatic nature of a proton transfer from a molecule to another under the context of a Zundel – Eigen transition.

Although being different, both Grotthuss and vehicular mechanisms can act simultaneously in real situations. As exemplified for bulk water, 22% of the conductivity is through vehicular mechanism because of self-diffusion of the water molecules.[7] In other homogeneous media, such as in heterocycle species (e.g. imidazole), the proton conductivity mechanism has been modeled in a different way: the pathway for the proton displacement occurs along unidimensional hydrogen bonded chain of molecules with the proton transmitter media in a Grotthuss-like mechanism.[7,34,35] Interestingly, this mechanism has been shown to be even more efficient when these molecules are confined in porous materials.[36,37]

2.4. Characterization of ionic transport in solids

According to the previous section, ionic transport in solids is efficiently characterized using electrical measurements, among them Complex Impedance Spectroscopy (CIS) is the basic technique we used in the scope of this work. Besides electrical measurements, computational approaches, Solid-State Nuclear Magnetic Resonance (SS-NMR) spectroscopy and Neutron Scattering (NS) methods are also used to investigate proton transport in MOFs. This section gives

the main achievements obtained from these approaches when applied on proton conducting MOFs, before a description of the main concepts in line with CIS.

2.4.1. Characterization of proton dynamics in MOFs

2.4.1.1. Computational methods

Modelling the proton transport in MOFs is very challenging since this process involves several concomitant phenomena: the bond breaking/formation associated with the proton motion, the dynamics of guest molecules, and the global or local structural rearrangements of the host framework. Accordingly, a few approaches using Density Functional Theory (DFT) calculations, *ab initio* molecular dynamics (AIMD) and molecular simulations based on empirical force fields have been developed in tandem with experimental tools or independently.

First, forcefields based Monte Carlo (MC) simulations were used to i) describe the preferential conformation/distribution of water and/or guest molecules, their interactions with the MOFs hosting framework to characterize the structure of the hydrogen-bonded network connecting guest/guest and guest/host species and ii) further establish the relationships between the resulting preferential pathway for the proton migration with the proton conduction properties of various MOFs, including 2D Zn-based MOFs, functionalized UiO-66s, MIL-163(Zr)…[13,38,39] Quantum calculations were also performed to determine the preferential arrangement of water by geometry optimization and to further elucidate the proton migration pathways.[36,40] DFT calculations were combined with IR experiments performed on the defective NU-1000 to demonstrate the relationship between the proton topology of the Zr_6-based nodes with the acid/base characteristics and the proton conductivity of the system.[41]

In these approaches, the bond topology is fixed, so that information on the bond breaking/formation associated with the proton motion cannot be handled. To tackle this challenge and further describe the structure, thermodynamics and dynamics of the hydrated proton in porous MOFs, a more complex method, based on the Empirical Valence Bond formalism (EVB) was implemented in MD simulations by Paesani *et al.*,[42] and later by the group.[43,44] Interestingly, the interconversion between Zundel and Eigen or more complex cation ($H_70_3^+$) species was evidenced to illustrate the water-mediated proton transfer mechanism in the flexible MIL-53(Cr) and UiO-66(Zr)-2CO_2H. As an alternative, AIMD approaches were further used to get dynamics

information, through the investigation of the charge transfer and bond breaking/formation processes occurring in proton conducting MOFs.[45] As an example, the proton hopping process via imidazole molecules highly aligned but still free to move in the 1D channels of MIL-53(Al) was successfully evidenced, while the increase of the conductivity with the imidazole loading was correlated to the increase of the imidazole dynamics within the porosity.[46,47] In the group, AIMD strategies were adopted to describe the structural rearrangements of MOF frameworks in the presence of guests. This methodology was applied to various hydrated MOFs or analogous solids.[48–52] As illustrated for MIP-177-HSO_4-LT,[51] these calculations revealed a Grotthuss-like mechanism initiated by the proton transfer from the acidic hydrogen-sulfate groups of MIP-177-SO_4H-LT towards neighbouring guest H_2O molecules subsequently followed by a proton shuttle over longer distances, through the H-bonded network formed by the guest water molecules along the channels. Although computational methods are powerful to provide a reliable illustration of the proton-conduction mechanism in MOFs at the atomic scale, their development is recent with only limited examples.

2.4.1.2. Solid-State Nuclear Magnetic Resonance spectroscopy (SS-NMR)

SS-NMR measurements are powerful to probe the proton dynamics in solids. Among the large panel of SS-NMR techniques, the Deuterium ^2H NMR and the Pulse Field Gradient PFG-NMR are optimal modes to provide crucial and complementary information on the conducting media and its interactions with the MOF framework.

The analysis of the ^2H NMR line shape and spin-relaxation times (T_1, T_2) at variable temperature allows to characterize the reorientational motions of deuterated species, even if the later display different mobilities and various H-bonding features. This method is then restricted to the investigation of proton dynamics at the molecular length scale, i.e. not exceeding several nanometres [53] corresponding to events of 10^{-10} - 10^{-3} s. When combined with conductivity measurements, it provides a characterization of the limiting step of the proton conduction mechanism, i.e. the charge transfer, via the exploration of the motional modes associated with breaking/formation of proton carriers such as H_3O^+.[54] A few proton conducting MOFs or coordination frameworks were investigated using ^2H NMR technique.[15,55–60] As an example, Sarango-Raminrez *et al.*,[59] studied the channel-like MOF-74(Mg) with open metal sites

coordinated to urea, whose amino groups are able to form H-bonds with adsorbed water molecules. The analysis of ^2H NMR data allowed to evidence that the adsorbed D_2O molecules confined inside the MOF porosity form ice-like tubes in interaction with ND_2 groups of urea. The later were shown to flip about their symmetry axis. Upon heating, the dynamical melting of the ice tube was further evidenced, in agreement with the higher mobility of the protic species: $D_3O^+$and D_2O display fast internal and uniaxial rotations, attributed to the proton exchange transfer. The corresponding rotation energy (ΔE = 0.16 eV) was in good agreement with the value deduced from the conductivity measurements, supporting the Grotthuss-like mechanism of the proton transfer. It was concluded that the polarized urea, due to its coordination to the open metal sites, involves strong H-bonds between water molecules, optimal for stabilizing the hydronium species.

For probing translational motions of protons in conducting solids, PFG NMR, via the analysis of the attenuated signal intensity decay rate, is an optimal mode. Since it probes dynamical processes on long time (10^{-3} - 1 s) and large length scale (1 - 100 μm), it provides the diffusion coefficients (D) of the mobile proton, but without distinguishing the mechanisms in play, i.e., hopping versus vehicular processes. In addition, the so-explored length scale requires relatively large crystallites to prevent the intercrystalline contribution, which can be a main issue for MOFs, as discussed later. Accordingly, only a few studies is reported on proton dynamics in MOFs using PFG-NMR.[61–63] As an illustration, Horike *et al.*, evaluated the H^+ diffusion coefficient in a Ca-based MOF, post-modified with LiCl to boost the conductivity properties up to 10^{-2} S.cm^{-1} at 298 K / 40% RH.[62] They showed that D(H^+) is comparable to that of Nafion under similar T/RH conditions. Noteworthy, D(Li^+) was also evaluated, since both H^+ and Li^+ nucleus can be tracked by PFG-NMR. As both ionic species display similar self-diffusion coefficients, it was concluded that the excellent conducting performances of the Ca-based MOF results from a synergic effect of both H^+ and Li^+ species. Importantly, electrical measurements cannot provide any information about the nature of the moving species, while PFG NMR combines quantitative data with the origin of ionic diffusion.

2.4.1.3. Neutron Scattering techniques (NS)

Proton transport in solids can be addressed using NS techniques through two modes, i.e., Inelastic Neutron Scattering (INS) and Quasi-Elastic Neutron Scattering (QENS). The incoherent scattering cross-section of hydrogen being much larger than that of any other common elements,

NS techniques allow to probe selectively the vibrational and the molecular (translational and rotational) motions of hydrogen-containing species in solid systems.

Typically, INS is used to characterize the internal vibrations modes of protic species, via the analysis of the inelastic features of solids. As a main advantage, it allows to qualitatively but also quantitatively distinguish different protic moieties relevant in proton conducting solids, such as -OH groups, H_2O molecules and H_3O^+ ions. However, INS mode is poorly reported in literature as a tool to characterize the vibrational modes of protic MOFs,[64] because it competes with optical spectroscopies, much easier to implement as they do not require deuterated systems.

On the other hand, QENS allows to elucidate the proton transport mechanism in solids at the molecular scale, since it provides dynamical parameters, i.e., diffusion coefficient, correlation times etc. In complement to PFG NMR, it operates on a shorter length range (0.1 - 3 nm), corresponding to faster motions (10^{-8} - 10^{-12} s). A very limited number of proton conducting MOFs were investigated using QENS,[43,44,65–67] due limitations inherent to NS, as it requires deuterated materials, the combination with complementary tools to elaborate a starting model for the analysis of the raw data. In this context, the research group where I worked combined electrical measurements, QENS experiments and a modelling approach to give a microscopic picture of the proton transport in UiO-66(Zr)-$(CO_2H)_2$.[43] Propitiously, QENS experiments evidenced the presence of two dynamical species: 'free' protons performing long-range diffusion and diffusing and rotating water molecules. The analysis of the self-diffusion coefficients for both species showed a faster translational motion of protons compared to that of water, suggesting a Grotthuss-like mechanism, further confirmed by MD simulations.

2.4.2. Complex Impedance Spectroscopy (CIS)

2.4.2.1. Fundamental of complex impedance spectroscopy

CIS is the basic technique to characterize electrical properties of solids or liquids. This encompasses electronic conduction as well as ionic conduction, electrochemical reactions, bulk and interfacial polarization among other processes involving motion of charges at short- or long-range scale. It provides the response of a sample incorporated inside a circuit to an alternating current or voltage as a function of the applied frequency.

Impedance (Z) reflects the opposition of a material to the flow of electric current in a circuit. It corresponds to the equivalent resistance (R) when direct current (dc) is replaced by alternative current (ac). Considering a linear system, the current response of the system (I(ω)) to the application of an alternating potential U(ω) = U_0 exp($j\omega t$) is shifted in phase (θ) as:

$$I(\omega) = I_0 exp(j\omega t - \theta) \quad \text{Eq. 2.14}$$

Where, U_0 and I_0 are the amplitudes of the signal, ω is the angular frequency (ω = 2πf, f being the frequency of the applied electrical field) and t corresponds to time. (Figure 2.4)

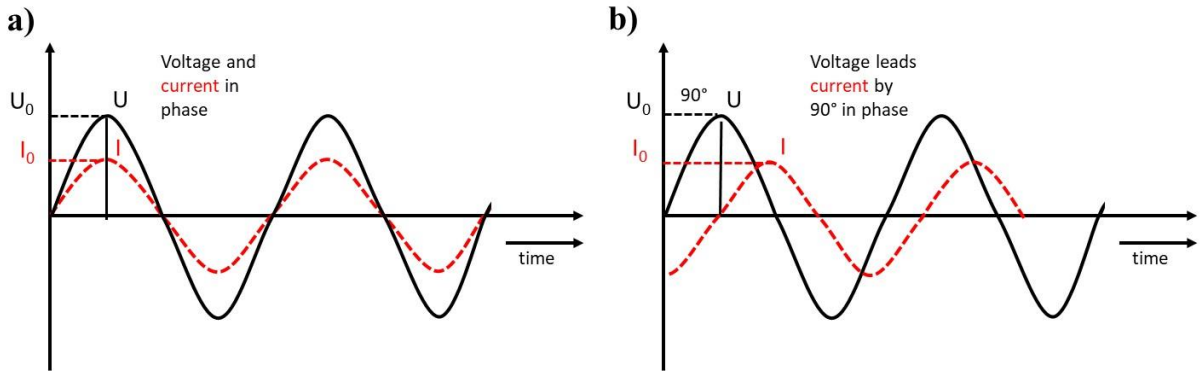

Figure 2.4 – Sinusoidal voltage and current signals versus time at fixed frequency ac power for **a)** the input signal and **b)** the output signal after passing through a hypothetical material.

By analogy with the Ohm's law, the impedance Z is defined as the ratio between voltage (U(ω)) and current I(ω) and is then expressed as follows:

$$Z(\omega) = U(\omega)/I(\omega)) \quad \text{Eq. 2.15}$$

$$Z(\omega) = Z_0(cos\theta - jsin\theta) \quad \text{Eq. 2.16}$$

$$Z(\omega) = Z_0 cos\theta + -jZ_0 sin\theta \quad \text{Eq. 2.17}$$

$$Z(\omega) = Z' + jZ'' \quad \text{Eq. 2.18}$$

According to equation 2.18, the impedance thus corresponds to a complex quantity, including real (Z') and imaginary (Z") parts corresponding to the in-phase and out of phase components, respectively. The impedance response can be modeled using equivalent circuits to represent the contributions of the different processes cited at the beginning of this section. Basic impedance elemental circuits are listed in the following:

(a) Resistor (R):

The impedance of a resistor has no imaginary component and the current is then in phase with the voltage, i.e., θ = 0. The impedance is thus independent on the angular frequency:

$$Z(\omega) = R \qquad \text{Eq. 2.19}$$

(b) Capacitor (C):

The impedance of a capacitor has no real component and the current is - 90° out of phase with the voltage. According to Eq. 2.20, the impedance of a capacitor tends to zero at high frequency, whereas it goes towards infinity at very low frequency.

$$Z(\omega) = {}^{1}/_{(jC_{\omega})} \qquad \text{Eq. 2.20}$$

(c) Inductor (L):

The impedance of an inductor has no real component and the current is + 90° out of phase with the voltage. The impedance is defined as:

$$Z(\omega) = j\omega L \qquad \text{Eq. 2.21}$$

The impedance of inductors and capacitors are expressed as a function of the frequency of the ac signal, and both the magnitude and phase angle of the impedance are frequency dependant. Finally, the global impedance response (Z_{total}) of a system corresponds to a combination of individual impedance elements connected in series or parallel. Equations 2.22 and 2.23 represent the combined impedance for equivalent circuits in both configurations, respectively:

for series configuration

$$Z_{total} = \sum_{k} Z_k \qquad \text{Eq. 2.22}$$

for parallel configuration

$$\frac{1}{Z_{total}} = \sum_{k} \frac{1}{Z_k} \qquad \text{Eq. 2.23}$$

2.4.2.2. Data representation

The most usual way of representing the impedance response is the Nyquist plot. In this graph, the imaginary part of the impedance, mostly represented with the negative sign, is plotted against its real part. At fixed frequency, the impedance is represented by a vector quantity Z, with the angle between the vector and the real-axis (Z') corresponding to the phase shift θ (Figure 2.5a). By performing measurements at different frequencies, the Z vector, i.e., the absolute impedance |Z|, its Z' or Z" components and the phase shift θ as well, changes resulting in a trace with a characteristic shape (Figure 2.5b), according to the combination of the equivalent circuits considered to account for the different dynamical processes involved in the system.

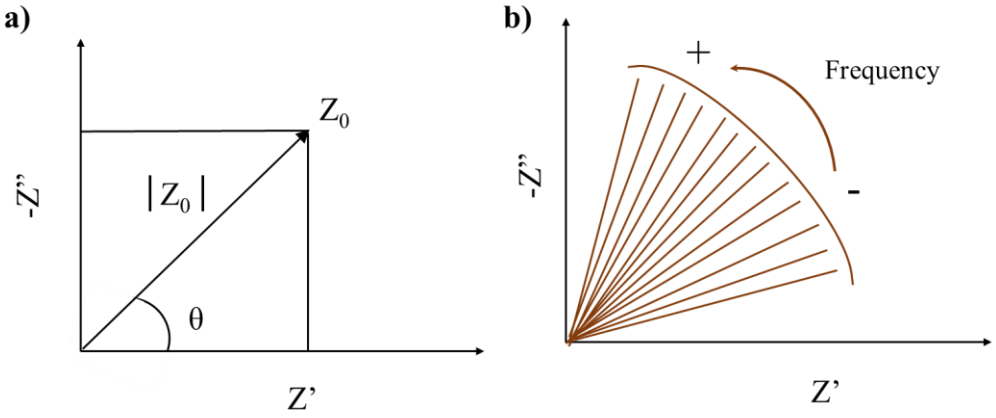

Figure 2.5 - a) Nyquist plot of the complex vector Z at fixed frequency, **b)** trace of complex vectors recorded at different frequencies of the ac electrical field.

The Nyquist plot is very popular, since specific information can be read directly from the plot in the case of the most common and simple circuit systems (see next section). However, Nyquist plot also presents some drawbacks: frequency does not appear explicitly and distinction between elemental contributions is sometimes difficult due to overlapping because of scaling effects. More importantly, the physical meaning of the equivalent circuits used to model the impedance response is not straightforward.

As an alternative to the Nyquist representation, Bode plots can be preferred for a better interpretation without any fitting procedure using equivalent circuits. The Bode plot basically represents the evolution of the magnitude (|Z|), the phase angle (θ), the real (Z') or imaginary (Z") parts of the impedance against the frequency in semi-logarithm or logarithm scales (log (f)). The

selection of the Y axe depends on the electrical properties of the system to be evidenced, i.e., the capacitive or the resistive properties. Figure 2.6 a, b, c & d illustrates Bode and Nyquist representations of pure resistor and pure capacitor, based on equations 2.19 and 2.20. Figure 2.6 e, f, g & h gives those representations for a RC equivalent circuit in parallel or in series, taking into account Equations 2.22 and 2.23. If the connection is serial, the impedance Z cannot be smaller than R, the capacitor contribution decreases with increasing the frequency. If the connection is parallel, the current follows the path of the lowest impedance: at high frequency, the impedance of the capacitor is very low and the major part of the current flows through the capacitor, while with decreasing the frequency, the impedance of the capacitor increases and a bigger fraction of the current flows through the resistor.

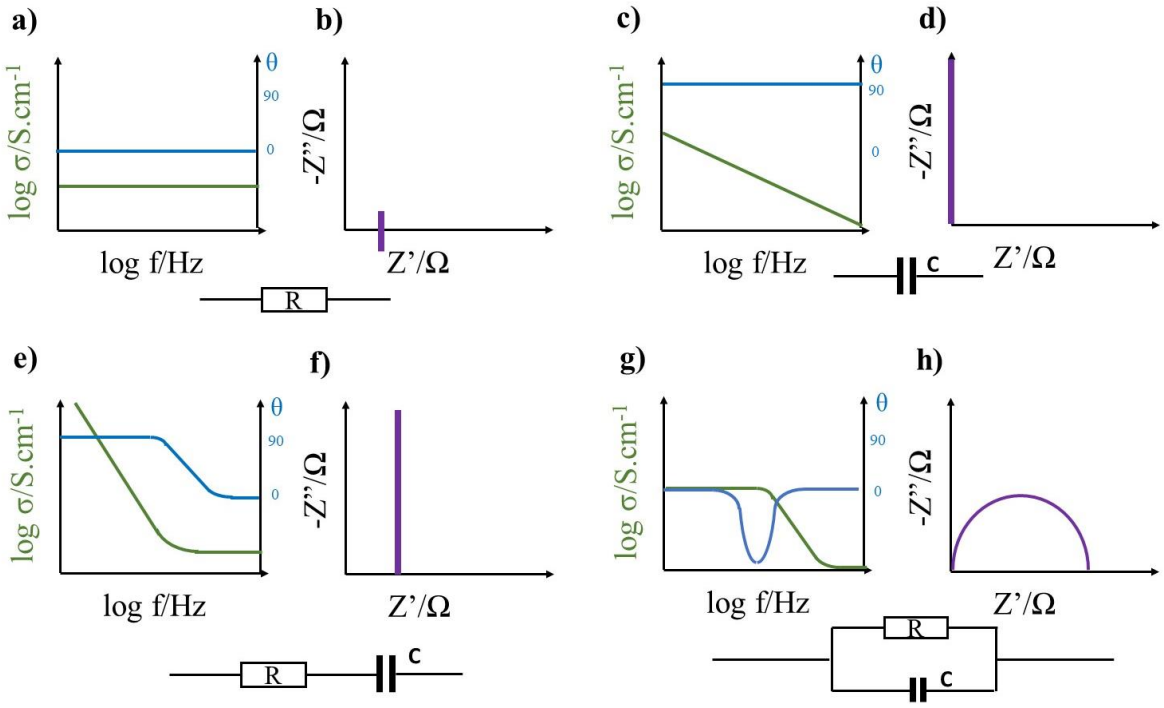

Figure 2.6 – Bode representation of the modulus Z (|Z|) and angle shift (θ) of the impedance for **a)** a pure resistor and **c)** a pure capacitor along with the corresponding Nyquist representations **b)** and **d)**. Bode representation of the modulus Z (|Z|) and angle shift (θ) of the impedance for a resistor and capacitor **e)** in series and **g)** in parallel along with the corresponding Nyquist representations **f)** and **h)** respectively.

2.4.2.3. Nyquist plot of the impedance for real simple cases

From a practical point of view, impedance of a single crystal is recorded by inserting the material between metallic electrodes. This configuration is firstly modelled by a resistor (R_{bulk})

connected in parallel with a capacitor (C_{bulk}), as depicted in Figure 2.7. R_{bulk} and C_{bulk} represent the solid resistance to the flow and charge separation, respectively. From the resistance value (R_{bulk}), the conductivity (σ) is calculated as follows:

$$\sigma = \frac{1}{R_{bulk}} \frac{l}{S} \qquad \text{Eq. 2.24}$$

Where, l represents the sample thickness and S is the surface area in contact with the electrode.

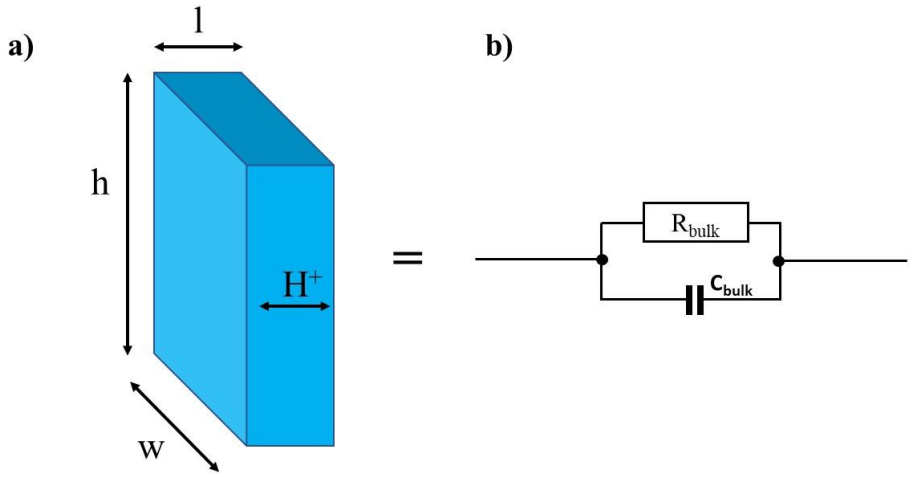

Figure 2.7 – a) Ideal single crystal of width (w), height (h), and thickness (l), modelled as **b)** a parallel combination of a resistor (R_{bulk}) and capacitor (C_{bulk}).

The total impedance (Z_{total}) is thus the sum of the reciprocal impedances and therefore is expressed as a function of R_{bulk} and C_{bulk}.

$$\frac{1}{Z_{total}} = \frac{1}{Z_{R_{bulk}}} + \frac{1}{Z_{C_{bulk}}} = \frac{1}{R_{bulk}} + j\omega C_{bulk} \qquad \text{Eq. 2.25}$$

By separating the real and the imaginary components, one obtains equation (2.26):

$$Z_{total} = \frac{R_{bulk}}{(1 + \omega R_{bulk} C_{bulk})^2} - j \frac{\omega R_{bulk}^2 C_{bulk}}{(1 + \omega R_{bulk} C_{bulk})^2} \qquad \text{Eq. 2.26}$$

Equation (2.26), when plotted over a range of ac frequencies, yields a semicircle in the Nyquist plot. As shown in Figure 2.8, the resistance of the system is extrapolated from the low frequency end intercept of the semi-circular arc on the real axis, and the capacitance of the system is determined at the top of the semi-circle. In this simple case, R_{bulk} and C_{bulk} can be extracted directly from the Nyquist plot, while for more complex systems, e.g., incomplete semi-circles or

multi-component equivalent circuits, the electrical features are obtained by reproducing the experimental data with equivalent circuit models.

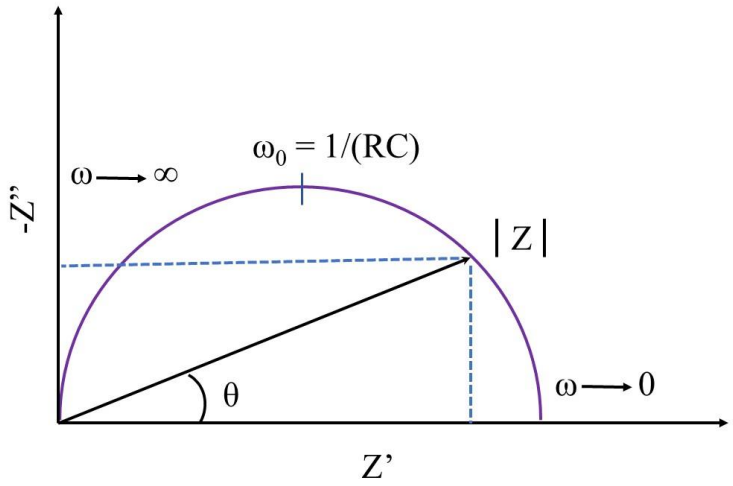

Figure 2.8 - Nyquist plot of the impedance for an ideal parallel RC circuit.

Noteworthy, in the case of real systems, the total impedance is rarely modelled using one single RC parallel circuit or even a limited or finite number of ideal resistors and capacitors, because of the contribution of i) grain boundaries for pelletized or powder samples, ii) metallic electrodes/sample interface, iii) surface roughness, iv) and most importantly distribution of the dynamical processes in the material. As an example, Figure 2.9a shows the Nyquist plot of the impedance for an ideal ionic conducting solid as a pellet inserted between metallic electrodes. A series of various equivalent circuits is needed to reproduce the experimental data in order to account for the different processes in play, including the impedances of i) the bulk solid, ii) the grain boundaries and iii) the charge accumulation to the solid/electrode interface resulting from blocking effects.[68] In addition, due to the surface roughness and the distribution of grains and ionic hopping sites, the characteristic the Z traces, e.g. capacitive tail or semi-circles assigned to each elemental component, are flattened and depressed from the real impedance axe (Figure 2.9b). In that case, constant phase elements (CPE) have to be considered instead of ideal capacitors (C).[69,70] (Figure 2. 9b).

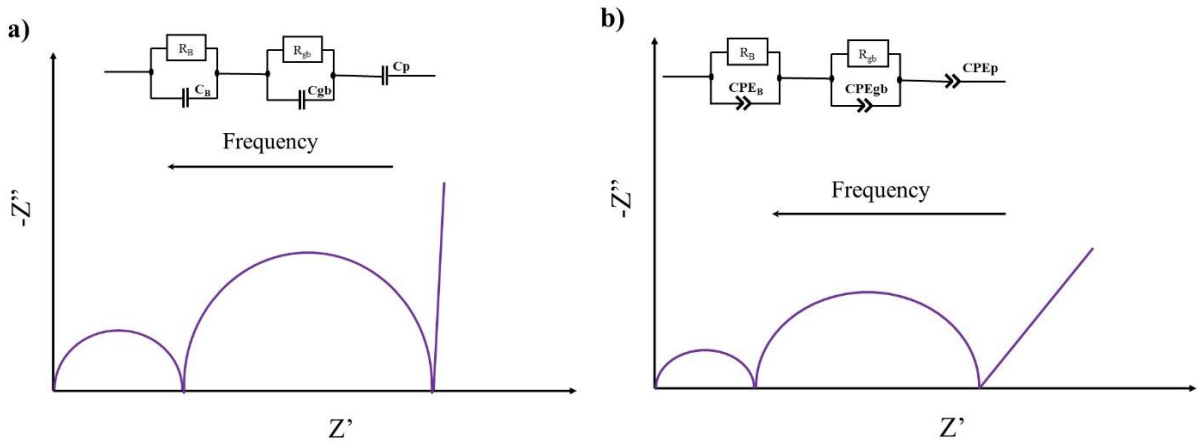

Figure 2.9 - Nyquist plot of the impedance for **a)** an ideal ionic conducting solid and **b)** a real corresponding system.

2.5. Shaping of MOFs-based solids for recording proton conducting properties from CIS

The proton conductivity of MOFs has been mostly measured using bulk powder or compacted pellets, in which the transport properties can be critically affected by not just the bulk structure of the MOF but also the ability of the protons to move between the MOF particles, i.e., the grain boundaries (Figure 2.10). As a consequence, MOFs can represent a hybrid in terms of conduction mechanism as conduction can occur through the bulk crystalline solid, through hydrated or guest-filled pores in the crystalline particles, and also necessarily across the grain boundaries. To establish whether interparticle conduction contributes to, dominates or impedes, proton conduction in MOFs, different alternatives were proposed.

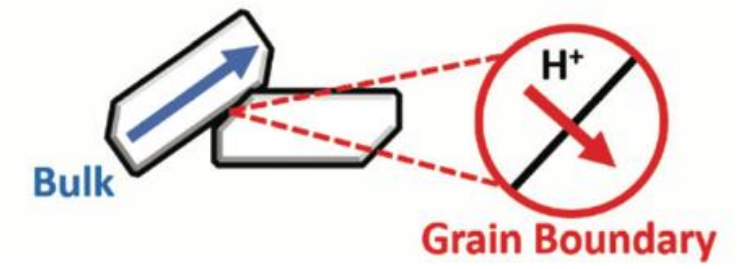

Figure 2.10 - Schematic representation of the bulk (blue) and grain boundary (red) contributions to the global conductivity measured in MOFs powder. Adapted from ref.[71]

Shimizu's group investigated the particle size impact on proton conduction, arguing that the largest particles involve the least amount of external surface area and thus should have the

lowest grain boundary contribution to the overall conduction.[71,72] They demonstrated that the conductivity of PCMOF21-AcO slightly decreases as the average particle size is reduced: σ is diminished by roughly one-third order of magnitude for particle size changing from 210 to 38 μm. The slightly higher conductivity collected on the larger particles supports that the grain boundary act as a small hurdle to proton conduction rather a main enabler, most probably by degrading proton mobility due to discontinuous proton transfer pathways. On the opposite, K. Zhang *et al.*, investigated proton conduction in UiO-66-NH_2 particles with different sizes, and concluded that protons selectively transfer from the faster pathway at the grain surface due to localized defects, while the bulk phase is supposed to be bypassed by the protons.[73] To further prove that the grain surface dominates the conductivity in UiO-66-NH_2 pellets, the particle surface was modified with organic phosphonic acid. The proton conductivity of the modified particles increases significantly, due to the specific chemical environment on the particle surface, which provides additional protons participating to a richer hydrogen bond network with free water located at the grain boundaries.

To minimize the contribution of surface conduction and eliminates grain boundary effects, which can either improve or hurdle the global conductivity, single crystal MOFs were considered. Noteworthy, this is still scarce as it requires MOFs crystals with enough size, sufficiently regular shape or adequate stability. However, it clearly provides several advantages: in addition to collecting intrinsic proton conduction, valuable information on the proton transport along specific directions in the crystalline solid can be evidenced, so that one can establish the relationships between the MOF structure and the corresponding anisotropic proton conduction. In the case of MOFs single crystal sufficiently large, metallic microelectrodes are connected to specific faces orientation of the crystal [72,74,83,84,75–82] (Figure 2.11a) or interdigital electrodes (IDE) are employed to arrange the MOFs single crystal in different positions to avoid the use of conducting pasted or electric glues, likely to create additional resistive or conductive interfaces [85–87] (Figure 2.11b). In the typical example of Co-MOF-74, a MOF displaying one-dimensional (1D) channels along the c-axis, the directional proton migration in the corresponding single crystal was evidenced:[84] the conductivity measured along the c-axis is three orders of magnitude higher than that collected along the a-axis (Figure 2.11c). It is also substantially higher than the response recorded on the pellet sample, due to the highly anisotropic structure of Co-MOF-74. Noteworthy, the discrepancy between the conductivity response of the single crystal versus that of the powder

characterized by random orientation, is obviously less pronounced for 2D and 3D structures,[72,75,76,83] for which the structural anisotropy is less marked, while it becomes negligible when measurements are recorded on anhydrous solids.[77,81,82]

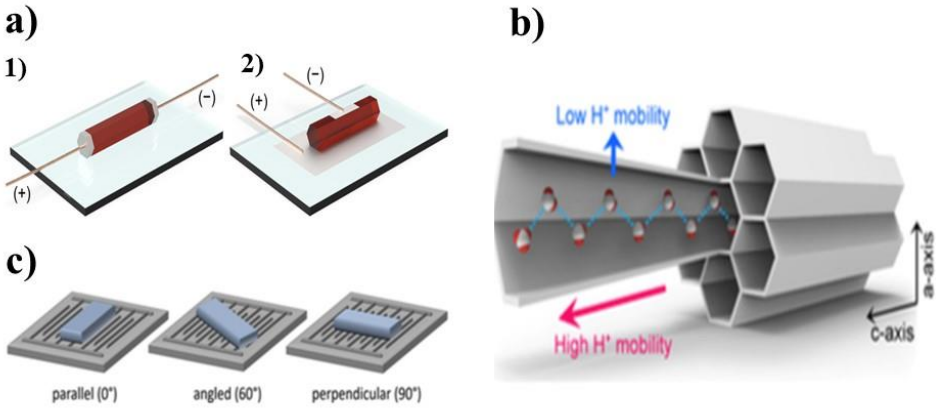

Figure 2.11 - Schematic illustration of **a)** the microelectrodes-connected Co-MOF-74 single crystals in **(1)** c-axis and **(2)** a-axis directions, **b)** a single crystal in variable orientations relative to the IDE substrate. **c)** Schematic representation of the directional proton transport in the 1D channels of Co-MOF-74. Adapted from refs [85] and [84].

Besides the single crystal samples, glassy state MOFs were equally envisaged to prepare grain boundary free materials along with flawless interfaces, for proton conduction applications at the anhydrous state. As reported,[88–93] most of the glassy-state proton conducting MOFs or Coordination Polymers (CP) show performance superior to that of their crystalline counterparts. In that case, the elimination of the grain boundary contribution to the global conductivity is not the main factor impacting the conductivity properties, as the isotropic disordered domains inherent to the glassy state is also expected to enhance proton dynamics. As an illustration, Kitagawa *et al*., prepared by a solvent-free mechanical milling process a glassy-state cadmium-based coordination polymer, which preserves the 2D structure of the crystalline material, albeit significant distortions.[89] The glassy-state material displays higher proton conduction properties compared to the crystalline state solid, in relation with the disorder and enhanced mobility of ligands in the glassy structure. Noteworthy, the H^+ conductivity of coordination polymers can be even more enhanced via the chemical doping during the mechanical vitrification impacting the thermal properties of the glass, i.e. the glass transition temperature (Tg) and crystallization temperature (Tc).[93] Despite some promises, only a few of glassy-state CPs show anhydrous proton conduction exceeding 10^{-3} $S.cm^{-1}$.

As an alternative to single crystals and glass, the preparation of dense and crystalline nanofilms of pure MOFs can also be considered to address the grain boundaries issues. However, this topic is very scarcely documented as MOF processability as a film still deserves improvements in terms of fabrication, i.e. selection of the substrate and fabrication methods, to improve the films density, thickness, mechanical/thermal/chemical stability among others.[94,95] As an example, Chao and co-workers demonstrated that the proton conductivity of HKUST-1 can be adjusted by its morphology, through the preparation of dense and controllable films, using an *in situ* substrate growth approach.[94] The proton conductivity was shown to significantly increase from ~10^{-6} (pellet) to ~10^{-4} S.cm^{-1} (microfilm) at 298 K/ 98% RH due to elimination of grain boundaries.

Regarding the difficulties in preparing pure MOF thick films, polymeric binders were added to MOF particles to create composites and further circumvent the contact and grain boundaries issues, as illustrated in Figure 2.12. Noteworthy, the efforts devoted to the preparation of MOFs-based mixed-matrix membranes (MMMs) were indeed mainly motivated by the need to develop MOF-based electrolytes for fuel cells applications as discussed in Chapter 1.

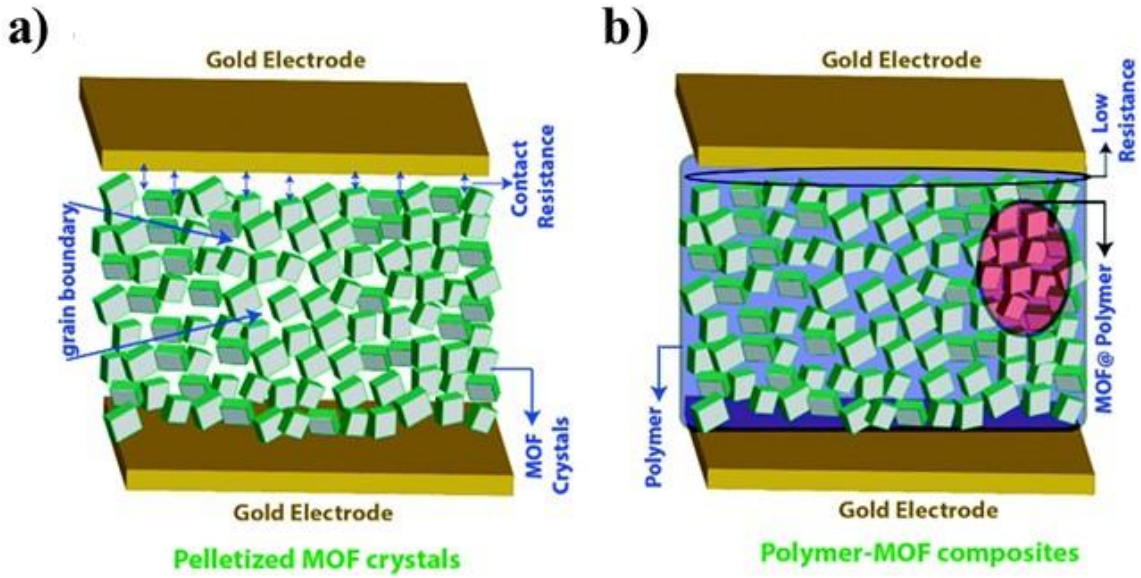

Figure 2.12 - Schematic view of **a)** grain boundary formation during the preparation of compact pellet of the powder sample and **b)** polymeric binder and MOFs inside a composite which reduces the grain boundary and contact resistances. Adapted from ref [96].

2.6. Experimental Setup

In this work, impedance measurements were carried out using a Broadband Dielectric Spectrometer Novocontrol alpha analyzer or a Solartron analytical Modulab XM MTS. An ac voltage of 20 mV was applied over a frequency domain from F = 0.01 Hz to F = 1 MHz, at fixed temperature in [133 K – 473 K] range, according to the apparatus used. The resistance value of the studied solids was deduced based on the analysis of the Nyquist and Bode representations for comparison. According to the Nyquist plots features, different procedures were considered to determine R_{bulk}. For the Nyquist plots showing a semi-circle, ZView Software was applied to fit impedance data sets with equivalent circuits, assembling the bulk resistance R and the bulk non-ideal capacitance CPE, while a second constant phase element CPE-2 was alternatively added to take into account for the electrodes if applicable. For the very low resistive solids, the Nyquist plot results only in the tail end of a semi-circle at high frequency, while at lower frequency a capacitive tail is observed which prevents the use of the equivalent-fitting procedure. In that case, the resistance was evaluated from the real-axis intercept of the tails. Once R_{bulk} elucidated, the sample conductivity was calculated according to equation 2.24.

Based on a previous study performed in the group, impedance measurements carried out on powders and pellets are comparable. To avoid the MOF structure collapse under mechanical pressure likely to occur during the pelletization process, we then considered powder samples in this work. The powder (~50 mg) was introduced in home-made sample holders (Figures 2.13), i.e., between two gold electrodes, in a parallel plate capacitor configuration, with an annular Teflon spacer to avoid short circuits and insure insulation. This configuration corresponds to the basic "two-probe" method for the electrical measurements. The sample surface was deduced from the surface of the smallest electrode, while the sample thickness was evaluated by subtracting the length of the empty sample holder and that of the filled one using a vernier caliper.

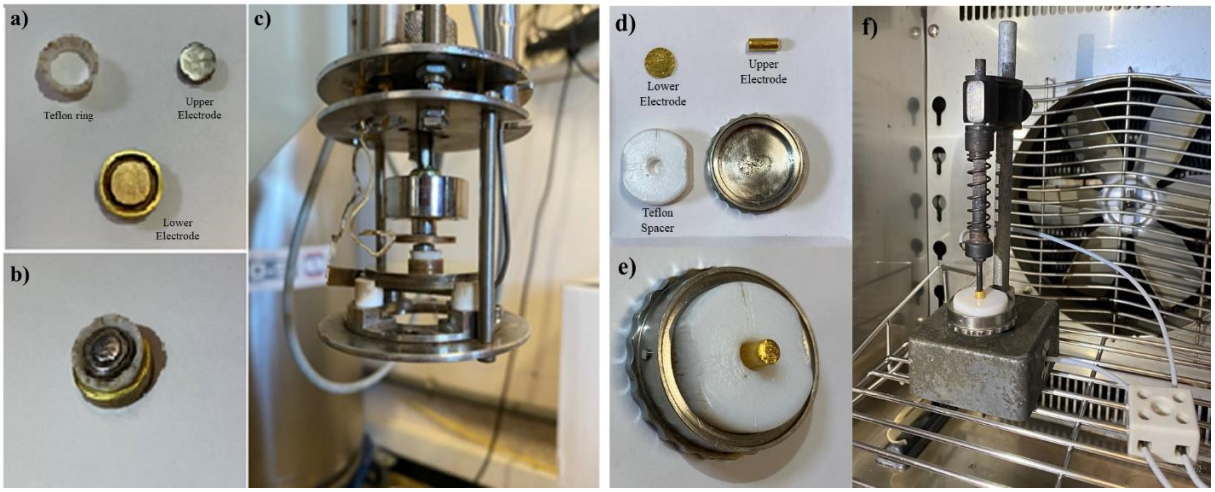

Figure 2.13 – Pictures of the sample holder and electrical contacts for measurements carried out using (**a-c**) Novocontrol cryostat and (**d-f**) the climatic chamber for measurements under controlled RH.

Impedance measurements were collected on anhydrous MOFs, after a preliminary *in situ* heating at the activation temperature specific to the studied MOF, for several hours, under nitrogen flow. This step was required to eliminate water and solvent molecules from the porosity of the solid. Measurements were equally undertaken on hydrated solids. For that purpose, they were inserted in an Espec Corp. SH-221 incubator, to control the temperature ($298 < T\,(K) < 363$) and the Relative Humidity ($40 < RH\,(\%) < 95$). The solid was equilibrated for 24 hours at given T / RH conditions, to ensure fixed water content before recording the impedance. Water vapor is created through evaporating liquid water by heating. It is introduced inside the climatic chamber where it is cooled down at specific temperature to control the total humidity inside the chamber.

REFERENCES

[1] J. Philibert, Atom movements : diffusion and mass transport in solids, Les Ulis, 1991. http://lib.ugent.be/catalog/rug01:000822542.

[2] P. Padma Kumar, S. Yashonath, Ionic Conduction in the Solid State, ChemInform. 37 (2006) 3315–3322. https://doi.org/10.1002/chin.200624229.

[3] J.L. Déportes, C.; Duclot, M.; Fabry, P.; Fouletier, J.; Hammou, A.; Kleitz, M.; Siebert, E.; Souquet, Electrochimie des solides, EDP sciences, 1994.

[4] S. Arrhenius, Über die Reaktionsgeschwindigkeit bei der Inversion von Rohrzucker durch Säuren, Zeitschrift Für Phys. Chemie. 4U (1889) 226–248. https://doi.org/10.1515/zpch-1889-0416.

[5] T.H. Norton, STUDIES IN CHEMICAL DYNAMICS., J. Am. Chem. Soc. 19 (1897) 268–269. https://doi.org/10.1021/ja02077a013.

[6] R.J.D. Tilley, Defects in Solids, in: Encycl. Inorg. Chem., John Wiley & Sons, Ltd, Chichester, UK, 2006. https://doi.org/10.1002/0470862106.ia062.

[7] K.-D. Kreuer, S.J. Paddison, E. Spohr, M. Schuster, Transport in Proton Conductors for Fuel-Cell Applications: Simulations, Elementary Reactions, and Phenomenology, Chem. Rev. 104 (2004) 4637–4678. https://doi.org/10.1021/cr020715f.

[8] D.W. Lim, M. Sadakiyo, H. Kitagawa, Proton transfer in hydrogen-bonded degenerate systems of water and ammonia in metal-organic frameworks, Chem. Sci. 10 (2019) 16–33. https://doi.org/10.1039/C8SC04475A.

[9] S.S. Nagarkar, S.M. Unni, A. Sharma, S. Kurungot, S.K. Ghosh, Two-in-One: Inherent Anhydrous and Water-Assisted High Proton Conduction in a 3D Metal-Organic Framework, Angew. Chemie Int. Ed. 53 (2014) 2638–2642. https://doi.org/10.1002/anie.201309077.

[10] K. Kreuer, On the complexity of proton conduction phenomena, Solid State Ionics. 136–137 (2000) 149–160. https://doi.org/10.1016/S0167-2738(00)00301-5.

[11] K.D. Kreuer, Proton conductivity: Materials and applications, Chem. Mater. 8 (1996) 610–641. https://doi.org/10.1021/cm950192a.

[12] M. Bazaga-García, R.M.P. Colodrero, M. Papadaki, P. Garczarek, J. Zoń, P. Olivera-Pastor, E.R. Losilla, L. León-Reina, M.A.G. Aranda, D. Choquesillo-Lazarte, K.D. Demadis, A. Cabeza, Guest Molecule-Responsive Functional Calcium Phosphonate Frameworks for Tuned Proton Conductivity, J. Am. Chem. Soc. 136 (2014) 5731–5739. https://doi.org/10.1021/ja500356z.

[13] P.G.M. Mileo, S. Devautour-Vinot, G. Mouchaham, F. Faucher, N. Guillou, A. Vimont, C. Serre, G. Maurin, Proton-Conducting Phenolate-Based Zr Metal-Organic Framework: A Joint Experimental-Modeling Investigation, J. Phys. Chem. C. 120 (2016) 24503–24510. https://doi.org/10.1021/acs.jpcc.6b04649.

[14] A. Jankowska, A. Zalewska, A. Skalska, A. Ostrowski, S. Kowalak, Proton conductivity of imidazole entrapped in microporous molecular sieves, Chem. Commun. 53 (2017) 2475–2478. https://doi.org/10.1039/C7CC00690J.

[15] D. Umeyama, S. Horike, M. Inukai, S. Kitagawa, Integration of Intrinsic Proton Conduction and Guest-Accessible Nanospace into a Coordination Polymer, J. Am. Chem. Soc. 135 (2013) 11345–11350. https://doi.org/10.1021/ja4051668.

[16] W.L. Jorgensen, Monte carlo results for hydrogen bond distributions in liquid water11Quantum and statistical mechanical studies of liquids, 9. Part 8 ref. [6]., Chem. Phys. Lett. 70 (1980) 326–329. https://doi.org/10.1016/0009-2614(80)85344-9.

[17] J.D. Smith, Energetics of Hydrogen Bond Network Rearrangements in Liquid Water, Science (80-.). 306 (2004) 851–853. https://doi.org/10.1126/science.1102560.

[18] T. Steinel, J.B. Asbury, J. Zheng, M.D. Fayer, Watching Hydrogen Bonds Break: A Transient Absorption Study of Water, J. Phys. Chem. A. 108 (2004) 10957–10964. https://doi.org/10.1021/jp046711r.

[19] V.P. Voloshin, Y.I. Naberukhin, Proper and improper hydrogen bonds in liquid water, J. Struct. Chem. 57 (2016) 497–506. https://doi.org/10.1134/S0022476616030112.

[20] K.-D. Kreuer, A. Rabenau, W. Weppner, Vehicle Mechanism, A New Model for the Interpretation of the Conductivity of Fast Proton Conductors, Angew. Chemie Int. Ed. English. 21 (1982) 208–209. https://doi.org/10.1002/anie.198202082.

[21] C.J.T. de Grotthuss, Sur la Décomposition de l'Eau et des Corps qu'Elle Tient en Dissolution à l'Aide de l'Electricité Galvanique, Ann. Chim. Phys. 58 (1806) 54–74.

[22] C.I.T. de Grotthius, LI. Memoir upon the decomposition of water, and of the bodies which it holds in solution, by means of galvanic electricity, Philos. Mag. 25 (1806) 330–339. https://doi.org/10.1080/14786440608563457.

[23] J. Escorihuela, R. Narducci, V. Compañ, F. Costantino, Proton Conductivity of Composite Polyelectrolyte Membranes with Metal-Organic Frameworks for Fuel Cell Applications, Adv. Mater. Interfaces. 6 (2018) 1801146. https://doi.org/10.1002/admi.201801146.

[24] T. Ueki, M. Watanabe, Macromolecules in Ionic Liquids: Progress, Challenges, and Opportunities, Macromolecules. 41 (2008) 3739–3749. https://doi.org/10.1021/ma800171k.

[25] T. Ogawa, T. Aonuma, T. Tamaki, H. Ohashi, H. Ushiyama, K. Yamashita, T. Yamaguchi, The proton conduction mechanism in a material consisting of packed acids, Chem. Sci. 5 (2014) 4878–4887. https://doi.org/10.1039/C4SC00952E.

[26] Y.-L.S. Tse, C. Knight, G.A. Voth, An analysis of hydrated proton diffusion in ab initio molecular dynamics, J. Chem.

Phys. 142 (2015) 014104. https://doi.org/10.1063/1.4905077.

[27] M.E. Tuckerman, On the Quantum Nature of the Shared Proton in Hydrogen Bonds, Science (80-.). 275 (1997) 817–820. https://doi.org/10.1126/science.275.5301.817.

[28] N. Agmon, The Grotthuss mechanism, Chem. Phys. Lett. 244 (1995) 456–462. https://doi.org/10.1016/0009-2614(95)00905-J.

[29] O. Markovitch, H. Chen, S. Izvekov, F. Paesani, G.A. Voth, N. Agmon, Special Pair Dance and Partner Selection: Elementary Steps in Proton Transport in Liquid Water, J. Phys. Chem. B. 112 (2008) 9456–9466. https://doi.org/10.1021/jp804018y.

[30] E. Wicke, M. Eigen, T. Ackermann, Über den Zustand des Protons (Hydroniumions) in wäßriger Lösung, Zeitschrift Fur Phys. Chemie. 1 (1954) 340–364. https://doi.org/10.1524/zpch.1954.1.5_6.340.

[31] G. Zundel, H. Metzger, Energiebänder der tunnelnden Überschuß-Protonen in flüssigen Säuren. Eine IR-spektroskopische Untersuchung der Natur der Gruppierungen H 5 O 2 +, Zeitschrift Für Phys. Chemie. 58 (1968) 225–245. https://doi.org/10.1524/zpch.1968.58.5_6.225.

[32] D. Marx, M.E. Tuckerman, J. Hutter, M. Parrinello, The nature of the hydrated excess proton in water, Nature. 397 (1999) 601–604. https://doi.org/10.1038/17579.

[33] G.A. Voth, The computer simulation of proton transport in biomolecular systems, Front. Biosci. 8 (2003) 1213. https://doi.org/10.2741/1213.

[34] W. Tatara, M.J. Wójcik, J. Lindgren, M. Probst, Theoretical Study of Structures, Energies, and Vibrational Spectra of the Imidazole−Imidazolium System, J. Phys. Chem. A. 107 (2003) 7827–7831. https://doi.org/10.1021/jp030065z.

[35] F. Toda, K. Tanaka, C. Foces-Foces, A.L. Llamas-Saiz, H.H. Limbach, F. Aguilar-Parrilla, R.M. Claramunt, C. López, J. Elguero, Intermolecular proton transfer in host-guest crystals: The case of pyrazole included in 1,1-di(2,4-dimethylphenyl)but-2-yn-1-ol, an X-ray and solid-state 13C/15N NMR study, J. Chem. Soc. Chem. Commun. (1993) 1139–1142. https://doi.org/10.1039/C39930001139.

[36] F.-M. Zhang, L.-Z. Dong, J.-S. Qin, W. Guan, J. Liu, S.-L. Li, M. Lu, Y.-Q. Lan, Z.-M. Su, H.-C. Zhou, Effect of Imidazole Arrangements on Proton-Conductivity in Metal–Organic Frameworks, J. Am. Chem. Soc. 139 (2017) 6183–6189. https://doi.org/10.1021/jacs.7b01559.

[37] S. Horike, D. Umeyama, M. Inukai, T. Itakura, S. Kitagawa, Coordination-network-based ionic plastic crystal for anhydrous proton conductivity, J. Am. Chem. Soc. 134 (2012) 7612–7615. https://doi.org/10.1021/ja301875x.

[38] S. Sanda, S. Biswas, S. Konar, Study of Proton Conductivity of a 2D Flexible MOF and a 1D Coordination Polymer at Higher Temperature, Inorg. Chem. 54 (2015) 1218–1222. https://doi.org/10.1021/ic502098h.

[39] F. Yang, H. Huang, X. Wang, F. Li, Y. Gong, C. Zhong, J.-R. Li, Proton Conductivities in Functionalized UiO-66: Tuned Properties, Thermogravimetry Mass, and Molecular Simulation Analyses, Cryst. Growth Des. 15 (2015) 5827–5833. https://doi.org/10.1021/acs.cgd.5b01190.

[40] M. Liu, L. Chen, S. Lewis, S.Y. Chong, M.A. Little, T. Hasell, I.M. Aldous, C.M. Brown, M.W. Smith, C.A. Morrison, L.J. Hardwick, A.I. Cooper, Three-dimensional protonic conductivity in porous organic cage solids, Nat. Commun. 7 (2016) 12750. https://doi.org/10.1038/ncomms12750.

[41] N. Planas, J.E. Mondloch, S. Tussupbayev, J. Borycz, L. Gagliardi, J.T. Hupp, O.K. Farha, C.J. Cramer, Defining the Proton Topology of the Zr 6 -Based Metal–Organic Framework NU-1000, J. Phys. Chem. Lett. 5 (2014) 3716–3723. https://doi.org/10.1021/jz501899j.

[42] F. Paesani, Molecular Mechanisms of Water-Mediated Proton Transport in MIL-53 Metal–Organic Frameworks, J. Phys. Chem. C. 117 (2013) 19508–19516. https://doi.org/10.1021/jp406163q.

[43] D.D. Borges, S. Devautour-Vinot, H. Jobic, J. Ollivier, F. Nouar, R. Semino, T. Devic, C. Serre, F. Paesani, G. Maurin, Proton Transport in a Highly Conductive Porous Zirconium-Based Metal–Organic Framework: Molecular Insight, Angew. Chemie Int. Ed. 55 (2016) 3919–3924. https://doi.org/10.1002/anie.201510855.

[44] D.D. Borges, R. Semino, S. Devautour-Vinot, H. Jobic, F. Paesani, G. Maurin, Computational Exploration of the Water Concentration Dependence of the Proton Transport in the Porous UiO-66(Zr)-(CO2H)2 Metal-Organic Framework, Chem. Mater. 29 (2017) 1569–1576. https://doi.org/10.1021/acs.chemmater.6b04257.

[45] T. Grancha, J. Ferrando-Soria, J. Cano, P. Amorós, B. Seoane, J. Gascon, M. Bazaga-García, E.R. Losilla, A. Cabeza, D. Armentano, E. Pardo, Insights into the Dynamics of Grotthuss Mechanism in a Proton-Conducting Chiral bioMOF, Chem. Mater. 28 (2016) 4608–4615. https://doi.org/10.1021/acs.chemmater.6b01286.

[46] E. Eisbein, J.O. Joswig, G. Seifert, Proton conduction in a MIL-53(Al) metal-organic framework: Confinement versus host/guest interaction, J. Phys. Chem. C. 118 (2014) 13035–13041. https://doi.org/10.1021/jp5043969.

[47] E. Eisbein, J.-O. Joswig, G. Seifert, Enhanced proton-transfer activity in imidazole@MIL-53(Al) systems revealed by molecular-dynamics simulations, Microporous Mesoporous Mater. 216 (2015) 36–41. https://doi.org/10.1016/j.micromeso.2015.03.022.

[48] P.G.M. Mileo, T. Kundu, R. Semino, V. Benoit, N. Steunou, P.L. Llewellyn, C. Serre, G. Maurin, S. Devautour-Vinot, Highly Efficient Proton Conduction in a Three-Dimensional Titanium Hydrogen Phosphate, Chem. Mater. 29 (2017) 7263–7271. https://doi.org/10.1021/acs.chemmater.7b01850.

[49] P.G.M. Mileo, K. Adil, L. Davis, A. Cadiau, Y. Belmabkhout, H. Aggarwal, G. Maurin, M. Eddaoudi, S. Devautour-Vinot, Achieving Superprotonic Conduction with a 2D Fluorinated Metal–Organic Framework, J. Am. Chem. Soc. 140 (2018) 13156–13160. https://doi.org/10.1021/jacs.8b06582.

[50] S. Wang, M. Wahiduzzaman, L. Davis, A. Tissot, W. Shepard, J. Marrot, C. Martineau-Corcos, D. Hamdane, G. Maurin, S. Devautour-Vinot, C. Serre, A robust zirconium amino acid metal-organic framework for proton conduction, Nat. Commun. 9 (2018) 4937. https://doi.org/10.1038/s41467-018-07414-4.

[51] M. Wahiduzzaman, S. Wang, J. Schnee, A. Vimont, V. Ortiz, P.G. Yot, R. Retoux, M. Daturi, J.S. Lee, J.-S. Chang, C. Serre, G. Maurin, S. Devautour-Vinot, A High Proton Conductive Hydrogen-Sulfate Decorated Titanium Carboxylate Metal−Organic Framework, ACS Sustain. Chem. Eng. 7 (2019) 5776–5783. https://doi.org/10.1021/acssuschemeng.8b05306.

[52] S. Nandi, H. Aggarwal, M. Wahiduzzaman, Y. Belmabkhout, G. Maurin, M. Eddaoudi, S. Devautour-Vinot, Revisiting the water sorption isotherm of MOF using electrical measurements, Chem. Commun. 55 (2019) 13251–13254. https://doi.org/10.1039/C9CC06012J.

[53] T. Robert, Nuclear Magnetic resonance Probes of Molecular Dynamics (Understanding Chemical Reactivity), Kluwer Academic Publisher, Boston, 1994.

[54] D.I. Kolokolov, M.S. Kazantsev, M. V. Luzgin, H. Jobic, A.G. Stepanov, Characterization and dynamics of the different protonic species in hydrated 12-tungstophosphoric acid studied by 2H NMR, J. Phys. Chem. C. 118 (2014) 30023–30033. https://doi.org/10.1021/jp510410k.

[55] S. Bureekaew, S. Horike, M. Higuchi, M. Mizuno, T. Kawamura, D. Tanaka, N. Yanai, S. Kitagawa, One-dimensional imidazole aggregate in aluminium porous coordination polymers with high proton conductivity, Nat. Mater. 8 (2009) 831–836. https://doi.org/10.1038/nmat2526.

[56] J.M. Taylor, R.K. Mah, I.L. Moudrakovski, C.I. Ratcliffe, R. Vaidhyanathan, G.K.H. Shimizu, Facile Proton Conduction via Ordered Water Molecules in a Phosphonate Metal−Organic Framework, J. Am. Chem. Soc. 132 (2010) 14055–14057. https://doi.org/10.1021/ja107035w.

[57] M. Inukai, S. Horike, W. Chen, D. Umeyama, T. Itakura, S. Kitagawa, Template-directed proton conduction pathways in a coordination framework, J. Mater. Chem. A. 2 (2014) 10404–10409. https://doi.org/10.1039/C4TA01261E.

[58] Z. Hassanzadeh Fard, N.E. Wong, C.D. Malliakas, P. Ramaswamy, J.M. Taylor, K. Otsubo, G.K.H. Shimizu, Superprotonic Phase Change to a Robust Phosphonate Metal–Organic Framework, Chem. Mater. 30 (2018) 314–318. https://doi.org/10.1021/acs.chemmater.7b04467.

[59] M.K. Sarango-Ramírez, D.-W.W. Lim, D.I. Kolokolov, A.E. Khudozhitkov, A.G. Stepanov, H. Kitagawa, Superprotonic Conductivity in Metal-Organic Framework via Solvent-Free Coordinative Urea Insertion., J. Am. Chem. Soc. 142 (2020) 6861–6865. https://doi.org/10.1021/jacs.0c00303.

[60] Y. Song, A.E. Khudozhitkov, J. Lee, H. Kang, D.I. Kolokolov, A.G. Stepanov, M. Yoon, Transformation of a proton insulator to a conductor: Via reversible amorphous to crystalline structure transformation of MOFs, Chem. Commun. 56 (2020) 4468–4471. https://doi.org/10.1039/d0cc00755b.

[61] K. Otake, K. Otsubo, T. Komatsu, S. Dekura, J.M. Taylor, R. Ikeda, K. Sugimoto, A. Fujiwara, C.-P. Chou, A.W. Sakti, Y. Nishimura, H. Nakai, H. Kitagawa, Confined water-mediated high proton conduction in hydrophobic channel of a synthetic nanotube, Nat. Commun. 11 (2020) 843. https://doi.org/10.1038/s41467-020-14627-z.

[62] S. Horike, Y. Kamitsubo, M. Inukai, T. Fukushima, D. Umeyama, T. Itakura, S. Kitagawa, Postsynthesis Modification of a Porous Coordination Polymer by LiCl To Enhance H + Transport, J. Am. Chem. Soc. 135 (2013) 4612–4615. https://doi.org/10.1021/ja3122872.

[63] J.M. Taylor, S. Dekura, R. Ikeda, H. Kitagawa, Defect Control To Enhance Proton Conductivity in a Metal–Organic Framework, Chem. Mater. 27 (2015) 2286–2289. https://doi.org/10.1021/acs.chemmater.5b00665.

[64] S. Pili, P. Rought, D.I. Kolokolov, L. Lin, I. Da Silva, Y. Cheng, C. Marsh, I.P. Silverwood, V. García Sakai, M. Li, J.J. Titman, L. Knight, L.L. Daemen, A.J. Ramirez-Cuesta, C.C. Tang, A.G. Stepanov, S. Yang, M. Schröder, Enhancement of Proton Conductivity in Nonporous Metal-Organic Frameworks: The Role of Framework Proton Density and Humidity, Chem. Mater. 30 (2018) 7593–7602. https://doi.org/10.1021/acs.chemmater.8b02765.

[65] S. Miyatsu, M. Kofu, A. Nagoe, T. Yamada, M. Sadakiyo, T. Yamada, H. Kitagawa, M. Tyagi, V. García Sakai, O. Yamamuro, Proton dynamics of two-dimensional oxalate-bridged coordination polymers, Phys. Chem. Chem. Phys. 16 (2014) 17295–17304. https://doi.org/10.1039/C4CP01432D.

[66] S. Pili, S.P. Argent, C.G. Morris, P. Rought, V. García-Sakai, I.P. Silverwood, T.L. Easun, M. Li, M.R. Warren, C.A. Murray, C.C. Tang, S. Yang, M. Schröder, Proton Conduction in a Phosphonate-Based Metal-Organic Framework Mediated by Intrinsic 'free Diffusion inside a Sphere', J. Am. Chem. Soc. 138 (2016) 6352–6355. https://doi.org/10.1021/jacs.6b02194.

[67] P. Rought, C. Marsh, S. Pili, I.P. Silverwood, V.G. Sakai, M. Li, M.S. Brown, S.P. Argent, I. Vitorica-Yrezabal, G. Whitehead, M.R. Warren, S. Yang, M. Schröder, Modulating proton diffusion and conductivity in metal–organic frameworks by incorporation of accessible free carboxylic acid groups, Chem. Sci. 10 (2019) 1492–1499. https://doi.org/10.1039/C8SC03022G.

[68] S.P.S. Jiang, S.P.; Love, J. G.; Badwal, Electrochemical techniques in studies of solid ionic conductors., Key Eng. Mater. 125–126 (1997) 81–132.

[69] J.-B. Jorcin, M.E. Orazem, N. Pébère, B. Tribollet, CPE analysis by local electrochemical impedance spectroscopy, Electrochim. Acta. 51 (2006) 1473–1479. https://doi.org/10.1016/j.electacta.2005.02.128.

[70] B. Hirschorn, M.E. Orazem, B. Tribollet, V. Vivier, I. Frateur, M. Musiani, Constant-Phase-Element Behavior Caused by Resistivity Distributions in Films, J. Electrochem. Soc. 157 (2010) C452. https://doi.org/10.1149/1.3499564.

[71] D.A. Levenson, J. Zhang, B.S. Gelfand, S.P. Kammampata, V. Thangadurai, G.K.H. Shimizu, Particle size dependence of proton conduction in a cationic lanthanum phosphonate MOF, Dalt. Trans. 49 (2020) 4022–4029. https://doi.org/10.1039/C9DT04229F.

[72] B. Joarder, J.-B. Bin Lin, Z. Romero, G.K.H.H. Shimizu, Single Crystal Proton Conduction Study of a Metal Organic Framework of Modest Water Stability, J. Am. Chem. Soc. 139 (2017) 7176–7179. https://doi.org/10.1021/jacs.7b03397.

[73] K. Zhang, G.-H. Wen, S.S.-S. Bao, L.-Q. Wu, J.-G. Jia, Studying the Proton Conduction through the Grain Surface of UiO-66-NH 2, ACS Appl. Energy Mater. 3 (2020) 8198–8204. https://doi.org/10.1021/acsaem.0c00547.

[74] M. Yoon, K. Suh, H. Kim, Y. Kim, N. Selvapalam, K. Kim, High and highly anisotropic proton conductivity in organic molecular porous materials, Angew. Chemie - Int. Ed. 50 (2011) 7870–7873. https://doi.org/10.1002/anie.201101777.

[75] D. Umeyama, S. Horike, M. Inukai, T. Itakura, S. Kitagawa, Inherent Proton Conduction in a 2D Coordination Framework, J. Am. Chem. Soc. 134 (2012) 12780–12785. https://doi.org/10.1021/ja304693r.

[76] Q. Tang, Y. Liu, S. Liu, D. He, J. Miao, X. Wang, G. Yang, Z. Shi, Z. Zheng, High Proton Conduction at above 100 °C Mediated by Hydrogen Bonding in a Lanthanide Metal–Organic Framework, J. Am. Chem. Soc. 136 (2014) 12444–12449. https://doi.org/10.1021/ja5069855.

[77] X. Zhao, C. Mao, X. Bu, P. Feng, Direct Observation of Two Types of Proton Conduction Tunnels Coexisting in a New Porous Indium–Organic Framework, Chem. Mater. 26 (2014) 2492–2495. https://doi.org/10.1021/cm500473f.

[78] S. Tominaka, A.K. Cheetham, Intrinsic and extrinsic proton conductivity in metal-organic frameworks, RSC Adv. 4 (2014) 54382–54387. https://doi.org/10.1039/c4ra11473f.

[79] S. Tominaka, F.-X. Coudert, T.D. Dao, T. Nagao, A.K. Cheetham, Insulator-to-Proton-Conductor Transition in a Dense Metal–Organic Framework, J. Am. Chem. Soc. 137 (2015) 6428–6431. https://doi.org/10.1021/jacs.5b02777.

[80] L. Qin, Y. Yu, P. Liao, W. Xue, Z. Zheng, X. Chen, Y. Zheng, A "Molecular Water Pipe": A Giant Tubular Cluster {Dy 72 } Exhibits Fast Proton Transport and Slow Magnetic Relaxation, Adv. Mater. 28 (2016) 10772–10779.

https://doi.org/10.1002/adma.201603381.

[81] S.-S. Bao, N.-Z. Li, J.M. Taylor, Y. Shen, H. Kitagawa, L.-M. Zheng, Co–Ca Phosphonate Showing Humidity-Sensitive Single Crystal to Single Crystal Structural Transformation and Tunable Proton Conduction Properties, Chem. Mater. 27 (2015) 8116–8125. https://doi.org/10.1021/acs.chemmater.5b03897.

[82] R. Li, S.-H. Wang, X.-X. Chen, J. Lu, Z.-H. Fu, Y. Li, G. Xu, F.-K. Zheng, G.-C. Guo, Highly Anisotropic and Water Molecule-Dependent Proton Conductivity in a 2D Homochiral Copper(II) Metal–Organic Framework, Chem. Mater. 29 (2017) 2321–2331. https://doi.org/10.1021/acs.chemmater.6b05497.

[83] Y.-S. Wei, X.-P. Hu, Z. Han, X.-Y. Dong, S.-Q. Zang, T.C.W. Mak, Unique Proton Dynamics in an Efficient MOF-Based Proton Conductor, J. Am. Chem. Soc. 139 (2017) 3505–3512. https://doi.org/10.1021/jacs.6b12847.

[84] S. Hwang, E.J. Lee, D. Song, N.C. Jeong, High Proton Mobility with High Directionality in Isolated Channels of MOF-74, ACS Appl. Mater. Interfaces. 10 (2018) 35354–35360. https://doi.org/10.1021/acsami.8b11816.

[85] A. Javed, T. Wagner, S. Wöhlbrandt, N. Stock, M. Tiemann, Proton Conduction in a Single Crystal of a Phosphonato-Sulfonate-Based Coordination Polymer: Mechanistic Insight, ChemPhysChem. 21 (2020) 605–609. https://doi.org/10.1002/cphc.202000102.

[86] H. Bunzen, A. Javed, D. Klawinski, A. Lamp, M. Grzywa, A. Kalytta-Mewes, M. Tiemann, H.-A.K. von Nidda, T. Wagner, D. Volkmer, Anisotropic Water-Mediated Proton Conductivity in Large Iron(II) Metal–Organic Framework Single Crystals for Proton-Exchange Membrane Fuel Cells, ACS Appl. Nano Mater. 2 (2019) 291–298. https://doi.org/10.1021/acsanm.8b01902.

[87] A. Javed, I. Strauss, H. Bunzen, J. Caro, M. Tiemann, Humidity-Mediated Anisotropic Proton Conductivity through the 1D Channels of Co-MOF-74, Nanomaterials. 10 (2020) 1263. https://doi.org/10.3390/nano10071263.

[88] N. Ma, S. Kosasang, A. Yoshida, S. Horike, Proton-conductive coordination polymer glass for solid-state anhydrous proton batteries, Chem. Sci. 12 (2021) 5818–5824. https://doi.org/10.1039/D1SC00392E.

[89] W. Chen, S. Horike, D. Umeyama, N. Ogiwara, T. Itakura, C. Tassel, Y. Goto, H. Kageyama, S. Kitagawa, Glass Formation of a Coordination Polymer Crystal for Enhanced Proton Conductivity and Material Flexibility, Angew. Chemie Int. Ed. 55 (2016) 5195–5200. https://doi.org/10.1002/anie.201600123.

[90] M. Inukai, Y. Nishiyama, K. Honjo, C. Das, S. Kitagawa, S. Horike, Glass-phase coordination polymer displaying proton conductivity and guest-accessible porosity, Chem. Commun. 55 (2019) 8528–8531. https://doi.org/10.1039/C9CC02744K.

[91] S.S. Nagarkar, S. Horike, T. Itakura, B. Le Ouay, A. Demessence, M. Tsujimoto, S. Kitagawa, Enhanced and Optically Switchable Proton Conductivity in a Melting Coordination Polymer Crystal, Angew. Chemie Int. Ed. 56 (2017) 4976–4981. https://doi.org/10.1002/anie.201700962.

[92] T. Ogawa, K. Takahashi, S.S. Nagarkar, K. Ohara, Y.L. Hong, Y. Nishiyama, S. Horike, Coordination polymer glass from a protic ionic liquid: proton conductivity and mechanical properties as an electrolyte, Chem. Sci. 11 (2020) 5175–5181. https://doi.org/10.1039/d0sc01737j.

[93] Y. Ohara, A. Hinokimoto, W. Chen, T. Kitao, Y. Nishiyama, Y. Hong, S. Kitagawa, S. Horike, Formation of coordination polymer glass by mechanical milling: dependence on metal ions and molecular doping for H + conductivity, Chem. Commun. 54 (2018) 6859–6862. https://doi.org/10.1039/C8CC02399A.

[94] Y. Qi, S. Lin, C. Chen, Y. Liu, Z. Qiao, X. Kuang, Q. Su, H.-Y. Chao, Increased proton conductivity of metal–organic framework micro-film prepared by a facile salt-free approach, J. Mater. Chem. A. 2 (2014) 8849. https://doi.org/10.1039/c4ta00336e.

[95] G. Xu, K. Otsubo, T. Yamada, S. Sakaida, H. Kitagawa, Superprotonic Conductivity in a Highly Oriented Crystalline Metal–Organic Framework Nanofilm, J. Am. Chem. Soc. 135 (2013) 7438–7441. https://doi.org/10.1021/ja402727d.

[96] T. Panda, P. Jhariat, P. Kumari, Structural features of Proton Conducting Metal Organic and Covalent Organic Frameworks, CrystEngComm. (2020). https://doi.org/10.1039/d0ce00902d.

Chapter 3

Multivariate sulfonic-based Titanium MOFs as super protonic conductors

3.1. Introduction

This chapter refers to a multicomponent approach we applied to a robust and eco-friendly 2D MOF architecture with the objective to deliberately conceive a platform of multivariate sulfonic-based solids MIP-207-$(SO_3H\text{-}IPA)_x$-$(BTC)_{1-x}$, resulting from the gradual substitution of the trimesate 1,3,5-benzenetricarboxylate (BTC) moieties by 5-SO_3H-isophthalate (SO_3H-IPA) derivatives with their free sulfonic groups pointing towards the porosity. The proton donor character of the pristine sample was steadily tuned according to the mixed ligands ratio x, as illustrated by the proton conductivity raise from 8.9×10^{-5} S.cm^{-1} to 2.6×10^{-2} S.cm^{-1} at 363 K/95% RH with x increasing from 0.00 to 0.28. Decisively, this series of MOFs remains stable under operating conditions, which further evidences that the multivariate strategy is appealing to design eco-compatible materials which fulfill the target application criteria, i.e., high proton conductivity coupled to good stability under working conditions. The microscopic proton transfer mechanism in these functionalized MOFs was further elucidated using AIMD simulations. These calculations supported that the -SO_3H groups act as proton donors and revealed that the proton transfer mechanism results from the solvation structure of protons through the fast and Zundel/hydronium interconversion along the continuous H-bonded network connecting the adsorbed water molecules.

3.2. Materials and methods

3.2.1. Synthesis Ti-(SO3H-IPA)$_x$-$(BTC)_{1-x}$ derivatives

The sulfonic-based titanium MOFs were synthesized by our collaborators, Dr. S. Wang and Dr. C. Serre, from the Institute of porous Materials from Paris -IMAP-. The Ti-BTC MOF, where BTC refers to 1,3,5-benzenetricarboxylate moieties, also labelled as MIP-207, was used as a building block. This material was prepared by mixing titanium tetraisopropanolate ($Ti(iPrO)_4$) with 1,3,5-benzenetricarboxylic acid in an acetic anhydride/acetic acid solution under reflux according to a procedure detailed in reference.[1] The Ti-$(SO_3H\text{-}IPA)_x$-$(BTC)_{1-x}$ derivatives were prepared by mixing into a round bottom flask (50 mL) $Ti(iPrO)_4$, BTC and lithium sulfoisophthalic acid (5-$LiSO_3$-IPA), whose amounts were adjusted for each sample according to Table 3.1. Acetic anhydride (10 mL) was added to disperse the solid with stirring at 298 K for 5 minutes, followed by adding acetic acid (10 mL). The system was heated to 423 K for 24 hours. After cooling down to 298 K, the reaction system was filtered to collect the crude Ti-$(SO_3H\text{-}IPA)_x$-$(BTC)_{1-x}$ product.

Centrifuge was applied when the sample particle was too small to do filtration. The sample was washed with boiling acetone for activation. All the chemicals were purchased from commercial sources and used without further purifications.

Table 3.1 - Detailed reaction conditions for preparing the Ti-$(SO_3H\text{-}IPA)_x$- $BTC)_{1-x}$ products.

MIP-207-$(SO_3H\text{-}IPA)_x$-$(BTC)_{1-x}$	**$Ti(iPrO)_4$ added / µL**	**BTC added / mg**	**5-$LiSO_3$-IPA added /mg**
X = 0.00	800	840	0
X = 0.06	800	756	101
X = 0.16	800	672	202
X = 0.28	800	588	303
X = 0.44	800	504	403
X = 0.66	800	420	504

3.2.2. Characterization of Ti-$(SO_3H\text{-}IPA)_x$-$(BTC)_{1-x}$ derivatives

Powder X-Ray Diffraction (PXRD) patterns of all materials in their pristine forms (Figure 3.1d) and after being maintained in the incubator used for the impedance measurements at 363 K/95% RH for 24 hours (Figure 3.2) were collected on a PANalytical X'Pert equipped with an X'Celerator detector and using a wavelength, λ =1.5406 Å from a generator operating at 40 kV and 30 mA. The structure of MIP-207 was obtained from Rietveld refinement as presented in reference.[2] The cell parameters for the substituted solids were obtained from Pawley refinement.

The substitution ratio of the prepared solids was evaluated using Scanning Electron Microscopy with Energy Dispersive X-ray Spectroscopy (SEM-EDX), Elemental Analysis (EA) and ^{1}H NMR. SEM-EDX data were collected using a FEI Magellan 400 scanning electron microscope, EA were obtained using a Flash EA 1112 (Thermofinnigan) apparatus and ^{1}H NMR spectra were recorded on a Bruker Avance 300 spectrometer.

As discussed in chapter 2, Impedance of the Ti-based MOFs derivatives was measured using a Solartron analytical Modulab XM MTS, over a frequency range from F = 0.01 Hz to F = 1 MHz under 20 mV of the applied ac voltage. The temperature [298 K - 363 K] and the relative

humidity [35% - 95%] were fixed using an Espec Corp. SH-221 incubator. Prior impedance recording, the solid was equilibrated under fixed T/RH conditions for 24 hours. The measurements were performed using powders introduced in a home-made sample holder (Figures 2.13a and 2.13d), allowing the use of the "two-probe" method for the electrical measurements. The resistance value of the studied solids was deduced from the analysis of the Nyquist plot ($-Z" = f(Z')$).

For the Nyquist plots showing a well-defined semi-circle (Figures 3.4, 3.9 and 3.10), ZView Software was applied to fit impedance data sets with equivalent circuits, assembling the bulk resistance R and the bulk non-ideal capacitance CPE, while a second constant phase element CPE-2 was alternatively added to take into account for the electrodes if applicable. For the very low resistive solids, the Nyquist plot results only in the tail end of a semi-circle at high frequency, while at lower frequency a capacitive tail is observed which prevents the use of the equivalent-fitting procedure (Figures 3.4, 3.9 and 3.10). In that case, the resistance was only evaluated from the real-axis intercept of the Nyquist plot.

The sample conductivity value was obtained using $\sigma = \frac{1}{R} * \frac{l}{S}$, where l and S are the sample thickness and area respectively. According to the Arrhenius Equation (Eq. 2.13, rewrote as $\sigma(T) = \frac{\sigma_0}{T} exp[\frac{-\Delta E}{kT}]$), the linear fitting of $ln(\sigma T)$ versus 1/T allowed us to determine the activated energy ΔE characterizing the proton transport process. These data are discussed in the following section.

3.3. Results and discussion

The starting crystalline Ti-BTC MOF, i.e., MIP-207, corresponds to the following chemical formula $Ti_8(\mu_2\text{-}O)_8(acetate)_8(BTC)_4$. It is composed of planar octameric Ti_8 oxo-clusters, which are interconnected by BTC linkers, thus forming a 2D layer (Figure 3.1b). The layer/layer cohesion is ensured by van der Waals interactions between acetate groups and between water/water and water/MOF framework under hydration conditions. The BTC organic ligand behaves somehow as an isophthalate type linker, with the uncoordinated residual carboxylic function pointing towards the voids, so that it is able to interact with guest molecules. This ditopic bonding configuration further offers the opportunity to modify the inner surface of Ti-BTC by substituting the BTC linker with functionalized isophthalic acid (IPA) of similar molecular size and able to

form equivalent angles between the two connection sites. Typically, 5-SO_3H-IPA was deliberately selected to impart accessible and highly acidic proton sources to the pristine solid. We thus systematically prepared a series of mixed-ligand analogous MIP-207 solids, labelled as MIP-207-(SO_3H-IPA)$_x$-(BTC)$_{1-x}$ where x the substitution ratio. According to Figure 3.1d, similar PXRD patterns were recorded for all MIP-207-(SO_3H-IPA)$_x$-(BTC)$_{1-x}$ derivatives, evidencing that these MOFs are isostructural to the pristine MIP-207 with similar cell parameters (see Table 3.2). This further supports that the partial replacement of BTC linker by similar ligands in terms of dimension and topology does not impact the crystal structure of the starting material. All these samples were maintained in the incubator used for the impedance measurements at 373 K and 95% RH for 24 hours and their PXRD patterns were subsequently collected to assess their structural robustness under operating conditions. The structural integrity was maintained for all samples up to x = 0.28 while the materials with x = 0.44 and 0.66 were found to exhibit a significant loss of crystallinity (Figure 3.2). MIP-207-(SO_3H-IPA)$_{0.44}$-(BTC)$_{0.56}$ got semi-pasty, and MIP-207-(SO_3H-IPA)$_{0.66}$-(BTC)$_{0.34}$ became liquid under humidity conditions.

Table 3.2 - Unit cell parameters for the MIP-207-(SO_3H-IPA)$_x$-(BTC)$_{1-x}$ products.

MIP-207-(SO_3H-IPA)$_x$-(BTC)$_{1-x}$	**a (Å)**	**b (Å)**	**c (Å)**	**Crystal system**
X = 0.00	24.22	24.22	7.82	Tetragonal
X = 0.06	24.08	24.08	7.93	Tetragonal
X = 0.16	24.12	24.12	7.94	Tetragonal
X = 0.28	24.06	24.06	7.92	Tetragonal
X = 0.44	24.00	24.00	7.93	Tetragonal
X = 0.66	24.08	24.08	7.79	Tetragonal

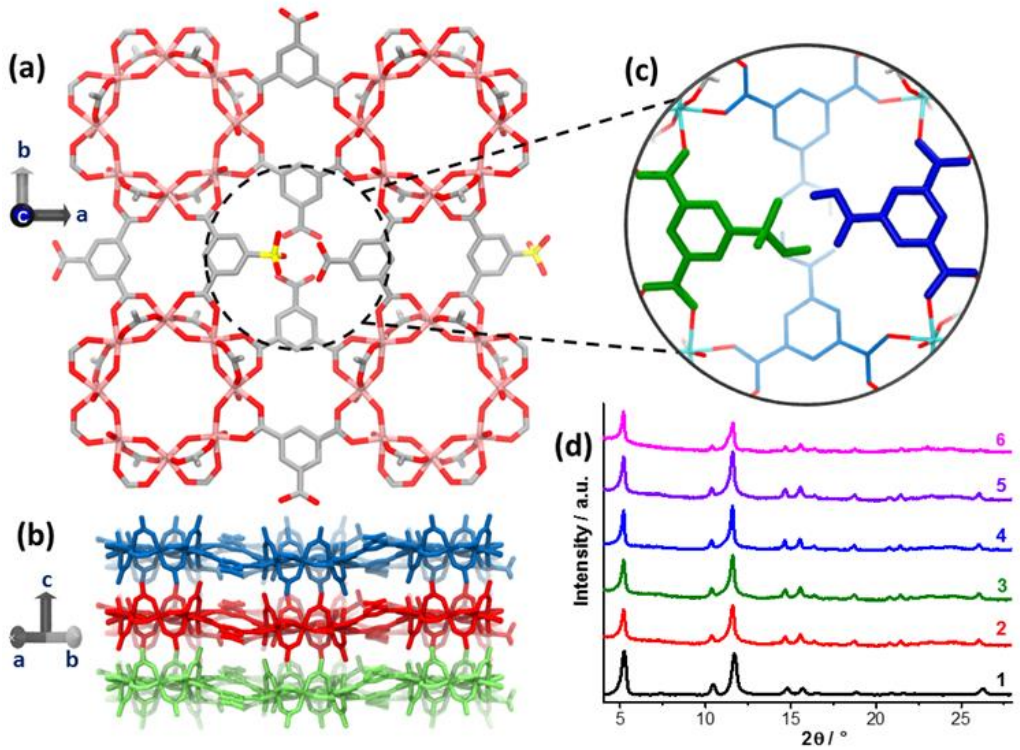

Figure 3.1 - Illustration of the MIP-207-$(SO_3H\text{-IPA})_x$.$(BTC)_{1-x}$ structure: **a)** viewed along the c-axis with the following atom color codes: C in grey, O in red, S in yellow, and Ti in pink., **b)** 2D layered view with each layer highlighted by distinct mono-color, **c)** a zoomed view on the organization of -SO_3H and -CO_2H moieties, where BTC ligands and SO_3H-IPA substitutes are presented in blue and green, respectively, and **d)** experimental PXRD patterns of the solid with x = (1) 0.00, (2) 0.06, (3) 0.16, (4) 0.28, (5) 0.44 and (6) 0.66.

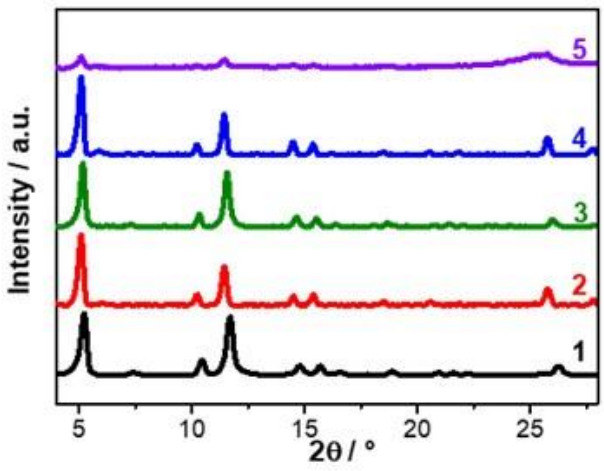

Figure 3.2 - PXRD patterns of MIP-207-$(SO_3H\text{-IPA})_x$-$(BTC)_{1-x}$ after 363 K/95% RH/24 hr exposure, for x = (**1**) 0.00, (**2**) 0.06, (**3**) 0.16, (**4**) 0.28 and (**5**) 0.44.

The substitution ratio was evaluated to range from 0 to 0.66 as confirmed by EDX, EA and NMR (see Tables 3.3-3.6). The S/Ti ratio are listed in Table 3.3 for all derivatives, corresponding to substitution ratios of the prepared solids ranging from 0.06 to 0.66. Data issued from EA are reported in Table 3.4, while Table 3.5 shows the good agreement between SEM-EDX and EA data. Finally, the analysis of the ^{1}H NMR spectra illustrated in Figure 3.3, further confirms the EA analysis, as shown by the consistent data reported in Table 3.6.

Table 3.3 - EDX results of MIP-207-$(SO_3H\text{-}IPA)_x$-$(BTC)_{1-x}$ products.

MIP-207-$(SO_3H\text{-}IPA)_x$-$(BTC)_{1-x}$	**S/Ti (atomic ratio)**
X = 0.06	4/96
X = 0.16	8/92
X = 0.28	15/85
X = 0.44	17/83
X = 0.66	35/65

Table 3.4 - EA results of MIP-207-$(SO_3H\text{-}IPA)_x$-$(BTC)_{1-x}$ products.

MIP-207-$(SO_3H\text{-}IPA)_x$-$(BTC)_{1-x}$			
x = 0.06		C	S
	%exp (wt%)	32.99	0.51
	N (C/S)	171.84	
	Chemical formula	**$Ti_8(\mu_2\text{-}O)_8\ (CH_3COO)_6\ (OH)_2\ (H_2O)\ (BTC)_{3.72}(5\text{-}SO_3H\ IPA)_{0.28}$**	
x = 0.16		C	S
	%exp (wt%)	31.60	1.09
	N (C/S)	77.45	
	Chemical formula	**$Ti_8(\mu_2\text{-}O)_8\ (CH_3COO)_6\ (OH)_2\ (H_2O)\ (BTC)_{3.39}(5\text{-}SO_3H\ IPA)_{0.61}$**	
x = 0.28		C	S
	%exp (wt%)	32.78	2.02
	N (C/S)	43.20	
	Chemical formula	**$Ti_8(\mu_2\text{-}O)_8\ (CH_3COO)_6\ (OH)_2\ (H_2O)\ (BTC)_{2.91}(5\text{-}SO_3H\ IPA)_{1.09}$**	
x = 0.44		C	S
	%exp (wt%)	31.98	3.29
	N (C/S)	25.95	
	Chemical formula	**$Ti_8(\mu_2\text{-}O)_8\ (CH_3COO)_6\ (OH)_2\ (H_2O)\ (BTC)_{2.22}(5\text{-}SO_3H\ IPA)_{1.78}$**	

x = 0.66		C	S
	%exp (wt%)	27.22	4.51
	N (C/S)	16.11	
	Chemical formula	$\mathbf{Ti_8(\mu_2\text{-}O)_8\ (CH_3COO)_6\ (OH)_2\ (H_2O)\ (BTC)_{1.20}(5\text{-}SO_3H\ IPA)_{2.80}}$	

Table 3.5 - Comparison of the substitution degree of MIP-207-$(SO_3H\text{-}IPA)_x$-$(BTC)_{1-x}$ products deduced from EDX and Elemental analysis.

MIP-207-$(SO_3H\text{-}IPA)_x$-$(BTC)_{1-x}$	**S/Ti ratio (atomic) from EDX**	**S/Ti ratio (atomic) from EA**
x = 0.06	4.0/96.0	3.4/96.6
x = 0.16	8.0/92.0	7.0/93.0
x = 0.28	15.0/85.0	11.6/88.4
x = 0.44	17.0/83.0	18.5/81.5
x = 0.66	35.0/65.0	25.9/74.1

Table 3.6 - Comparison of the substitution degree of MIP-207-$(SO_3H\text{-}IPA)_x$-$(BTC)_{1-x}$ products deduced from NMR and Elemental analysis.

MIP-207-$(SO_3H\text{-}IPA)_x$-$(BTC)_{1-x}$	**(BTC/SO_3H-IPA) ratio from NMR**	**(BTC/SO_3H-IPA) ratio from EA**
x = 0.06	1.00/0.07	1.00/0.07
x = 0.16	1.00/0.20	1.00/0.18
x = 0.28	1.00/0.40	1.00/0.37
x = 0.44	1.00/0.80	1.00/0.80
x = 0.66	1.00/2.00	1.00/2.33

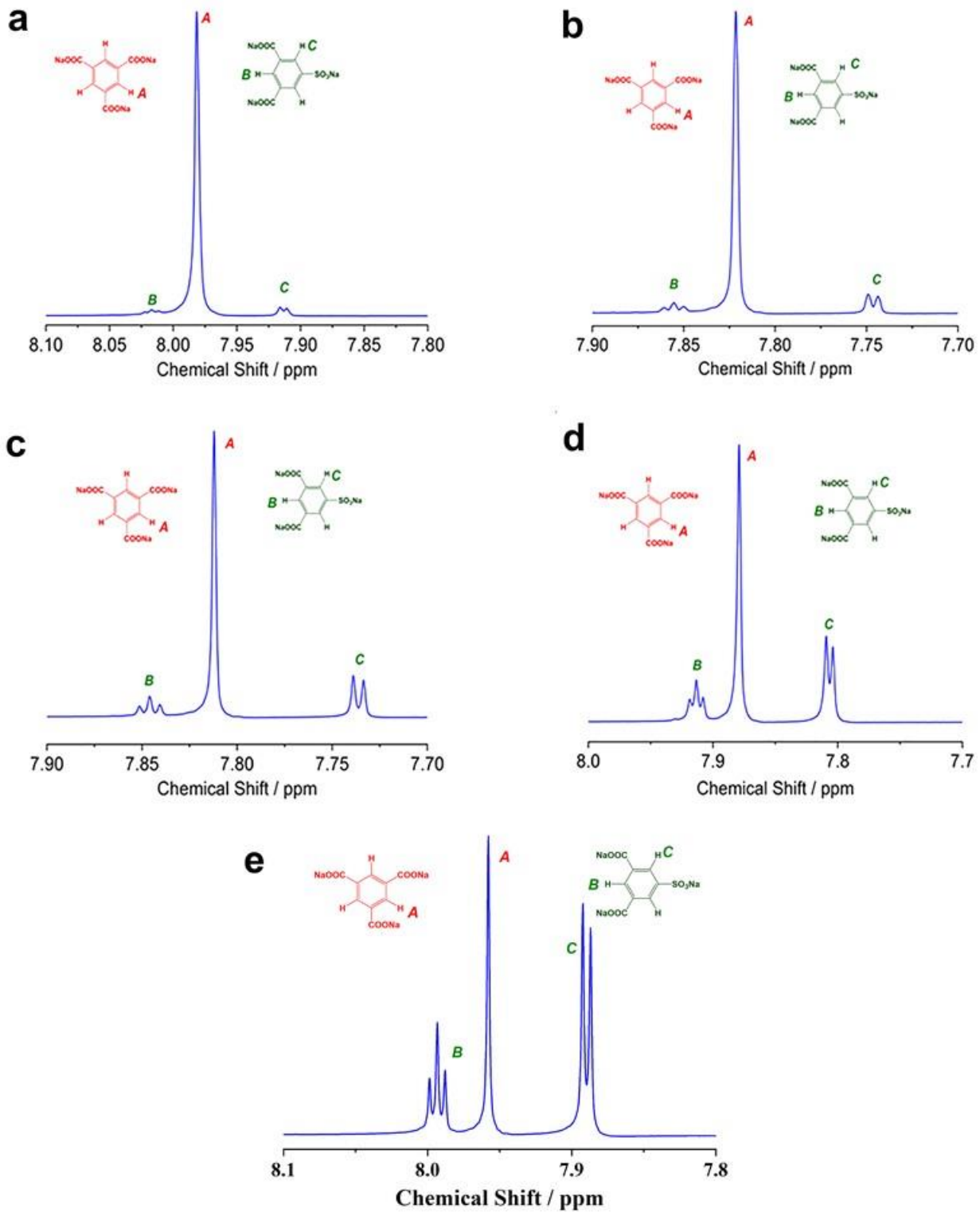

Figure 3.3 - ^{1}H NMR spectra of decomposed MIP-207-$(SO_3H\text{-IPA})_x$-$(BTC)_{1-x}$ samples in $NaOH/D_2O$ with x = a) 0.06, b) 0.16, c) 0.28, d) 0.44 and e) 0.66.

The proton-conducting behaviours of MIP-207-$(SO_3H\text{-}IPA)_x$-$(BTC)_{1-x}$ with x up to 0.28 were further explored by ac impedance spectroscopy under varying temperature (T) and 95% RH (Figure 3.4). The conductivities (σ) deduced from the analysis of the Nyquist plots recorded at 363 K/95% RH are listed in Table 3.7 and further illustrated in Figure 3.6. As targeted, σ gradually increases with the SO_3H-IPA amount and raises by more than two orders of magnitude, i.e., from 8.9 x 10^{-5} S.cm^{-1} to 2.6 x 10^{-2} S.cm^{-1}, for x varying from 0.00 to 0.28 in MIP-207-$(SO_3H\text{-}IPA)_x$-$(BTC)_{1-x}$. This substantial increase confirms the expected benefit of grafting sulfonic functions to boost the proton conduction performance of Ti-BTC. Importantly, the excellent level of performance for MIP-207-$(SO_3H\text{-}IPA)_{0.28}$-$(BTC)_{0.72}$ makes this material among the best proton conducting MOFs under these T/RH conditions, around 10^{-2} S.cm^{-1}.[3–22]

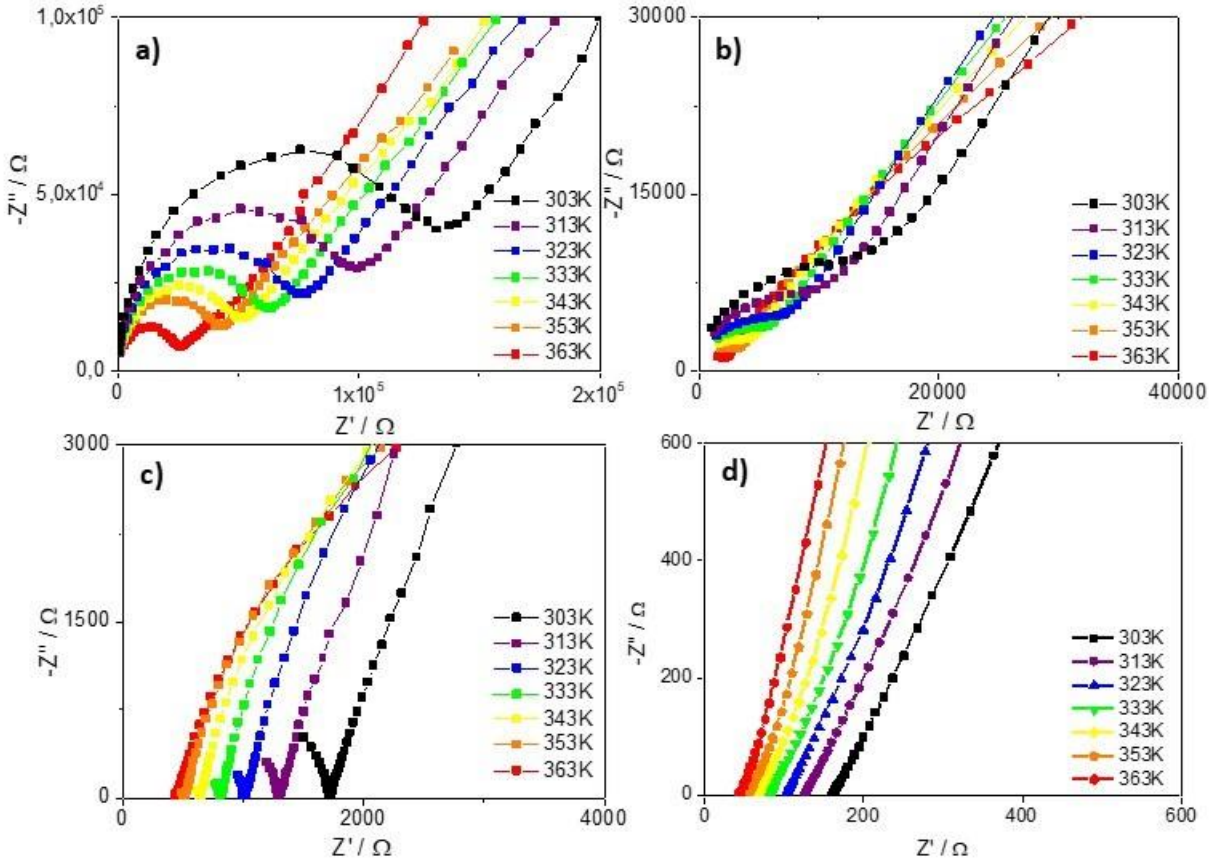

Figure 3.4 - Nyquist plots of the impedance recorded from 363 K to 298 K under 95% RH, for MIP-207-$(SO_3H\text{-}IPA)_x$-$(BTC)_{1-x}$ powder with x = a) 0.00, b) 0.06, c) 0.16 and d) 0.28.

Table 3.7 - Conductivity values deduced from the circuit equivalent fitting or the extrapolation procedures applied on the Nyquist plots, for the MIP-207-$(SO_3H\text{-}IPA)_x$-$(BTC)_{1-x}$ powder at different RH/T conditions.

Ti-BTC RH = 95%	**T / K**	**σ / S.cm^{-1}**	**T / K**	**σ / S.cm^{-1}**	**ΔE / eV**
l = 0.338 cm S = 0.1256 cm^2	298	1.8 x 10^{-5}	333	4.2 x 10^{-5}	0.25
	303	2.1 x 10^{-5}	343	5.2 x 10^{-5}	
	313	2.7 x 10^{-5}	353	6.1 x 10^{-5}	
	323	3.5 x 10^{-5}	363	8.9 x 10^{-5}	
MIP-207-$(SO_3H\text{-}IPA)_{0.06}$-$(BTC)_{0.94}$ RH = 95%	**T / K**	**σ / S.cm^{-1}**	**T / K**	**σ / S.cm^{-1}**	**ΔE / eV**
l = 0.326 cm S = 0.1256 cm^2	298	2.0 x 10^{-4}	333	4.1 x 10^{-4}	0.25
	303	2.2 x 10^{-4}	343	5.3 x 10^{4}	
	313	2.4 x 10^{-4}	353	7.0 x 10^{-4}	
	323	3.3 x 10^{-4}	363	9.7 x 10^{-4}	
MIP-207-$(SO_3H\text{-}IPA)_{0.16}$-$(BTC)_{0.84}$ RH = 95%	**T / K**	**σ / S.cm^{-1}**	**T / K**	**σ / S.cm^{-1}**	**ΔE / eV**
l = 0.285 cm S = 0.1256 cm^2	298	1.2 x 10^{-3}	333	2.9 x 10^{-3}	0.25
	303	1.4 x 10^{-3}	343	3.8 x 10^{-3}	
	313	1.8 x 10^{-3}	353	4.6 x 10^{-3}	
	323	2.4 x 10^{-3}	363	6.4 x 10^{-3}	
MIP-207-$(SO_3H\text{-}IPA)_{0.28}$-$(BTC)_{0.72}$ RH = 95%	**T / K**	**σ / S.cm^{-1}**	**T / K**	**σ / S.cm^{-1}**	**ΔE / eV**
l = 0.209 cm S = 0.1256 cm^2	298	3.8 x 10^{-2}	333	8.4 x 10^{-2}	0.26
	303	4.2 x 10^{-2}	343	1.6 x 10^{-2}	
	313	5.4 x 10^{-2}	353	2.0 x 10^{-2}	
	323	6.7 x 10^{-2}	363	2.6 x 10^{-2}	
MIP-207-$(SO_3H\text{-}IPA)_{0.28}$-$(BTC)_{0.72}$ RH = 0%	**T / K**	**σ / S.cm^{-1}**	**T / K**	**σ / S.cm^{-1}**	**ΔE / eV**
l = 0.042 cm S = 0.3631 cm^2	383	1.2 x 10^{-13}	413	1.2 x 10^{-12}	1.11
	393	2.6 x 10^{-13}	423	2.7 x 10^{-12}	
	403	5.6 x 10^{-13}			

MIP-207-(SO_3H-IPA)$_{0.28}$-(BTC)$_{0.72}$ T = 363 K	**RH / %**	**σ / S.cm^{-1}**	**RH / %**	**σ / S.cm^{-1}**
l = 0.190 cm S = 0.1256 cm^2	35	1.1 x 10^{-5}	75	3.7 x 10^{-3}
	45	6.8 x 10^{-5}	85	1.0 x 10^{-2}
	55	4.1 x 10^{-4}	95	2.6 x 10^{-2}
	65	1.2 x 10^{-3}		

Temperature dependence of the conductivity for MIP-207-(SO_3H-IPA)$_x$-(BTC)$_{1-x}$ was evaluated at 95% RH from the analysis of the Nyquist plots. All samples demonstrated a significant increase of conductivity with temperature according to the Arrhenius equation (Figure 3.5). The corresponding activation energy is 0.25 eV for the pristine Ti-BTC, which refers to a Grotthuss-like proton transfer mechanism ($\Delta E < 0.40$ eV), as regularly observed for water-mediated proton conducting MOFs bearing free carboxylic acid functions.[3,4,15] Notably, ΔE does not change for the ligand-substituted derivatives, i.e. neither with the pore walls decoration with the -SO_3H groups nor with the sulfonic groups concentration. This demonstrates that the conductivity enhancement with the substitution ratio x, as illustrated in Figure 3.6, results from the increase of the concentration of the strongest proton donor -SO_3H, while the topology of the continuous H-bonded network providing the H^+ pathway is likely unchanged.

The best material, MIP-207-(SO_3H-IPA)$_{0.28}$-(BTC)$_{0.72}$ was further explored in-depth. Figure 3.7 depicts the proton conductivity data collected over 24 hours impedance measurements during a cooling/heating cycle at 95% RH. The deviation between the cooling and heating profiles is negligible, illustrating the reversible conductive behaviour of the material with any memory effect as a prerequisite for further processing.

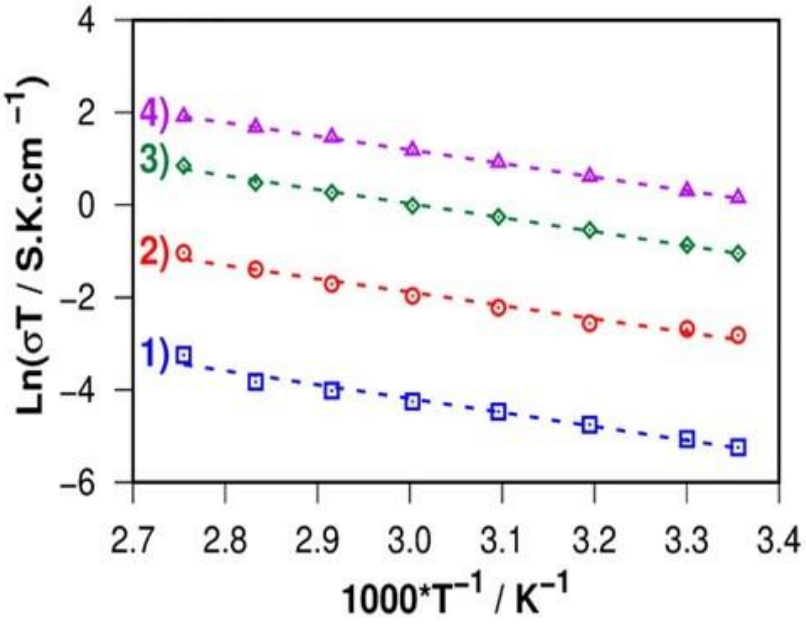

Figure 3.5 - Arrhenius type plot of the conductivity for MIP-207-$(SO_3H\text{-}IPA)_x$-$(BTC)_{1-x}$ under 95% RH, for (1) x = 0, (2) x = 0.06, (3) x = 0.16 and (4) x = 0.28. Dashed lines correspond to the linear least-square fit.

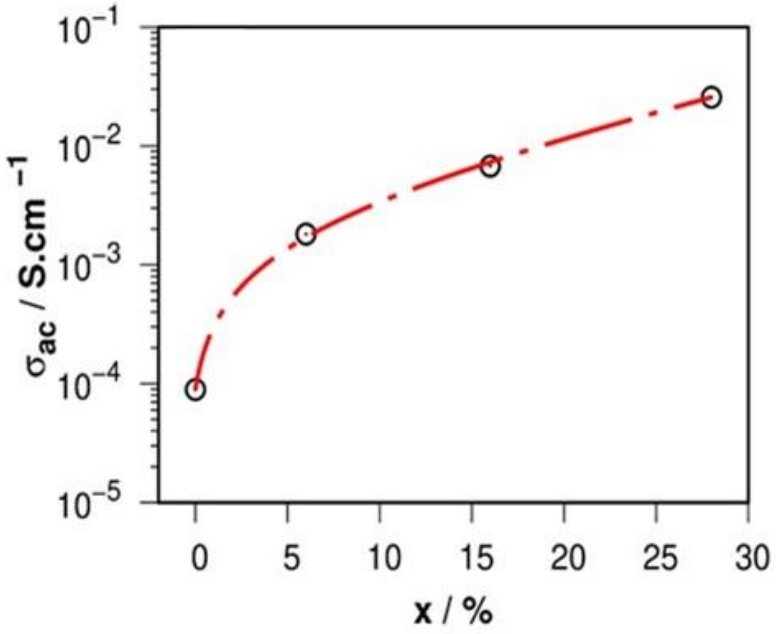

Figure 3.6 - Evolution of the conductivity (σ) for MIP-207-$(SO_3H\text{-}IPA)_x$-$(BTC)_{1-x}$ recorded at 363 K /95% RH vs the BTC substitution degree x.

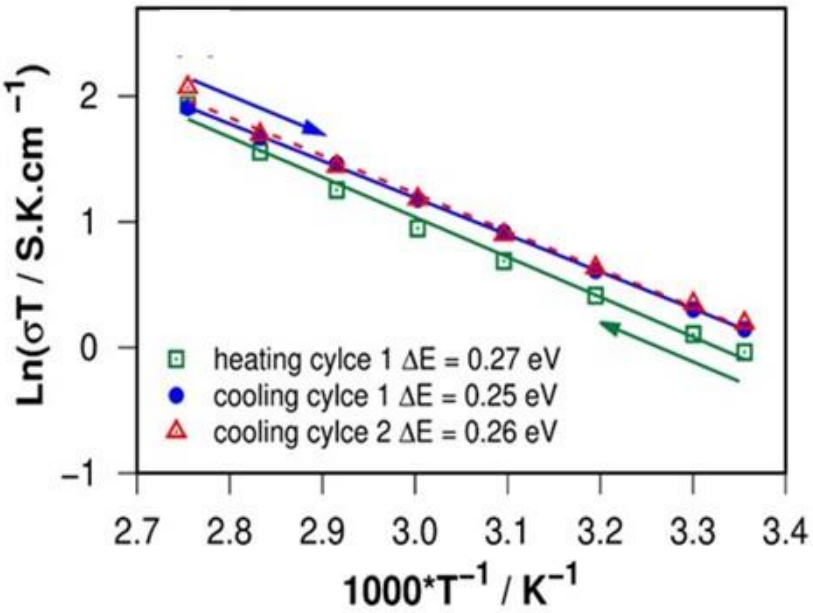

Figure 3.7 - Arrhenius type plot of the conductivity for MIP-207-$(SO_3H\text{-}IPA)_{0.28}$-$(BTC)_{0.72}$ under 95% RH, for repeated cycle 1 (filled square) and 2 (open square), under cooling (blue) and heating (red). Lines correspond to the linear least-square fit.

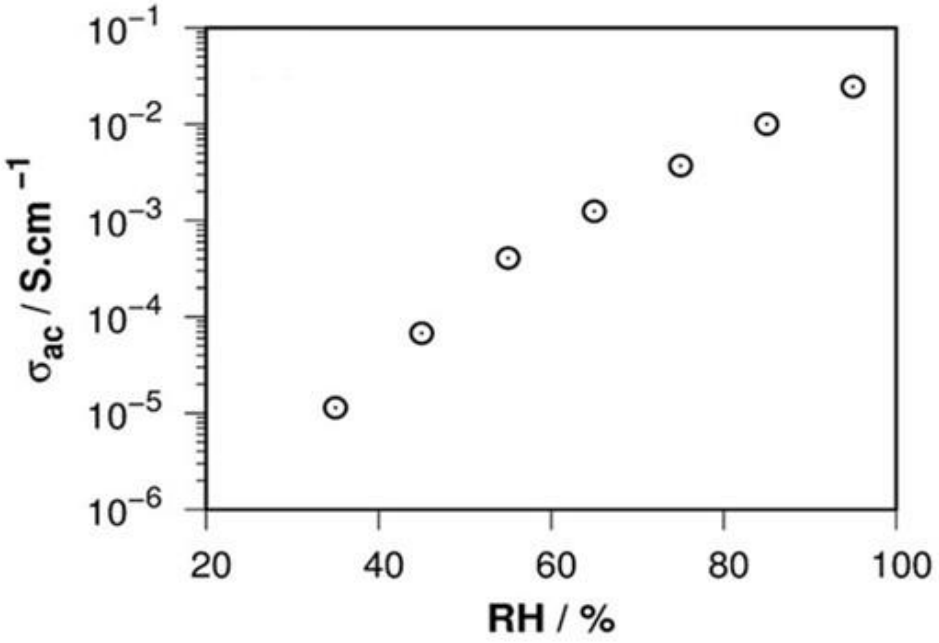

Figure 3.8 - Humidity dependence of the conductivity for MIP-207-$(SO_3H\text{-}IPA)_{0.28}$-$(BTC)_{0.72}$ recorded at 363 K.

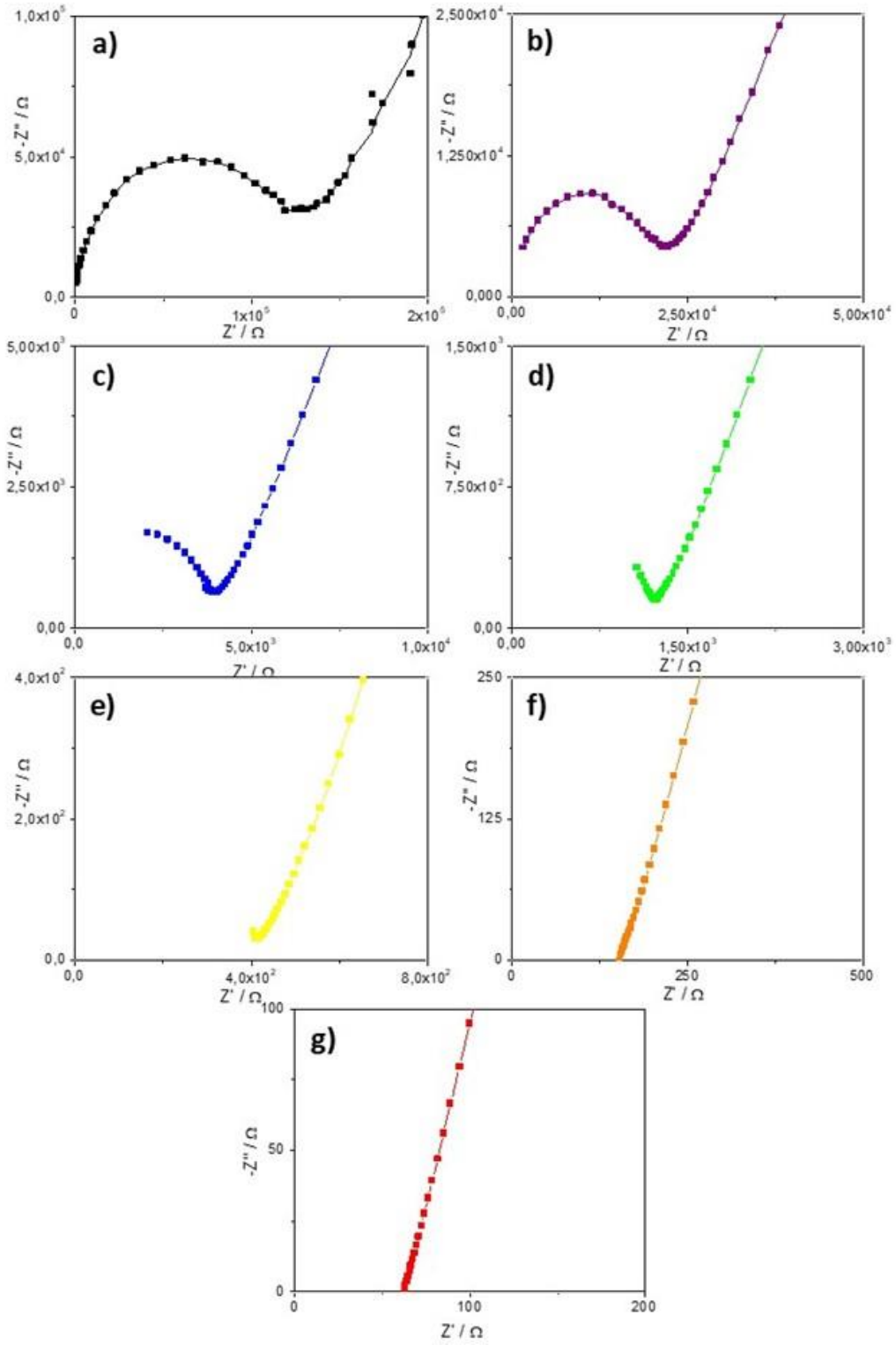

Figure 3.9 - Nyquist plots of the impedance for MIP-207-$(SO_3H\text{-}IPA)_{0.28}$-$(BTC)_{0.72}$ powder recorded at 363 K for RH = **a)** 35%, **b)** 45%, **c)** 55%, **d)** 65%, **e)** 75%, **f)** 85% and **g)** 95%.

The role of water vapor on the conductivity performance of MIP-207-$(SO_3H\text{-}IPA)_{0.28}$-$(BTC)_{0.72}$ was characterized by recording variable RH impedance measurements at 363 K (Figure 3.9). Figure 3.8 evidences the conductivity drop from 2.6×10^{-2} S.cm^{-1} to 1.1×10^{-5} S.cm^{-1} when RH decreases from 95% to 35%. This observation strongly suggests that water contributes to the proton transfer within the material.[3,4,15] This statement is confirmed by the insulating behavior of MIP-207-$(SO_3H\text{-}IPA)_{0.28}$-$(BTC)_{0.72}$ at the anhydrous state as shown by the characteristic profile of the impedance Nyquist plot, which mainly results from an incomplete semi-circle combined with high impedance values (Figure 3.10). For T < 383 K, Nyquist plots show no semi-circle, while the impedance values are very low, illustrated that the material behaves as an insulator. For T > 383 K, Nyquist plots show part of semi-circle, evidencing that proton transfer in Ti-BTC requires high temperature. This means that the H^+ long-range transfer from -SO_3H donors to -CO_2H or -SO_3H acceptors is highly improbable in the dry state as supported by the high activation energy for the proton conductivity (ΔE = 1.11 eV, Figure 3.11 and Table 3.7). Accordingly, the introduction of guest molecules is a pre-requisite to promote the proton transfer into the pores of the material. This suggests that under RH conditions, the interconnection between SO_3H-proton donors and acceptors is ensured by the water molecules through the creation of a continuous H-bonded network.

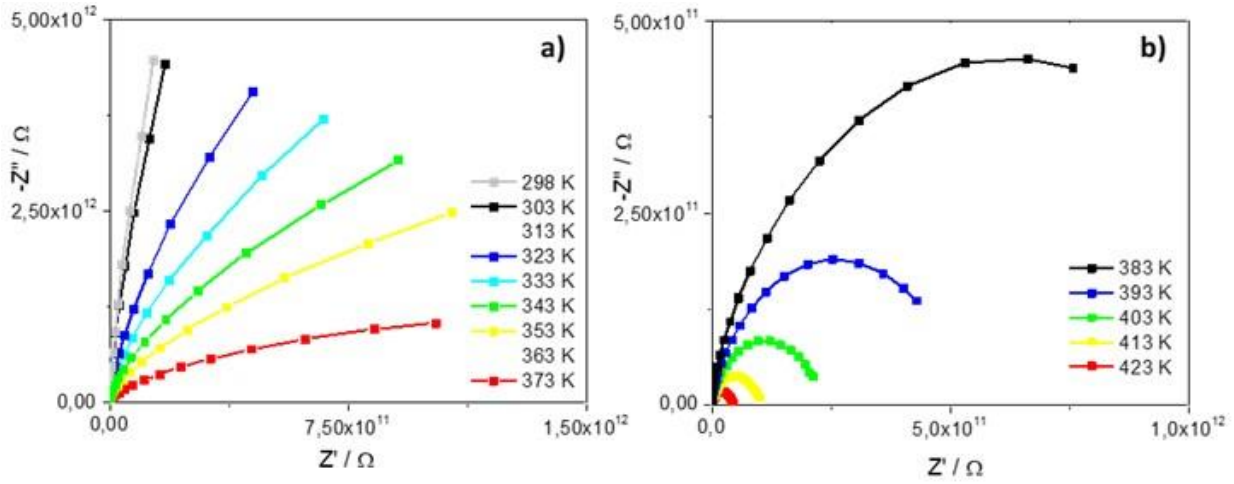

Figure 3.10 - Nyquist plots of the impedance for the anhydrous MIP-207-$(SO_3H\text{-}IPA)_{0.28}$-$(BTC)_{0.72}$ powder recorded under 0% RH for temperatures ranging from **a)** 298 K to 373 K and **b)** 383 K to 423 K.

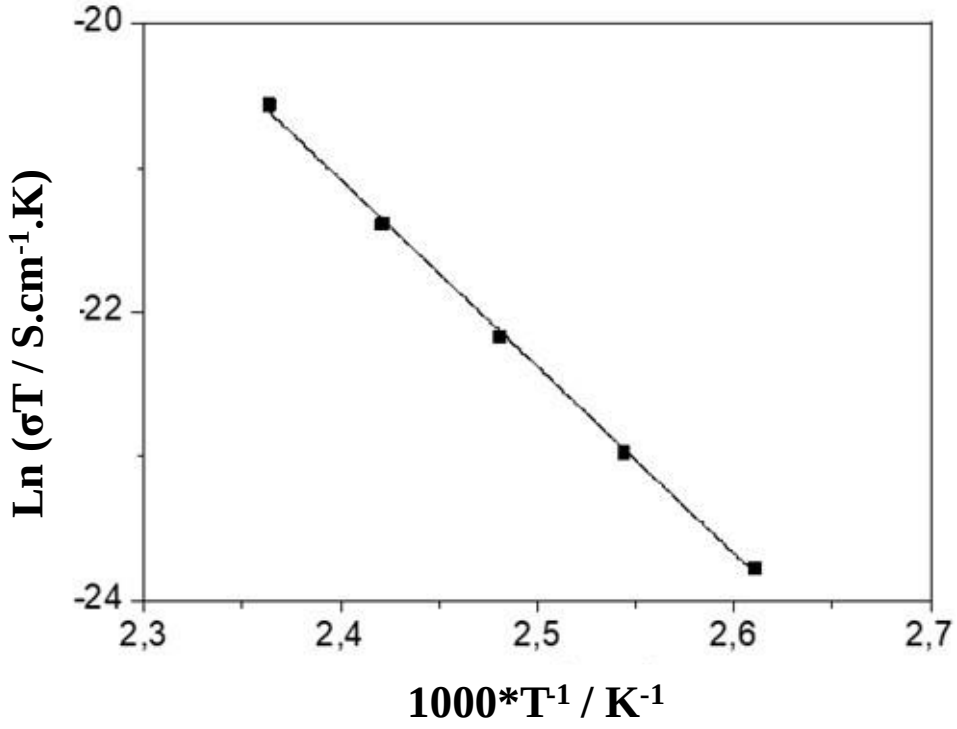

Figure 3.11 - Arrhenius type plot of the conductivity for MIP-207-$(SO_3H\text{-}IPA)_{0.28}$-$(BTC)_{0.72}$ under 0% RH. The line corresponds to the linear least-square fit.

Molecular simulations were further implemented by colleagues in the group to gain insight into the microscopic mechanism describing the proton conduction performance of MIP-207-$(SO_3H\text{-}IPA)_{0.28}$-$(BTC)_{0.72}$. A structure model for MIP-207-$(SO_3H\text{-}IPA)_{0.25}$-$(BTC)_{0.75}$ was built considering that 25% of the BTC ligands were randomly substituted by –$(SO_3H\text{-}IPA)$ and 25% of the acetates of the Ti–oxo cluster were also replaced arbitrarily by H_2O and OH moieties according to the NMR results (Figure 3.3). This structure model was then geometry optimized at the DFT level, while the cell parameters were fixed according to the experimental PXRD data for MIP-207-$(SO_3H\text{-}IPA)_{0.28}$-$(BTC)_{0.72}$ (Table 3.2). Grand canonical Monte Carlo (GCMC) simulations further evidenced that this structure can host 60 water molecules per unit cell, in agreement with the uptake deduced from the experimental adsorption isotherm, i.e., 56.7 molecules/u.c. (Figure 3.12).

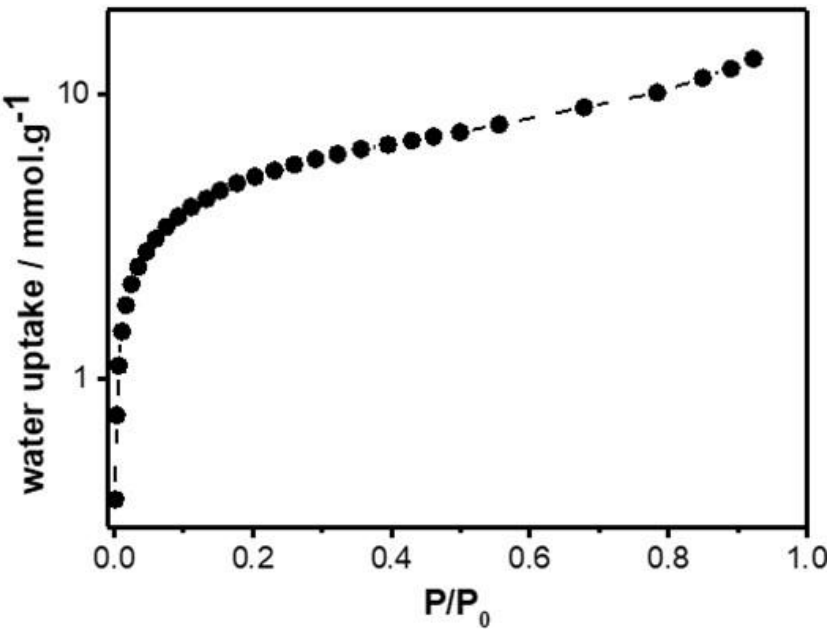

Figure 3.12 - Water adsorption isotherm of MIP-207-$(SO_3H\text{-}IPA)_{0.28}$-$(BTC)_{0.72}$ collected at 298 K using a Micromeritics Tristar instrument at 298 K. The sample was firstly outgassed at 393 K for 8 hours under dynamic vacuum. The water uptake at the plateau, i.e., 7.4 $mmol.g^{-1}$, corresponds to the physisorption of 56.7 H_2O per MIP-207-$(SO_3H\text{-}IPA)_{0.28}$-$(BTC)_{0.72}$ unit cell.

This water-loaded structure was then geometry optimized at the DFT-level and used as a starting configuration for further AIMD simulations. Analysis of the AIMD trajectory over 10 ps revealed the formation of a persistent 3D percolating hydrogen bonded network which offers an optimal situation for the long-range transfer of the proton from the -SO_3H function throughout the entire porosity of the solid with the adsorbed water molecules acting as charge carriers. The radial distribution functions (RDFs) for the O_w-O_{SO3H} and O_w-O_w pairs (Figure 3.13) show a main peak at ~2.7 Å and 2.9 Å respectively, signature of strong hydrogen bonds between the sulfonic groups and the adsorbed water molecules as well as between the adsorbed species themselves.[23] Moreover the RDFs for the other O_w-O pairs with O corresponding to the oxygen atoms of the -CO_2H and of the terminal –OH and –H_2O groups exhibit a first peak at 2.9–3.1 Å (Figure 3.13). This clearly manifests that these functional groups can act as anchoring sites to ensure the formation of the percolated hydrogen bond network.

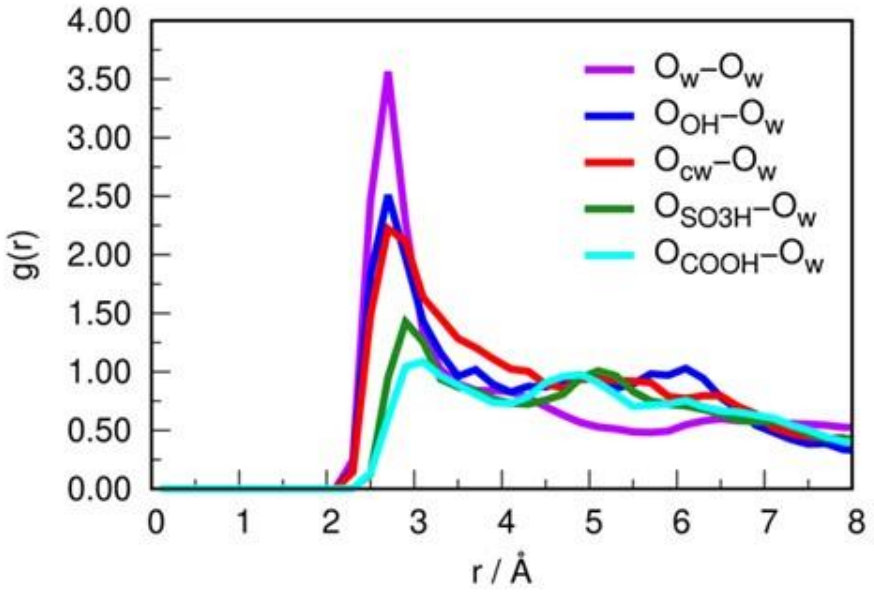

Figure 3.13 - Radial distribution functions of O-O atomic pairs of frameworks and adsorbed water molecules within the pore of MIP-207-$(SO_3H\text{-IPA})_{0.25}$-$(BTC)_{0.75}$, calculated from a 10 ps MD trajectory. O_{cw} represents the oxygen atoms of the coordinated water molecules.

An illustration of the resulting Grotthuss-like mechanism illustrating the proton transfer in this water-mediated proton conducting MOF is provided in Figure 3.14. The process starts with a disruption of the initial $(O–H)_{SO3H}\cdots O_{CO2H}$ hydrogen bond formed between the SO_3H and CO_2H groups facing each other and there is a subsequent reorientation of the proton of the $–SO_3H$ group in order to form a hydrogen bond with an adjacent adsorbed water molecule (Figures 3.14a-b). This proton is then transferred to the adsorbed water molecule to form a H_3O^+ species (Figure 3.14c). This hydronium ion then migrates towards a second water molecule to form a Zundel species ($H_5O_2^+$) as shown Figure 3.14d. This $H_5O_2^+$ ion breaks apart to deliver a proton to a second water molecule which forms a new H_3O^+ ion as shown in Figure 3.14e that further forms another Zundel species (Figure 3.14f) and so forth. We evidenced that the release of the acidic protons from the $–SO_3H$ groups occurs as fast as in Nafion^{TM},[24] typically after ~400 fs as illustrated in Figure 3.14. Noteworthy, the same scenario involving the $-CO_2H$ group rather than $–SO_3H$ as the proton donor was never observed over the whole AIMD trajectory. This clearly supports that the proton transfer exclusively proceeds via the $-SO_3H$ group since this group is more acidic than the $–CO_2H$. Interestingly, brief disruptions in the extended hydrogen bond networks can happen which however recover quickly maintaining an ideal pathway.

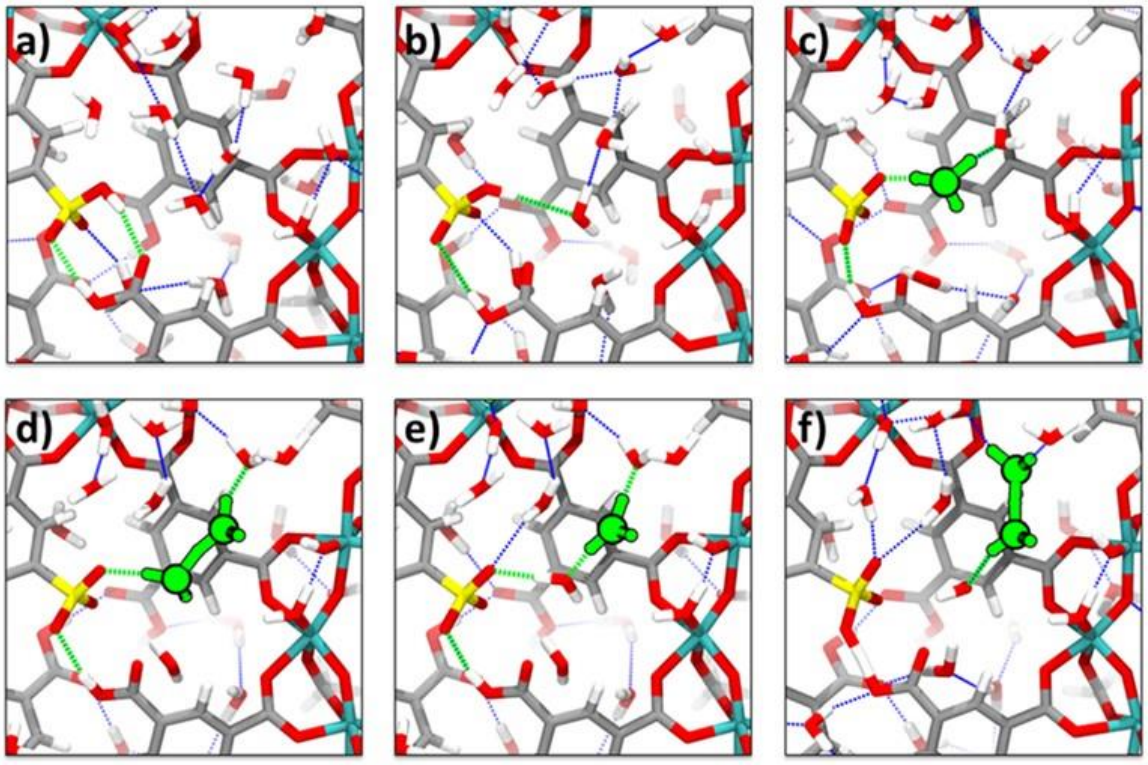

Figure 3.14 - Illustration of the evolution of the hydrogen bonded network and the characteristic propagation of one proton issued from the -SO_3H group of the ligand and its release towards the pores of MIP-207-$(SO_3H\text{-}IPA)_{0.25}$-$(BTC)_{0.75}$ as captured from the AIMD simulations performed at 400 K: **a)** initial $OSO_3H\cdots OCO_2H$ hydrogen bonded complex, **b)** formation of a strong hydrogen bond between the proton of the -SO_3H group and an adjacent adsorbed water molecule observed at 306 fs, **c)** transfer of the proton to the adjacent water molecule and creation of a hydronium ion (H_3O^+) observed at 402 fs, **d)** formation of a Zundel species ($H_5O_2^+$) observed at 465 fs, **e)** interconversion of a Zundel species to a new hydronium ion observed at 490 fs and **f)** subsequent formation of Zundel species with neighbouring water molecule observed at 570 fs.

Notably, depending on the spatial organization of the adsorbed water molecules around the acidic protons of the –SO_3H groups, we observed that the protons of some –SO_3H groups show a spring like shuttle movements featuring interchangeable donor-acceptor hydrogen bond configurations with the neighboring –CO_2H groups (configurations b and c as depicted in Figure 3.15). A very similar behavior can also be observed between two –CO_2H groups facing each other (Figure 3.16). This local motion refers to the dielectric relaxation behavior of the proton, which locally switches between 2 equilibrium positions. Since this process does not involve any water molecules assistance, it is likely to occur at the anhydrous state leading to the absence of long-range proton transport as experimentally evidenced by the incomplete semi-circle profile of the Nyquist plot in Figure 3.10.

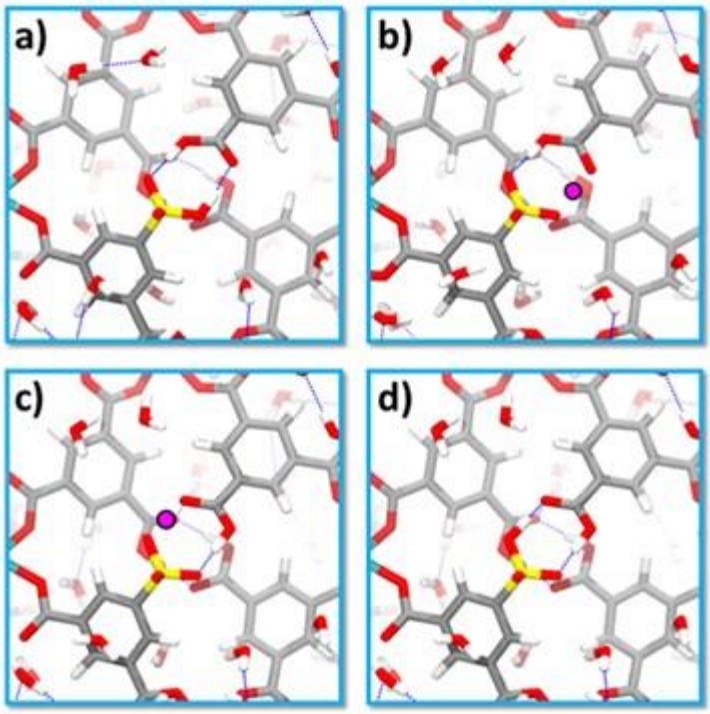

Figure 3.15 - Illustration of the SO_3H proton entrapped in the vicinity of a CO_2H group where SO_3H and CO_2H exchange their protons and form interchangeable hydrogen bonds (a-d) in MIP-207-$(SO_3H\text{-}IPA)_{0.25}$-$(BTC)_{0.75}$.

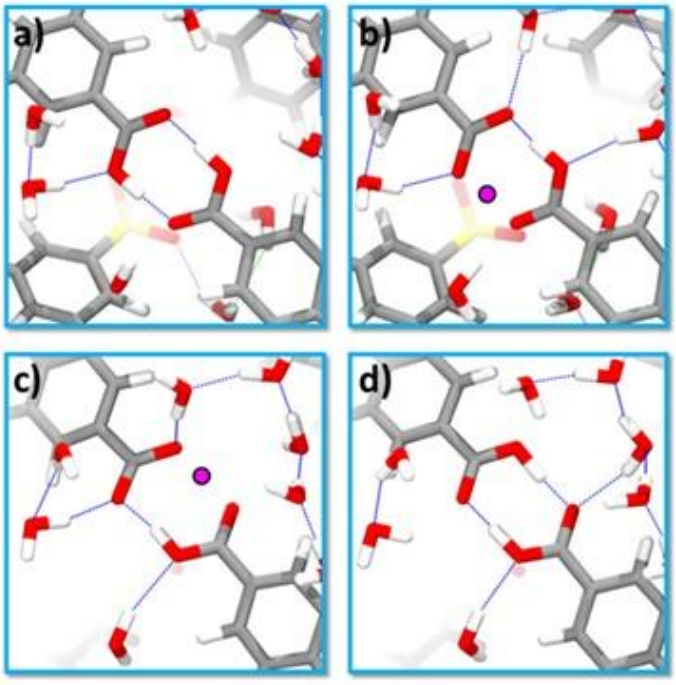

Figure 3.16 - Illustration of the proton exchange between 2-CO_2H facing groups forming interchangeable hydrogen bonds **(a-d)** in MIP-207-$(SO_3H\text{-}IPA)_{0.25}$-$(BTC)_{0.75}$.

3.4. Conclusion

A series of proton conducting mixed-linker MOFs was devised with proton conduction performances tuned by means of a multivariate strategy which enabled a gradual substitution of the 1,3,5-Benzenetricarboxylate (BTC) ligands of the pristine Ti-based MOF (MIP-207) by SO_3H-Isophtalate (SO_3H-IPA) secondary linkers as precursors. MIP-207-$(SO_3H\text{-IPA})_{0.28}$-$(BTC)_{0.72}$ was identified as the optimal candidate combining a remarkable proton conductivity, i.e., $\sigma = 2.6 \times 10^{-2}$ $S.cm^{-1}$ at 363 K/95% RH and a very good stability under operating conditions. The corresponding proton transfer mechanism was elucidated at the microscopic scale by ab initio molecular dynamics simulations which demonstrated a fast proton release from -SO_3H groups to the adsorbed water molecules and the subsequent formation of a percolated H-bonded network along the porosity of the MOF. This study paves the way towards the development of alternative proton conductors incorporating the optimal features to achieve performance as high as the benchmark Nafion^{TM} while addressing the critical issue of stability under working conditions.

REFERENCES

[1] S. Wang, H. Reinsch, N. Heymans, M. Wahiduzzaman, C. Martineau-Corcos, G. De Weireld, G. Maurin, C. Serre, Toward a Rational Design of Titanium Metal-Organic Frameworks, Matter. 2 (2020) 440–450. https://doi.org/10.1016/j.matt.2019.11.002.

[2] S. Wang, N. Xhaferaj, M. Wahiduzzaman, K. Oyekan, X. Li, K. Wei, B. Zheng, A. Tissot, J. Marrot, W. Shepard, C. Martineau-Corcos, Y. Filinchuk, K. Tan, G. Maurin, C. Serre, Engineering Structural Dynamics of Zirconium Metal-Organic Frameworks Based on Natural C4 Linkers, J. Am. Chem. Soc. 141 (2019) 17207–17216. https://doi.org/10.1021/jacs.9b07816.

[3] P. Ramaswamy, N.E. Wong, G.K.H. Shimizu, MOFs as proton conductors – challenges and opportunities, Chem. Soc. Rev. 43 (2014) 5913–5932. https://doi.org/10.1039/C4CS00093E.

[4] D.-W. Lim, H. Kitagawa, Proton Transport in Metal–Organic Frameworks, Chem. Rev. 120 (2020) 8416–8467. https://doi.org/10.1021/acs.chemrev.9b00842.

[5] P. Ramaswamy, N.E. Wong, B.S. Gelfand, G.K.H. Shimizu, A Water Stable Magnesium MOF That Conducts Protons over 10 –2 S cm –1, J. Am. Chem. Soc. 137 (2015) 7640–7643. https://doi.org/10.1021/jacs.5b04399.

[6] S. Khatua, A.K. Bar, J.A. Sheikh, A. Clearfield, S. Konar, Achieving Amphibious Superprotonic Conductivity in a CuI Metal–Organic Framework by Strategic Pyrazinium Salt Impregnation, Chem. - A Eur. J. 24 (2018) 872–880. https://doi.org/10.1002/chem.201704088.

[7] X. Wang, Y. Wang, M.A. Silver, D. Gui, Z. Bai, Y. Wang, W. Liu, L. Chen, J. Diwu, Z. Chai, S. Wang, Superprotonic conduction through one-dimensional ordered alkali metal ion chains in a lanthanide-organic framework, Chem. Commun. 54 (2018) 4429–4432. https://doi.org/10.1039/C8CC00572A.

[8] W.J. Phang, W.R. Lee, K. Yoo, D.W. Ryu, B. Kim, C.S. Hong, pH-Dependent Proton Conducting Behavior in a Metal-Organic Framework Material, Angew. Chemie Int. Ed. 53 (2014) 8383–8387. https://doi.org/10.1002/anie.201404164.

[9] P.G.M. Mileo, K. Adil, L. Davis, A. Cadiau, Y. Belmabkhout, H. Aggarwal, G. Maurin, M. Eddaoudi, S. Devautour-Vinot, Achieving Superprotonic Conduction with a 2D Fluorinated Metal–Organic Framework, J. Am. Chem. Soc. 140 (2018) 13156–13160. https://doi.org/10.1021/jacs.8b06582.

[10] M. V. Nguyen, T.H.N. Lo, L.C. Luu, H.T.T. Nguyen, T.N. Tu, Enhancing proton conductivity in a metal–organic framework at T > 80 °C by an anchoring strategy, J. Mater. Chem. A. 6 (2018) 1816–1821. https://doi.org/10.1039/C7TA10148A.

[11] Y.-H. Han, Y. Ye, C. Tian, Z. Zhang, S.-W. Du, S. Xiang, High proton conductivity in an unprecedented anionic metalloring organic framework (MROF) containing novel metalloring clusters with the largest diameter, J. Mater. Chem. A. 4 (2016) 18742–18746. https://doi.org/10.1039/C6TA07939C.

[12] S. Shalini, S. Aggarwal, S.K. Singh, M. Dutt, T.G. Ajithkumar, R. Vaidhyanathan, 10000-Fold Enhancement in Proton Conduction by Doping of Cesium Ions in a Proton-Conducting Zwitterionic Metal-Organic Framework, Eur. J. Inorg. Chem. 2016 (2016) 4382–4386. https://doi.org/10.1002/ejic.201600364.

[13] X. Lai, Y. Liu, G. Yang, S.S. Liu, Z. Shi, Y. Lu, F. Luo, S.S. Liu, Controllable proton-conducting pathways via situating polyoxometalates in targeting pores of a metal–organic framework, J. Mater. Chem. A. 5 (2017) 9611–9617. https://doi.org/10.1039/C6TA10958F.

[14] L. Qin, Y. Yu, P. Liao, W. Xue, Z. Zheng, X. Chen, Y. Zheng, A "Molecular Water Pipe": A Giant Tubular Cluster {Dy 72 } Exhibits Fast Proton Transport and Slow Magnetic Relaxation, Adv. Mater. 28 (2016) 10772–10779. https://doi.org/10.1002/adma.201603381.

[15] Y. Ye, L. Gong, S. Xiang, Z. Zhang, B. Chen, Metal–Organic Frameworks as a Versatile Platform for Proton Conductors, Adv. Mater. 32 (2020) 1907090. https://doi.org/10.1002/adma.201907090.

[16] W.J. Phang, H. Jo, W.R. Lee, J.H. Song, K. Yoo, B. Kim, C.S. Hong, Superprotonic conductivity of a uio-66 framework functionalized with sulfonic acid groups by facile postsynthetic oxidation, Angew. Chemie Int. Ed. 54 (2015) 5142–5146. https://doi.org/10.1002/anie.201411703.

[17] M. Wahiduzzaman, S. Nandi, V. Yadav, T. Kiran, G.G. Maurin, H. Chun, S. Devautour-Vinot, K. Taksande, G.G. Maurin, H. Chun, S. Devautour-Vinot, Superionic conduction in a zirconium-formate molecular solid, J. Mater. Chem. A. 8 (2020) 17951–17955. https://doi.org/10.1039/d0ta05424k.

[18] W. Chen, J. Wang, L. Zhao, W. Dai, Z. Li, G. Li, Enhancing proton conductivity of a highly water stable 3D Sr(II) metal-organic framework by exposure to aqua-ammonia vapor, J. Alloys Compd. 750 (2018) 895–901. https://doi.org/10.1016/j.jallcom.2018.04.087.

[19] S.-Z. Huang, S.-S. Liu, H. Zhang, Z. Han, G. Zhao, X.-Y. Dong, S.-Q. Zang, Dual-Functional Proton-Conducting and pH-Sensing Polymer Membrane Benefiting from a Eu-MOF, ACS Appl. Mater. Interfaces. 12 (2020) 28720–28726. https://doi.org/10.1021/acsami.0c08103.

[20] X.S. Xing, Z.H. Fu, N.N. Zhang, X.Q. Yu, M.S. Wang, G.C. Guo, High proton conduction in an excellent water-stable gadolinium metal-organic framework, Chem. Commun. 55 (2019) 1241–1244. https://doi.org/10.1039/c8cc08700h.

[21] X. Liang, B. Li, M. Wang, J. Wang, R. Liu, G. Li, Effective Approach to Promoting the Proton Conductivity of Metal–Organic Frameworks by Exposure to Aqua–Ammonia Vapor, ACS Appl. Mater. Interfaces. 9 (2017) 25082–25086. https://doi.org/10.1021/acsami.7b07635.

[22] H. Wu, F. Yang, X.-L. Lv, B. Wang, Y.-Z. Zhang, M.-J. Zhao, J.-R. Li, A stable porphyrinic metal–organic framework pore-functionalized by high-density carboxylic groups for proton conduction, J. Mater. Chem. A. 5 (2017) 14525–14529. https://doi.org/10.1039/C7TA03917D.

[23] M. Wahiduzzaman, S. Wang, J. Schnee, A. Vimont, V. Ortiz, P.G. Yot, R. Retoux, M. Daturi, J.S. Lee, J.-S.S. Chang, C. Serre, G. Maurin, S. Devautour-Vinot, A High Proton Conductive Hydrogen-Sulfate Decorated Titanium Carboxylate Metal-Organic Framework, ACS Sustain. Chem. Eng. 7 (2019) 5776–5783. https://doi.org/10.1021/acssuschemeng.8b05306.

[24] K. Sagarik, M. Phonyiem, C. Lao-Ngam, S. Chaiwongwattana, Mechanisms of proton transfer in Nafion®: Elementary reactions at the sulfonic acid groups, Phys. Chem. Chem. Phys. 10 (2008) 2098–2112. https://doi.org/10.1039/b718480h.

Chapter 4

Robust ionic liquid@MOF composite as a versatile superprotonic conductor

4.1. Introduction

Ionic Liquids (ILs) are organic salts known as efficient charge transfer agents owing to their low volatility, wide liquid range, good ionic conductivity and high thermal/chemical stability.[1] They have been successfully incorporated in the MOF pores (IL@MOF) for the development of conductors applicable to different fields including Li or Na batteries, redox flow batteries and PEMFC.[2,3,12–20,4–11] Regarding proton conducting IL@MOFs, imidazolium based-ILs were mainly explored with the consideration of a variety of counter ions, e.g. halogen,[2,17] sulfonate,[10] dicyanamide [14] and thiocyanate [7] in order to tune their chemical compatibility with the MOF matrices. Incorporation of binary ILs in the MOF pores were also envisaged resulting in Brønsted acid–base buffers shown to introduce both H^+-source and H^+-defect sites promoting the H^+ hopping process.[8,10,11] In these previous works, ILs were mostly impregnated in microporous MOFs, including NH_2-MIL-53(Cr),[2] ZIF-8(Zn),[3] UiO-67(Zr) [4,17] among others,[5–9] while mesoporous MOFs e.g. MIL-101(Cr) [10–13] or PCN-777(Zr) [14] were considered to enable high IL loadings. In comparison with the behavior of the bulk ILs, the proton transport properties of the confined ILs were found to be enhanced as a result of the optimal spatial distribution of ILs within the MOF pores. Notably the MOFs matrices considered so far do not exhibit any relevant intrinsic proton conductivity. Moreover, it is worth noting that ZIF-8(Zn) and UiO-67(Zr) do not exhibit a good chemical stability in aqueous solution and/or water vapor,[21–23] which strongly limits their practical use in PEMFC applications under hydration conditions. As a consequence, these composites were mostly investigated under anhydrous conditions with protonic conductivity reaching 10^{-2} S.cm^{-1} at 343 K,[14] while only a very few of them were tested under humid conditions, but restricted to low RH level (RH ≈ 25%) to most probably avoid IL leaching and/or MOF degradation. In the latter case, protonic conductivity of range [3×10^{-5} - 4×10^{-2} S.cm^{-1}] were recorded at T < 353 K.[2,3,12,13,17,4–11]

Herein, MOF is aimed to act not only as a host scaffold of IL but also as a source of acidic protons. Therefore, we selected the mesoporous MIL-101(Cr)-SO_3H that combines i) mesoporous cages to confine a large amount of ILs, ii) sulfonic acid functionalized terephthalate linkers with Brønsted acid functions able to deliver protons and iii) an excellent chemical and thermal stability. This sulfonic acid-functionalized MOF was previously shown to exhibit high H^+ conductivity under humid conditions.[24–26] Regarding the IL, 1-Ethyl-3-methyl Imidazolium chloride

(EMIMCl) was chosen as its loading in the UiO-67(Zr) pores led to attractive proton conductivity performance at the anhydrous state.[17] Remarkably the protonic conductivity of the resulting composite, labelled EMIM@MIL-101-SO_3H, was found to be amongst the highest values reported so far for IL@MOF composites at the anhydrous state ($\sigma_{(473\ K)}= 1.5 \times 10^{-3}$ S.cm^{-1}). Decisively, this composite also exhibits an unprecedented protonic conductivity under low/mild humidity conditions ($\sigma > 1.0 \times 10^{-1}$ S.cm^{-1} at 343 K for RH = [60%-80%]). This makes EMIM@MIL-101-SO_3H as an optimal versatile superprotonic conductor for future PEMFC applications operating under a variety of working conditions for both mobile and transportation power applications.

4.2. Materials and methods

4.2.1. Synthesis of MIL-101(Cr)-SO_3H

The synthesis of MIL-101(Cr)-SO_3H was performed by our collaborators, Prof. N. Strunou from ILV, following the procedure reported previously.[27] 400 mg of $Cr(NO_3)_3 \cdot 9H_2O$ (1 mmol) and 840 mg of 2-sulfoterephthalic acid (3 mmol, BDC-SO_3H) were dissolved in 5 mL of 27 mM tetramethylammonium hydroxide (TMAOH) solution. This reaction mixture was heated in a 15 mL Teflon reactor under autogenous pressure at 463 K for 24 h. After cooling down to room temperature and centrifugation, the solid product was washed three times with water and three times with absolute ethanol. The resulting material was stored in ethanol.

MIL-101(Cr)-SO_3H is a mesoporous 3D MOF, isostructural as MIL-101(Cr). It is comprised of trimeric chromium (III) octahedral clusters interconnected by 2-sulfonic-1,4-benzene dicarboxylic acid (2-SO_3H-BDC) molecules resulting in an MTN zeotype structure (Figure 4.1). It is comprised of two types of mesoporous cages. As reported,[27] it shows excellent hydrothermal and chemical stability with highly dense and uniform acidic sites, which makes it attractive for the immobilization of microperoxidase 8 (MP8) dedicated to heterogeneous biocatalytic purposes.

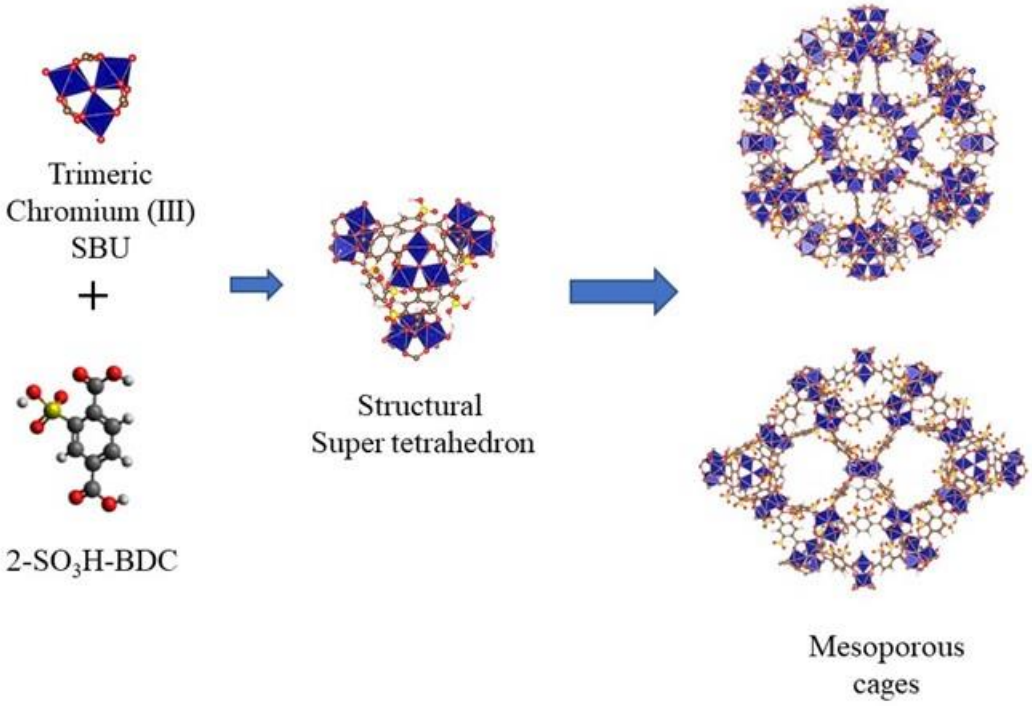

Figure 4.1 – Schematic representation of MIL-101(Cr)-SO_3H.

4.2.2. Preparation of EMIM@MIL-101-SO_3H

A saturated solution of 1-Ethyl-3-Methyl Imidazolium Chloride (EMIMCl) was prepared by introducing 6500 mg (44.3 mmol) of EMIMCl in 5 mL of aqueous solution, while the pH was fixed at 3. 900 mg (1 mmol) MIL-101(Cr)-SO_3H was suspended in the EMIMCl saturated solution and stirred magnetically for 24 h at room temperature. The solid was filtered, washed using 4 mL of methanol solution and dried at 373 K for 8 hr.

4.2.3. Characterization of EMIMCl, MIL-101(Cr)-SO_3H, EMIM@MIL-101-SO_3H

The Powder X-ray diffraction (PXRD) patterns of MIL-101(Cr)-SO_3H and EMIM@MIL-101-SO_3H were collected on a PANalytical X'Pert diffractometer equipped with an X'Celerator detector (λ =1.5406 Å), with an operating voltage of 40 kV and a beam current of 30 mA.

EA of MIL-101(Cr)-SO_3H and EMIM@MIL-101-SO_3H was performed using a Flash EA 1112 (Thermofinnigan) apparatus.

Nitrogen sorption measurements were performed at 77 K using a Micromeritics, Tristar 3000 analyzer. MIL-101(Cr)-SO_3H and EMIM@MIL-101-SO_3H were out-gassed by heating at 393 K for 16 h under vacuum (<10^{-5} Torr) before N_2 physisorption measurements.

Scanning Electron Microscopy SEM images were recorded on gold coated MIL-101(Cr)-SO_3H and EMIM@MIL-101-SO_3H samples using a JEOL JSM-7001F microscope equipped with an energy-dispersive X-ray (EDX) spectrometer with a X-Max SDD (Silicon Drift Detector) by Oxford.

Infrared spectra were recorded on EMIMCl, MIL-101(Cr)-SO_3H and EMIM@MIL-101-SO_3H using a FTIR Magna 550 Nicolet spectrophotometer using the technique of pressed KBr pellets at a resolution of 4 cm^{-1}.

Thermogravimetric Analysis (TGA) coupled with Mass spectroscopy (TGA-MS) measurements were collected on EMIM@MIL-101-SO_3H using a STA 449 F1 Jupiter - QMS 403D Aëolos Netzsch system, from 298 K to 973 K under heating (q = 2 $K.min^{-1}$) and 100 mL min^{-1} of an Argon flow. TGA measurements of EMIMCl and MIL-101(Cr)-SO_3H were equally carried out under O_2 flow.

Differential Scanning Calorimetry (DSC) experiments were carried out on EMIMCl and EMIM@MIL-101-SO_3H using a DSC 1 device from METTLER TOLEDO, in sealed Al-pans (40 mL) under dried N_2 atmosphere (250 mL min^{-1}). EMIM@MIL-101-SO_3H was in-situ heated at 473 K for 2 h, before recording the signal under subsequent cooling (from 373 K to 150 K) and heating (from 150 K to 373 K) using a ramp of 7 $K.min^{-1}$.

The water sorption isotherm was measured on EMIM@MIL-101-SO_3H using a DVS gravimetric sorption system (from Surface Measurement systems). The apparatus was automatically operated to precisely control the water vapor pressure (0-95 RH%) and temperature (303 K). Prior to adsorption experiments, the samples were dehydrated at 423 K for 8 h under high vacuum (< 10^{-6} torr).

Impedance measurements of EMIMCl, MIL-101(Cr)-SO_3H and EMIM@MIL-101-SO_3H were performed on a Broadband Dielectric Spectrometer, Novocontrol alpha analyzer, over a frequency range from 10^{-2} Hz to 1 MHz with an applied ac voltage of 20 mV. Measurements were collected on the anhydrous EMIM@MIL-101-SO_3H, after a preliminary in situ heating at 473 K

for 2 h under nitrogen flow. According to TGA results (see results and discussion part), the solid is fully dehydrated, while no IL release occurs under these operating conditions. Measurements were equally undertaken on the humidified solid, which was introduced into an Espec Corp. SH-221 incubator, to control the temperature 298 < T (K) < 363 and the relative humidity 40 < RH (%) < 95. The solid was equilibrated for 24 hr at given T and RH values, to ensure fixed water content before recording the impedance. The measurements were performed using powders introduced in the home-made sample holder mentioned in Chapter 2. All data are discussed in the following section.

4.3. Result and discussion

MIL-101(Cr)-SO_3H was fully characterized by combining PXRD, Fourrier-Transform Infra-red (FT-IR), Thermogravimetric Analysis (TGA) and N_2 adsorption. According to the elemental analysis, 68% of the organic linker of the MOF was functionalized by –SO_3H groups (Table 4.1).

Table 4.1 - EA results of MIL-101(Cr)-SO_3H and EMIM@MIL-101-SO_3H.

MIL-101(Cr)-SO_3H		
% exp (wt%)		Weight ratio, m(C)/m(S) = 4.34
C	27.93	-SO_3H functionalization degree = 68.6%
S	6.43	
EMIM@MIL-101-SO_3H before PC measurements		
% exp (wt%)		Weight ratio, m(C)/m(N) = 3.61
C	34.7	
N	9.6	
EMIM@MIL-101-SO_3H after PC measurements recorded at 298 K-473 K / 0% RH		
% exp (wt%)		Weight ratio, m(C)/m(N) = 3.66
C	37.4	
N	10.2	
EMIM@MIL-101-SO_3H after PC measurements recorded at 343 K / 80% RH for 6 days		
% exp (wt%)		Weight ratio, m(C)/m(N) = 3.67
C	35.6	
N	9.7	

The EMIM@MIL-101-SO_3H composite was further prepared at room temperature through post-impregnation method, using a saturated solution of EMIMCl (see 4.2.2.). As illustrated in

Figure 4.2, the PXRD pattern of the composite displays the characteristic Bragg peaks of MIL-101(Cr)-SO_3H, thereby showing that the crystalline structure of the MOF is preserved upon EMIMCl impregnation. Noteworthy, the lower intensity of the Bragg peaks at low angles for EMIM@MIL-101-SO_3H results from the modification of the electron density in the MOF pores and a disordered distribution of the EMIMCl confined in the mesoporous cages of the MOF,[14–16,26] as previously reported for $CaCl_2$/MIL-101(Cr) and $SrBr_2$/MIL-101(Cr) composites.[28,29]

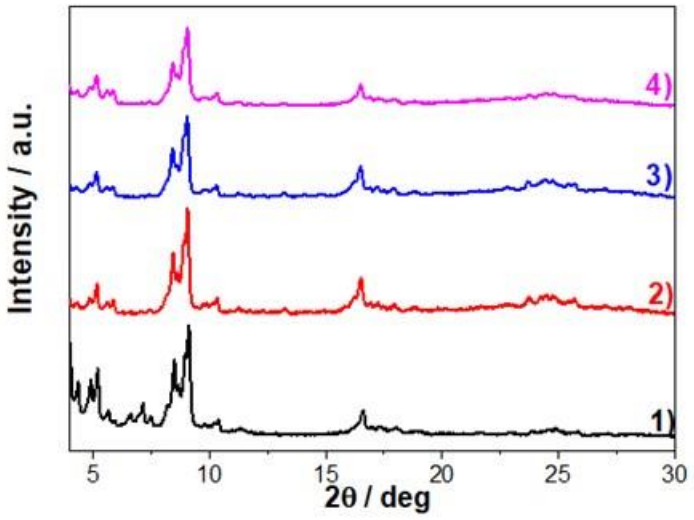

Figure 4.2 - PXRD patterns of **(1)** the pristine MIL-101(Cr)-SO_3H, **(2)** EMIM@MIL-101-SO_3H before conductivity measurements, **(3)** EMIM@MIL-101-SO_3H after conductivity measurements recorded in the temperature range of 273-473 K and **(4)** EMIM@MIL-101-SO_3H after conductivity measurements recorded at 363 K and RH ranging from 35% to 80%.

The SEM images of the EMIM@MIL-101-SO_3H composite showed that the morphology of MOF crystallites is not altered after the IL impregnation (Figures 4.3 and 4.4). SEM and SEM-XEDS confirmed that there is no recrystallized EMIM salt at the outer surface of MOF particles. This is fully consistent with the PXRD pattern of the composite, showing the absence of any Bragg peaks that can be assigned to the recrystallized EMIMCl salt. This indicates that EMIMCl is exclusively confined in the mesopores of MIL-101(Cr)-SO_3H. An EMIMCl loading of ~42±5 wt% was determined by combining elemental analysis and SEM-XEDS. (C = 34.7±0.3 wt%; N = 9.6±0.3 wt%; S = 3.2±0.3 wt%; Cr = 6.5±0.3 wt%; Cl = 10.5±0.3 wt%).

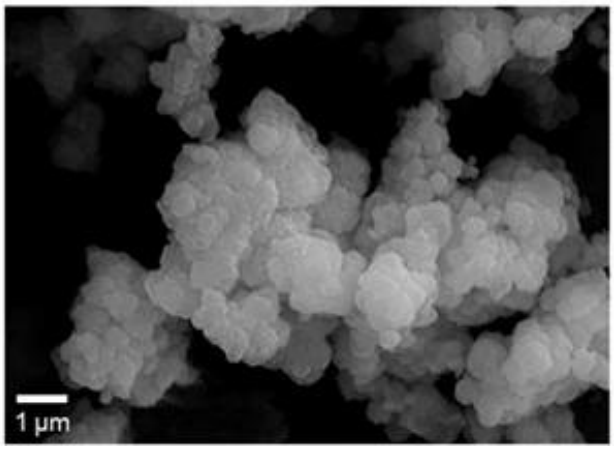

Figure 4.3 - SEM image of MIL-101(Cr)-SO_3H.

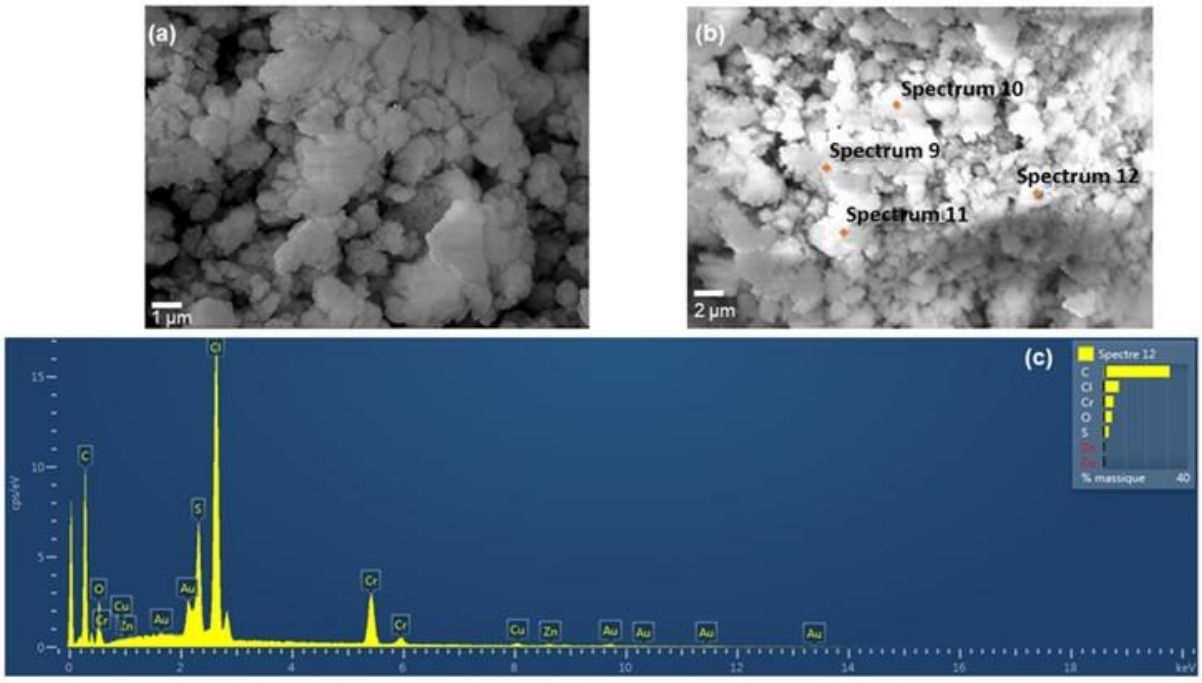

Figure 4.4 – a) and b) SEM images of EMIM@MIL-101-SO_3H and **c)** XEDS spectrum of EMIM@MIL-101-SO_3H in the case of (b).

N_2 sorption isotherms revealed that the composites adsorb only a negligible amount of N_2. This is consistent with the adsorption of a large amount of EMIMCl in both mesoporous cages of MIL-101(Cr)-SO_3H (Figure 4.5).

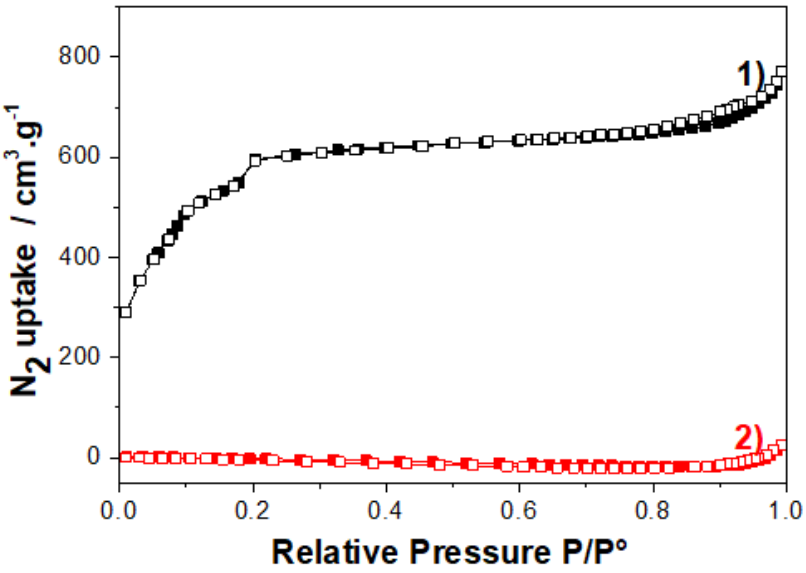

Figure 4.5 - Nitrogen sorption isotherms of **(1)** MIL-101(Cr)-SO_3H and **(2)** EMIM@MIL-101-SO_3H: filled and empty symbols correspond to the adsorption and the desorption branches, respectively.

The thermal stability of EMIM@MIL-101-SO_3H was investigated using TGA coupled with Mass Spectrometry (TGA-MS) (Figure 4.6). The first weight loss is assigned to the departure of water in agreement with the increase of the Evolved Gas Analysis signal (EGA) specific to H_2O (m/z = 17 and 18). The sharp weight loss decrease observed in the [500 K – 550 K] temperature range corresponds to the thermal decomposition of the incorporated EMIMCl, as shown by the characteristic fragments of the IL (m/z = 15, 29, 50, 52 and 64 for -CH_3/NH, C_2H_5, CH_3Cl from ^{35}Cl, CH_3Cl from ^{37}Cl and C_2H_5Cl from ^{35}Cl respectively, while the m/z = 66 signal assigned to C_2H_5Cl from ^{37}Cl is negligible in relation with the lower natural abundance of isotope ^{37}Cl versus ^{35}Cl).[30,31] Interestingly, the EMIM@MIL-101-SO_3H degradation occurs in the same temperature domain as that observed for the decomposition of the bulk IL and MIL-101(Cr)-SO_3H (Figure 4.7). For 550 K < T < 650 K, EMIMCl degradation occurs concomitantly with that of the organic linker of the MOF, while the weight loss observed in the [650 K – 750 K] temperature domain results from the complete degradation of the MOF framework. Remarkably, EMIM@MIL-101-SO_3H, exhibits a higher thermal stability (up to 500 K) than most of the previously reported IL@MOFs,[3,11,12,14] which makes this composite applicable in the target intermediate temperature domain. Figure 4.7 (b) represents TGA curves for the pristine MOF.

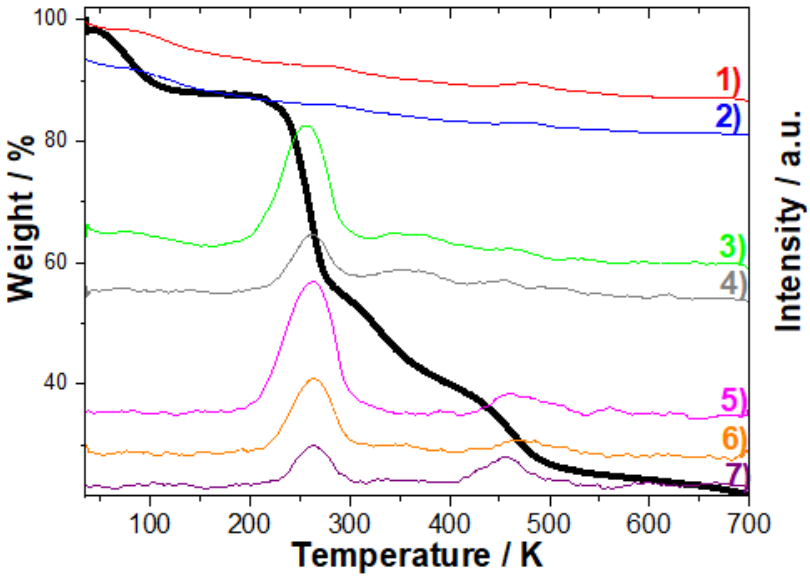

Figure 4.6 - TGA plot (wt%) of EMIM@MIL-101-SO_3H and the corresponding EGA curves specific to fragments of water and EMIMCl: lines 1, 2, 3, 4, 5, 6 and 7 refer to m/z = 17, 18, 15, 29, 50, 52 and 64 respectively.

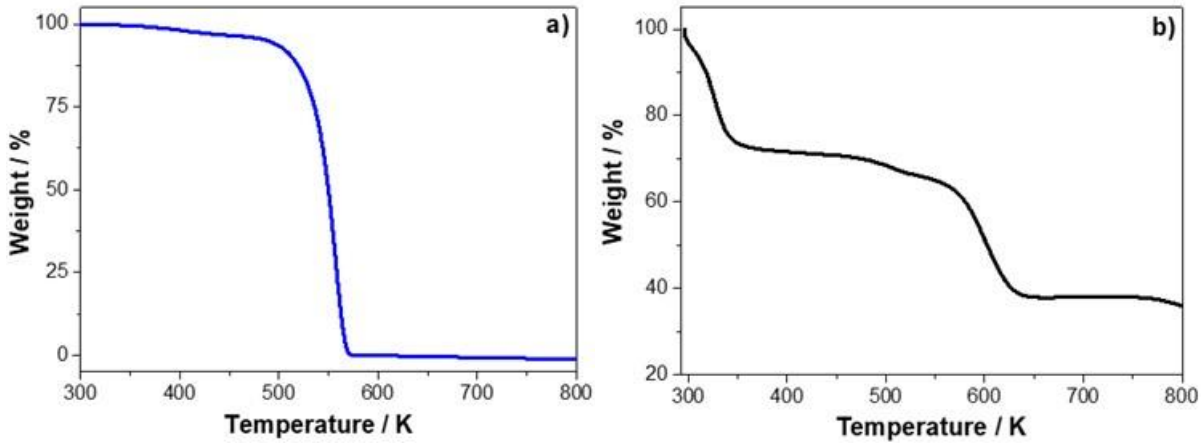

Figure 4.7 - TGA curve (wt%) of **a)** bulk EMIMCl and **b)** MIL-101(Cr)-SO_3H.

To further evidence that EMIMCl is confined in the MOF pore, DSC thermogram of the bulk IL was compared to that of the composite EMIM@MIL-101-SO_3H (Figure 4.8). Upon heating from 183 K to 383 K, the bulk IL exhibits one endothermic peak around 220 K, corresponding to the glass transition ($Tg_{(EMIMCl)}$), followed by the cold crystallization exothermic peak centered around 260 K.[32] The endothermic peak observed at 346 K coincides with the EMIMCl melting point.[30,31,33] In contrast, the DSC signal of EMIM@MIL-101-SO_3H shows

a flat response in the whole temperature range, in line with the absence of a IL phase change due to confinement effects. This behavior is consistent with that observed for ILs confined in porous solids [3,17,34,35] and thus confirms the adsorption of IL in the MIL-101(Cr)-SO_3H pores and not at the outer surface of MOF particles as also supported by PXRD and SEM-EDX analysis discussed above.

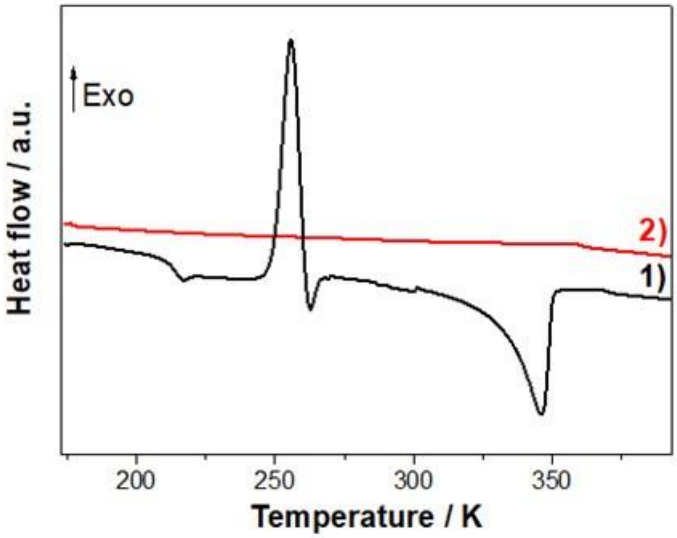

Figure 4.8 - DSC heating profiles of **(1)** EMIMCl and **(2)** EMIM@MIL-101-SO_3H.

It further supports that the confined EMIMCl behaves as a glassy liquid across the whole temperature range.[36] The specific electrostatic interactions between $EMIM^+$ cations and Cl^- anions in this glass-like liquid state combined with the EMIM/MOF and Cl/MOF interactions make the IL difficult to be released from the porosity compared with other single molecular guests.[17] The EMIM@MIL-101-SO_3H composite was also characterized by FT-IR spectroscopy (Figure 4.9). The complete assignment of the main vibration bands is given in Table 4.2. The FT-IR spectrum of EMIM@MIL-101-SO_3H does not show any significant shift of the vibration bands in comparison with those of the pure MOF and EMIMCl. This suggests weak Van der Waals and hydrogen interactions between the two components. However, it is well known that coordinatively unsaturated Cr sites (CUS) of MIL-101(Cr) can covalently interact with N-donor ligands.[37,38] In particular, the covalent grafting of methylimidazole onto the Cr CUS of MIL-101(Cr) was previously demonstrated by combining multiple spectroscopic techniques (EPR, UV-Vis, FT-

IR).[37] It can thus be assumed that the imidazole ring of EMIMCl is also covalently grafted onto the Cr site of MIL-101(Cr)-SO_3H.

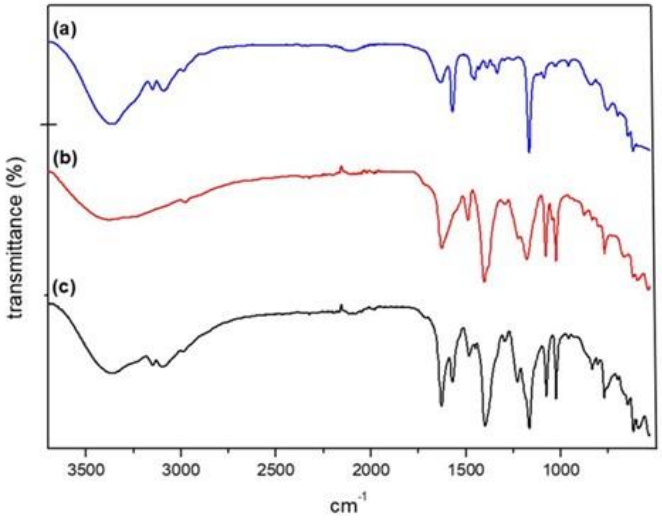

Figure 4.9 - FT-IR spectra of **a)** EMIMCl, **b)** MIL-101(Cr)-SO_3H, **c)** EMIM@MIL-101-SO_3H.

Table 4.2 - Main FT-IR vibration bands of EMIMCl, MIL-101(Cr)-SO_3H and EMIM@MIL-101-SO_3H with the corresponding assignment.

Vibration bands cm^{-1}			**Assignment**
MIL-101(Cr)-SO_3H	**EMIMCl**	**EMIM@MIL-101-SO_3H**	
	3151	3148	ν(C-H)
	3083	3088	ν (C-H)
1628	1630	1628	ν(C-O) as + δ(H-O-H)
	1574	1568	Imidazole skeleton
1485		1479	ν(C-O)s
	1448	1450	Imidazole skeleton
1403		1397	ν(S=O) as
	1330		Imidazole skeleton
1178	1167	1166	ν(S=O) s + Imidazole skeleton
1077		1077	ν(S-O)
1026		1026	ν(S-O)
840		840	ν(Cr-O)
773		773	ν(C-S)

AC impedance measurements were first recorded on EMIM@MIL-101-SO_3H at the anhydrous state. The composite was preliminary *in situ* heated for 2 h at 473 K under nitrogen flow to avoid the IL degradation, as evidenced by TGA (Figure 4.6). The real (Z') and imaginary (Z") parts of the impedance are depicted in the Nyquist plots (Figure 4.10) and listed in Table 4.3. With increasing the temperature, the impedance drastically decreases and the typical semi-circle profile in the low temperature domain is dominated by the capacitive tail associated with the protonic conductivity of the composite. This trend is much more pronounced than that observed for the bulk EMIMCl (Figure 4.11) and sharply contrasts with the insulating behavior of the MOF (no semi-circle profile combined with high impedance values, e.g., $Z > 10^{12}$ Ohm whatever T, Figure 4.12). This observation supports a change of the MOF electrical behavior upon the adsorption of the IL, which allows the long-range transport of the H^+ issued from the $–SO_3H$ functions of the MOF. The total impedance of EMIM@MIL-101-SO_3H was extrapolated from the low frequency end intercept of the arc on the real axis or from the linear region of the capacitive tail to the real axis, according to the Nyquist plot profile.

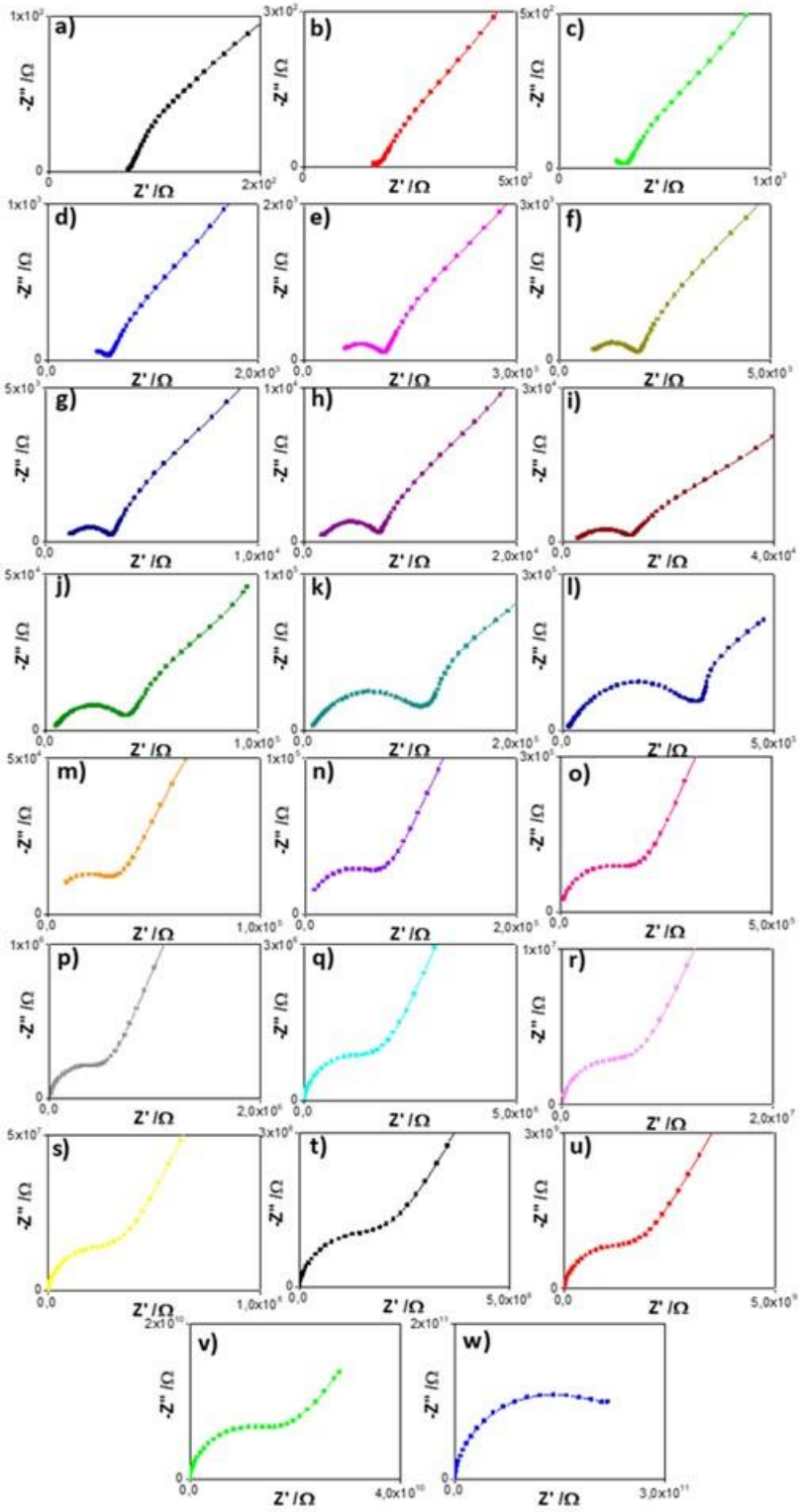

Figure 4.10 - Nyquist plots of the impedance for the dehydrated EMIM@MIL-101-SO_3H powder recorded under 0% RH, at **a)** 473 K, **b)** 463 K, **c)** 453 K, **d)** 443 K, **e)** 433 K, **f)** 423 K, **g)** 413 K, **h)** 403 K, **i)** 393 K, **j)** 383 K, **k)** 373 K, **l)** 363 K, **m)** 353 K, **n)** 343 K, **o)** 333 K, **p)** 323 K, **q)** 313 K, **r)** 303 K, **s)** 293 K, **t)** 283 K, **u)** 273 K, **v)** 263 K and **w)** 253 K.

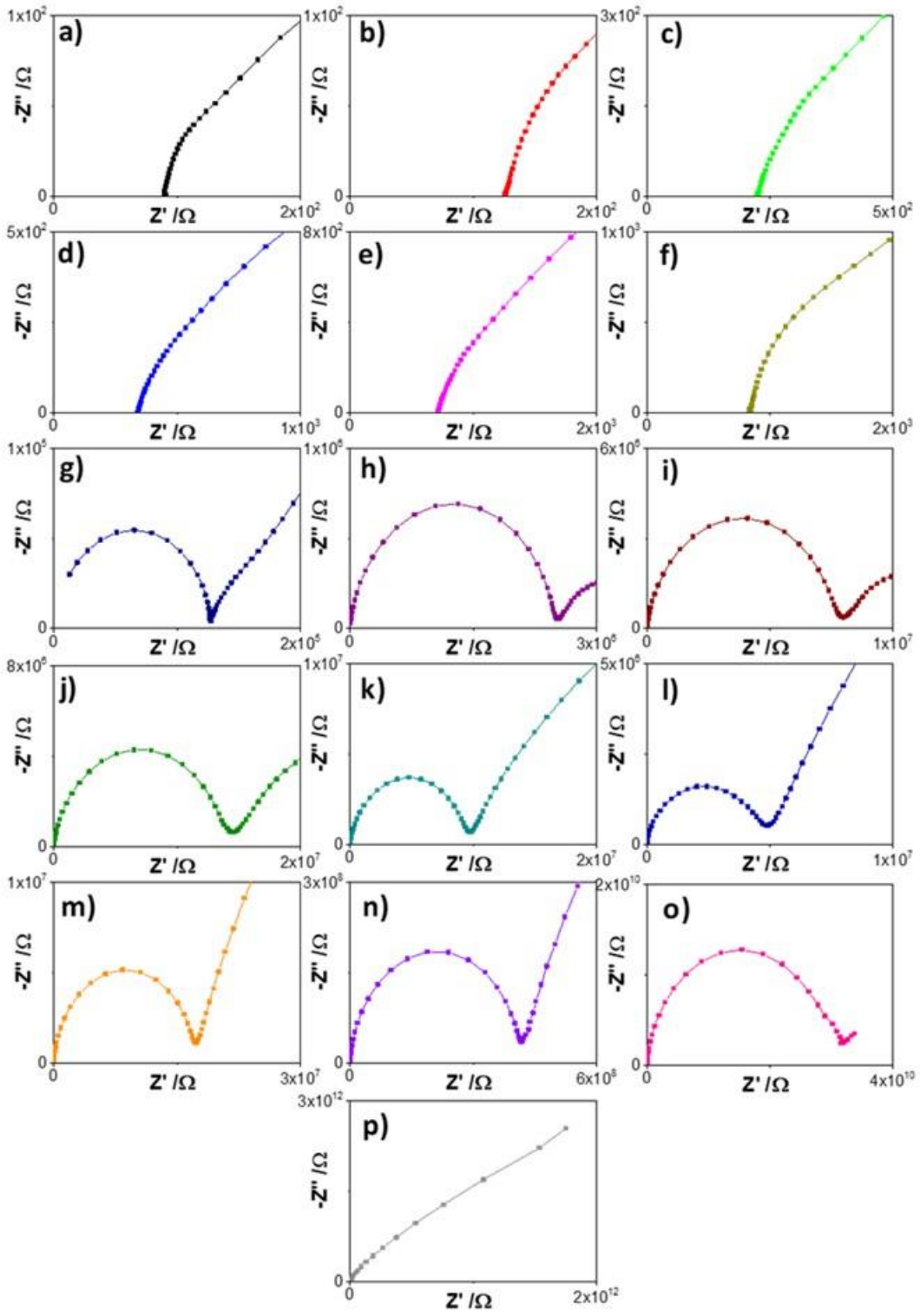

Figure 4.11 - Nyquist plots of the impedance for the bulk EMIMCl recorded under 0% RH, at **a)** 323 K, **b)** 313 K, **c)** 303 K, **d)** 293 K, **e)** 283 K, **f)** 273 K, **g)** 263 K, **h)** 253 K, **i)** 243 K, **j)** 233 K, **k)** 223 K, **l)** 213 K, **m)** 203 K, **n)** 193 K, **o)** 183 K and **p)** 173 K.

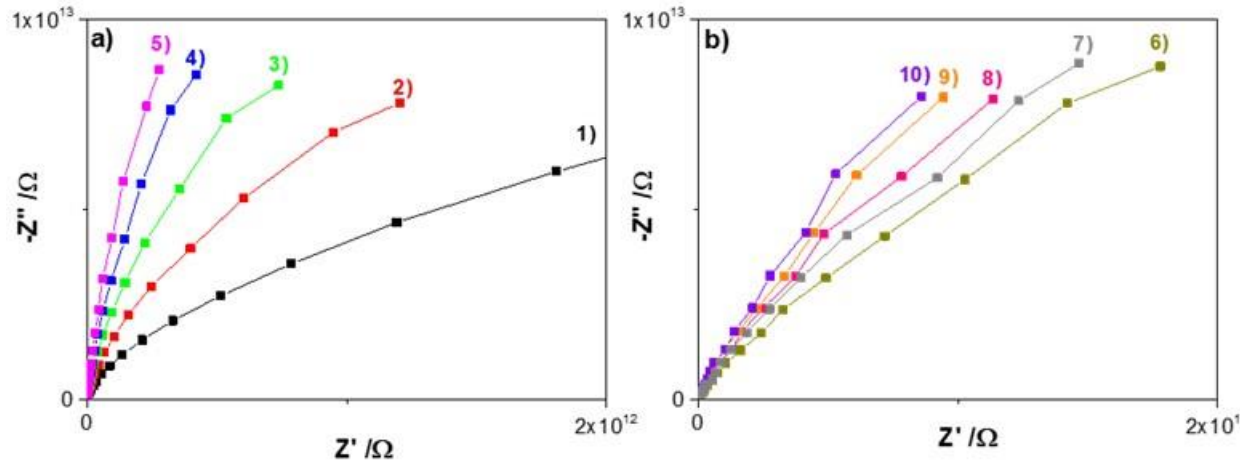

Figure 4.12 - Nyquist plots of the impedance for the dehydrated MIL-101(Cr)-SO_3H recorded under 0% RH, at (**1**) 393 K, (**2**) 383 K, (**3**) 373 K, (**4**) 363 K, (**5**) 353 K, (**6**) 343 K, (**7**) 333 K, (**8**) 323 K, (**9**) 313 K and (10) 303 K.

Table 4.3 - Conductivity values deduced from the Nyquist plots, for EMIMCl and the anhydrous EMIM@MIL-101-SO_3H powders at different T conditions. l and S are the sample thickness and surface.

Anhydrous EMIM@MIL-101-SO_3H RH = 0% (l = 0.044 cm, S = 0.3631 cm^2)							
T / K	**σ / S.cm^{-1}**	**T / K**	**σ / S.cm^{-1}**	**T / K**	**σ / S.cm^{-1}**	**T / K**	**σ / S.cm^{-1}**
473	1.6 x 10^{-3}	463	7.2 x 10^{-4}	453	4.0 x 10^{-4}	443	3.0 x 10^{-4}
433	2.0 x 10^{-4}	423	1.4 x 10^{-4}	413	9.8 x 10^{-5}	403	6.4 x 10^{-5}
393	4.1 x 10^{-5}	383	2.4 x 10^{-5}	373	1.4 x 10^{-5}	363	7.4 x 10^{-6}
353	3.5 x 10^{-6}	343	1.4 x 10^{-6}	333	5.1 x 10^{-7}	323	2.0 x 10^{-7}
313	6.6 x 10^{-8}	303	1.5 x 10^{-8}	293	2.9 x 10^{-9}	283	4.8 x 10^{-10}
273	6.0 x 10^{-11}	263	6.0 x 10^{-12}	253	5.1 x 10^{-13}	243	5.9 x 10^{-14}
Bulk EMIMCl RH = 0% (l = 0.098 cm, S = 0.3631 cm^2)							
T / K	**σ / S.cm^{-1}**	**T / K**	**σ / S.cm^{-1}**	**T / K**	**σ / S.cm^{-1}**	**T / K**	**σ / S.cm^{-1}**
323	3.0 x 10^{-3}	313	2.1 x 10^{-3}	303	1.2 x 10^{-3}	293	7.9 x 10^{-4}
283	5.0 x 10^{-4}	273	3.2 x 10^{-4}	263	2.1 x 10^{-6}	253	1.4 x 10^{-7}
243	2.8 x 10^{-8}	233	2.5 x 10^{-8}	223	2.8 x 10^{-8}	213	5.5 x 10^{-8}
203	1.9 x 10^{-8}	193	6.5 x 10^{-10}	183	8.5 x 10^{-12}		

As demonstrated,[39,40] the extrapolation procedure for analyzing Nyquist plots is perfectly suitable for determining the impedance of the system, as well as the equivalent circuits fitting approach or Bode representation. The conductivity, σ, was furthermore deduced from the formula $\sigma = \frac{1}{Z} * \frac{l}{S}$, where l and S are the sample thickness and area, respectively. The temperature dependence of the conductivity for EMIMCl and EMIM@MIL-101-SO_3H exhibits distinct behaviors (Figure 4.13), in agreement with the typical DSC profiles of both respective solids (Figures 4.9). For bulk EMIMCl, the conductivity increase with the temperature is disrupted in the [220 K – 270 K] temperature range, consistent with the glass transition and the crystallization of the IL as shown by the DSC experiments. By contrast, the conductivity of EMIM@MIL-101-SO_3H steadily rises with the temperature, in line with the absence of phase changes for the confined IL up to 473 K. The conductivity of EMIMCl in bulk phase is higher than in confined phase in the whole temperature domain, in relation with the higher viscosity of the system.[36]

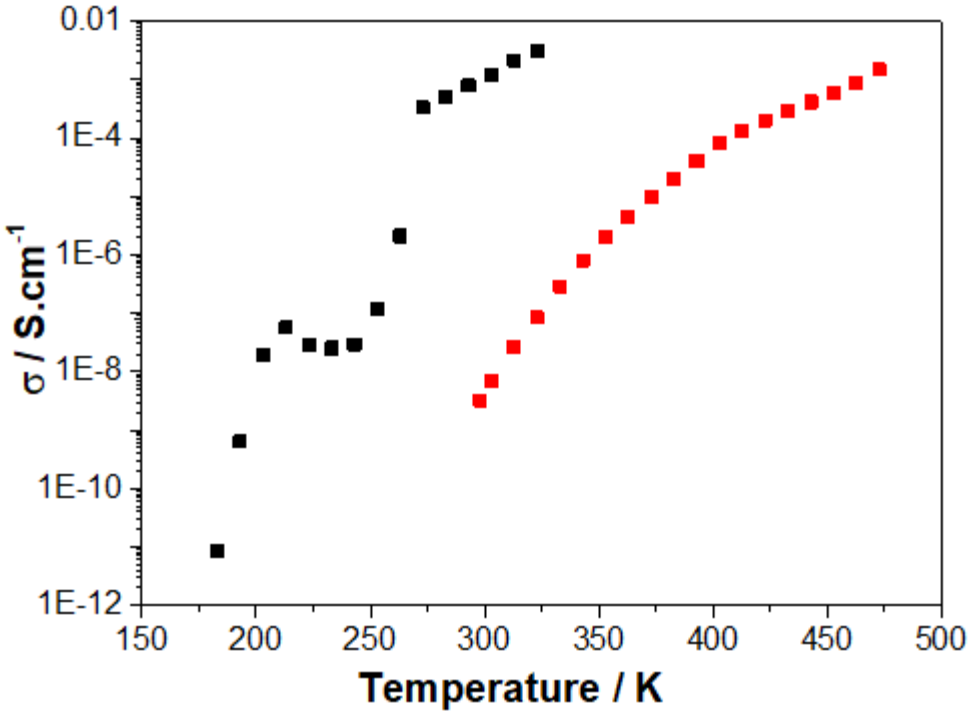

Figure 4.13 - Temperature dependence of the conductivity for EMIMCl (black) and EMIM@MIL-101-SO_3H (red) at the anhydrous state in the temperature range of 180 K-473 K on heating.

In addition, the glassy-like liquid behavior of EMIMCl confined in MIL-101(Cr)-SO_3H is evidenced by the huge decrease of the conductivity with decreasing temperature.[36] For IL localized nearby the MOF pore wall, additional structuring influences arise from the steric constraints and field effects at the interface, impacting the IL viscosity and the resulting charge carrier dynamics.[36] Moreover, the temperature dependence of the conductivity for EMIMCl@MIL-101-SO_3H shown in Figure 4.14 is captured by applying the empirical Vogel–Fulcher–Tammann (VTF) equation: $\sigma T^{1/2} = \sigma_0 exp - [{}^{\Delta E}/_{k(T - T_{0)}}]$, where σ_0 is the conductivity at infinite temperature, k is the Boltzmann constant, ΔE corresponds to the activation energy associated with the proton transfer mechanism and T_0 = $Tg_{(EMIMCl)}$-50, with $Tg_{(EMIMCl)}$ assessed by the DSC experiments (Tg = 218 K). The VTF model typically considered to describe the proton dynamics behavior of bulk ILs [33,41] was equally employed for characterizing the (EMI)[$N(CN)_2$]@PCN-777 composite.[14] The VTF model refers to the inter-relation between the protonic conductivity and the segmental relaxation of the media in which ions are moving. For EMIM@MIL-101-SO_3H, the cooperative conductivity process results from the H^+ transport assisted by the dynamics of the IL involving local motions due to their weak interactions with the MOF framework, as evidenced from IR analysis. The proton dynamics is rather restricted due to confinement effects, as stated by the higher activation energy deduced from the VTF fit parameters for EMIM@MIL-101-SO_3H (ΔE = 0.26 eV) than for bulk EMIMCl (ΔE = 0.04 eV).[41] Noteworthy, the contribution of Cl^- species to the global charge transport process cannot be completely ruled out. Most importantly, as the temperature increases, the protonic conductivity is substantially enhanced from 3.3 x 10^{-9} S.cm^{-1} at 298 K to 1.5 x 10^{-3} S.cm^{-1} at 473 K (Table 4.3), a level of performance comparable with the best proton conducting IL@MOF, i.e. EMIM@UiO-67 (σ = 1.6 x 10^{-3} S.cm^{-1} at 473 K) reported so far as the sole IL@MOF composite stable in the temperature domain explored herein.[2] The comparable performance is certainly fortuitus, as UiO-67 and MIL-101(Cr)-SO_3H display different features in terms of topology, pore diameter, strength of the proton source, pore volume occupancy by EMIMCl, impacting the charge carrier density and mobility. The distinct viscosity of the ionic liquid and specific topology of the H-bonded network connecting the proton donor/acceptor sites involved in both systems are then counter-balanced, resulting in a similar conductivity value recorded at 473 K. Notably the others IL@MOF were not investigated at 473 K due to IL release or MOF degradation.[3,11,12,14] Here we demonstrate that EMIM@MIL-101-SO_3H shows structural integrity and IL retention upon

heating up to 473 K, as evidenced by similar PXRD patterns (Figure 4.2) and EA data (Table 4.1), respectively before and after protonic conductivity measurements.

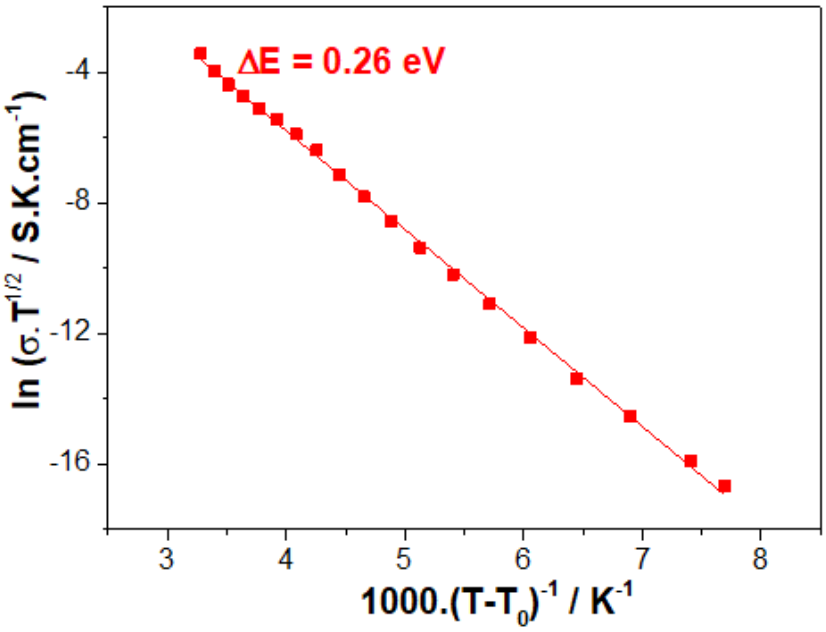

Figure 4.14 - VTF type plot of the conductivity for the EMIM@MIL-101-SO_3H at the anhydrous state, the solid line corresponds to the linear least-square fit.

Impedance measurements were further recorded under humid conditions to introduce additional hydrogen-bonded charge carriers, beneficial for the charge transport. As shown in Figure 4.15, the Nyquist plots of the impedance recorded at 343 K for RH varying from 35% to 80% results from capacitive tails along with very low levels of impedance. The corresponding conductivity values show a peculiar RH dependence (Table 4.4 and Figure 4.16). The conductivity substantially increases at low RH by more than 4 orders of magnitude from RH = 0% (σ = 1.4 x 10^{-6} $S.cm^{-1}$) to RH = 35% (σ = 4.8 x 10^{-2} $S.cm^{-1}$). Note that this sharp σ raise is likely to occur at even lower RH, but was not measurable due to equipment limitations.

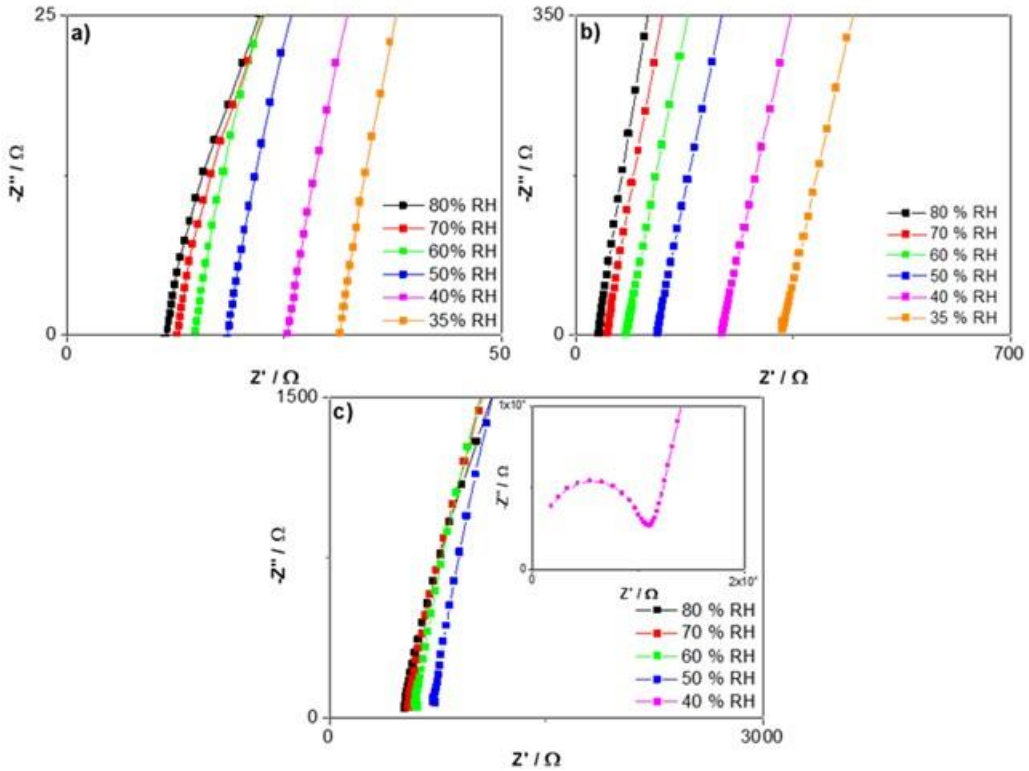

Figure 4.15 - Nyquist plots of the impedance for EMIM@ MIL-101-SO_3H recorded at **a)** 343 K and **b)** 303 K and **c)** MIL-101(Cr)-SO_3H recorded at 343 K for RH varying from 35% to 80%.

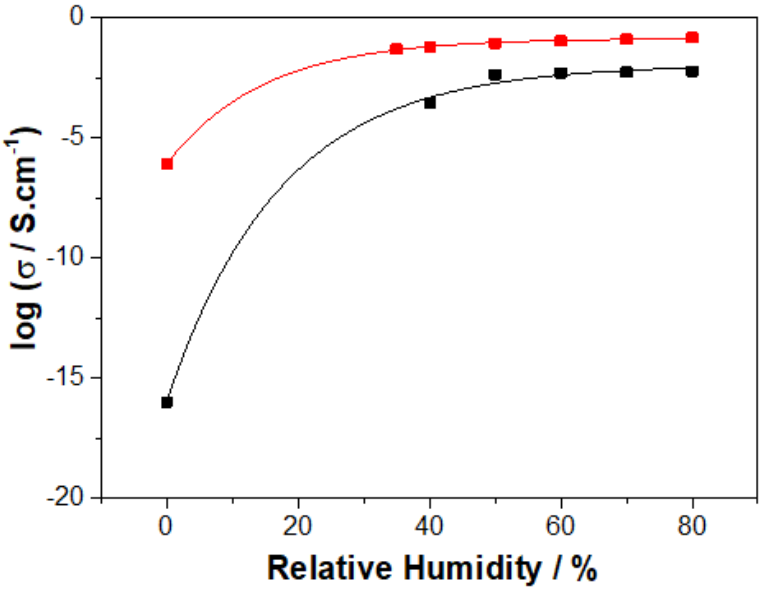

Figure 4.16 - Humidity dependence of the conductivity recorded at 343 K for MIL-101(Cr)-SO_3H (black) and EMIM@MIL-101-SO_3H (red) in the relative humidity range of 0%-80%, lines are exponential fits to guide the eyes.

Table 4.4 - Conductivity values deduced from the Nyquist plots, for MIL-101(Cr)-SO_3H and EMIM@MIL-101-SO_3H powders at different RH/T conditions. l and S are the sample thickness and surface.

Hydrated EMIM@MIL-101-SO_3H							
T = 343 K (l = 0.186 cm, S = 0.1256 cm^2)				**T = 298 K (l = 0.148 cm, S = 0.1256 cm^2)**			
RH / %	**σ / $S.cm^{-1}$**	**RH / %**	**σ / $S.cm^{-1}$**	**RH / %**	**σ / $S.cm^{-1}$**	**RH / %**	**σ / $S.cm^{-1}$**
80	1.4×10^{-1}	70	1.2×10^{-1}	80	3.2×10^{-2}	70	2.3×10^{-2}
60	1.0×10^{-1}	50	8.4×10^{-2}	60	1.4×10^{-2}	50	9.0×10^{-3}
40	6.0×10^{-2}	35	4.8×10^{-2}	40	5.0×10^{-3}	35	3.5×10^{-3}
Hydrated MIL-101(Cr)-SO_3H T = 343 K (l = 0.376 cm, S = 0.1256 cm^2)							
RH / %	**σ / $S.cm^{-1}$**	**RH / %**	**σ / $S.cm^{-1}$**	**RH / %**	**σ / $S.cm^{-1}$**	**RH / %**	**σ / $S.cm^{-1}$**
80	5.6×10^{-3}	70	5.4×10^{-3}	60	5.0×10^{-3}	50	4.2×10^{-3}
40	2.7×10^{-4}						
Hydrated EMIM@MIL-101-SO_3H RH = 80% (l = 0.270 cm, S = 0.1256 cm^2)							
T / K	**σ / $S.cm^{-1}$**	**T / K**	**σ / $S.cm^{-1}$**	**T / K**	**σ / $S.cm^{-1}$**	**T / K**	**σ / $S.cm^{-1}$**
343	1.4×10^{-1}	333	1.3×10^{-1}	323	1.0×10^{-1}	313	8.3×10^{-2}
303	6.4×10^{-2}	298	5.5×10^{-2}				
Hydrated MIL-101(Cr)-SO_3H RH = 80% (l = 0.313 cm, S = 0.1256 cm^2)							
T / K	**σ / $S.cm^{-1}$**	**T / K**	**σ / $S.cm^{-1}$**	**T / K**	**σ / $S.cm^{-1}$**	**T / K**	**σ / $S.cm^{-1}$**
343	5.1×10^{-3}	333	4.3×10^{-3}	323	3.5×10^{-3}	313	2.8×10^{-3}
303	2.1×10^{-3}	298	1.8×10^{-3}				

As previously shown for ILs [42,43] the conductivity enhancement under humidity is related to the decrease of the environment viscosity, resulting from the dissociation of the anion/cation pairs of the IL, and the solvation of ions by water molecules. With increasing RH from 35% to 80%, the conductivity increases by a factor 3 ($\sigma_{343\ K/35\%\ RH} = 4.8 \times 10^{-2}$ $S.cm^{-1}$ and $\sigma_{343\ K/80\%\ RH} = 1.4 \times 10^{-1}$ $S.cm^{-1}$). Noteworthy this typical σ vs RH profile is temperature independent, as shown by the similar trend recorded at 303 K (Figure 4.17). To explain this water-dependent protonic conductivity profile, water adsorption isotherm was recorded at 303 K (Figure 4.18). A low water uptake ($m_{ads} = 0.07\ g_{H2O}.g_{sample}^{-1}$) is observed at very low relative pressure ($P/P_0 < 0.1$) since the composite shows only a limited pore accessibility to H_2O due to the high content of confined EMIMCl.

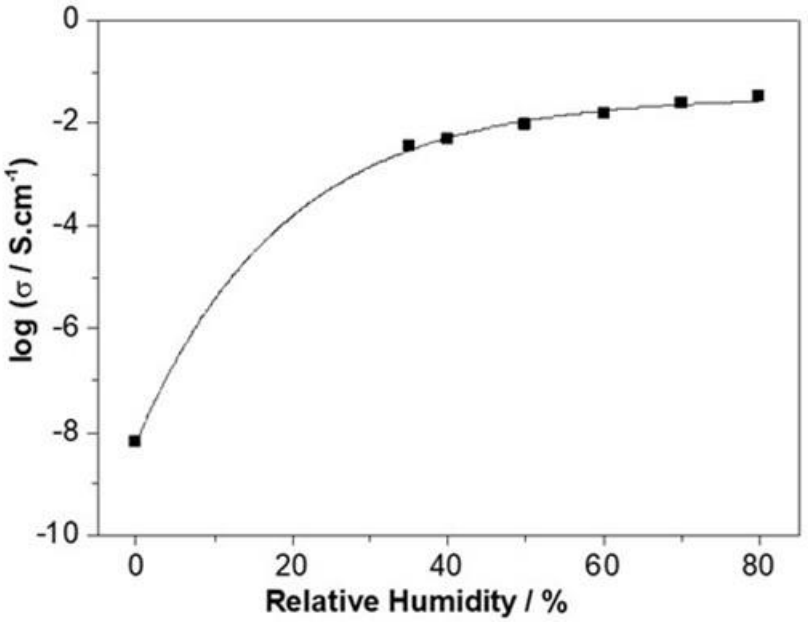

Figure 4.17 - Humidity dependence of the conductivity for EMIM@MIL-101-SO_3H recorded at 303 K. The exponential line is a guide for the eyes.

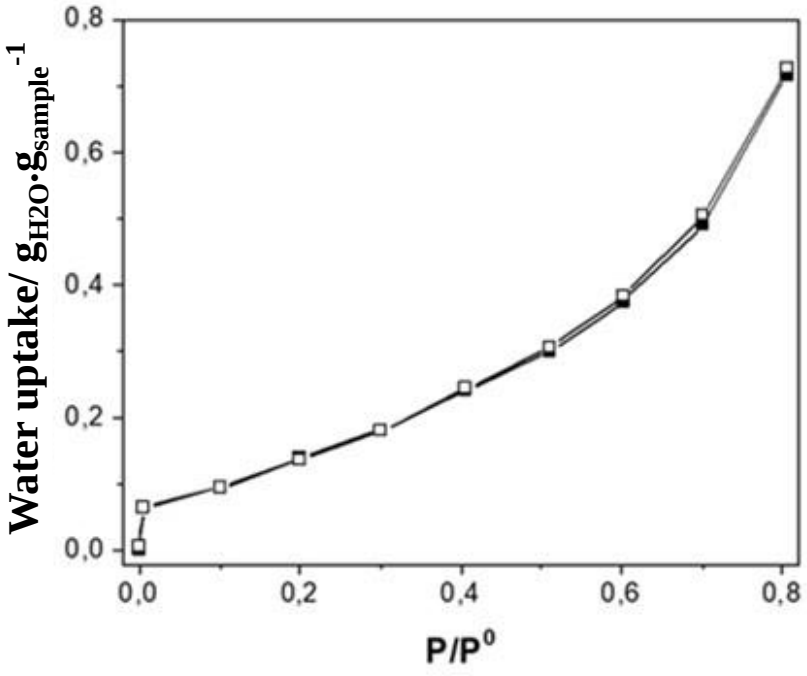

Figure 4.18 - Water sorption isotherm of EMIM@MIL-101-SO_3H recorded at 303 K. Full and empty squares refer to the adsorption and desorption branches, respectively.

However, this water amount is enough to boost the protonic conductivity of the composite observed at low RH. With increasing the relative water pressure from 10% to 80%, the water uptake exponentially rises and the adsorption and desorption branches perfectly match. Both features support that the water molecules are adsorbed at the outer-surface of the MOF in the corresponding RH domain. Assuming that all water molecules behave as charge carriers, the conductivity should follow the trend of the water uptake with increasing RH, as it is defined as $\sigma = n\mu e$, where n, μ and e are the charge carriers density, mobility and charge, respectively. On the opposite, the conductivity increment with RH is negligible compared to the exponential increase of the amount of adsorbed water molecules. This supports that the conductivity performance of the composite mainly results from the charge transport at the internal porosity of the composite, even if the contribution from the water molecules adsorbed at the outer-surface of the material cannot be totally ruled out.

Figure 4.19 reports the temperature-dependence of the protonic conductivity for EMIM@MIL-101-SO_3H and MIL-101(Cr)-SO_3H in the 298-343 K temperature range and RH = 80%, obtained from nyquist plot displayed in Figure 4.20. Both set of data follow the Arrhenius law, $\sigma T = \sigma_0 exp - [{}^{\Delta E}/_{kT}]$, with comparable low activation energy (ΔE = 0.22 eV), in line with an efficient Grotthus-like mechanism of the H^+ propagation since ΔE < 0.40 eV, as mainly observed for water-mediated proton conducting MOFs.[24,40,44–49] As reported in other MOFs,[45,46] protons are assumed to be released from the acidic groups, i.e. the -SO_3H groups, towards neighboring water molecules adsorbed in the pores at low RH. They are further shuttled inside the porosity of the MOF, via the H-bonded network connecting -SO_3H, adsorbed water molecules, $EMIM^+$ cations and Cl^- anions species. This mechanism is assumed to remain the same at higher RH, since the composition of guest molecules, i.e. IL and water contents in the MOF pores, is similar all along the RH domain.[50] One notes that the chloride species solvated by water molecules are likely to contribute to the charge transport mechanism. As previously evidenced for the proton conducting MIP-202(Zr),[40] Cl^- species are able to participate to the hydrogen-bonded network resulting from the interconnection of acidic sources, water molecules and chlorine counter ions. More importantly, ΔE slightly diminishes upon hydration for EMIM@MIL-101-SO_3H (ΔE = 0.26 eV at the anhydrous state), alongside an increase of the protonic conductivity as described above.

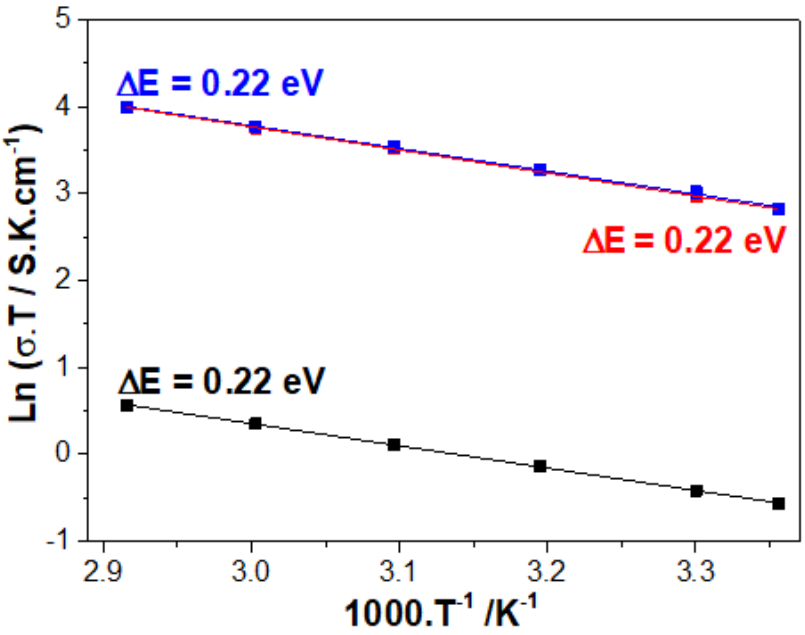

Figure 4.19 - Arrhenius type plot of the conductivity for MIL-101(Cr)-SO_3H (black) and EMIM@MIL-101-SO_3H (red: cycle 1, blue: cycle 2) under 80% RH, the lines correspond to the linear least-square fit.

In addition, the conductivity performance is maintained after 2 cycles, corroborating the absence of any IL leaching in presence of water vapor. Indeed, the exceptional conductivity value recorded at 343 K and 80% RH ($\sigma = 1.4 \times 10^{-1}$ S.cm^{-1}) is maintained over several days, in line with the long-term stability of the composite under operating conditions (Figure 4.21). Accordingly, the comparable PXRD pattern (Figure 4.2) and EA (Table 4.1) of EMIM@MIL-101-SO_3H collected before and after conductivity measurements under humidity state the structural and chemical robustness of EMIM@MIL-101-SO_3H, along with the maintained IL loading under this working condition. Such results are in line with the efficient confinement of the IL in the mesoporous cages of MIL-101(Cr)-SO_3H, even in the presence of water. This is a clear advantage compared to the previously reported MIL-101(Cr)/$CaCl_2$ composites that showed a slight release of the salt.[28,29] The imidazole group of the IL is most probably covalently grafted to the Cr CUS of the MOF as it was previously demonstrated for the 1-methyl imidazole@MIL-101(Cr) by combining multiple complementary UV-vis, FT-IR and NIR spectroscopies.[37]

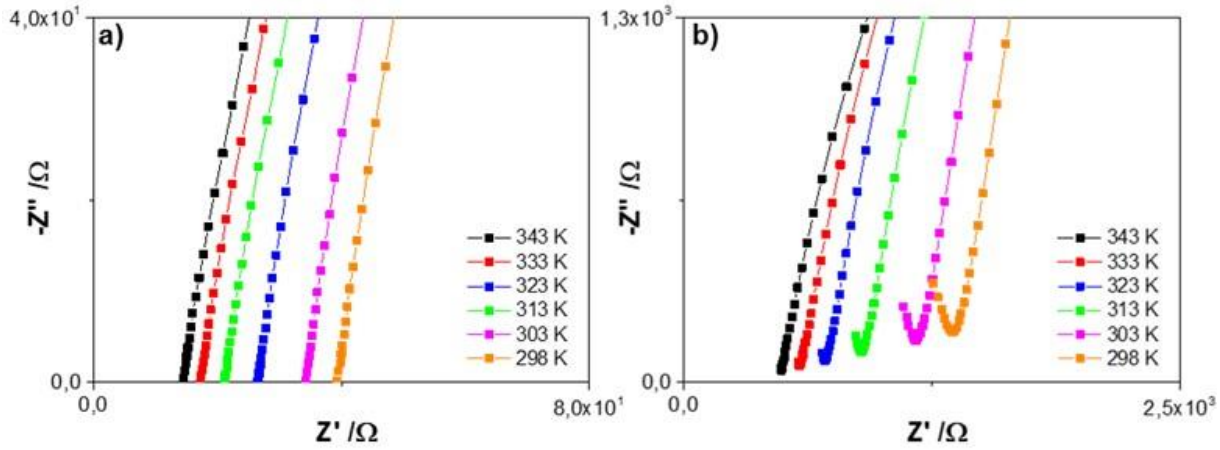

Figure 4.20 - Nyquist plots of the impedance for **a)** EMIM@MIL-101-SO_3H and **b)** MIL-101(Cr)-SO_3H recorded under 80% RH, for T varying from 343 K to 298 K.

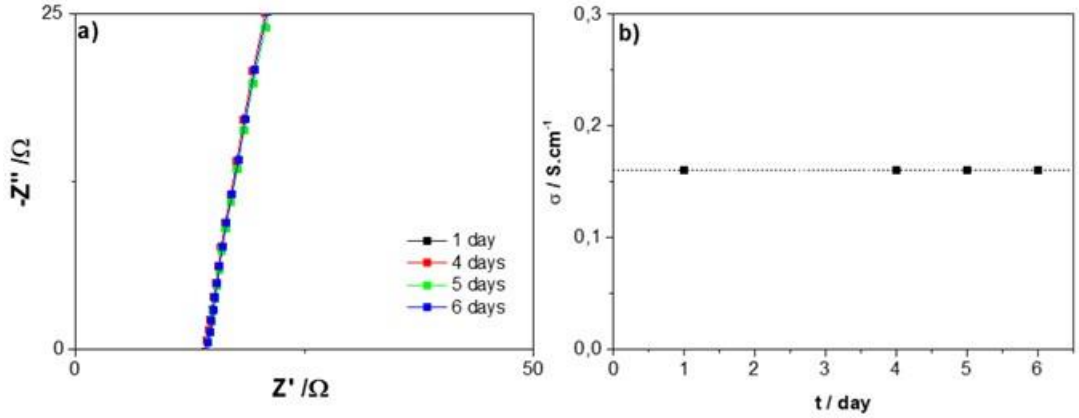

Figure 4.21 - Time dependence of the conductivity of EMIM@MIL-101-SO_3H recorded at 343 K under 80% RH.

Remarkably, the protonic conductivity recorded at is 20 to 250-fold higher for EMIM@MIL-101-SO_3H than for MIL-101(Cr)-SO_3H, for RH = 40% to 80%, respectively (Table 4.4 and Figure 4.15). This reveals the synergistic role played by the water molecules and IL moieties in participating to the H^+ transport process throughout the composite. There are only a few studies on the σ-RH dependence of IL@MOFs mostly restricted to the low humidity domain. Table 4.5 compares the conductivity performance of EMIM@MIL-101-SO_3H with respect to other existing IL@MOF composites. At low humidity level, the conductivity of EMIM@MIL-101-SO_3H significantly surpasses that of EMIMBr@MIL-53(Al)-NH_2 by almost 3 orders of magnitude,[2] and it competes with that of [BSO_3Hmim][HSO_4]@MIL-101,[13] which was

identified as the best protonic conducting IL@MOF solid reported so far at low humidity level. Interestingly, our composite outperforms by far other ternary based composites (IL/MOF/polymer), like (BMIM)BF_4/UiO-67/PAN [4] and hydroxyethyl(trimethyl)ammonium/ZIF-8/PVA.[51] At higher RH (60% < RH < 80%), EMIM@MIL-101-SO_3H shows outstanding performance ($\sigma_{(343\ K/60\%-80\%\ RH)} \geq 10^{-1}$ $S.cm^{-1}$) and competes with the best performing water-assisted proton conducting MOFs or coordination polymers which have been investigated at higher RH (> 90%).[24,25,56–58,26,40,45,46,52–55] Propitiously, EMIM@MIL-101-SO_3H is the sole MOF-based system showing excellent protonic conductivity under moderate RH (35-40%). Decisively, our composite displays only a very small variation of σ between RH = 80% and 40%. This offers a key alternative to the water management issues, that the benchmark Nafion^{TM} based proton exchanged membranes have to face due to the membrane dehydration at T > 353 K.[59]

Table 4.5 - Comparison of the protonic conductivity of EMIM@MIL-101-SO_3H and other IL@MOFs composites under low to mild humidity conditions.

Composite	**σ / $S.cm^{-1}$**	**T / RH**	**Ref**
EMIMBr@MIL-53(Al)-NH_2	3.0×10^{-5}	353 K – 26%	[2]
[BSO_3Hmim][HSO_4]@MIL-101	$4.4\ 10^{-2}$	323 K – 23%	[4]
(BMIM)BF_4/UiO-67/PAN	2.5×10^{-4}	363 K – 35%	[9]
hydroxyethyl(trimethyl) ammonium@ZIF-8/PVA	9.8×10^{-4}	333 K – 33%	[51]
EMIM@MIL-101-SO_3H	4.8×10^{-2}	343 K / 35%	This work
EMIM@MIL-101-SO_3H	1.4×10^{-1}	343 K / 60%-80%	This work

4.4. Conclusion

In summary, the impregnation of EMIMCl ionic liquid in the mesopores of MIL-101(Cr)-SO_3H was demonstrated to boost the intrinsic proton conducting performance of the parent MOF

under both anhydrous and humid conditions. The good IL/MOF compatibility combined with the high chemical and thermal stability of the resulting composite led to an efficient confinement of the IL in the MOF pores up to 500 K, i.e., a temperature rarely explored for MOF-based composites. EMIM@MIL-101-SO_3H shows excellent protonic conductivity at 473 K (σ = 1.5 x 10^{-3} $S.cm^{-1}$), which ranks this material amongst the best anhydrous proton conducting MOFs investigated in the intermediate temperature domain. Remarkably, this composite equally shows excellent protonic conductivity under low humidity conditions ($\sigma_{353\ K/35\%\ RH}$ = 4.8 x 10^{-2} $S.cm^{-1}$), while it displays a steadily and exceptional σ(343 K) value exceeding 10^{-1} $S.cm^{-1}$ under moderate relative humidity (60% < RH < 80%). The competitive proton conducting performance of EMIM@MIL-101-SO_3H under both humid and anhydrous conditions is unprecedented and makes this composite as a promising candidate in the field of solid-state proton conductors under versatile conditions.

REFERENCES

[1] J.S. Wilkes, P. Wasserscheid, T. Welton, Ionic Liquids in Synthesis, in: Ion. Liq. Synth., Wiley-VCH Verlag GmbH & Co. KGaA, Weinheim, Germany, 2007: pp. i–xxv. https://doi.org/10.1002/9783527621194.fmatter.

[2] J. Liu, X. Zou, C. Liu, K. Cai, N. Zhao, W. Zheng, G. Zhu, Ionothermal synthesis and proton-conductive properties of NH 2 -MIL-53 MOF nanomaterials, CrystEngComm. 18 (2016) 525–528. https://doi.org/10.1039/C5CE02141C.

[3] K. Fujie, K. Otsubo, R. Ikeda, T. Yamada, H. Kitagawa, Low temperature ionic conductor: Ionic liquid incorporated within a metal-organic framework, Chem. Sci. 6 (2015) 4306–4310. https://doi.org/10.1039/c5sc01398d.

[4] J. Du, G. Yu, H. Lin, P. Jie, F. Zhang, F. Qu, C. Wen, L. Feng, X. Liang, Enhanced proton conductivity of metal organic framework at low humidity by improvement in water retention, J. Colloid Interface Sci. 573 (2020) 360–369. https://doi.org/10.1016/j.jcis.2020.04.023.

[5] Y. Yoshida, K. Fujie, D.W. Lim, R. Ikeda, H. Kitagawa, Superionic Conduction over a Wide Temperature Range in a Metal–Organic Framework Impregnated with Ionic Liquids, Angew. Chemie - Int. Ed. 58 (2019) 10909–10913. https://doi.org/10.1002/anie.201903980.

[6] K. Fujie, H. Kitagawa, Ionic liquid transported into metal–organic frameworks, Coord. Chem. Rev. 307 (2016) 382–390. https://doi.org/10.1016/j.ccr.2015.09.003.

[7] F.P. Kinik, A. Uzun, S. Keskin, Ionic Liquid/Metal–Organic Framework Composites: From Synthesis to Applications, ChemSusChem. 10 (2017) 2842–2863. https://doi.org/10.1002/cssc.201700716.

[8] L.H. Chen, B. Bin Wu, H.X. Zhao, L.S. Long, L.S. Zheng, High temperature ionic conduction mediated by ionic liquid incorporated within the metal-organic framework UiO-67(Zr), Inorg. Chem. Commun. 81 (2017) 1–4. https://doi.org/10.1016/j.inoche.2017.04.019.

[9] P. Chen, S. Liu, Z. Bai, Y. Liu, Enhanced ionic conductivity of ionic liquid confined in UiO-67 membrane at low humidity, Microporous Mesoporous Mater. 305 (2020) 110369. https://doi.org/10.1016/j.micromeso.2020.110369.

[10] W.X. Chen, H.R. Xu, G.L. Zhuang, L.S. Long, R. Bin Huang, L.S. Zheng, Temperature-dependent conductivity of Emim+ (Emim+ = 1-ethyl-3-methyl imidazolium) confined in channels of a metal-organic framework, Chem. Commun. 47 (2011) 11933–11935. https://doi.org/10.1039/c1cc14702a.

[11] R. Dutta, A. Kumar, Structural and Dielectric Properties of Ionic Liquid Doped Metal Organic Framework based Polymer Electrolyte Nanocomposites, J. Phys. Conf. Ser. 765 (2016). https://doi.org/10.1088/1742-6596/765/1/012020.

[12] Y. Yoshida, H. Kitagawa, Ionic Conduction in Metal-Organic Frameworks with Incorporated Ionic Liquids, ACS Sustain.

Chem. Eng. 7 (2019) 70–81. https://doi.org/10.1021/acssuschemeng.8b05552.

[13] W.L. Xue, W.H. Deng, H. Chen, R.H. Liu, J.M. Taylor, Y. kun Li, L. Wang, Y.H.Y. Deng, W.H. Li, Y.Y. Wen, G.G.E. Wang, C.Q.C.Q. Wan, G. Xu, MOF-Directed Synthesis of Crystalline Ionic Liquids with Enhanced Proton Conduction, Angew. Chemie - Int. Ed. 60 (2021) 1290–1297. https://doi.org/10.1002/anie.202010783.

[14] S. Shalini, T.P. Vaid, A.J. Matzger, Salt nanoconfinement in zirconium-based metal-organic frameworks leads to pore-size and loading-dependent ionic conductivity enhancement, Chem. Commun. 56 (2020) 7245–7248. https://doi.org/10.1039/d0cc03147j.

[15] X.-L.L. Sun, W.-H.H. Deng, H. Chen, H.-L.L. Han, J.M. Taylor, C.-Q.Q. Wan, G. Xu, A Metal–Organic Framework Impregnated with a Binary Ionic Liquid for Safe Proton Conduction above 100 °C, Chem. - A Eur. J. 23 (2017) 1248–1252. https://doi.org/10.1002/chem.201605215.

[16] H. Chen, S.-Y.Y. Han, R.-H.H. Liu, T.-F.F. Chen, K.-L.L. Bi, J.-B.B. Liang, Y.-H.H. Deng, C.-Q.Q. Wan, High conductive, long-term durable, anhydrous proton conductive solid-state electrolyte based on a metal-organic framework impregnated with binary ionic liquids: Synthesis, characteristic and effect of anion, J. Power Sources. 376 (2018) 168–176. https://doi.org/10.1016/j.jpowsour.2017.11.089.

[17] Q. Xu, X. Zhang, S. Zeng, L. Bai, S. Zhang, Ionic Liquid Incorporated Metal Organic Framework for High Ionic Conductivity over Extended Temperature Range, ACS Sustain. Chem. Eng. 7 (2019) 7892–7899. https://doi.org/10.1021/acssuschemeng.9b00543.

[18] A. Singh, R. Vedarajan, N. Matsumi, Modified Metal Organic Frameworks (MOFs)/Ionic Liquid Matrices for Efficient Charge Storage, J. Electrochem. Soc. 164 (2017) H5169–H5174. https://doi.org/10.1149/2.0191708jes.

[19] Z. Wang, H. Zhou, C. Meng, W. Xiong, Y. Cai, P. Hu, H. Pang, A. Yuan, Enhancing Ion Transport: Function of Ionic Liquid Decorated MOFs in Polymer Electrolytes for All-Solid-State Lithium Batteries, ACS Appl. Energy Mater. 3 (2020) 4265–4274. https://doi.org/10.1021/acsaem.9b02543.

[20] J.M. Tuffnell, J.K. Morzy, N.D. Kelly, R. Tan, Q. Song, C. Ducati, T.D. Bennett, S.E. Dutton, Comparison of the ionic conductivity properties of microporous and mesoporous MOFs infiltrated with a Na-ion containing IL mixture, Dalt. Trans. 49 (2020) 15914–15924. https://doi.org/10.1039/d0dt02576c.

[21] M. Benzaqui, R. Semino, F. Carn, S.R. Tavares, N. Menguy, M. Giménez-Marqués, E. Bellido, P. Horcajada, T. Berthelot, A.I. Kuzminova, M.E. Dmitrenko, A. V. Penkova, D. Roizard, C. Serre, G. Maurin, N. Steunou, Covalent and Selective Grafting of Polyethylene Glycol Brushes at the Surface of ZIF-8 for the Processing of Membranes for Pervaporation, ACS Sustain. Chem. Eng. 7 (2019) 6629–6639. https://doi.org/10.1021/acssuschemeng.8b05587.

[22] H. Zhang, J. James, M. Zhao, Y. Yao, Y. Zhang, B. Zhang, Y.S. Lin, Improving hydrostability of ZIF-8 membranes via surface ligand exchange, J. Memb. Sci. 532 (2017) 1–8. https://doi.org/10.1016/j.memsci.2017.01.065.

[23] K. Wang, H. Huang, X. Zhou, Q. Wang, G. Li, H. Shen, Y. She, C. Zhong, Highly Chemically Stable MOFs with Trifluoromethyl Groups: Effect of Position of Trifluoromethyl Groups on Chemical Stability, Inorg. Chem. 58 (2019) 5725–5732. https://doi.org/10.1021/acs.inorgchem.9b00088.

[24] F. Yang, G. Xu, Y. Dou, B. Wang, H. Zhang, H. Wu, W. Zhou, J.-R. Li, B. Chen, A flexible metal–organic framework with a high density of sulfonic acid sites for proton conduction, Nat. Energy. 2 (2017) 877–883. https://doi.org/10.1038/s41560-017-0018-7.

[25] X.-M. Li, L.-Z. Dong, S.-L. Li, G. Xu, J. Liu, F.-M. Zhang, L.-S. Lu, Y.-Q. Lan, Synergistic Conductivity Effect in a Proton Sources-Coupled Metal–Organic Framework, ACS Energy Lett. 2 (2017) 2313–2318. https://doi.org/10.1021/acsenergylett.7b00560.

[26] S. Devautour-Vinot, E.S. Sanil, A. Geneste, V. Ortiz, P.G. Yot, J.S. Chang, G. Maurin, Guest-Assisted Proton Conduction in the Sulfonic Mesoporous MIL-101 MOF, Chem. - An Asian J. 14 (2019) 3561–3565. https://doi.org/10.1002/asia.201900608.

[27] E. Gkaniatsou, R. Ricoux, K. Kariyawasam, I. Stenger, B. Fan, N. Ayoub, S. Salas, G. Patriarche, C. Serre, J.P. Mahy, N. Steunou, C. Sicard, Encapsulation of Microperoxidase-8 in MIL-101(Cr)-X Nanoparticles: Influence of Metal-Organic Framework Functionalization on Enzymatic Immobilization and Catalytic Activity, ACS Appl. Nano Mater. 3 (2020) 3233–3243. https://doi.org/10.1021/acsanm.9b02464.

[28] A. Permyakova, S. Wang, E. Courbon, F. Nouar, N. Heymans, P. D'Ans, N. Barrier, P. Billemont, G. De Weireld, N. Steunou, M. Frère, C. Serre, Design of salt–metal organic framework composites for seasonal heat storage applications, J. Mater. Chem. A. 5 (2017) 12889–12898. https://doi.org/10.1039/C7TA03069J.

[29] P. D'Ans, E. Courbon, A. Permyakova, F. Nouar, C. Simonnet-Jégat, F. Bourdreux, L. Malet, C. Serre, M. Frère, N. Steunou, A new strontium bromide MOF composite with improved performance for solar energy storage application, J. Energy Storage. 25 (2019) 100881. https://doi.org/10.1016/j.est.2019.100881.

[30] A. Efimova, G. Hubrig, P. Schmidt, Thermal stability and crystallization behavior of imidazolium halide ionic liquids, Thermochim. Acta. 573 (2013) 162–169. https://doi.org/10.1016/j.tca.2013.09.023.

[31] A. Efimova, L. Pfützner, P. Schmidt, Thermal stability and decomposition mechanism of 1-ethyl-3-methylimidazolium halides, Thermochim. Acta. 604 (2015) 129–136. https://doi.org/10.1016/j.tca.2015.02.001.

[32] E. Gómez, N. Calvar, Á. Domínguez, Thermal Behaviour of Pure Ionic Liquids, in: Ion. Liq. - Curr. State Art, InTech, 2015: pp. 199–228. https://doi.org/10.5772/59271.

[33] F. Liu, X. Zhong, J. Xu, A. Kamali, Z. Shi, Temperature Dependence on Density, Viscosity, and Electrical Conductivity of Ionic Liquid 1-Ethyl-3-Methylimidazolium Fluoride, Appl. Sci. 8 (2018) 356. https://doi.org/10.3390/app8030356.

[34] K. Fujie, T. Yamada, R. Ikeda, H. Kitagawa, Introduction of an Ionic Liquid into the Micropores of a Metal-Organic Framework and Its Anomalous Phase Behavior, Angew. Chemie Int. Ed. 53 (2014) 11302–11305. https://doi.org/10.1002/anie.201406011.

[35] Y. Xin, C. Wang, Y. Wang, J. Sun, Y. Gao, Encapsulation of an ionic liquid into the nanopores of a 3D covalent organic framework, RSC Adv. 7 (2017) 1697–1700. https://doi.org/10.1039/C6RA27213D.

[36] S. Marion, S.J. Davis, Z.-Q. Wu, A. Radenovic, Nanocapillary confinement of imidazolium based ionic liquids, Nanoscale. 12 (2020) 8867–8874. https://doi.org/10.1039/D0NR01164A.

[37] W.R. Webb, M.E. Potter, D.J. Stewart, S.J. Elliott, P.J.A. Sazio, Z. Zhang, H. Luo, J. Teng, L. Zhang, C. Ivaldi, I. Miletto, E. Gianotti, R. Raja, The Significance of Metal Coordination in Imidazole-Functionalized Metal–Organic Frameworks for Carbon Dioxide Utilization, Chem. – A Eur. J. 26 (2020) 13606–13610. https://doi.org/10.1002/chem.202001561.

[38] Y.K. Hwang, D.-Y. Hong, J.-S. Chang, S.H. Jhung, Y.-K. Seo, J. Kim, A. Vimont, M. Daturi, C. Serre, G. Férey, Amine Grafting on Coordinatively Unsaturated Metal Centers of MOFs: Consequences for Catalysis and Metal Encapsulation, Angew. Chemie. 120 (2008) 4212–4216. https://doi.org/10.1002/ange.200705998.

[39] M. Wahiduzzaman, S. Nandi, V. Yadav, K. Taksande, G. Maurin, H. Chun, S. Devautour-Vinot, Superionic conduction in a zirconium-formate molecular solid, J. Mater. Chem. A. 8 (2020) 17951–17955. https://doi.org/10.1039/D0TA05424K.

[40] S. Wang, M. Wahiduzzaman, L. Davis, A. Tissot, W. Shepard, J. Marrot, C. Martineau-Corcos, D. Hamdane, G. Maurin, S. Devautour-Vinot, C. Serre, A robust zirconium amino acid metal-organic framework for proton conduction, Nat. Commun. 9 (2018) 4937. https://doi.org/10.1038/s41467-018-07414-4.

[41] J. Vila, C. Franjo, J.M. Pico, L.M. Varela, O. Cabeza, Temperature Behavior of the Electrical Conductivity of Emim-Based Ionic Liquids in Liquid and Solid States, Port. Electrochim. Acta. 25 (2007) 163–172. https://doi.org/10.4152/pea.200701163.

[42] W. Silva, M. Zanatta, A.S. Ferreira, M.C. Corvo, E.J. Cabrita, Revisiting Ionic Liquid Structure-Property Relationship: A Critical Analysis, Int. J. Mol. Sci. 21 (2020) 7745. https://doi.org/10.3390/ijms21207745.

[43] J. Jacquemin, P. Husson, A.A.H. Padua, V. Majer, Density and viscosity of several pure and water-saturated ionic liquids, Green Chem. 8 (2006) 172–180. https://doi.org/10.1039/B513231B.

[44] C.J.T. de Grotthuss, Sur la Décomposition de l'Eau et des Corps qu'Elle Tient en Dissolution à l'Aide de l'Electricité Galvanique, Ann. Chim. Phys. 58 (1806) 54–74.

[45] M. Wahiduzzaman, S. Wang, J. Schnee, A. Vimont, V. Ortiz, P.G. Yot, R. Retoux, M. Daturi, J.S. Lee, J.-S.S. Chang, C. Serre, G. Maurin, S. Devautour-Vinot, A High Proton Conductive Hydrogen-Sulfate Decorated Titanium Carboxylate Metal-Organic Framework, ACS Sustain. Chem. Eng. 7 (2019) 5776–5783. https://doi.org/10.1021/acssuschemeng.8b05306.

[46] S. Nandi, S. Wang, M. Wahiduzzaman, V. Yadav, K. Taksande, G. Maurin, C. Serre, S. Devautour-Vinot, Multivariate Sulfonic-Based Titanium Metal–Organic Frameworks as Super-protonic Conductors, ACS Appl. Mater. Interfaces. 13 (2021) 20194–20200. https://doi.org/10.1021/acsami.1c03644.

[47] A. Shigematsu, T. Yamada, H. Kitagawa, Wide Control of Proton Conductivity in Porous Coordination Polymers, J. Am. Chem. Soc. 133 (2011) 2034–2036. https://doi.org/10.1021/ja109810w.

[48] J.M. Taylor, K.W. Dawson, G.K.H. Shimizu, A Water-Stable Metal–Organic Framework with Highly Acidic Pores for Proton-Conducting Applications, J. Am. Chem. Soc. 135 (2013) 1193–1196. https://doi.org/10.1021/ja310435e.

[49] M. Bazaga-García, R.M.P. Colodrero, M. Papadaki, P. Garczarek, J. Zoń, P. Olivera-Pastor, E.R. Losilla, L. León-Reina, M.A.G. Aranda, D. Choquesillo-Lazarte, K.D. Demadis, A. Cabeza, Guest Molecule-Responsive Functional Calcium Phosphonate Frameworks for Tuned Proton Conductivity, J. Am. Chem. Soc. 136 (2014) 5731–5739. https://doi.org/10.1021/ja500356z.

[50] S. Tominaka, A.K. Cheetham, Intrinsic and extrinsic proton conductivity in metal-organic frameworks, RSC Adv. 4 (2014) 54382–54387. https://doi.org/10.1039/c4ra11473f.

[51] C. Liu, S. Feng, Z. Zhuang, D. Qi, G. Li, C. Zhao, X. Li, H. Na, Towards basic ionic liquid-based hybrid membranes as hydroxide-conducting electrolytes under low humidity conditions, Chem. Commun. 51 (2015) 12629–12632. https://doi.org/10.1039/c5cc03462k.

[52] S. Mukhopadhyay, J. Debgupta, C. Singh, R. Sarkar, O. Basu, S.K. Das, Designing UiO-66-Based Superprotonic Conductor with the Highest Metal–Organic Framework Based Proton Conductivity, ACS Appl. Mater. Interfaces. 11 (2019) 13423–13432. https://doi.org/10.1021/acsami.9b01121.

[53] Y.Y. Cai, Q. Yang, Z.Y. Zhu, Q.H. Sun, A.M. Zhu, Q.G. Zhang, Q.L. Liu, Achieving efficient proton conduction in a MOF-based proton exchange membrane through an encapsulation strategy, J. Memb. Sci. 590 (2019) 1–8. https://doi.org/10.1016/j.memsci.2019.117277.

[54] X.-M. Li, J. Liu, C. Zhao, J.-L. Zhou, L. Zhao, S.-L. Li, Y.-Q. Lan, Strategic hierarchical improvement of superprotonic conductivity in a stable metal–organic framework system, J. Mater. Chem. A. 7 (2019) 25165–25171. https://doi.org/10.1039/C9TA10286H.

[55] R.F. Mendes, P. Barbosa, E.M. Domingues, P. Silva, F. Figueiredo, F.A. Almeida Paz, Enhanced proton conductivity in a layered coordination polymer, Chem. Sci. 11 (2020) 6305–6311. https://doi.org/10.1039/D0SC01762K.

[56] S.-S. Liu, Z. Han, J.-S. Yang, S.-Z. Huang, X.-Y. Dong, S.-Q. Zang, Sulfonic Groups Lined along Channels of Metal–Organic Frameworks (MOFs) for Super-Proton Conductor, Inorg. Chem. 59 (2020) 396–402. https://doi.org/10.1021/acs.inorgchem.9b02649.

[57] S.M. Elahi, S. Chand, W. Deng, A. Pal, M.C. Das, Polycarboxylate-Templated Coordination Polymers: Role of Templates for Superprotonic Conductivities of up to 10 −1 S cm −1, Angew. Chemie Int. Ed. 57 (2018) 6662–6666. https://doi.org/10.1002/anie.201802632.

[58] V.G. Ponomareva, K.A. Kovalenko, A.P. Chupakhin, D.N. Dybtsev, E.S. Shutova, V.P. Fedin, Imparting high proton conductivity to a metal-organic framework material by controlled acid impregnation, J. Am. Chem. Soc. 134 (2012) 15640–15643. https://doi.org/10.1021/ja305587n.

[59] H. Zhang, P.K. Shen, Recent Development of Polymer Electrolyte Membranes for Fuel Cells, Chem. Rev. 112 (2012) 2780–2832. https://doi.org/10.1021/cr200035s.

Chapter 5

Superionic conduction in the Zirconium-formate molecular solid

5.1. Introduction

The previous chapters are dedicated to the promotion of MOFs as proton conducting solids. In the following, we extended the strategy developed above to another class of materials, through the investigation of a molecular crystal. In that case, charge carriers are no more restricted to protons, since other ionic species are expected to be involved in the conducting process.

Similarly to proton conducting solids, solid state ionic conductors have attracted considerable attention owing to their great potentials in the field of electrochemical devices for energy storage/conversion (fuel cells, electrolysers, supercapacitors and batteries) as well as in the environmental monitoring area (humidity/gas sensors or electrochromic windows).[1,2] Compared to liquid analogues, they show many advantages, including long cycle life, short charging time, environmental safety, low internal corrosion, flexibility in packaging and ability to miniaturize devices. Plethora of ion conducting materials have been identified and are classified according to their intrinsic vs extrinsic disorder, amorphous vs crystalline structure, bulk vs interfacial control, cationic vs anionic conduction and ionic vs mixed ionic–electronic conduction.[3,4] Ag^+, Na^+, Li^+, O^{2-}, H^+ and F^- are the most common mobile ions present in the iconic ionic conductors,[3,4] e.g., α-AgI, β-alumina, Nasicon, Lisicon, fluorite based oxide (doped zirconium dioxide), perovskite-type oxide, polymers (Nafion^{TM}), etc. Refining known solid-state ionic conductors or developing new ones with enhanced performances is still the subject of intense activity in the field of material science.

Molecular crystals are a versatile functional-material platform that might be of interest in the area of solid state ionics. Their structural/chemical versatility combined with appropriate flexibility of component units offers an opportunity to create a broad range of functional materials with a fine control of their 3D ordered structures at the molecular level, giving a high degree of freedom to design conduction paths for rapid ion diffusion. So far, only a very few molecular crystals have been envisaged as ionic conductors.[5–11] Typically, supramolecular solid electrolytes with Li^+ as mobile species have been mostly considered,[5–10] however their ionic conductivity performances are too low to rival with the traditional inorganic or polymer-based electrolytes benchmark materials.[12–14] Furthermore, the associated charge transport mechanism remains to be elucidated and this lack of fundamental understanding clearly hampers further development of this family of materials as ionic conductors. This calls for a more systematic

exploration of this class of materials to assess the real potential of these solids as well as a deeper fundamental understanding of the microscopic mechanism which is expected to promote molecular crystals at a higher level in terms of ionic conductivity. Moreover, water was demonstrated to play a pivotal role in guest-assisting ionic conduction for diverse families of solids including zeolites, clays and MOFs via the formation of an extended hydrogen bond network that makes the ion transport more efficient.[15–19] However, this latter strategy has never been applied so far to boost the ionic conductivity performances of molecular crystals.

Therein, we explored the ionic conductivity of ZF-3, a zirconium-formate molecular solid containing KCl ion pairs in a stoichiometric amount.[20] Remarkably ZF-3 switches from an insulator (σ = 5.1 x 10^{-10} S.cm^{-1} at 363 K/0% RH to a superionic conductor upon hydration (σ = 5.2 x 10^{-2} S.cm^{-1} at 363 K/95% RH). This material retains the integrity of its crystal structure under operating conditions and maintains this high level of performance over time. Molecular simulations revealed that the presence of water considerably boosts the dynamics of Cl^- species consecutive of the creation of Cl^-/H_2O core-shell structures throughout the pores of ZF-3. This favourable scenario is at the origin of the excellent water-assisted ionic conductivity of ZF-3.

5.2. Materials and methods

5.2.1. Synthesis of ZF-3

The ZF-3 material was synthesized by our collaborator, Prof. Hyungphil Chun, from the University of Hanyang, Republic of Korea. It was prepared according to the procedure detailed in reference.[20] All the chemicals were purchased from commercial sources and used without further purifications.

To a DMF-CH_3CN (10 mL, 1:1 v/v) solution containing $ZrCl_4$ (507.4 mg, 2.18 mmol), KNO_3 (73.3 mg, 0.725 mmol) and 14 M HNO_3 (1.825 mL, 26.2 mmol) were added. The turbid mixture was vigorously stirred for 1 hour and then directly filtered into four screw-capped vials (Wheaton) with Teflon rubber liner. After heating to 383 K for 1 d, colorless cube-shaped crystals were collected (180 mg). The as-synthesized product was thoroughly washed DMF, CH_3CN and CH_3OH-CH_3CN mixture, and evacuated at 323 K before subjected for measurements. X-ray single crystal crystallography establishes the following formula $[Zr_{36}O_{24}(OH)_{48}(HCO_2)_{48}].3KCl$.

5.2.2. Characterization of ZF-3

The XRPD patterns of the solids before and after conductivity measurements were collected on a PANalytical X'Pert equipped with an X'Celerator detector and using a wave-length, λ =1.5406 Å with an operating voltage of 40 kV and a beam current of 30 mA. Data are discussed in the section dedicated to results and discussion.

Impedance measurements were performed on the anhydrous and hydrated solids on a Broadband Dielectric Spectrometer Novocontrol alpha analyzer and a Solartron analytical Modulab XM MTS respectively, over a frequency range from F = 0.01 Hz to F = 1 MHz with an applied ac voltage of 20 mV. Measurements were collected on the anhydrous ZF-3 after a preliminary in situ heating at 373 K for 2 hours. Measurements were equally undertaken on the hydrated solid, which was introduced into an Espec Corp. SH-221 incubator, to control the temperature 298 < T (K) < 363 and the Relative Humidity 35 < RH (%) < 95. The solid was equilibrated for 24 hours at given T and RH values, to ensure fixed water content before recording the impedance. The measurements were performed using powders introduced in the home-made sample holder shown in Figures 3.13d and 3.13f, allowing the use of the "two-probe" method for the electrical measurements. The resistance value of the studied solids was deduced using different methods depending on the Nyquist plot (-Z" = f(Z')) or the Bode representation (σ_{ac} = f (F)).

For the Nyquist plots showing a well-defined semi-circle (Figures 5.3 and 5.9), ZView Software was applied to fit impedance data sets with equivalent circuits, assembling the bulk resistance R and the bulk non-ideal capacitance CPE, while a second constant phase element CPE-2 was alternatively added to take into account for the electrodes if applicable. As previously detailed, the sample conductivity value was obtained using $\sigma = \frac{1}{Z} * \frac{l}{S}$, where l and S are the sample thickness and area respectively. Resistance obtained from the semi-circle extrapolation to the real-axis was also considered. Both procedures converge towards comparable values of σ, supporting that both approaches can be equally considered (see Table 5.1).

For the very low resistive ZF-3 (Figures 5.5), the Nyquist plot results only in the tail end of a semi-circle at high frequency, while at lower frequency a capacitive tail is observed which prevents the use of the equivalent-fitting procedure. In that case, the resistance was only evaluated from the real-axis intercept of the Nyquist plot.

Alternatively, the bulk conductivity of ZF-3 was also extracted from the dc plateau of the Bode representation, following the formula $\sigma_{ac} = \frac{1}{Z} * \frac{l}{S}$. Typically, σ_{ac} results from the combination of 3 contributions: $\sigma_{ac}(F,T) = \sigma_{MWS}(F,T) + \sigma_{dc}(T) + \sigma'(F,T)$. The polarization component $\sigma'(F,T)$, corresponding to the increasing part of the signal at high frequency, arises from the local rearrangement of charges or dipoles causing dipolar reorientation. The dc conductivity plateau $\sigma_{dc}(T)$, resulting from the long-range distribution of charge, dominates the intermediate frequency region and is frequency independent. In the case of highly conductive materials, the Maxwell Wagner Sillars contribution $\sigma_{MWS}(F,T)$ due to the ionic charge accumulation to the sample/electrode interface is observed at low frequency. In insulators, $\sigma_{MWS}(F,T) \approx 0$ and $\sigma_{dc}(T) \approx 0$, so that only the polarization conductivity is detectable.

Table 5.1 lists the conductivity values data obtained from the Nyquist plot analysis, using either the extrapolation or the equivalent circuit approaches, and those deduced from the Bode representation. As shown, results are consistent, further evidencing that the data analysis can be carried out by either of these methods.

As shown in chapters 3 and 4, the ΔE activated energy associated with the proton transport process was deduced from the linear fitting of $ln(\sigma T)$ versus 1/T, according to the Arrhenius equation (cf Eq. 2.13, rewrote as $\sigma(T) = \frac{\sigma_0}{T} exp[\frac{-\Delta E}{kT}]$).

5.3. Result and discussion

ZF-3, with the following chemical formula $[Zr_{36}O_{24}(OH)_{48}(HCO_2)_{48}].3KCl$, was solvothermally synthesized following the procedure previously reported (see section V.2.1).[20] ZF-3 is composed of 6 cyclic molecular hexamers of $[Zr_6O_4(OH)_4]$ units interconnected by bridging formate ligands, resulting in a molecular structure with a hexagonal shape (Figure 5.1). The zirconium-formate macrocyclic molecule consists of two types of μ-OH hydroxyl groups: i) μ_3-OH groups belonging to the Zr_6 cluster, similar to UiO-66 type MOFs and ii) bridging μ_2-OH groups (Zr-O(H)-Zr) as detailed in Figure 5.1. These hexagonal disc-like macromolecules self-assemble into a superstructure with hollow supercages. The cohesion of the system is ensured by ion-dipole interactions, involving three K^+, Cl^- ions pairs located between adjacent hexameric $[Zr_{36}]$ clusters as well as by van der Waals interactions between formate ligands.

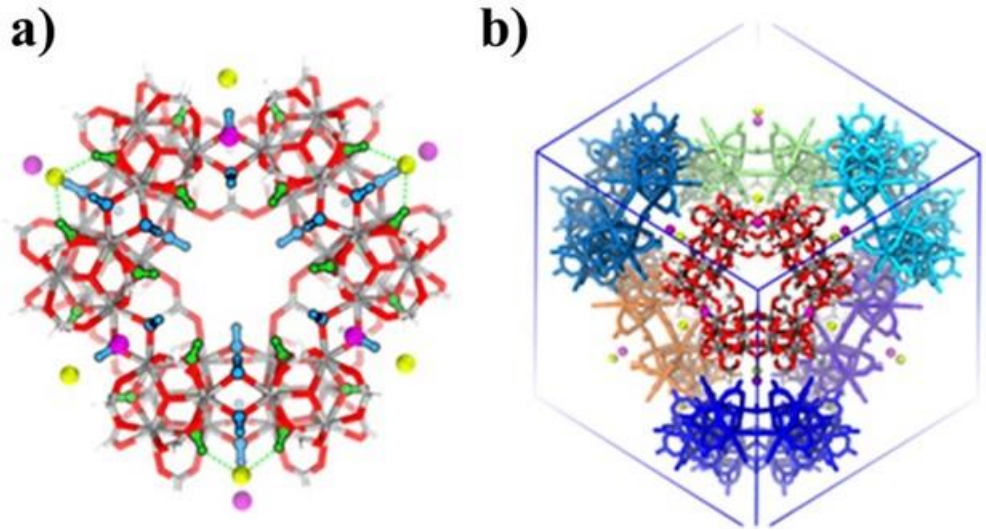

Figure 5.1 – a) Illustration of a single Zirconium-Formate macrocycle in which the position of hydrophilic μ_2-OH, μ_3-OH sites as well as K^+ and Cl^- ions are highlighted in blue, green, magenta and yellow spheres, respectively. **b)** Unit cell representation of ZF-3, with macrocycles presented in random mono colors (except one) for an easy distinction of intermolecular arrangements.

The ionic conductivity of ZF-3 was measured by complex impedance spectroscopy under anhydrous conditions at temperatures ranging from 283 K to 373 K (Figure 5.2a and 5.3). In the bode representation of the conductivity vs frequency, the electrical signal is mainly dominated by the polarization conductivity $\sigma'(\omega)$, while the dc conductivity plateau is only observed for the highest temperature domain (T > 333 K). This observation combined with a measured low conductivity value ($< 10^{-9}$ S.cm^{-1}) is a signature of an insulating behavior for the pristine ZF-3. This means that the dynamics of the ionic species is restricted to local relaxations, while the condition for the ion diffusion over long range is adverse. The ion hopping required for charge transport does not happen since the potential conductive ions occupy crystallographic sites that are quite far from each other. To support these experimental findings, force field Molecular Dynamics (MD) simulations, carried out by colleagues in the group, were performed in the NVT ensemble at 400 K starting with the DFT-optimized empty ZF-3 structure to determine if any free motions of K^+ and Cl^- are possible. A 10 ns MD run clearly ruled out this possibility, both ions showing only tiny displacements around their original positions as demonstrated by their corresponding Mean Square Displacement (MSD) profiles averaged over the whole MD trajectory (Figure 5.4). This restricted dynamics of both K^+ and Cl^- ions, resulting in very local motions, is consistent with

the existence of strong ion-dipole interactions between these ions and the oxygen/hydrogen atoms of the μ-OH groups and the formate groups, responsible for the self-assembly of the hexameric clusters of ZF-3 (Figure 5.1).[20]

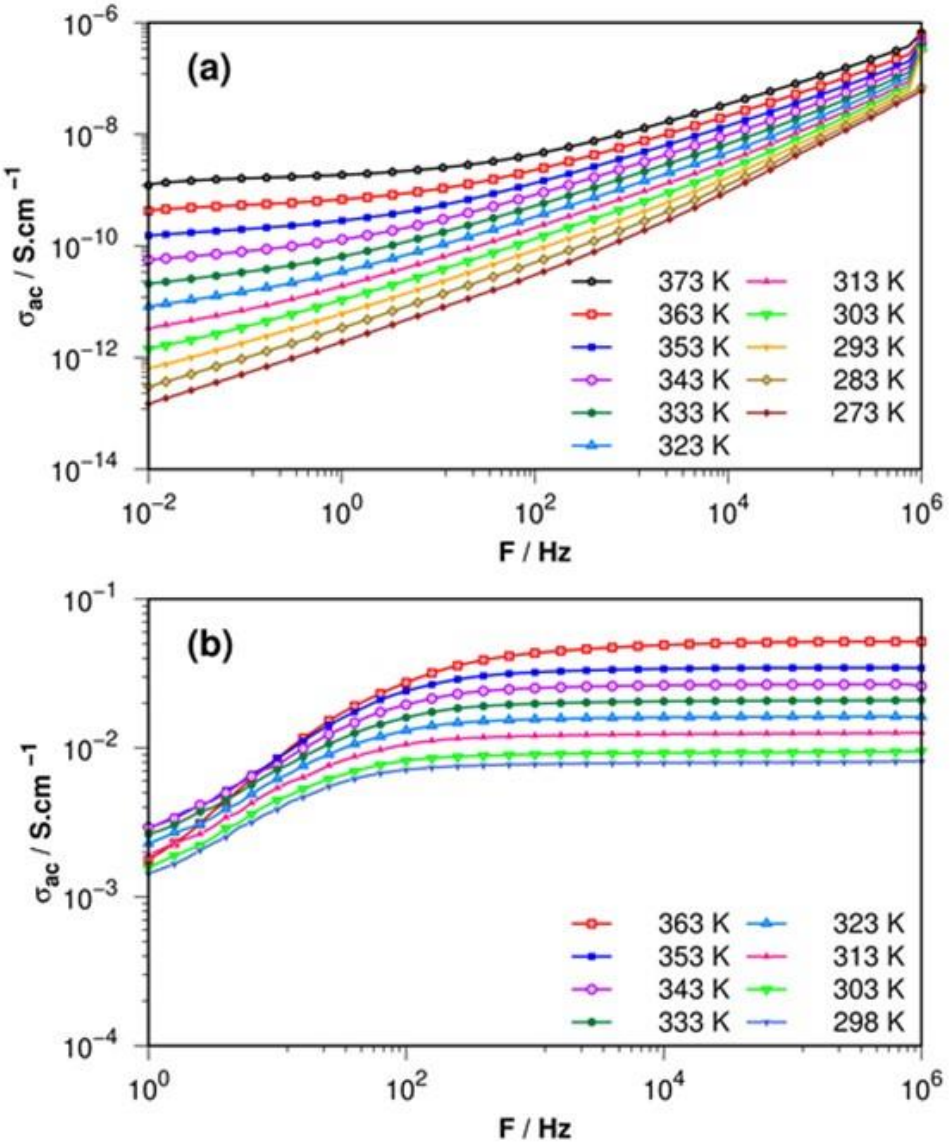

Figure 5.2 – Bode diagram of the conductivity for the ZF-3 powder recorded at various temperature under **a)** 0% and **b)** 95% RH.

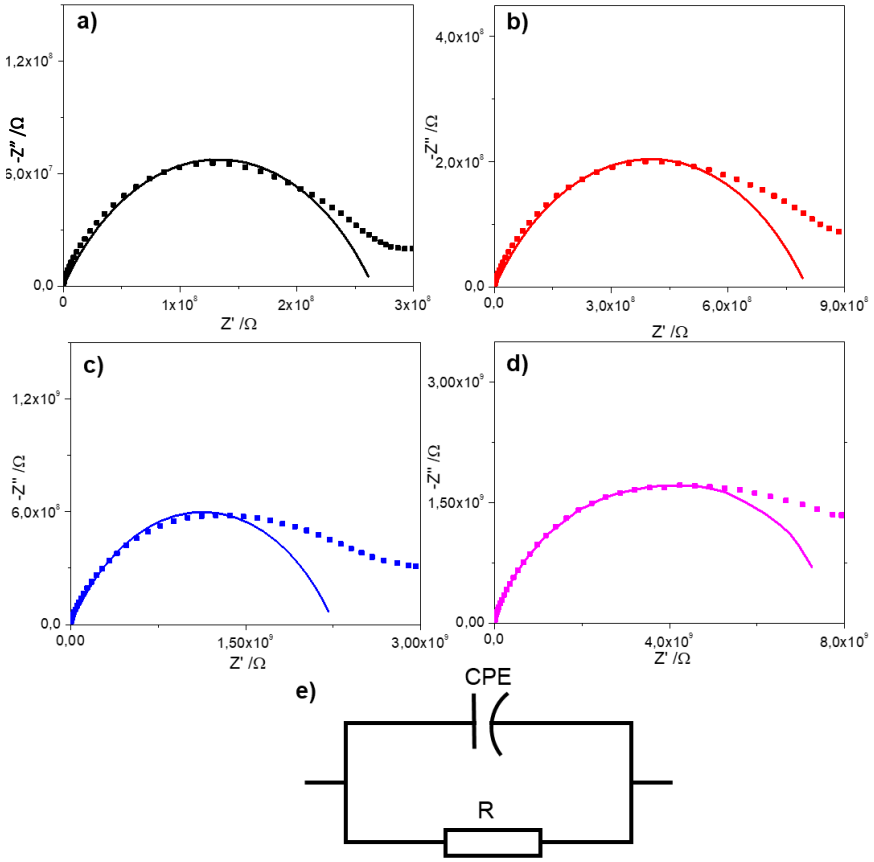

Figure 5.3 - Nyquist plots of the impedance for the anhydrous (RH = 0%) ZF-3 powder recorded at **a)** 373 K, **b**) 363 K, **c**) 353 K and **d)** 343 K. The filled symbols are the measured impedance data and the line corresponds to the fit of the data using **e)** the equivalent circuit model. **NOTE**: For data recorded at T < 343 K, the resulting semi-circle is incomplete, preventing any analysis with the equivalent circuit model.

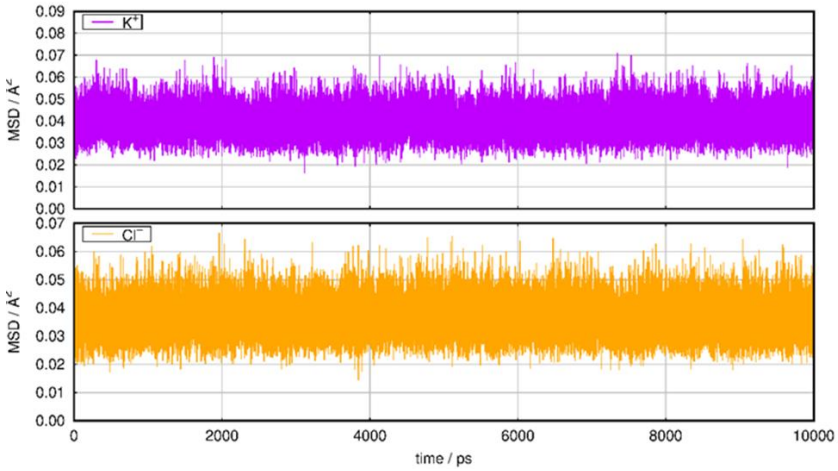

Figure 5.4 - Mean square displacement (MSD) of K^+, Cl^- ions calculated from the NVT-MD simulation performed at 400 K for ZF-3 phase in this dry state.

Impedance measurements were further recorded under humidity (95% RH), for temperatures varying from 363 K to 298 K. Figure 5.2b shows that the scenario drastically contrasts compared with the behavior recorded at the anhydrous state. Under 95% RH, the conductivity profile of ZF-3 is dominated by the dc conductivity plateau (σ_{dc}), preceded by the conductivity drop in the low frequency domain which is assigned to the Maxwell Wagner Sillars response (σ_{MWS}). The σ_{MWS} contribution, due to the charge accumulation to the sample/electrode interface, reflects the ionic features of the charge carriers, while K^+, Cl^- and/or H^+ are likely to be involved in the ionic transport process. The conductivity values recorded at the dc plateau, consistent with those deduced from the Nyquist plots analysis (Figure. 5.5 and Table 5.1), increase from 8.0 x 10^{-3} S.cm^{-1} to 5.2 x 10^{-2} S.cm^{-1} when heating from 298 K to 363 K at 95% RH. These very high σ values ($\sigma > 10^{-4}$ S.cm^{-1}) relate to the superconducting behavior of the hydrated ZF-3.[21]

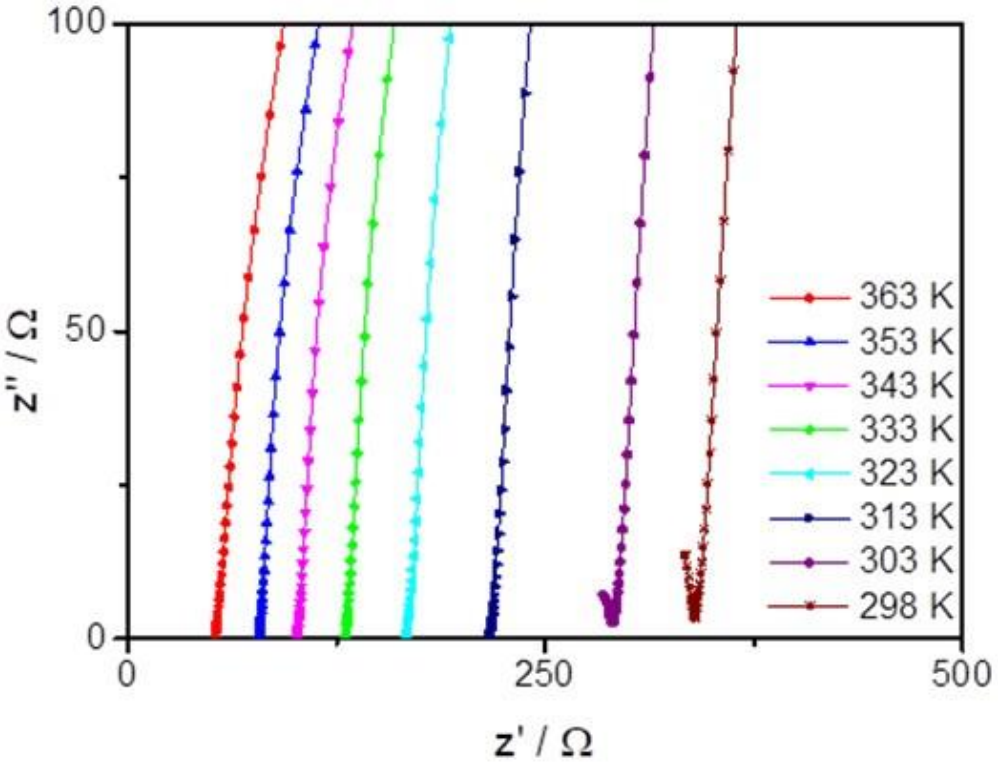

Figure 5.5 - Nyquist plot of the impedance for the hydrated (RH = 95%) ZF-3 powder recorded from 363 K to 298 K.

Table 5.1 - Conductivity values deduced from the circuit equivalent fitting and the extrapolation procedures applied on the Nyquist plots, as well as from the conductivity plateau in the Bode diagram for the ZF-3 powder at different RH/T conditions.

Anhydrous Conditions RH = 0%	**T / K**	**σ / S.cm^{-1} Nyquist plot: Equivalent circuit**	**σ / S.cm^{-1} Bode plot**
l = 0.17 cm **S = 0.36 cm^2**	373	1.7 x 10^{-9}	1.8 x 10^{-9}
	363	5.7 x 10^{-9}	5.1 x 10^{-10}
	353	1.9 x 10^{-10}	1.6 x 10^{-10}
	343	7.1 x 10^{-11}	5.7 x 10^{-11}
Humid Conditions RH = 95%	**T / K**	**σ / S.cm^{-1} Nyquist plot: Extrapolation**	**σ / S.cm^{-1} Bode plot**
l = 0.33 cm **S = 0.12 cm^2**	363	5.2 x 10^{-2}	5.2 x 10^{-2}
	353	3.4 x 10^{-2}	3.4 x 10^{-2}
	343	2.6 x 10^{-2}	2.7 x 10^{-2}
	333	2.1 x 10^{-2}	2.1 x 10^{-2}
	323	1.6 x 10^{-2}	1.6 x 10^{-2}
	313	1.2 x 10^{-2}	1.3 x 10^{-2}
	303	9.2 x 10^{-3}	9.3 x 10^{-3}
	298	7.9 x 10^{-3}	8.0 x 10^{-3}
Isothermal Conditions T = 363 K	**RH / %**	**σ / S.cm^{-1} Nyquist plot: Equivalent circuit**	**σ / S.cm^{-1} Nyquist plot: Extrapolation**	**σ / S.cm^{-1} Bode plot**
l = 0.33 cm **S = 0.12 cm^2**	95	-	5.2 x 10^{-2}	5.2 x 10^{-2}
	85	1.6 x 10^{-3}	1.5 x 10^{-3}	1.6 x 10^{-3}
	75	1.6 x 10^{-4}	1.6 x 10^{-4}	1.6 x 10^{-4}
	65	9.0 x 10^{-5}	8.9 x 10^{-5}	8.9 x 10^{-5}
	55	1.2 x 10^{-6}	1.2 x 10^{-6}	1.2 x 10^{-6}
	45	1.0 x 10^{-6}	9.9 x 10^{-7}	9.7 x 10^{-7}
	35	6.4 x 10^{-7}	6.4 x 10^{-7}	6.5 x 10^{-7}

The excellent level of performances for the hydrated ZF-3 is unprecedented for a molecular crystal and makes this solid as a very attractive ionic conductor under these T/RH conditions. This range of conductivity values is similar to that observed for the best proton conductive MOFs.[18,19,30–39,22,40–42,23–29] Noteworthy, this very high conductivity is maintained over several days, i.e., at least 4 days (Figure 5.6), while the structural integrity of the solid is preserved under operating conditions (363 K/95% RH), as confirmed by the good agreement between PXRD patterns collected for the sample before and after conductivity measurements (Figure 5.8). This emphasizes the robustness of ZF-3 upon adsorption of water vapor, which interestingly contrasts with its high solubility in liquid water.[20] This supports that the macrocycles are not separated upon adsorption of water vapor, which is in line with the reversible water adsorption behaviour of this molecular solid as evidenced by cyclic measurements in reference.[20]

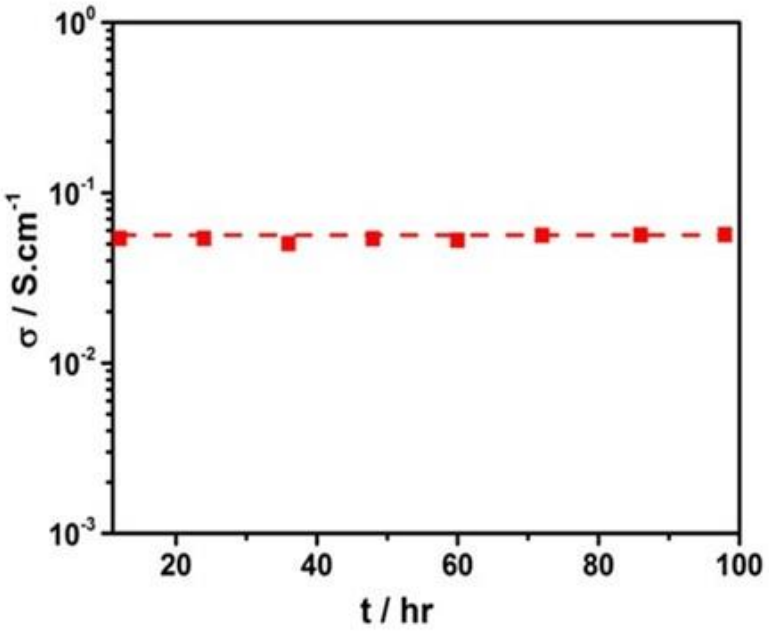

Figure 5.6 – Time dependence of the conductivity recorded at 363 K and 95% RH for the ZF-3 powder. The dashed line is a guide for the eye, and corresponds to σ value at infinite time, i.e., $\sigma = 0.056$ S.cm^{-1}.

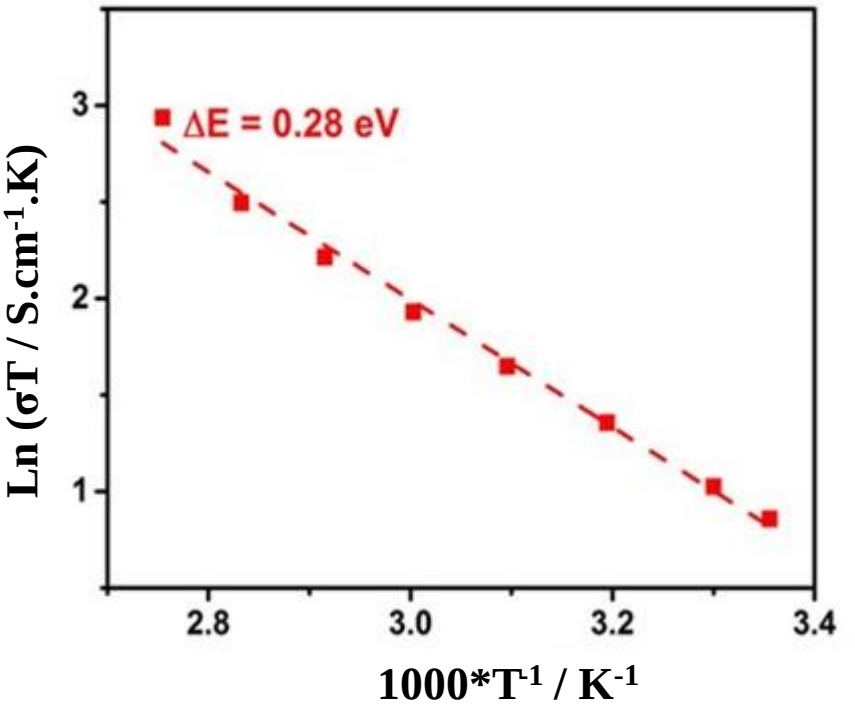

Figure 5.7 – Arrhenius type plot of the conductivity of ZF-3 powder under 95% RH. The dashed line corresponds to the linear least-square fit.

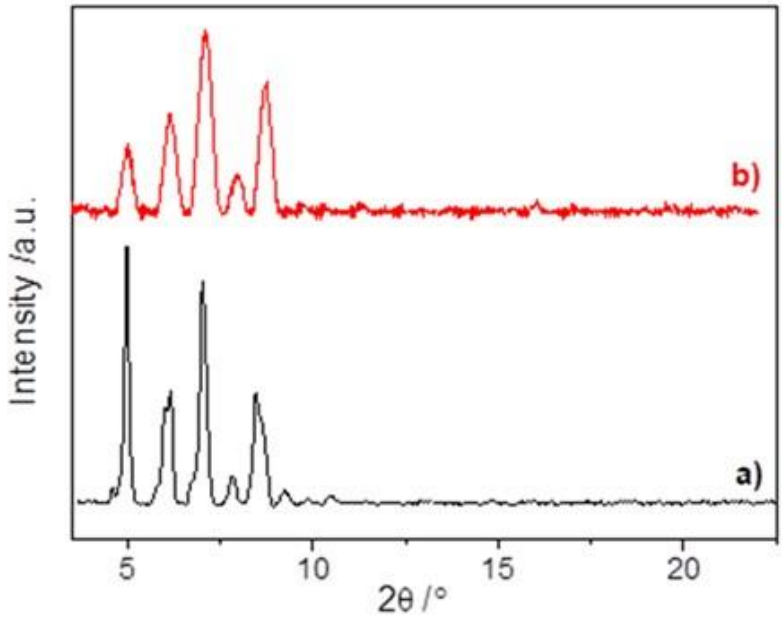

Figure 5.8 - PXRD patterns of the ZF-3 powder **a)** before and **b)** after impedance measurements recorded at 363 K/95% RH/96 hr.

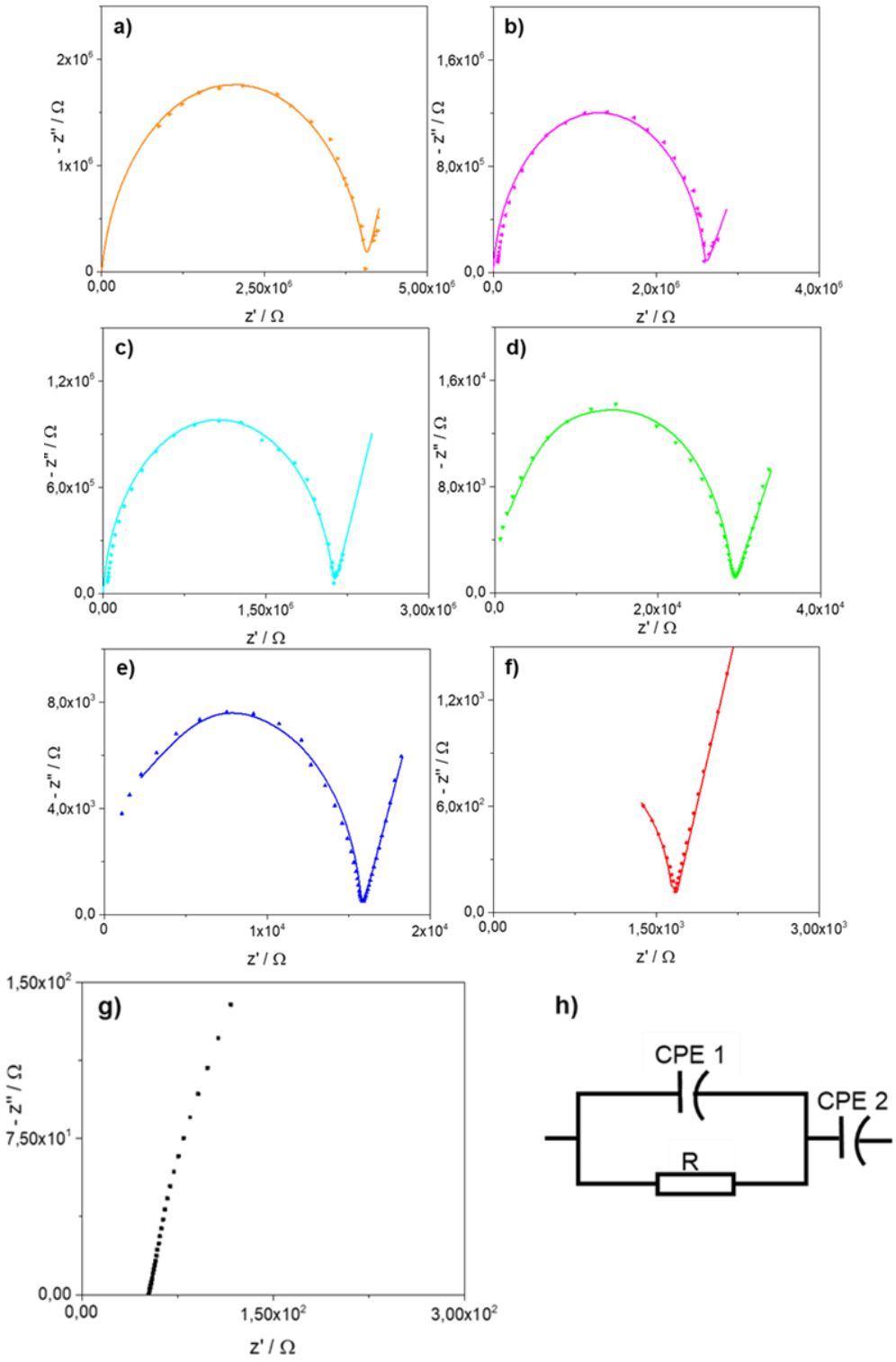

Figure 5.9 - Nyquist plots of the impedance for ZF-3 powder recorded at 363 K and RH = **a)** 35%, **b)** 45%, **c)** 55%, **d)** 65%, **e)** 75%, **f)** 85% and **g)** 95% RH. The filled symbols are the measured impedance data and the line corresponds to the fit of the data using **h)** the equivalent circuit model.

The Arrhenius plot of the conductivity measured at 95% RH ($\ln(\sigma \times T) = f(1/T)$) is illustrated in Figure 5.7 and results to an activation energy ΔE of 0.28 eV. This relatively low energy value suggests an efficient transfer of the ions within the pores of the material. Impedance measurements were further carried out at 363 K under increasing RH (Figure 5.9). A RH-conductivity dependence is clearly evidenced with values increasing from 6.5×10^{-7} $S.cm^{-1}$ to 5.2×10^{-2} $S.cm^{-1}$ when RH raises from 35% to 95% (see Table 5.1). The significant increment of the conductivity with increasing humidity unambiguously reveals that the water molecules assist the ion transport in ZF-3.

As a further stage, AIMD and force field MC/ MD/ simulations were performed to shed light into the microscopic origin of the water-assisted ionic conductivity of ZF-3. MC simulations were first performed to unravel the preferential distribution of water molecules in the pores of ZF-3. As a first stage, the reliability of the force-field we used to describe the water/host interactions was confirmed by the excellent agreement between grand canonical MC adsorption enthalpy (-62.0 $kJ.mol^{-1}$) and the experimental isosteric heat of adsorption (-64.9…-63.7 $kJ.mol^{-1}$).[20] The DFT-optimized ZF-3 structure was thus loaded by ~20 wt% of water corresponding to the saturation capacity determined previously by adsorption measurements.[20] Analysis of the minimum energy MC snapshots demonstrated that water molecules preferentially form a percolated hydrogen-bonded network throughout the entire porosity of ZF-3, as illustrated in Figure 5.10, with a corresponding mean O_w–O_W distance of 2.78 Å as seen in the RDF plotted for the corresponding atom pairs (Figure 5.11). This hydrogen-bonded network connects the hydrophilic μ_3-OH and μ_2-OH groups of the macrocycles as well as the free Cl^- ions (Figure 5.12).

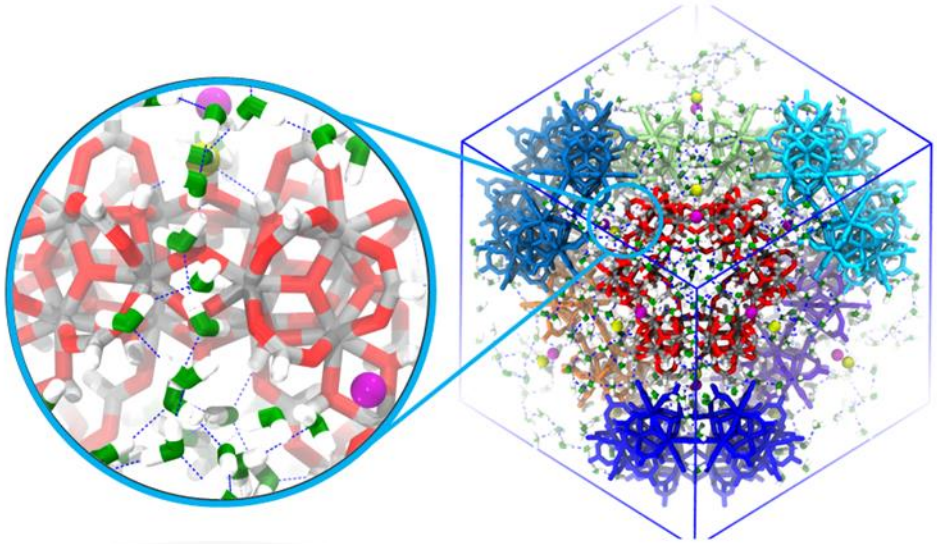

Figure 5.10 - Illustration of an extended hydrogen bonded network formed by the adsorbed water molecules, K^+, Cl^- ions, and within the porosity of ZF-3 system. A small portion of a typical configuration of water arrangement near the hydrophilic μ_2-OH, and μ_3-OH sites is magnified for a clear view. Except one, Zr-formate macrocycles are presented in random mono colors for an easy distinction of intermolecular arrangements.

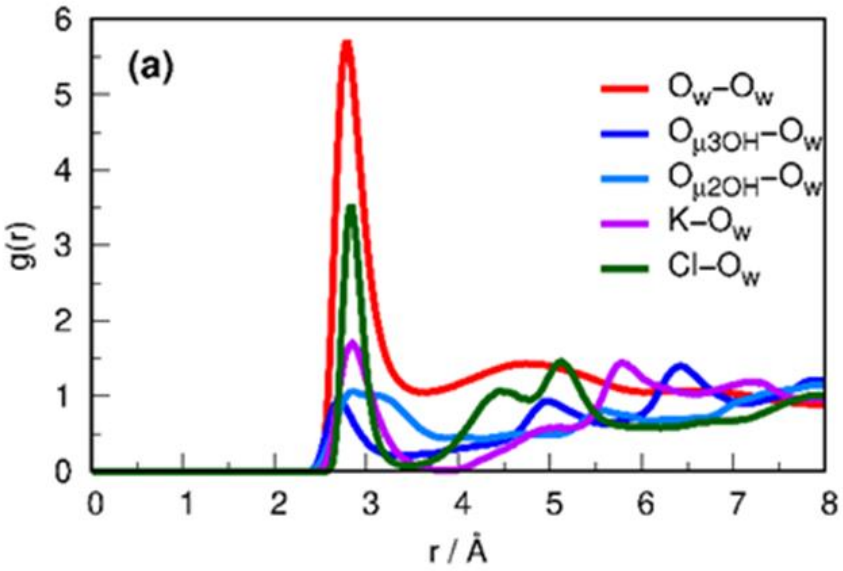

Figure 5.11 - Radial distribution functions of intermolecular O-O pairs of water-water, water–μ_2OH, –μ_3OH moieties on the pore wall of the ZF-3-KCl structure, as well as the intermolecular O–Cl, O–K pairs calculated from the Monte Carlo simulations performed for the hydrated ZF-3.

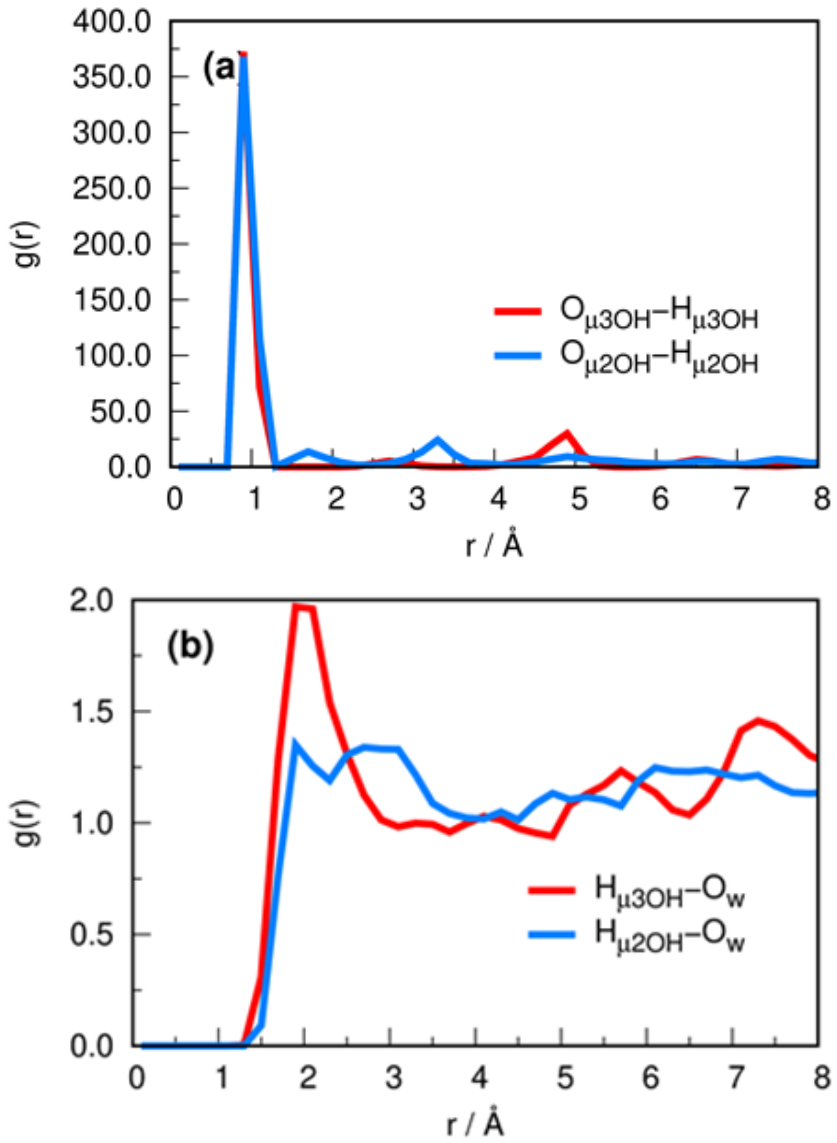

Figure 5.12 - Radial distribution functions characterizing: **a)** intramolecular O-H bond distance of μ-OH moieties and **b)** intermolecular H(μ-OH)..O_w pairs separation distance derived from the 6 ps AIMD trajectory obtained at T = 600 K.

The RDFs calculated for diverse water/atom pairs evidenced that the water molecules interact more preferentially with Cl^- (higher intensity of the RDF peak for the corresponding O_W–Cl pair) than with K^+ and both μ_3-OH and μ_2-OH functions (Figure 5.11). AIMD simulations were further conducted for the hydrated system to envisage the possible proton migration from the μ-OH functions to either H_2O or Cl^-. Typically, proton release from an acidic function grafted to a material is a relatively fast process which usually happen in a few picoseconds timescale. A careful inspection of the AIMD trajectory corresponding to a 10 ps-run clearly ruled out any proton

transfer. This was confirmed by the analysis of the RDF plotted for different atom pairs revealing that the O-H bond length for both μ_3-OH and μ_2-OH moieties fluctuates by only ±0.15% around its mean value ~1.0 Å while the μ-OH...Ow distance is never found shorter than 1.3 Å. These calculations deliver a proof that the conductivity of ZF-3 is not of protonic nature but rather originates from the mobility of the free K^+ and Cl^- present in the pores.

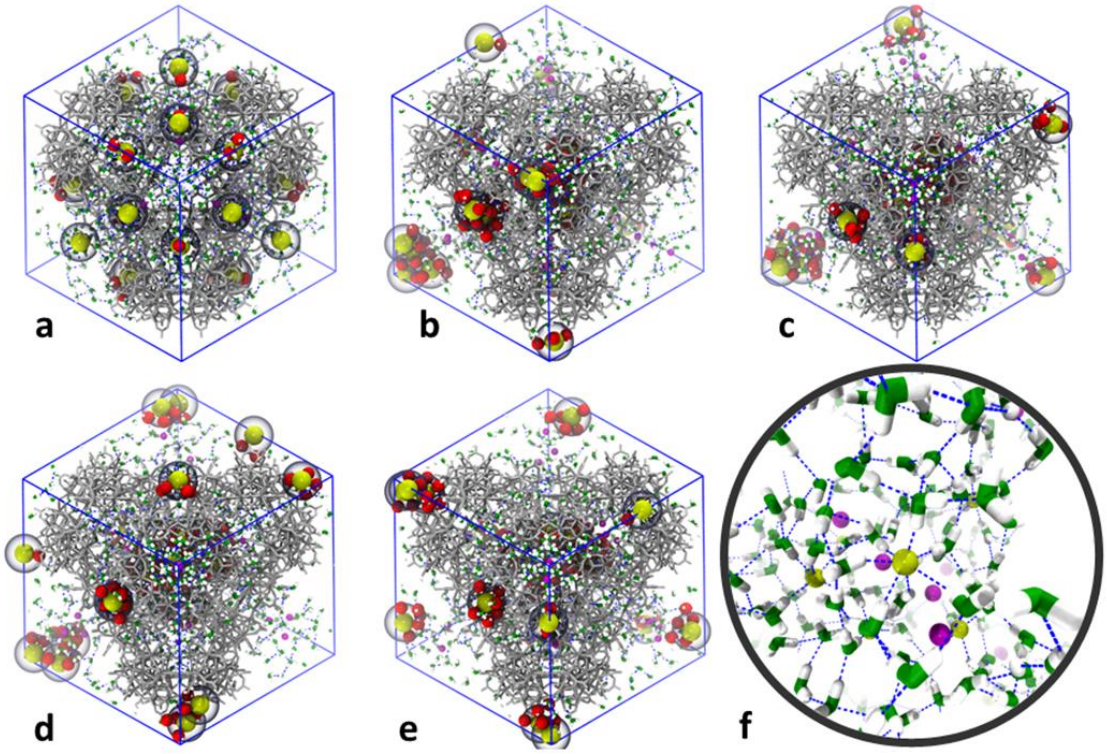

Figure 5.13 – Illustration of representation motions of K^+, Cl^- and H_2O captured at 0-4 ns in a 1 ns interval **(a-e)** from the NVT-MD simulation performed at 400 K for the hydrated ZF-3. **f)** A typical molecular arrangement of O_W-H..Cl..H-O_W water-bridge configuration where a single Cl^- ion participates up to 7 hydrogen bonds with neighbouring water molecules, is presented in the sub fig- f. K^+, Cl^- and O_W atoms are represented in purple, yellow, and green spheres, respectively. The O_W atoms lying within the 4 angstroms vicinity of Cl^- ions are highlighted in red and encapsulated with a transparent sphere.

Force field MD simulations were then carried out for the hydrated ZF-3 system at 400 K to probe the dynamics of both water and K^+ and Cl^- at longer time scale. These calculations were performed starting with a minimum energy MC configuration and using the same microscopic models and parameters used in the MC simulations. It appears that upon hydration, Cl^- ions undergo a translational motion while K^+ ions show only local displacements around their mean positions. This is illustrated in Figure 5.13, which reports the positions occupied by these ion

species over a typical 4 ns range. This is further unambiguously demonstrated by the MSDs plotted for each ionic species over the MD trajectory (Figure 5.14), which show more significant motions of Cl^- vs K^+, ~ 200 $Å^2$ and 10 $Å^2$ respectively for 4 ns MD run. Furthermore, a moderate magnitude of the MSD for Cl^- combined with its non-linear profile over time prevents the assessment of its self-diffusion coefficient. Indeed, such a dynamics refers to a medium-range mobility rather than a diffusion process as defined in the Fickian formalism. On the other hand, a quite fast long-range reorganization of the confined water molecules was evidenced. The corresponding MSD plot shows a linear regime over time (Figure 5.14). The derived self- diffusivity, D_s of 5.6×10^{-9} $m^2.s^{-1}$ at 400 K using the Einstein relation [43] is significantly faster than the values usually encountered for water confined in porous materials.[44–46]

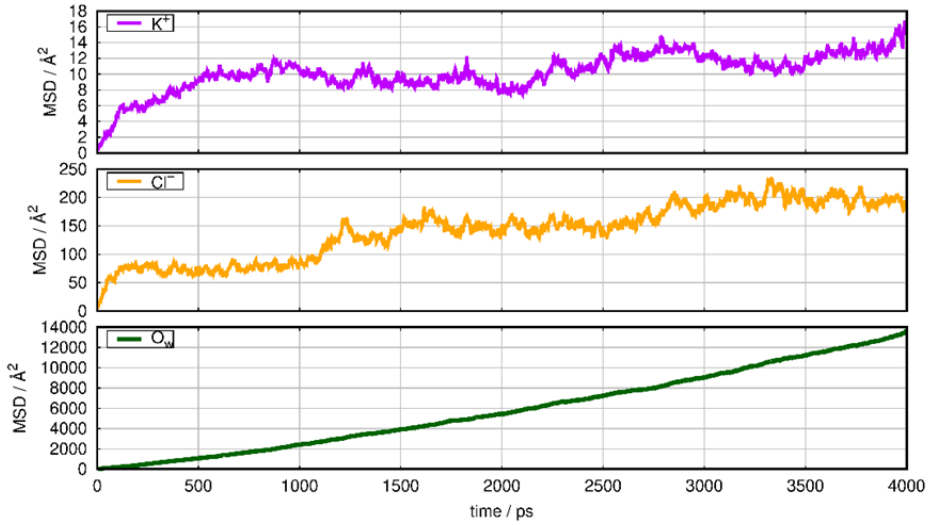

Figure 5.14 - Mean square displacement (MSD) of K^+, Cl^- and O_W atoms calculated from NVT-MD simulations performed at 400 K for ZF-3 phase in its hydrated state.

A careful analysis of the MD trajectory further revealed that water preferentially forms a core-shell type configuration assembling up to 7 water molecules hydrogen bonded to a single Cl^- ion (Figure 5.13). Noteworthy, the chlorine hydration shell is substantially similar to that reported in solution.[47] This H_2O/Cl^- core-shell reorganizes on very short time scales, ~50% of the water molecules in the coordination sphere of Cl^- being exchanged within a 2 ps range (see Figure 5.15). The dynamics of the $O_W…O_W$ and O_W...Cl^- pairs were further assessed in terms of their hydrogen bond intermittent life times (τ_i) calculated from the corresponding time correlation functions.[48] As depicted in Figure 5.16, τ_i ($O_W…O_W$) was found to be about twice longer than τ_i (O_W.. Cl^-) (26 ps vs 10 ps). Interestingly, τi ($O_W…O_W$) is faster than the value we previously reported for water

confined in a microporous MOF (47.9 ps for Y-shp-MOF-5 [49]). Such a relatively fast reorganization of water contributes to the high ion mobility within the ZF-3 porosity.

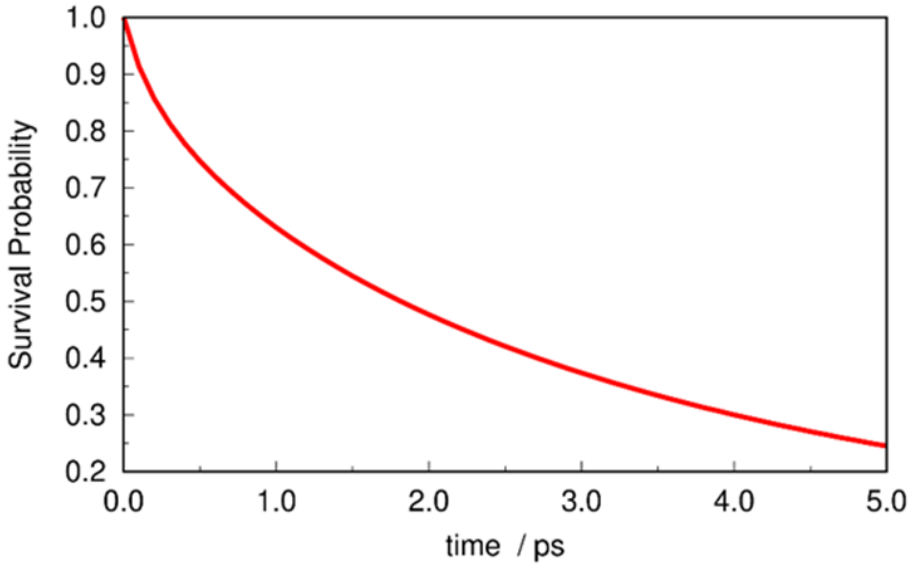

Figure 5.15 - Survival probability of core-shell like complexes formed by water molecules around 4 Å of Cl^- ions calculated for 5 ps windows derived from the NVT-MD trajectory obtained for the ZF-3 hydrated phase at 400 K.

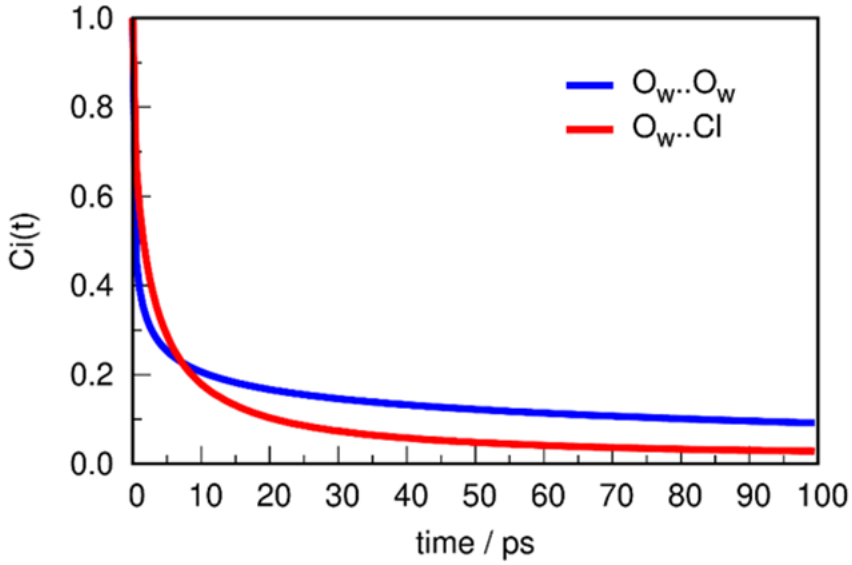

Figure 5.16 - Comparison of the intermittent hydrogen bond autocorrelation functions for $O_w..O_w$ and $O_w..Cl^-$ complexes calculated for 100 ps windows derived from the NVT-MD trajectory obtained for the ZF-3 hydrated phase at 400 K.

5.4. Conclusion

Besides a good ionic conductivity under humidity, ZF-3 might be a promising candidate to be integrated in impedance-based humidity sensors. From an electrical point of view, ZF-3 is very sensitive to water, as shown by the 8 orders of magnitude gap between conductivity values recorded at the anhydrous and the hydrated states (see Table 5.1, σ (363 K/0% RH) = 5.1 x 10^{-10} $S.cm^{-1}$ vs σ (363 K/95% RH) = 5.2 x 10^{-2} $S.cm^{-1}$). This sharp conductivity change with RH converges or even more surpasses that recorded for other zeolite or MOFs based devices already reported in the literature.[28,50–53] Furthermore, the conductivity dependence with RH perfectly follows the water uptake profile obtained from the volumetric adsorption isotherm (qnFigure 5.17).[20] The excellent correlation between conductivity and volumetric measurements highlights the good linearity response of ZF-3, one of the characteristics along with the sensitivity, to be fulfilled for considering ZF-3 with great promises for humidity sensors applications. Noteworthy, investigation of molecular cristals as humidity sensors is still scarce.

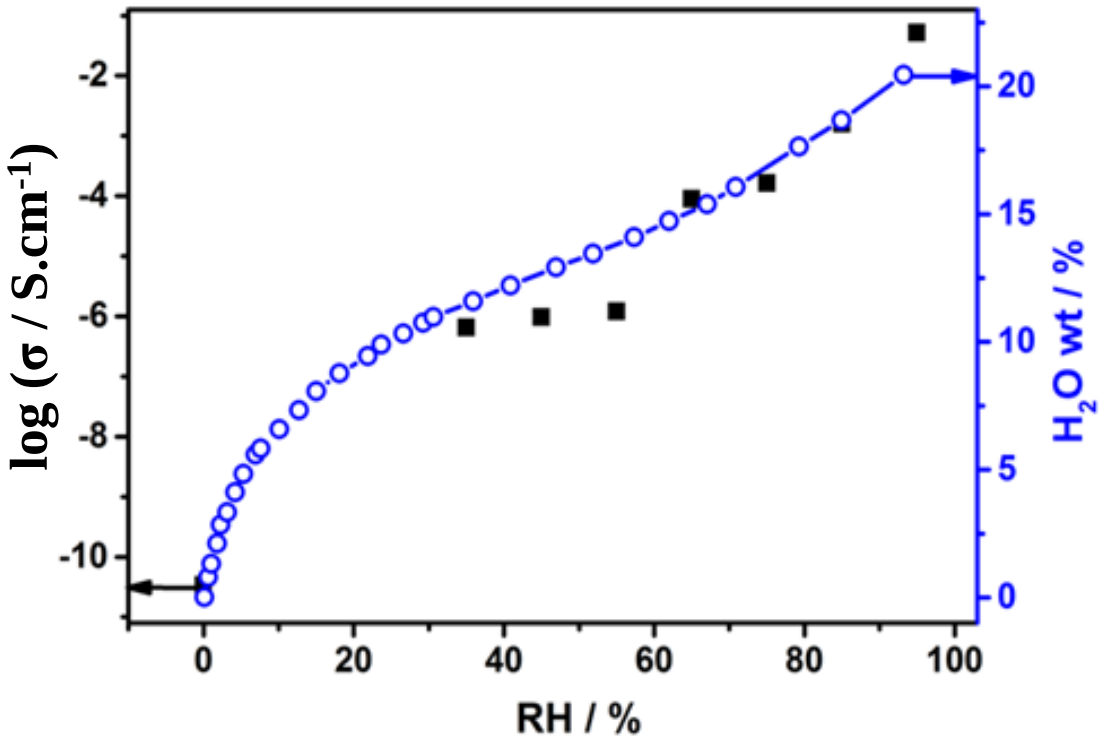

Figure 5.17 – Correlation between the Relative Humidity dependence of the conductivity recorded at 363 K and the water vapor uptake collected at 298 K for the ZF-3 powder (taken from reference [20]).

This study, further inspired from our investigations carried out on proton conducting MOFs (chapters 3 and 4), demonstrates that the combined experimental/modelling strategy we developed to understand conducting mechanism in MOFs is not restricted to this class of materials.

REFERENCES

[1] H. Tuller, Ionic Conduction and Applications, in: S. Kasap, P. Capper (Eds.), Springer Handb. Electron. Photonic Mater., Springer US, Boston, MA, 2007: pp. 213–228. https://doi.org/10.1007/978-0-387-29185-7_11.

[2] K.H.J. Buschow, R.W. Cahn, M.C. Flemings, B. Ilschner, E.J. Kramer, S. Mahajan, Encyclopedia of Materials: Science and Technology, MRS Bull. 29 (2004) 512. https://doi.org/10.1557/mrs2004.147.

[3] K. Funke, Solid State Ionics: from Michael Faraday to green energy—the European dimension, Sci. Technol. Adv. Mater. 14 (2013) 043502. https://doi.org/10.1088/1468-6996/14/4/043502.

[4] O. Yamamoto, Solid state ionics: a Japan perspective, Sci. Technol. Adv. Mater. 18 (2017) 504–527. https://doi.org/10.1080/14686996.2017.1328955.

[5] T. Nakamura, T. Akutagawa, K. Honda, A.E. Underhill, A.T. Coomber, R.H. Friend, A molecular metal with ion-conducting channels, Nature. 394 (1998) 159–162. https://doi.org/10.1038/28128.

[6] M. Moriya, D. Kato, W. Sakamoto, T. Yogo, Structural Design of Ionic Conduction Paths in Molecular Crystals for Selective and Enhanced Lithium Ion Conduction, Chem. - A Eur. J. 19 (2013) 13554–13560. https://doi.org/10.1002/chem.201300106.

[7] M. Moriya, K. Nomura, W. Sakamoto, T. Yogo, Precisely controlled supramolecular ionic conduction paths and their structure–conductivity relationships for lithium ion transport, CrystEngComm. 16 (2014) 10512–10518. https://doi.org/10.1039/C4CE01417K.

[8] M. Moriya, Construction of nanostructures for selective lithium ion conduction using self-assembled molecular arrays in supramolecular solids, Sci. Technol. Adv. Mater. 18 (2017) 634–643. https://doi.org/10.1080/14686996.2017.1366816.

[9] H. Zhu, D.R. MacFarlane, J.M. Pringle, M. Forsyth, Organic Ionic Plastic Crystals as Solid-State Electrolytes, Trends Chem. 1 (2019) 126–140. https://doi.org/10.1016/j.trechm.2019.01.002.

[10] Oki, Moriya, Synthesis of an Adduct-Type Organic Ionic Crystal with Solid-State Ionic Conductivity from A Thiocyanate-Based Ionic Liquid and B(C6F5)3, Crystals. 9 (2019) 567. https://doi.org/10.3390/cryst9110567.

[11] C.D. Assouma, A. Crochet, Y. Chérémond, B. Giese, K.M. Fromm, Kinetics of Ion Transport through Supramolecular Channels in Single Crystals, Angew. Chemie Int. Ed. 52 (2013) 4682–4685. https://doi.org/10.1002/anie.201208195.

[12] A.D. Sendek, G. Cheon, M. Pasta, E.J. Reed, Quantifying the Search for Solid Li-Ion Electrolyte Materials by Anion: A Data-Driven Perspective, J. Phys. Chem. C. 124 (2020) 8067–8079. https://doi.org/10.1021/acs.jpcc.9b10650.

[13] M. Montanino, S. Passerini, G.B. Appetecchi, Electrolytes for rechargeable lithium batteries, in: Recharg. Lithium Batter., Elsevier, 2015: pp. 73–116. https://doi.org/10.1016/B978-1-78242-090-3.00004-3.

[14] Q. Li, J. Chen, L. Fan, X. Kong, Y. Lu, Progress in electrolytes for rechargeable Li-based batteries and beyond, Green Energy Environ. 1 (2016) 18–42. https://doi.org/10.1016/j.gee.2016.04.006.

[15] M.C. Pitman, A.C.T. van Duin, Dynamics of Confined Reactive Water in Smectite Clay–Zeolite Composites, J. Am. Chem. Soc. 134 (2012) 3042–3053. https://doi.org/10.1021/ja208894m.

[16] E. Fois, G. Tabacchi, The different organization of Water in zeolite L and its MOF mimic, ChemRxiv. 234 (2019) 495–511. https://doi.org/10.26434/chemrxiv.7761791.v1.

[17] N.W. Ockwig, R.T. Cygan, L.J. Criscenti, T.M. Nenoff, Molecular dynamics studies of nanoconfined water in clinoptilolite and heulandite zeolites, Phys. Chem. Chem. Phys. 10 (2008) 800–807. https://doi.org/10.1039/B711949F.

[18] X. Wang, Y. Wang, M.A. Silver, D. Gui, Z. Bai, Y. Wang, W. Liu, L. Chen, J. Diwu, Z. Chai, S. Wang, Superprotonic conduction through one-dimensional ordered alkali metal ion chains in a lanthanide-organic framework, Chem. Commun. 54 (2018) 4429–4432. https://doi.org/10.1039/C8CC00572A.

[19] S. Wang, M. Wahiduzzaman, L. Davis, A. Tissot, W. Shepard, J. Marrot, C. Martineau-Corcos, D. Hamdane, G. Maurin, S. Devautour-Vinot, C. Serre, A robust zirconium amino acid metal-organic framework for proton conduction, Nat. Commun. 9 (2018) 4937. https://doi.org/10.1038/s41467-018-07414-4.

[20] J.I. Choi, H. Chun, M.S. Lah, Zirconium-Formate Macrocycles and Supercage: Molecular Packing versus MOF-like Network for Water Vapor Sorption, J. Am. Chem. Soc. 140 (2018) 10915–10920. https://doi.org/10.1021/jacs.8b06757.

[21] M.B. Salamon, Physics of Superionic Conductors, Springer Berlin Heidelberg, Berlin, Heidelberg, 1979. https://doi.org/10.1007/978-3-642-81328-3.

[22] D.-W. Lim, H. Kitagawa, Proton Transport in Metal–Organic Frameworks, Chem. Rev. 120 (2020) 8416–8467. https://doi.org/10.1021/acs.chemrev.9b00842.

[23] Y. Ye, L. Gong, S. Xiang, Z. Zhang, B. Chen, Metal–Organic Frameworks as a Versatile Platform for Proton Conductors, Adv. Mater. 32 (2020) 1907090. https://doi.org/10.1002/adma.201907090.

[24] M. Wahiduzzaman, S. Wang, J. Schnee, A. Vimont, V. Ortiz, P.G. Yot, R. Retoux, M. Daturi, J.S. Lee, J.-S.S. Chang, C. Serre, G. Maurin, S. Devautour-Vinot, A High Proton Conductive Hydrogen-Sulfate Decorated Titanium Carboxylate Metal-Organic Framework, ACS Sustain. Chem. Eng. 7 (2019) 5776–5783. https://doi.org/10.1021/acssuschemeng.8b05306.

[25] S. Shalini, S. Aggarwal, S.K. Singh, M. Dutt, T.G. Ajithkumar, R. Vaidhyanathan, 10000-Fold Enhancement in Proton Conduction by Doping of Cesium Ions in a Proton-Conducting Zwitterionic Metal-Organic Framework, Eur. J. Inorg. Chem. 2016 (2016) 4382–4386. https://doi.org/10.1002/ejic.201600364.

[26] D.D. Borges, S. Devautour-Vinot, H. Jobic, J. Ollivier, F. Nouar, R. Semino, T. Devic, C. Serre, F. Paesani, G. Maurin, Proton Transport in a Highly Conductive Porous Zirconium-Based Metal-Organic Framework: Molecular Insight, Angew. Chemie - Int. Ed. 55 (2016) 3919–3924. https://doi.org/10.1002/anie.201510855.

[27] S. Hwang, E.J. Lee, D. Song, N.C. Jeong, High Proton Mobility with High Directionality in Isolated Channels of MOF-74, ACS Appl. Mater. Interfaces. 10 (2018) 35354–35360. https://doi.org/10.1021/acsami.8b11816.

[28] P.G.M. Mileo, K. Adil, L. Davis, A. Cadiau, Y. Belmabkhout, H. Aggarwal, G. Maurin, M. Eddaoudi, S. Devautour-Vinot, Achieving Superprotonic Conduction with a 2D Fluorinated Metal–Organic Framework, J. Am. Chem. Soc. 140 (2018) 13156–13160. https://doi.org/10.1021/jacs.8b06582.

[29] W. Chen, J. Wang, L. Zhao, W. Dai, Z. Li, G. Li, Enhancing proton conductivity of a highly water stable 3D Sr(II) metal-organic framework by exposure to aqua-ammonia vapor, J. Alloys Compd. 750 (2018) 895–901. https://doi.org/10.1016/j.jallcom.2018.04.087.

[30] S. Nandi, S. Wang, M. Wahiduzzaman, V. Yadav, K. Taksande, G. Maurin, C. Serre, S. Devautour-Vinot, Multivariate Sulfonic-Based Titanium Metal–Organic Frameworks as Super-protonic Conductors, ACS Appl. Mater. Interfaces. 13 (2021) 20194–20200. https://doi.org/10.1021/acsami.1c03644.

[31] W.J. Phang, W.R. Lee, K. Yoo, D.W. Ryu, B. Kim, C.S. Hong, pH-Dependent Proton Conducting Behavior in a Metal-Organic Framework Material, Angew. Chemie Int. Ed. 53 (2014) 8383–8387. https://doi.org/10.1002/anie.201404164.

[32] W.J. Phang, H. Jo, W.R. Lee, J.H. Song, K. Yoo, B. Kim, C.S. Hong, Superprotonic conductivity of a uio-66 framework functionalized with sulfonic acid groups by facile postsynthetic oxidation, Angew. Chemie Int. Ed. 54 (2015) 5142–5146. https://doi.org/10.1002/anie.201411703.

[33] X.S. Xing, Z.H. Fu, N.N. Zhang, X.Q. Yu, M.S. Wang, G.C. Guo, High proton conduction in an excellent water-stable gadolinium metal-organic framework, Chem. Commun. 55 (2019) 1241–1244. https://doi.org/10.1039/c8cc08700h.

[34] S.-Z. Huang, S.-S. Liu, H. Zhang, Z. Han, G. Zhao, X.-Y. Dong, S.-Q. Zang, Dual-Functional Proton-Conducting and pH-Sensing Polymer Membrane Benefiting from a Eu-MOF, ACS Appl. Mater. Interfaces. 12 (2020) 28720–28726. https://doi.org/10.1021/acsami.0c08103.

[35] X. Liang, B. Li, M. Wang, J. Wang, R. Liu, G. Li, Effective Approach to Promoting the Proton Conductivity of Metal–Organic Frameworks by Exposure to Aqua–Ammonia Vapor, ACS Appl. Mater. Interfaces. 9 (2017) 25082–25086. https://doi.org/10.1021/acsami.7b07635.

[36] H. Wu, F. Yang, X.-L. Lv, B. Wang, Y.-Z. Zhang, M.-J. Zhao, J.-R. Li, A stable porphyrinic metal–organic framework pore-functionalized by high-density carboxylic groups for proton conduction, J. Mater. Chem. A. 5 (2017) 14525–14529. https://doi.org/10.1039/C7TA03917D.

[37] P. Ramaswamy, N.E. Wong, B.S. Gelfand, G.K.H. Shimizu, A Water Stable Magnesium MOF That Conducts Protons over 10 –2 S cm –1, J. Am. Chem. Soc. 137 (2015) 7640–7643. https://doi.org/10.1021/jacs.5b04399.

[38] S. Khatua, A.K. Bar, J.A. Sheikh, A. Clearfield, S. Konar, Achieving Amphibious Superprotonic Conductivity in a CuI Metal–Organic Framework by Strategic Pyrazinium Salt Impregnation, Chem. - A Eur. J. 24 (2018) 872–880. https://doi.org/10.1002/chem.201704088.

[39] M. V. Nguyen, T.H.N. Lo, L.C. Luu, H.T.T. Nguyen, T.N. Tu, Enhancing proton conductivity in a metal–organic framework at T > 80 °C by an anchoring strategy, J. Mater. Chem. A. 6 (2018) 1816–1821. https://doi.org/10.1039/C7TA10148A.

[40] Y.-H. Han, Y. Ye, C. Tian, Z. Zhang, S.-W. Du, S. Xiang, High proton conductivity in an unprecedented anionic metalloring organic framework (MROF) containing novel metalloring clusters with the largest diameter, J. Mater. Chem. A. 4 (2016) 18742–18746. https://doi.org/10.1039/C6TA07939C.

[41] X. Lai, Y. Liu, G. Yang, S.S. Liu, Z. Shi, Y. Lu, F. Luo, S.S. Liu, Controllable proton-conducting pathways via situating polyoxometalates in targeting pores of a metal–organic framework, J. Mater. Chem. A. 5 (2017) 9611–9617. https://doi.org/10.1039/C6TA10958F.

[42] L. Qin, Y. Yu, P. Liao, W. Xue, Z. Zheng, X. Chen, Y. Zheng, A "Molecular Water Pipe": A Giant Tubular Cluster {Dy 72 } Exhibits Fast Proton Transport and Slow Magnetic Relaxation, Adv. Mater. 28 (2016) 10772–10779. https://doi.org/10.1002/adma.201603381.

[43] D. Frenkel, B. Smit, Understanding molecular simulation _ from algorithms to applications (2002, Academic Press).pdf, (2002).

[44] F. Salles, S. Bourrelly, H. Jobic, T. Devic, V. Guillerm, P. Llewellyn, C. Serre, G. Ferey, G. Maurin, Molecular Insight into the Adsorption and Diffusion of Water in the Versatile Hydrophilic/Hydrophobic Flexible MIL-53(Cr) MOF, J. Phys. Chem. C. 115 (2011) 10764–10776. https://doi.org/10.1021/jp202147m.

[45] D.D. Borges, S. Devautour-Vinot, H. Jobic, J. Ollivier, F. Nouar, R. Semino, T. Devic, C. Serre, F. Paesani, G. Maurin, Proton Transport in a Highly Conductive Porous Zirconium-Based Metal–Organic Framework: Molecular Insight, Angew. Chemie Int. Ed. 55 (2016) 3919–3924. https://doi.org/10.1002/anie.201510855.

[46] P.G.M. Mileo, T. Kundu, R. Semino, V. Benoit, N. Steunou, P.L. Llewellyn, C. Serre, G. Maurin, S. Devautour-Vinot, Highly Efficient Proton Conduction in a Three-Dimensional Titanium Hydrogen Phosphate, Chem. Mater. 29 (2017) 7263–7271. https://doi.org/10.1021/acs.chemmater.7b01850.

[47] R. Mancinelli, A. Botti, F. Bruni, M.A. Ricci, A.K. Soper, Hydration of Sodium, Potassium, and Chloride Ions in Solution and the Concept of Structure Maker/Breaker, J. Phys. Chem. B. 111 (2007) 13570–13577. https://doi.org/10.1021/jp075913v.

[48] D.C. Rapaport, Hydrogen bonds in water, Mol. Phys. 50 (1983) 1151–1162. https://doi.org/10.1080/00268978300102931.

[49] I. Skarmoutsos, M. Eddaoudi, G. Maurin, Highly Efficient Rare-Earth-Based Metal–Organic Frameworks for Water Adsorption: A Molecular Modeling Approach, J. Phys. Chem. C. 123 (2019) 26989–26999. https://doi.org/10.1021/acs.jpcc.9b07402.

[50] A. Weiss, N. Reimer, N. Stock, M. Tiemann, T. Wagner, Surface-modified CAU-10 MOF materials as humidity sensors: impedance spectroscopic study on water uptake, Phys. Chem. Chem. Phys. 17 (2015) 21634–21642. https://doi.org/10.1039/C5CP01988E.

[51] J. Zhang, L. Sun, C. Chen, M. Liu, W. Dong, W. Guo, S. Ruan, High performance humidity sensor based on metal organic framework MIL-101(Cr) nanoparticles, J. Alloys Compd. 695 (2017) 520–525. https://doi.org/10.1016/j.jallcom.2016.11.129.

[52] Y. Gao, P. Jing, N. Yan, M. Hilbers, H. Zhang, G. Rothenberg, S. Tanase, Dual-mode humidity detection using a lanthanide-based metal–organic framework: towards multifunctional humidity sensors, Chem. Commun. 53 (2017) 4465–4468. https://doi.org/10.1039/C7CC01122A.

[53] J. Zou, H. He, J. Dong, Y. Long, A guest/host material of LiCl/H-STI (stilbite) zeolite assembly: preparation, characterization and humidity-sensitive propertiesElectronic supplementary information (ESI) available: XRD patterns of ZSM-39 system, silica gel system, quartz system, ZSM-5 sy, J. Mater. Chem. 14 (2004) 2405. https://doi.org/10.1039/b316040h.

General Conclusions and Perspectives

This thesis focused on the exploration of new proton conducting MOFs with outstanding performances for solid-state electrolyte applications. Distinct strategies were successfully considered to incorporate intra-framework proton sources through adequate functionalization of the organic linkers of the MOF or to introduce extra-proton carriers in the MOF pores to impart efficient proton pathways. The corresponding engineered materials were fully characterized and their conducting performances were screened over various temperature/relative humidity conditions. In complement to this experimental effort, a modelling approach developed in the group was conducted to unravel the microscopic proton transfer mechanism of the best proton conducting solids. This joint experimental/modelling strategy, which has been developed in the group along the last decade, was demonstrated to be particularly powerful to fully characterize these proton-conducting MOFs. We then further extended this approach to another class of materials, a molecular crystal containing KCl pairs, for ionic conduction purposes.

More specifically, inspired by the high conductivity performance of Nafion^{TM} in relation with the hydrophilicity of its terminal sulfonic acid groups, we firstly substituted the pending –CO_2H moieties of the BTC linkers of MIP-207 by -SO_3H groups using a multicomponent approach. The series of the multivariate MIP-207-$(SO_3H\text{-IPA})_x$-$(BTC)_{1-x}$ was demonstrated to combine high proton conductivity ($\sigma > 10^{-2}$ S.cm^{-1}) with other key criteria for the application purpose, such as good thermal/water stability under working conditions (T = 363 K, RH = 95%) and eco-friendly/scalable synthesis preparation. Noteworthy, the main sulfonic-based MOFs reported in the literature rarely fulfil all these criteria, demonstrating that the application of the mixed-ligand strategy to fine-tune the pristine MOFs is largely advantageous.

A second strategy explored the incorporation of ionic liquids as proton transfer agents in a Brønsted acid grafted MOF, MIL-101(Cr)–SO_3H. The objective was to use a stable mesoporous MOF that acts not only as a host scaffold for the ionic liquid but also as a source of acidic protons. Through the impregnation of EMIMCl ionic liquid, MIL-101(Cr)–SO_3H was revealed as a highly performing proton conducting composite at the anhydrous state ($\sigma_{473\,K} = 1.5 \times 10^{-3}$ S.cm^{-1}) as well as under humidity ($\sigma_{(343\ K/60\%–80\%\ RH)} \geq 0.10$ S.cm^{-1}) conditions. It is the first time that the combination of efficient proton transfer agents with intrinsic proton conducting MOF is explored,

which undoubtedly demonstrates great promises to design proton conducting solid electrolytes in versatile conditions.

Apart from the strategies detailed in chapters 3 and 4, we equally developed other approaches to boost the proton conductivity of MOFs, which are not described in this manuscript as they are still at their infancy: Noteworthy, we explored the proton conductivity enhancement induced by the material structural change upon temperature and water adsorption, considering two different MOFs: a Zn-based MOF with intrinsic HSO_4 proton donners, from the University of Pittsburg -Prof. N. Rosi- and a Mo-based MOF with coordinated water as proton source, from the King Abdullah University of Science and Technology – Prof. M. Eddaoudi-. We observed that these materials become super-protonic conductors due to a phase transition, which seems to favour an efficient H-bonded pathway for the proton transport, resulting from the reorganization of the water molecules in the pores and a change of their interactions with the proton donor beared by the MOF skeleton. Further investigations are now in progress to confirm this microscopic mechanism.

Conclusively, this work further supports that the MOFs richness in terms of functionality, topology and pore size/shape offers a large panel of strategies to efficiently design materials with exceptional proton conductivity properties. Based on this, we enlarged our investigation to the exploration of super-ionic conductivity of another class of materials, i.e., molecular crystals. Noteworthy, the ionic conduction properties of molecular crystals are much less studied than those of porous solids like MOFs, zeolites, mesoporous silica or clays, more particularly under humidified conditions because of hydrothermal stability issues. In this work, we selected ZF-3, a zirconium-formate molecular crystal containing KCl ion pairs and showing robustness over humid conditions. We established the key role of water in boosting its guest-assisted ionic conduction performance. Remarkably, a transition from insulating towards superionic behaviour was evidenced upon hydration. We showed that this behavior results from faster dynamics of Cl^- species consecutive of the creation of Cl^-/H_2O core-shell structures throughout the pores of ZF-3 in the presence of water molecules.

In summary, this study paves the way towards the development of alternative proton and ionic conductors based on MOFs and in a less extend on molecular crystals. This work led to the publication of 3 articles in well-established journals:

1 - “Superionic conduction in a zirconium-formate molecular solid”, M. Wahiduzzaman, S Nandi, V Yadav, K. Taksande, G Maurin, H Chun, S. Devautour-Vinot, *J. Mat. Chem. A*, **8**, 17951 (2020).

2 - “Multivariate Sulfonic-based Titanium Metal-Organic Frameworks as Super-Protonic Conductors”, S. Nandi, S. Wang, M. Wahiduzzaman, V. Yadav, K. Taksande, G. Maurin, C. Serre, S. Devautour-Vinot, *ACS Appl. Mater. Interfaces*, **13**, 20194 (2021).

3 – “Robust ionic liquid@MOF composite as a versatile superprotonic conductor”, K. Taksande, E. Gkaniatsou, C. Simonnet-Jégat, C. Livage, G. Maurin, N. Steunou and S. Devautour-Vinot, *Dalton Trans.*, **50**, 15914, (2021).

Despite the fact that the materials investigated in the scope of this study combine targeted values of conductivity with thermal and hydrolytic stability, challenges are still required before addressing them at the application level. The incorporation of these electrolytes into membrane electrode assemblies calls for the preparation of composites with polymers, which was not addressed in this work. In this context, efforts are still needed in improving the compatibility between the polymer and the second component, i.e., MOF or molecular crystal, with two objectives: the increase of the MOF/molecular crystal loading within the polymer matrix in order to multiple conductivity pathways and maintain high conductivity levels of the added component and the conservation of the mechanical properties of the membrane. Once this challenge addressed, the incorporation of MOFs and molecular crystals into functional devices can be envisaged with great promises to compete with Nafion^{TM} or other commercial materials for diverse energy and environmental related technologies.

Appendix

Appendix 1 - Listing of anhydrous and water-mediated proton conducting MOFs, their topology, pore, guests, proton conductivity value and operating conditions published in the literature according to the reviews of Kitagawa *et al.* (2021), Kumar Biradha et al. (2021) and Ruqiang Zou *et al.* (2020). Appendix 1.1 & 1.2 reports the full list of MOFs that display a superprotonic behavior ($\sigma > 10^{-3}$ S.cm^{-1}).

Appendix 1.1 – PC@MOF Low Temperature domain (< 373 K)

Material	Features and Topology	Pore Guests	Sigma (S.cm^{-1})	Conditions	Reference
H_2SO_4@MIL-101-SO_3H	3D Framework	H_2O, H_2SO_4	1.82	343 K, 90% RH	[1]
[Gd(H_4nmp)(H_2O)$_2$]Cl.2H_2O [a] [Gd$_2$(H_3nmp)$_2$].xH_2O [a]	3D framework with 2D charged layers	H_2O, Cl H_2O	5.10 x 10^{-1} 3.79 x 10^{-2}	367 K, 98% RH	[2]
ZrTSaT ZrTST	3D Framework	H_2O	3.7 x 10^{-1} 1.9 x 10^{-3}	363 K, 90% RH	[3]
Cr-MIL-88B-PSA [b] Cr-MIL-88B-PESA [c]	Spindle-shaped morphology with 1D open channel	H_2O, SO_3H	1.58 x 10^{-1} 4.50 x 10^{-2}	373 K, 85% RH	[4]
IM-UiO-66-AS [d]	3D framework	H_2O, SO_3H, Im	1.54 x 10^{-1}	353 K, 98% RH	[5]
NH_4Br@MIL-101-Cr	3D framework	NH_4Br, H_2O	1.53 x 10^{-1}	363 K, 100% RH	[6]
PMNS-1 PMNS2 MIL-88B@-NH2	3D framework	H_2O	1.52 x 10^{-1} 4.68 x 10^{-2} 3.92 x 10^{-3}	353 K, 100% RH	[7]
Co-tri Co-tetra Co-fdc [e]	1D structures	H_2O	1.49 x 10^{-1} 4.15 x 10^{-2} 4.85 x 10^{-3}	353 K, 98% RH	[8]
EMIMCl@MIL-101(Cr)SO_3H	3D framework	H_2O, EMIMCl	1.40 x 10^{-1}	343 K, 80% RH	[9]
BUT-8(Cr)-SO_3H	3D framework with 1D pores	H_2O	1.27 x 10^{-1}	353 K, 100% RH	[10]
PCMOF2 ½ (Pz) [f] PCMOF2 ½ (Tz) [g] PCMOF2 (Pz) [f]	3D honeycomb with 1D channels	Pz, H_2O Tz, H_2O Pz, H_2O	1.10 x 10^{-1} 1.17 x 10^{-1} 4.60 x 10^{-2}	358 K, 90% RH	[11]
MOF – 802 CD@MOF - 802	3D framework	H_2O, CD-Carbon dots	1.50 x 10^{-2} 1.13 x 10^{-1}	298 K, 98% RH	[12]
H_3PO_4@MIL-101-SO_3H H_2SO_4@MIL-101-NH_2	3D Framework	H_2O, H_3PO_4	0.90 x 10^{-1} 5.80 x 10^{-2}	358 K, 95% RH	[13]
UiO-66-(SO_3H)$_2$	3D framework post-synthetic oxidized	H_2O	8.40 x 10^{-2}	353 K, 90% RH	[14]
{H[($N(CH_3)_4$)$_2$][Gd_3($NIPA)_6$]}3H_2O [h]	3D framework	H_2O	7.17 x 10^{-2}	348 K, 98% RH	[15]

CPM-103a CPM-103b	3D framework with cubic cavities	H_2O	5.80×10^{-2} 4.80×10^{-2}	295 K, 98% RH	[16]
$[Zr_{36}O_{24}(OH)_{48}(HCO_2)_{48}]\cdot 3KCl$	Hexagonal disc-like macromolecule	H_2O	5.20×10^{-2}	363 K, 95% RH	[17]
Fe-CAT-5 Ti-CAT-5	3D extended metal catecholates framework	H_2O, DMA	5.00×10^{-2} 8.20×10^{-4}	298 K, 98% RH	[18]
$[Sr(\mu_2\text{-}H_2PhIDC)2(H_2O)4]\cdot 2H_2On$ [i]	3D framework with irregular 1D pores	NH_3, H_2O	4.76×10^{-2}	363 K, 98% RH	[19]
$\{[Eu_5(OH)_6(TZI)_3(DMA)1.5](H_2O)10.5\cdot DMA\cdot 0.5H_2O\}n$ [j]	3D framework	H_2O, tetrazolium	4.45×10^{-2}	373 K, 93% RH	[20]
1-Butylsulfonate-3-methylimidazolium bisulfate@MIL-101	3D framework	H_2O, SO_4H	4.40×10^{-2}	323 K, ~23% RH	[21]
$\{[Co_3(mClPhIDC)_2(H_2O)_6]\cdot 2H_2O\}n$ [k] $\{[Co_3(p\text{-}ClPhHIDC)_3(H_2O)_3]\cdot 6H_2O\}n$ [l]	3D framework with 1D open channels	H_2O NH_3, H_2O	2.89×10^{-2} 4.25×10^{-2}	373 K, 98% RH	[22]
$\{[(Me_2NH_2)_3(SO_4)]_2[Zn_2(ox)_3]\}n$ [m]	3D supramolecular structure	H_2O, DMA^+, SO_4^{2-}	4.20×10^{-2}	298 K, 98% RH	[23]
H_2SO_4@MIL-101 H_3PO_4@MIL-101	3D micro and mesoporous	H_2O, H_2SO_4 H_2O, H_3PO_4	4.00×10^{-2} 2.50×10^{-4}	296 K, 20% RH	[24]
$Co(DCDPP)\cdot 5H_2O$ [n]	3D framework with 1D pores	H_2O	3.90×10^{-2}	353 K, 97% RH	[25]
BUT – 76 BUT - 77	3D framework	H_2O	3.08×10^{-2} 8.55×10^{-3}	353 K, 100% RH	[26]
$Mg_2(H_2O)_4(H_2L)\cdot H_2O$ [o] (PCMOF-10)	2D layered architecture	H_2O	3.55×10^{-2}	343 K, 95% RH	[27]
$[In_2(OH)_2(BPTC)]\cdot 6H_2O$ (InOF-1) $[Ni_2(BPTC)(HCOOH)_2]\cdot 3H_2O$ (NiOF-1)	Helical 3D framework with 1D channel	H_2O, HCOOH/OH	7.86×10^{-3} 3.41×10^{-2}	328 K, 95% RH	[28]
H_3PO_4@MIL-100	3D framework	H_3PO_4, H_2O	3.00×10^{-2}	343 K, 80% RH	[29]
Cu^I-MOF	Interpenetrated 3D network with 1D channels	$Pz.3H_2SO_4$ Pz.6HCl $Pz.2H_3PO_4$	3.00×10^{-2} 2.94×10^{-2} 1.25×10^{-2}	353 K, 95% RH 353 K, 95% RH 348 K, 95% RH	[30]
$Na_2[Eu(SDB)_2(COO)]\cdot 0.375DMF\cdot 0.4H_2O$ [p]	3D frameworks with 1D pores	H_2O	2.91×10^{-2}	363 K, 90% RH	[31]
VNU-15	3D framework	H_2O, DMA	2.90×10^{-2}	368 K, 60% RH	[32]
$[Fe^{III}_6(\mu_6\text{-}O)L_4Cl_6]^{2-}$	1D framework	H_2O	2.84×10^{-2}	358 K, 98% RH	[33]
MIP-177-SO_4H-LT [q]	3D framework with array of hexagonal 1D channels	H_2O, SO_4H	2.60×10^{-2}	298 K, 95% RH	[34]

MIP-207-(SO_3H-IPA)x-(BTC)$_{1-x}$ [r]	2D layered structure	H_2O, SO_3H	2.60×10^{-2}	363 K, 95% RH	[35]
{[Tb_4(TTHA)$_2$(H_2O)$_4$]7H_2O}$_n$ [s]	3D network structure	H_2O, -COOH	2.57×10^{-2}	333 K, 98% RH	[36]
Cd-BQ	Diamond like network with 2D intersected channels	H_2O, $Me_2NH_2^+$	2.30×10^{-2}	303 K, 95% RH	[37]
H^+@Ni-MOF-74 [t]	3D framework with functionalized groups 1D hexagonal pores	H_2O	2.20×10^{-2}	353 K, 95% RH	[38]
PCMOF2 ½	3D honeycomb with 1D channels	H_2O	2.10×10^{-2}	358 K, 90% RH	[39]
KAUST-7’	2D layers macromolecularly connected through H-bonds	H_2O	2.00×10^{-2}	363 K, 95% RH	[40]
($C_6H_{14}N_2$)-[$NiV_2O_6H_8(P_2O_7)_2$]·2H_2O	3D open framework	H_2O	2.00×10^{-2}	333 K, 86% RH	[41]
PCM-1	1D framework	H_2O	1.85×10^{-2}	353 K, 98% RH	[42]
Im@(NENU-3) [u] Im-Cu@(NENU-3a) [u]	3D framework	H_2O, Imidazole	1.82×10^{-2} 3.16×10^{-4}	343 K, 90% RH	[43]
$His_{8.2}$@VNU-23 [v]	3D framework with 1D pores	H_2O	1.79×10^{-2}	368 K, 85% RH	[44]
MROF-1	3D framework with 1D pores	H_2O	1.72×10^{-2}	343 K, 97% RH	[45]
Im@NiL2	3D framework	H_2O, Imidazole	1.72×10^{-2}	353 K, 98% RH	[46]
$Mg_4(C_8O_4H_4)_4(C_5NOH_5)$4Cs·7$H_2O$	2D layered material	H_2O, Cs^+	1.61×10^{-2}	363 K, 90% RH	[47]
TETA@HPW-MIL101 [w]	3D framework	H_2O, TETA, HPW	1.52×10^{-2}	353 K, 100% RH	[48]
$NaCu_3(mtz)_4$	3D framework with 1D channels	H_2O	1.33×10^{-2}	343 K, 100% RH	[49]
Im-Fe-MOF [u] Im@Fe-MOF [u] Fe-MOF	3D framework with 1D channels	H_2O, Imidazole	1.21×10^{-2} 4.23×10^{-3} 1.20×10^{-4}	333 K, 98% RH	[50]
PCC-72	3D framework with 1D channels	H_2O	1.20×10^{-2}	368 K, 95% RH	[51]
CPM-102	3D framework with two types of 1D channels	H_2O, NH_4^+ cations	1.10×10^{-2}	295 K, 98% RH	[52]
Cu(H_2spip)Cl_2·H_2O [x] Cu_2H_2(Hspip)$_2Cl_4$·H_2O [x] Cu(Hspip)(HPO_4)·H_2O [x]	2D layered material	H_2O	1.09×10^{-2} 6.47×10^{-3} 6.90×10^{-4}	368 K, 97% RH	[53]
POM-OF	3D open framework with 1D helical channels	H_2O	1.04×10^{-2}	353, 75% RH	[54]

$(DMA)_3[Zr(HL)F_2]$ [y]	3D framework	H_2O	1.00×10^{-2}	353 K, 95% RH	[55]
$[Cu_2(phen)_2(AcO)_2(H_2O)_2][Al(OH)_6Mo_6O_{18}]M^+(nH_2O)$ ($M^+ = H^+, Li^+, Na^+, K^+$)	3D framework with 1D pores	H_2O, M^+	$\sim 1.0 \times 10^{-2}$	290 K, 80% RH	[56]
$Zn_3(bpdc)_2(pdc)(DMF)\cdot 6DMF$ [z]	3D framework with 1D pores	H_2O, DMF	9.50×10^{-3}	333 K, 97% RH	[57]
JLU-Liu44	3D framework	H_2O, $Me_2NH_2^+$	8.40×10^{-3}	300 K, 98% RH	[58]
ZrPP-1	3D framework with 1D rodlike chains	H_2O, $Me_2NH_2^+$	8.00×10^{-3}	298 K, 98% RH	[59]
$La(H_5DTMP)\cdot 7H_2O$ [aa]	3D framework with small 1D channels	H_2O	8.00×10^{-3}	297 K, 98% RH	[60]
$(NH_4)_2(adp)[Zn_2(ox)_3]\cdot 3H_2O$ [ab]	2D honeycomb sheets	H_2O, $NH4^+$, adp	8.00×10^{-3}	298 K, 98% RH	[61]
$[Him]_2Tb_2(ox)_4(H_2O)_2\cdot 2H_2O$ [ac] $[Hmim]_2Eu_2(ox)_4(H_2O)_2\cdot 2H_2O$ [ac] $[Him]_2Eu_2(ox)_4(H_2O)_2\cdot 2H_2O$ [ac]	3D open framework	H_2O, Imidazolium	7.70×10^{-2} 7.10×10^{-3} 4.60×10^{-3}	343 K, 98% RH 353 K, 98% RH 353 K, 98% RH	[62]
MOF-808	3D breathing framework	H_2O	7.58×10^{-3}	315 K, 99% RH	[63]
UiO-66	3D with defects created by addition of fatty acids	H_2O	6.93×10^{-3}	338 K, 95% RH	[64]
CaPiPhtA-NH_3 [ad]	3D framework with 1D channel	H_2O, NH_3	6.60×10^{-3}	297 K, 98% RH	[65]
La-PCMOF-5	3D Pillared layer	H_2O	6.00×10^{-3}	358 K, 95% RH	[66] [67]
VNU-17	3D framework with 1D pores	H_2O	5.90×10^{-3}	343 K, 85% RH	[68]
UiO-66	3D with defects created by vacancies of ligands	H_2O	5.62×10^{-3}	338 K, 95% RH	[69]
Na-HPAA [ae] Li-HPAA K-HPAA	1D framework Pillared layered "house of cards" structure	H_2O	5.60×10^{-3} 1.10×10^{-4} 1.30×10^{-3}	297 K, 98% RH	[70]
$[Co^{II}(ox)(bphy)\cdot 0.2(DMF)]_n$ [af]	Concatenated "Star of David" 3D framework	H_2O	5.50×10^{-3}	353 K, 98% RH	[71]
$H_3L\cdot 0.5[Cu_2(OH)_4\cdot 6H_2O]\cdot 4H_2O$ [ag]	1D-columnar assembly	H_2O, phosphinic acid	5.50×10^{-3}	333 K, 95% RH	[72]
Zn(II) MOF, [Zn(L)Cl]n (1)	2D framework	H_2O	4.72×10^{-3}	348 K, 95% RH	[73]
{[Ln(L)(Ox)(H_2O)]n·xH_2O} [ah] (Ln = Gd^{3+}, x =3)	2D stacked sheets forming a 1D pores	H_2O	4.70×10^{-3}	348 K, 95% RH	[74]
$K_3Na_2H_{10}\{MnIII[MnII\ 6\ (m_6\text{-}O)(tmp)_4(OAc)4.5(C_2H_5COO)1.5]_2(OAc)1.5\ (C_2H_5COO)_{0.5}\}18H_2O$ [ai]	3D framework with 1D channel	H_2O	4.69×10^{-3}	368 K, 97% RH	[75]

Co-MOF-74	3D framework		4.50×10^{-3}	363 K, 95% RH	[76]
DT-UiO-66-NH_2	3D framework	H_2O, DT	4.47×10^{-3}	373 K, 100% RH	[77]
{[Co_3(DMPhIDC)$_2$(H_2O)$_6$]·2H_2O}n ak {[Co_3(m-BrPhIDC)$_2$(H_2O)$_6$]·2H_2O}n al	3D frameworks with 1D pores	H_2O, NH_3	4.41×10^{-3} 5.07×10^{-4}	373 K, 1.5MNH_3.H_2O	[78]
Ce-MOF-808	3D framework	H_2O	4.40×10^{-3}	298 K, 99% RH	[79]
A$_2$[Cr_3O(OOCH)$_6$(etpy)$_3$]$_2$[α-$SiW_{12}O_{40}$]·nH_2O (A = Li, Na, K, Cs) am	3D framework	H_2O, Li^+/Na^+/K^+/ Cs^+	4.40×10^{-3} (Na^+) 1.90×10^{-3} (Li^+) 1.60×10^{-3} (K^+)	323 K, 95% RH	[80]
(Me_2NH_2)[Eu(L)] an	2D layered material	H_2O, NH_2^+	3.76×10^{-3}	373 K, 98% RH	[81]
[In(EBTC)][(CH_3)2NH_2](DMF)(H_2O)$_5$ (1) ao	3D framework with 1D channels	H_2O, $[(CH_3)_2NH_2]^+$	3.49×10^{-3}	298 K, 99% RH	[82]
(N_2H_5)[CeEu(C_2O_4)$_4$(N_2H_5)]·4H_2O (N_2H_5)[Nd_2(C_2O_4)$_4$(N_2H_5)].4H_2O (2)	3D framework with a double channel	H_2O	3.42×10^{-3} 2.70×10^{-3}	298 K, 100% RH	[83]
UiO-66-SO_3H UiO-66-$(COOH)_2$	3D framework with functionalized groups	H_2O	3.40×10^{-3} 1.00×10^{-3}	303 K, 97% RH	[84]
In-IA-2D-1 ap	2D layers	H_2O, $[(CH_3)_2NH_2]^+$	3.40×10^{-3}	300 K, 98% RH	[85]
[La_2(H_2L)$_{1.5}$(AcO)$_3$·(H_2O)$_{5.59}$] aq (particle size: >210 μm) PCMOF21-AcO	3D framework	H_2O	3.08×10^{-3}	358 K, 95% RH	[86]
(ZH, [Mg(H_2O)$_6$][NaFexAl1x(C_2O_4)$_3$].3H$_2$O, x= 0.6)	2D open framework layers	H_2O, $Mg(H_2O)_6^{2+}$	3.00×10^{-3}	298 K, 90% RH	[87]
MFM-512 MFM-511 MFM-510	3D open structure (512 &511) 2D sheet structure (510)	H_2O, -COOH	2.90×10^{-3} 5.10×10^{-5} 2.10×10^{-5}	298 K, 99% RH	[88]
Cu^I-MOF (Tz) g	Interpenetrated 3D network with 1D channels	H_2O, Tz	2.89×10^{-3}	353 K, 95% RH	[89]
{[M(H_2O)$_8$][H(H_2O)$_{2.5}$](HINO)$_4$(PM $o_{12}O_{40}$)}$_n$ (M = Co, Ni) ar	3D supramolecular framework with 1D channels	H_2O	2.83×10^{-3}	373 K, 98% RH	[90]
[Nd(mpca)$_2$Nd(H_2O)$_6$Mo(CN)$_8$]·nH_2 O as	3D framework 1D channels	H_2O	2.80×10^{-3}	294 K, 98% RH	[91]
[Me_2NH_2][Eu(ox)$_2$(H_2O)] 3H_2O at	3D framework with 1D pores	H_2O	2.73×10^{-3}	328 K, 95% RH	[92]
V[Cr(CN)$_6$]$_{2/3}$·zH_2O	3D Prussian blue analogues	H_2O	2.60×10^{-3} 1.60×10^{-3}	323 K, 100% RH 293 K, 100% RH	[93]

$Co[Cr(CN)_6]_{2/3}\cdot zH_2O$			1.70×10^{-3} 1.30×10^{-3}	308 K, 100% RH 293 K, 100% RH	
$\{[Cu(dmbipy)(H_2O)_3]_2[SiW_{12}O_{40}]\}\cdot 7H_2O$ [au]	3D framework	H_2O	2.60×10^{-3}	373 K, 98% RH	[94]
$[Tm_2Ni_3(oda)_6(H_2O)_6]\cdot 14H_2O$ [av]	Honeycomb structure with 1D channels	H_2O	2.43×10^{-3}	343 K, 100% RH	[95]
UiO-66-$(COOH)_2$	3D framework	H_2O	2.30×10^{-3}	363 K, 95% RH	[96]
$[\{(Zn_{0.25})_8(O)\}Zn_6(L)_{12}(H_2O)_{29}$-$(DMF)_{69}(NO_3)_2]n$ [aw]	2D sheets interpenetrated forming 3-fold 1D channels	H_2O, DMF	2.30×10^{-3}	298 K, 95% RH	[97]
Ni-BDP-COOH [ax]	3D framework with bipyramidal pores	H_2O	2.22×10^{-3}	353 K, 97% RH	[98]
CFA-17	3D framework with squared-shaped 1D channels	H_2O	2.10×10^{-3}	295 K, 95% RH	[99]
$(H_3O)[(Mn_4(CAM)_3]\cdot H_2O$	3D Framework	H_2O	2.06×10^{-3}	298 K, 100% RH	[100]
Cu-DSOA [ay]	3D framework with two hydrophilic channels	H_2O	1.90×10^{-3}	358 K, 98% RH	[101]
[Zn(p-IPhHIDC)]n (1) [Co(p-IPhHIDC)]n (2)	2D framework	H_2O	1.90×10^{-3} 1.07×10^{-3}	373 K, 98% RH	[102]
FJSM-CA FJSM-CA-Sr FJSM-CA-Ba FJSM-CA-UO_2	Bowl-shaped clusters 2D layered network	H_2O, $Sr^{2+}/Ba^{2+}/[UO_2]^{2+}$	1.88×10^{-3} 1.45×10^{-3} 1.03×10^{-3} 1.87×10^{-3}	358 K, 98% RH	[103]
MOF-801	3D framework	H_2O	1.88×10^{-3}	298 K, 98% RH	[104]
$(C_3N_2H_5)_4[MnCr_2(ox)_6]\cdot 5H_2O$ [at]	3D framework with 1D pores	H_2O, Imidazolium	1.86×10^{-3}	295 K, 88% RH	[105]
YCu161	2D framework	H2O	1.84×10^{-3}	295 K, 88% RH	[106]
$(C_2H_{10}N_2)[Mn_2(HPO_4)_3](H_2O)$	2D layered material	H_2O, ethylenediamine	1.64×10^{-3}	293 K, 99% RH	[107]
$MgH_6ODTMP\cdot 6H_2O$ [az]	3D pillared framework with 2 types of 1D channels	H_2O	1.60×10^{-3}	292 K, 100% RH	[108]
$\{H[Cu(Hbpdc)(H_2O)_2]_2[PM_{12}O_{40}]\cdot n H_2O\}$ [ba] (M = Mo, W and n = 7.5-8)	3D framework with 1D hydrophilic channels	H_2O	1.56×10^{-3} (W) 1.25×10^{-3} (Mo)	373 K, 98% RH	[109]
$[Cu(p\text{-}IPhHIDC)]_n$ (p-IPhHIDC =2-(p-N-imidazol-1-yl)-phenyl-1H-imidazole-4,5-dicarboxylicacid) [bb]	3D framework formed from association of 2D net-like structures	H_2O	1.51×10^{-3}	373 K, 98% RH	[110]
NENU-530 NENU-531	3D framework with 1D channels	H_2O, SO_4^{2-}	1.50×10^{-3} 1.73×10^{-4}	348 K, 98% RH	[111]

$[Cu_2(Htzehp)_2(4,4'\text{-bipy})]\cdot 3H_2O$ [bc]	2D layered material	H_2O	1.43×10^{-3}	353 K, 95% RH	[112]
$[Ni_3(HL)_2(H_2O)_{10}]4H_2O$ [bd]	3D framework with 1D chain structure and supramolecular network	H_2O	1.43×10^{-3}	297 K, 98% RH	[113]
$\{Fe(ox)(H_2O)_2\}$ [at]	1D chain	H_2O	1.30×10^{-3}	298 K, 98% RH	[114]
PCMOF-17	3D framework with 1D squared shaped pores	H_2O, $Me_2NH_2^+$	1.25×10^{-3}	298 K, 40% RH	[115]
Ln–SCP [be]	3D framework with double cuboid cavities	H_2O, SO_4^{2-}	1.19×10^{-3} (Eu)	298 K, 97% RH	[116]
$\{[M_2Cl_2(BTC)_{4/3}]\cdot(Me_2NH_2)^+_2\cdot 4/3H_2O\}n$ [bf] (M = Co, Mn)	Isostructural 3D network	H_2O, $(Me_2NH_2)^+$	1.19×10^{-3} (Co) 2.60×10^{-4} (Mn)	292 K, 65% RH	[117]
Cd2(pdc)(H2O)(DMA)2	3D Framework with regular rectangular pore channel	H_2O, $Me_2NH_2^+$	1.15×10^{-3}	363 K, 98% RH	[118]
$[Cu_2(DHBDI)_3(SO_4)_2]n$	3D Framework	H_2O	1.14×10^{-3}	363 K, 98% RH	[119]
$(CH_3NH_3)_2Ag_4Sn_3S_8$	3D framework with 1D pores	H_2O, CH_3NH_3	1.14×10^{-3}	340 K, 99% RH	[120]
[SmK(BPDSDC)(DMF)(H_2O)]·x(solvent) [bg]	3D framework with 1D channels	H_2O, DMF	1.11×10^{-3}	353 K, 98% RH	[121]
$(NH_4)_4[MnCr_2(ox)_6]_3\cdot 4H_2O$ [at]	3D chiral (quartz-like) anionic framework	H_2O, NH_4^+ ions	1.1×10^{-3}	295 K, 96% RH	[122]
Cu(HL)L [bh]	2D sheets connected supramolecularly forming a 3D framework	H_2O	1.08×10^{-3}	298 K, 97% RH	[123]
{Na[Cd(MIDC)]}n [bi]	3D framework with 1D channels	H_2O	1.04×10^{-3}	373 K, 98% RH	[124]
$[Co^{III}Ca^{II}(notpH_2)(H_2O)_2]ClO_4\cdot 4H_2O$ [bj]	2D layered structure	H_2O, ClO_4^- anions	1.00×10^{-3}	298 K, 95% RH	[125]
$Mg(HCO_2)\cdot 2H_2O$ $Co(HCO_2)\cdot 2H_2O$	Diamond network structure	H_2O	1.00×10^{-3} 1.04×10^{-6}	298 K, 90% RH	[126]
$ZrF[H_3(O_3PCH_2NHCH_2NHCH_2COO)_2]$	1D chains connected in herringbone fashion	H_2O	~1.0×10^{-3}	413 K, 95% RH	[127]
$Zr_3H_8[(O_3PCH_2)_2NCH_2COO]_4\cdot 2H_2O$	2D layered structure		~1.0×10^{-3}		
$Zr[(O_3PCH_2)(HO_3PCH_2)NHCH_2COOH]_2\cdot 2H_2O$	3D framework		~1.0×10^{-4}		
Cu-SAT	2D layered network distorted octahederal geometry	H_2O	0.53×10^{-3}	353 K, 98% RH	[128]

[a] H_6nmp = Nitrilotris(methylenephosphonic acid). [b] PSA = 3-pyridinesulfonic acid, [c] PESA = 2-(4-pyridyl)-ethanesulfonic acid. [d] AS = amino and sulfonic acid groups. [e] bpy = 4,4'-bipyridine; fdc = furan dicarboxylate. [f] Pz = 1H-pyrazole; [g] Tz = 1H-1,2,4-triazole. [h] H_2NIPA = 5-nitroisophthalicacid). [i] H_3PhIDC = 2-phenyl-4,5-imidazole dicarboxylic acid. [j] TZI = 5-(1H-tetrazol-5-yl)isophthalic acid. [k] m-ClPhH3IDC = 2-(m-chlorophenyl)imidazole-4,5-dicarboxylic acid); [l] p-ClPhH_3IDC = 2-(p-chlorophenyl)imidazole-4,5-dicarboxylic acid). [m] ox = oxalate. [n] H_2DCDPP = 5,15-di(4-carboxylphenyl)-10,20-di(4-pyridyl)porphyrin. [o] H_6L = 2,5-dicarboxy-1,4-benzene-diphosphonic acid. [p] H_2SDB = 4,4′-sulfonyldibenzoic acid; DMF = N, N-dimethyl formamide. [q] LT = low temperature. [r] BTC = 1,3,5-benzenetricarboxylate; SO3H-IPA = 5-SO3H-isophthalate. [s] H_6TTHA = 1,3,5-Triazine-2,4,6-triamine hexaacetic acid. [t] $dobdc_4$−=2,5-dioxido-1,4-benzenedicarboxylate. [u] Im = Imidazole. [v] His = Histamine. [w] TETA = triethylenetetramine. [x] H_2spip = 2-sulfophenylimidazo(4,5-f)(1,10)-phenanthroline. [y] DMA = dimethylammonium; H_6L = 2,4,6-tris(4-phosphonophenyl) pyridine). [z] bpdc = 4,4′-biphenyldicarboxylic acid; pdc = pyridine-3,5-dicarboxylate. [aa] H_8DTMP = hexamethylenediamine-N,N,N′,N′-tetrakis(methylenephosphonic acid). [ab] adp = adipic acid; ox = oxalate. [ac] ox = oxalate, im = imidazole, mim = methylimidazole. [ad] PiPhtA = 5-(dihydroxyphosphoryl)isophthalic acid. [ae] HPAA = R,S-hydroxyphosphonoacetic acid. [af] bphy = 1,2-bi-s(4-pyridyl)hydrazine; ox^{2-} = oxalate anion; DMF = N,N-dimethylformamide. [ag] H_3L = triphosphaazatriangulene. [ah] H_2L = mucic acid; OxH_2 = oxalic acid. [ai] H_3tmp = 1,1,1-tris-(hydroxymethyl)propane. [aj] NMP = N-methyl-2-pyrrolidone. [ak] DMPhH_3IDC = 2-(3,4-dimethylphenyl)-imidazole-4,5-dicarboxylic acid. [al] m-BrPhH_3IDC = 2-(m-bromophenyl)-imidazole-4,5-dicarboxylic acid. [am] etpy = 4-ethylpyridine. [an] H_4L = 5-(phosphonomethyl)isophthalic acid. [ao] H_4EBTC = 1,1′-ethynebenzene-3,3′,5,5′-tetracarboxylic acid. [ap] IA = isophthalic acid. [aq] H_4L = N,N′-4,4′-Bipiperidinebis(methylenephosphonic acid). [ar] HINO = isonicotinic acid N-oxide. [as] mpca = 5-methyl-2-pyrazinecarboxylate. [at] H_2ox = oxalic acid. [au] dmbipy = 4,4′-dimethyl-2,2′-bipyridine. [av] oda = oxydiacetate. [aw] H_2L = 1,3-bis(4-carboxyphenyl)imidazolium. [ax] H_2BDP=1,4-bis(4-

pyrazolyl)benzene. [ay] DSOA = disulfonate-4,400-oxydibenzoic acid. [az] H_8ODTMP = octamethylenediamine-N,N,N′,N′-tetrakis(methylenephosphonic acid). [ba] H_2bpdc= 2,2'-bipyridyl-3,3'-dicarboxylic acid. [bb] p-IPhH3IDC=2-(p-N-imidazol-1-yl)-phenyl-1 H-imidazole-4,5-dicarboxylic acid. [bc] H_3tzehp = N-[2-(1H-tetrazol-5-yl)ethyl]-L-hydroxyproline. [bd] H_4L = 4-F-$C_6H_4CH_2N(CH_2PO_3H_2)_2$. [be] Ln-SCP = lanthanide sulfate–carboxylpyrazolate. [bf] H_3BTC = 1,3,5-benzenetricarboxylic acid. [bg] H_4–BPDSDC = biphenyl-3,3′-disulfonyl-4,4′-dicarboxylic acid; DMF = dimethylformamide. [bh] L = 4-(1H-imidazolyl) benzoic acid. [bi] H_3MIDC = 2-methyl-1H-imidazole-4,5-dicarboxylic acid. [bj] notpH_6 = 1,4,7-triazacyclononane-1,4,7-triyl-tris-(methylenephosphonic acid).

Appendix 1.2 – PC@MOF Intermediate Temperature domain (373 < T K< 473)

Material	Features and topology	Pore Guest	Sigma ($S.cm^{-1}$)	Condition	Reference
Cu-MOF	Interpenetrated 3D network with 1D channels (impregnated with acids) Pellet	Pz·6HCl Pz·3H_2SO_4 Pz·3H_3PO_4	2.17×10^{-2} 3.83×10^{-3} 3.00×10^{-5}	353 K	[30]
FJU-106	3D framework	-COOH	1.80×10^{-2}	343 K	[129]
PIZOF	3D framework	H_2O, TEA-TFA	4.80×10^{-3}	423 K	[130]
EMIMCl@MIL-101(Cr)SO_3H	3D framework	H_2O, EMIMCl	1.5×10^{-3}	473 K	[9]
$[(CH_3)_2NH_2][In(L)]\cdot 2.5DMF\cdot 2H_2O$ (FJU-16)	4-fold interpenetrated framework single net structure Pellet	(Me_2NH_2) H_2O DMF	1.25×10^{-3}	353 K	[131]
$[(CH_3)_2NH_2][In(L)]\cdot 4.5DMF\cdot 16H_2O$ (FJU-17)	2-fold interpenetrated framework single net structure Pellet		1.08×10^{-2}	373 K	
$[Zn(H_2PO_4)_2(C_2N_3H_3)_2]n\cdot xH_3PO_4$	Stacked 2D sheets Pellet	H_3PO_4	4.60×10^{-3}	423 K	[132]
$[Eu_2(CO_3)(ox)_2(H_2O)_2]\cdot 4H_2O$	Microcrystalline material with MOF channels ordered 1D H-bonded arrays Pellet	-	2.08×10^{-3}	423 K	[133]
SA-EIMS@MIL-101 MSA-EIMS@MIL-101 PTSA-EIMS@MIL-101	3D framework Pellet	EIMS, SA/MSA/PTSA	1.89×10^{-3} 1.02×10^{-3} 2.78×10^{-4}	423 K	[134]
His@[Al(OH)(ndc)]n	3D framework with 1D channels Pellet	Histamine	1.70×10^{-3}	423 K	[135]
EMIMCI@UiO-67(Zr)	3D framework Pellet	EMIMCI	1.67×10^{-3}	473 K	[136]
Imidazole@UiO-67	3D framework Pellet	Imidazole	1.44×10^{-3}	393 K	[137]
$[Zn_3(H_2PO_4)_6](Hbim)$	1D chains templated by benzimidazole molecules	Benzimidazole	1.30×10^{-3}	393 K	[138]
(Me_2NH_2)[Eu(L)]	2D layered material Pellet	$(Me_2NH_2)^+$	1.25×10^{-3}	423 K	[81]
28% Im@MOF-217	Double interpenetrated structure Octahedral shaped crystals Pellet	Imidazole	1.10×10^{-3}	373 K	[139]

Appendix 1.3 – Listing of anhydrous and water-mediated proton conducting MOF based Mixed Matrix Membranes, their proton conductivity value and operating conditions published in the literature.

Material	Conductivity ($S.cm^{-1}$)	Temperature (K)	Relative Humidity (%)	Reference
SPEEK@MIL-101-SO_3H	3.06×10^{-1}	352	100	[140]
Nafion/GO@ZIF-8	2.80×10^{-1}	393	40	[141]
SPEEK/$H_3PW_{12}O_{40}$@MIL-101	2.72×10^{-1}	338	100	[142]
SPEEK/S-UiO-66@GO	2.68×10^{-1}	343	95	[143]
PSS@ZIF-8	2.59×10^{-1}	353	100	[144]
Fe-MIL-101-NH_2-SPPO	2.50×10^{-1}	363	98	[145]
Nafion/Phytic acid @MIL-101	2.28×10^{-1}	373	100	[146]
SPEEK/ZIF-8/CNT	2.06×10^{-1} 5.02×10^{-2}	343 393	95 30	[147]
MIL-101-NH_2-SO_3H@SNF-PAEK-3	1.92×10^{-1}	353	100	[148]
MNCS@SNF-PAEK-1.5	1.88×10^{-1}	353	-	[149]
Nafion@UiO-66-SO_3H	1.71×10^{-1}	353	95	[150]
DNA@ZIF-8/PSS	1.70×10^{-1}	348	97	[151]
Eu-MOF/Nafion	1.67×10^{-1}	363	-	[20]
PVE/PAMS/ZIF-8	1.34×10^{-1}	353	100	[152]
CS/H_2SO_4@MIL-101	9.50×10^{-2}	373	100	[153]
PBI@ZIF-8 PBI@ZIF-67 PBI@ZIF-8: ZIF-67	3.1×10^{-3} 4.1×10^{-2} 9.2×10^{-2}	473	0	[154]
CS/A-6 + B-15	5.2×10^{-2} 3.78×10^{-3}	373 393	98 0	[155]
SPEEK@ZIF-8 SPEEK@ZIF-67 SPEEK@ZIF-8: ZIF-67	1.60×10^{-2} 1.50×10^{-2} 2.90×10^{-2}	373	-	[156]
SPEEK@NH_2-MIL-53	1.70×10^{-2}	353	100	[157]
IM-UiO-66-AS@PP	1.19×10^{-2}	353	98	[5]
Nafion/H_3PO_4@HKUST-1	1.18×10^{-2}	298	100	[158]
Nafion@CPO-27-Mg Nafion@MIL-53-Al	1.1×10^{-2} 9.8×10^{-3}	323 323	100 100	[159]
MOF-808@PVDF	7.58×10^{-3}	315	99	[63]
IL@MIL-101/PP-x	4.30×10^{-3}	323	~23	[21]
ZIF-8@PVPA	3.20×10^{-3}	413	0	[160]
DHZIF-8/Nafion	2.55×10^{-3} 3.66×10^{-3}	353 393	95 0	[161]
PEI/TBA@ZIF-8 PEI/TBA@ZIF-67	1.90×10^{-3} 1.80×10^{-3}	348	95	[162]

PEI/TBA@ZIF-8: ZIF-67	3.00×10^{-3}			
Nafion-Zr-MOF-808-SO_3H	2.98×10^{-3}	353	35	[163]
PMoVx@MIL-101-C/PVA/PVP-Y	1.96×10^{-3}	353	98	[164]
MOF-801@PP-x	1.84×10^{-3}	325	98	[104]
{[$Fe^{III}_3L_2(H_2O)_6$]•3(OH)}n/PVDF/PVP	1.77×10^{-3}	353	98	[165]
JUC-200@PVA-10	1.25×10^{-3}	323	97	[166]
BUT-77@PP	1.25×10^{-3}	353	100	[26]
Cu-SAT/PVDF-PVP	0.8×10^{-3}	353	98	[128]
MOF 1-PVP-50	3.2×10^{-4}	298	97	[167]
MOH-808@PVDF-x	1.56×10^{-4}	338	-	[63]

REFERENCES

[1] X.-M. Li, L.-Z. Dong, S.-L. Li, G. Xu, J. Liu, F.-M. Zhang, L.-S. Lu, Y.-Q. Lan, Synergistic Conductivity Effect in a Proton Sources-Coupled Metal–Organic Framework, ACS Energy Lett. 2 (2017) 2313–2318. https://doi.org/10.1021/acsenergylett.7b00560.

[2] R.F. Mendes, P. Barbosa, E.M. Domingues, P. Silva, F. Figueiredo, F.A. Almeida Paz, Enhanced proton conductivity in a layered coordination polymer, Chem. Sci. 11 (2020) 6305–6311. https://doi.org/10.1039/D0SC01762K.

[3] Y. He, J. Dong, Z. Liu, M.-Q. Li, J. Hu, Y. Zhou, Z. Xu, J. He, Dense Dithiolene Units on Metal–Organic Frameworks for Mercury Removal and Superprotonic Conduction, ACS Appl. Mater. Interfaces. (2021). https://doi.org/10.1021/acsami.1c20762.

[4] S.-S. Liu, Z. Han, J.-S. Yang, S.-Z. Huang, X.-Y. Dong, S.-Q. Zang, Sulfonic Groups Lined along Channels of Metal–Organic Frameworks (MOFs) for Super-Proton Conductor, Inorg. Chem. 59 (2020) 396–402. https://doi.org/10.1021/acs.inorgchem.9b02649.

[5] X.-M. Li, J. Liu, C. Zhao, J.-L. Zhou, L. Zhao, S.-L. Li, Y.-Q. Lan, Strategic hierarchical improvement of superprotonic conductivity in a stable metal–organic framework system, J. Mater. Chem. A. 7 (2019) 25165–25171. https://doi.org/10.1039/C9TA10286H.

[6] Y. Du, K. Zhang, Z. Liu, S. Liu, G. Huang, Y. Huang, Q. Qin, J. Luo, B. Xu, G. Zhang, Encapsulating NH4Br in metal organic framework: achieving remarkable proton conduction in wide relative humidity range, Dalt. Trans. (2021). https://doi.org/10.1039/D1DT02253A.

[7] Z.-H. Li, H. Zeng, G. Zeng, C. Ru, G. Li, W. Yan, Z. Shi, S. Feng, Multivariate Synergistic Flexible Metal-Organic Frameworks with Superproton Conductivity for Direct Methanol Fuel Cells, Angew. Chemie Int. Ed. (2021). https://doi.org/10.1002/anie.202112922.

[8] S.M. Elahi, S. Chand, W. Deng, A. Pal, M.C. Das, Polycarboxylate-Templated Coordination Polymers: Role of Templates for Superprotonic Conductivities of up to 10 −1 S cm −1, Angew. Chemie Int. Ed. 57 (2018) 6662–6666. https://doi.org/10.1002/anie.201802632.

[9] K. Taksande, E. Gkaniatsou, C. Simonnet-Jégat, C. Livage, G. Maurin, N. Steunou, S. Devautour-Vinot, Robust ionic liquid@MOF composite as a versatile superprotonic conductor, Dalt. Trans. 50 (2021) 15914–15923. https://doi.org/10.1039/D1DT02877D.

[10] F. Yang, G. Xu, Y. Dou, B. Wang, H. Zhang, H. Wu, W. Zhou, J.-R. Li, B. Chen, A flexible metal–organic framework with a high density of sulfonic acid sites for proton conduction, Nat. Energy. 2 (2017) 877–883. https://doi.org/10.1038/s41560-017-0018-7.

[11] S. Kim, B. Joarder, J.A. Hurd, J. Zhang, K.W. Dawson, B.S. Gelfand, N.E. Wong, G.K.H.H. Shimizu, Achieving Superprotonic Conduction in Metal-Organic Frameworks through Iterative Design Advances, J. Am. Chem. Soc. 140 (2018) 1077–1082. https://doi.org/10.1021/jacs.7b11364.

[12] J. Zhang, R. Zhang, Y. Liu, Y.-R. Kong, H.-B. Luo, Y. Zou, L. Zhai, X.-M. Ren, Acidic Groups Functionalized Carbon

Dots Capping Channels of a Proton Conductive Metal–Organic Framework by Coordination Bonds to Improve the Water-Retention Capacity and Boost Proton Conduction, ACS Appl. Mater. Interfaces. (2021). https://doi.org/10.1021/acsami.1c20884.

[13] W. Zhang, Y. Lu, S. Zhang, T. Dang, H. Tian, Z. Zhang, S. Liu, Proton conductors with wide operating temperature domains achieved by applying a dual-modification strategy to MIL-101, Dalt. Trans. (2021). https://doi.org/10.1039/D1DT02686K.

[14] W.J. Phang, H. Jo, W.R. Lee, J.H. Song, K. Yoo, B. Kim, C.S. Hong, Superprotonic conductivity of a uio-66 framework functionalized with sulfonic acid groups by facile postsynthetic oxidation, Angew. Chemie Int. Ed. 54 (2015) 5142–5146. https://doi.org/10.1002/anie.201411703.

[15] X.S. Xing, Z.H. Fu, N.N. Zhang, X.Q. Yu, M.S. Wang, G.C. Guo, High proton conduction in an excellent water-stable gadolinium metal-organic framework, Chem. Commun. 55 (2019) 1241–1244. https://doi.org/10.1039/c8cc08700h.

[16] Q.G. Zhai, C. Mao, X. Zhao, Q. Lin, F. Bu, X. Chen, X. Bu, P. Feng, Cooperative Crystallization of Heterometallic Indium-Chromium Metal-Organic Polyhedra and Their Fast Proton Conductivity, Angew. Chemie - Int. Ed. 54 (2015) 7886–7890. https://doi.org/10.1002/anie.201503095.

[17] M. Wahiduzzaman, S. Nandi, V. Yadav, K. Taksande, G. Maurin, H. Chun, S. Devautour-Vinot, Superionic conduction in a zirconium-formate molecular solid, J. Mater. Chem. A. 8 (2020) 17951–17955. https://doi.org/10.1039/D0TA05424K.

[18] N.T.T. Nguyen, H. Furukawa, F. Gándara, C.A. Trickett, H.M. Jeong, K.E. Cordova, O.M. Yaghi, Three-Dimensional Metal-Catecholate Frameworks and Their Ultrahigh Proton Conductivity, J. Am. Chem. Soc. 137 (2015) 15394–15397. https://doi.org/10.1021/jacs.5b10999.

[19] W. Chen, J. Wang, L. Zhao, W. Dai, Z. Li, G. Li, Enhancing proton conductivity of a highly water stable 3D Sr(II) metal-organic framework by exposure to aqua-ammonia vapor, J. Alloys Compd. 750 (2018) 895–901. https://doi.org/10.1016/j.jallcom.2018.04.087.

[20] S.-Z. Huang, S.-S. Liu, H. Zhang, Z. Han, G. Zhao, X.-Y. Dong, S.-Q. Zang, Dual-Functional Proton-Conducting and pH-Sensing Polymer Membrane Benefiting from a Eu-MOF, ACS Appl. Mater. Interfaces. 12 (2020) 28720–28726. https://doi.org/10.1021/acsami.0c08103.

[21] J. Du, G. Yu, H. Lin, P. Jie, F. Zhang, F. Qu, C. Wen, L. Feng, X. Liang, Enhanced proton conductivity of metal organic framework at low humidity by improvement in water retention, J. Colloid Interface Sci. 573 (2020) 360–369. https://doi.org/10.1016/j.jcis.2020.04.023.

[22] X. Liang, B. Li, M. Wang, J. Wang, R. Liu, G. Li, Effective Approach to Promoting the Proton Conductivity of Metal–Organic Frameworks by Exposure to Aqua–Ammonia Vapor, ACS Appl. Mater. Interfaces. 9 (2017) 25082–25086. https://doi.org/10.1021/acsami.7b07635.

[23] S.S. Nagarkar, S.M. Unni, A. Sharma, S. Kurungot, S.K. Ghosh, Two-in-One: Inherent Anhydrous and Water-Assisted High Proton Conduction in a 3D Metal-Organic Framework, Angew. Chemie Int. Ed. 53 (2014) 2638–2642. https://doi.org/10.1002/anie.201309077.

[24] V.G. Ponomareva, K.A. Kovalenko, A.P. Chupakhin, D.N. Dybtsev, E.S. Shutova, V.P. Fedin, Imparting high proton conductivity to a metal-organic framework material by controlled acid impregnation, J. Am. Chem. Soc. 134 (2012) 15640–15643. https://doi.org/10.1021/ja305587n.

[25] H. Wu, F. Yang, X.-L. Lv, B. Wang, Y.-Z. Zhang, M.-J. Zhao, J.-R. Li, A stable porphyrinic metal–organic framework pore-functionalized by high-density carboxylic groups for proton conduction, J. Mater. Chem. A. 5 (2017) 14525–14529. https://doi.org/10.1039/C7TA03917D.

[26] G.-R. Si, F. Yang, T. He, X.-J. Kong, W. Wu, T. Li, K. Wang, J.-R. Li, Enhancing proton conductivity in Zr-MOFs through tuning metal cluster connectivity, J. Mater. Chem. A. (2022). https://doi.org/10.1039/d1ta09348g.

[27] P. Ramaswamy, N.E. Wong, B.S. Gelfand, G.K.H. Shimizu, A Water Stable Magnesium MOF That Conducts Protons over 10 –2 S cm –1, J. Am. Chem. Soc. 137 (2015) 7640–7643. https://doi.org/10.1021/jacs.5b04399.

[28] H. Gao, Y.-B. He, J.-J. Hou, X.-M. Zhang, In Situ Aliovalent Nickle Substitution and Acidic Modification of Nanowalls Promoted Proton Conductivity in InOF with 1D Helical Channel, ACS Appl. Mater. Interfaces. 13 (2021) 38289–38295. https://doi.org/10.1021/acsami.1c09001.

[29] V.G. Ponomareva, A.M. Cheplakova, K.A. Kovalenko, V.P. Fedin, Exceptionally Stable H 3 PO 4 @MIL-100 System: A Correlation between Proton Conduction and Water Adsorption Properties, J. Phys. Chem. C. 124 (2020) 23143–23149.

https://doi.org/10.1021/acs.jpcc.0c06407.

[30] S. Khatua, A.K. Bar, J.A. Sheikh, A. Clearfield, S. Konar, Achieving Amphibious Superprotonic Conductivity in a CuI Metal–Organic Framework by Strategic Pyrazinium Salt Impregnation, Chem. - A Eur. J. 24 (2018) 872–880. https://doi.org/10.1002/chem.201704088.

[31] X. Wang, Y. Wang, M.A. Silver, D. Gui, Z. Bai, Y. Wang, W. Liu, L. Chen, J. Diwu, Z. Chai, S. Wang, Superprotonic conduction through one-dimensional ordered alkali metal ion chains in a lanthanide-organic framework, Chem. Commun. 54 (2018) 4429–4432. https://doi.org/10.1039/c8cc00572a.

[32] T.N. Tu, N.Q. Phan, T.T. Vu, H.L. Nguyen, K.E. Cordova, H. Furukawa, High proton conductivity at low relative humidity in an anionic Fe-based metal-organic framework, J. Mater. Chem. A. 4 (2016) 3638–3641. https://doi.org/10.1039/c5ta10467j.

[33] L.-D. Lin, Z. Li, D. Zhao, J.-H. Liu, X.-X. Li, S.-T. Zheng, Development of a new Lindqvist-like Fe6 cluster secondary building unit for MOFs, Chem. Commun. 55 (2019) 10729–10732. https://doi.org/10.1039/C9CC04999A.

[34] M. Wahiduzzaman, S. Wang, J. Schnee, A. Vimont, V. Ortiz, P.G. Yot, R. Retoux, M. Daturi, J.S. Lee, J.-S.S. Chang, C. Serre, G. Maurin, S. Devautour-Vinot, A High Proton Conductive Hydrogen-Sulfate Decorated Titanium Carboxylate Metal-Organic Framework, ACS Sustain. Chem. Eng. 7 (2019) 5776–5783. https://doi.org/10.1021/acssuschemeng.8b05306.

[35] S. Nandi, S. Wang, M. Wahiduzzaman, V. Yadav, K. Taksande, G. Maurin, C. Serre, S. Devautour-Vinot, Multivariate Sulfonic-Based Titanium Metal–Organic Frameworks as Super-protonic Conductors, ACS Appl. Mater. Interfaces. 13 (2021) 20194–20200. https://doi.org/10.1021/acsami.1c03644.

[36] L. Feng, H.S. Wang, H.L. Xu, W.T. Huang, T.Y. Zeng, Q.R. Cheng, Z.Q. Pan, H. Zhou, A water stable layered Tb(iii) polycarboxylate with high proton conductivity over 10-2 S cm-1 in a wide temperature range, Chem. Commun. 55 (2019) 1762–1765. https://doi.org/10.1039/c8cc08706g.

[37] H. Gao, Y.-B. He, J.-J. Hou, Q.-G. Zhai, X.-M. Zhang, Enhanced Proton Conductivity by Aliovalent Substitution of Cadmium for Indium in Dimethylaminium-Templated Metal Anilicates, ACS Appl. Mater. Interfaces. 12 (2020) 41605–41612. https://doi.org/10.1021/acsami.0c13125.

[38] W.J. Phang, W.R. Lee, K. Yoo, D.W. Ryu, B. Kim, C.S. Hong, pH-Dependent Proton Conducting Behavior in a Metal-Organic Framework Material, Angew. Chemie Int. Ed. 53 (2014) 8383–8387. https://doi.org/10.1002/anie.201404164.

[39] S. Kim, K.W. Dawson, B.S. Gelfand, J.M. Taylor, G.K.H. Shimizu, Enhancing Proton Conduction in a Metal–Organic Framework by Isomorphous Ligand Replacement, J. Am. Chem. Soc. 135 (2013) 963–966. https://doi.org/10.1021/ja310675x.

[40] P.G.M. Mileo, K. Adil, L. Davis, A. Cadiau, Y. Belmabkhout, H. Aggarwal, G. Maurin, M. Eddaoudi, S. Devautour-Vinot, Achieving Superprotonic Conduction with a 2D Fluorinated Metal–Organic Framework, J. Am. Chem. Soc. 140 (2018) 13156–13160. https://doi.org/10.1021/jacs.8b06582.

[41] L. Zhang, X. Liu, X. Sun, J. Jian, G. Li, H. Yuan, Proton Conduction in Organically Templated 3D Open-Framework Vanadium–Nickel Pyrophosphate, Inorg. Chem. 58 (2019) 4394–4398. https://doi.org/10.1021/acs.inorgchem.8b03526.

[42] S.C. Pal, S. Chand, A.G. Kumar, P.G.M. Mileo, I. Silverwood, G. Maurin, S. Banerjee, S.M. Elahi, M.C. Das, A Co(<scp>ii</scp>)-coordination polymer for ultrahigh superprotonic conduction: an atomistic insight through molecular simulations and QENS experiments, J. Mater. Chem. A. 8 (2020) 7847–7853. https://doi.org/10.1039/D0TA00417K.

[43] Y. Ye, W. Guo, L. Wang, Z. Li, Z. Song, J. Chen, Z. Zhang, S. Xiang, B. Chen, Straightforward Loading of Imidazole Molecules into Metal-Organic Framework for High Proton Conduction, J. Am. Chem. Soc. 139 (2017) 15604–15607. https://doi.org/10.1021/jacs.7b09163.

[44] M. V. Nguyen, T.H.N. Lo, L.C. Luu, H.T.T. Nguyen, T.N. Tu, Enhancing proton conductivity in a metal–organic framework at T > 80 °C by an anchoring strategy, J. Mater. Chem. A. 6 (2018) 1816–1821. https://doi.org/10.1039/C7TA10148A.

[45] Y.-H. Han, Y. Ye, C. Tian, Z. Zhang, S.-W. Du, S. Xiang, High proton conductivity in an unprecedented anionic metalloring organic framework (MROF) containing novel metalloring clusters with the largest diameter, J. Mater. Chem. A. 4 (2016) 18742–18746. https://doi.org/10.1039/C6TA07939C.

[46] J. Hu, H. Zhang, Z. Feng, Q.-R. Luo, C.-M. Wu, Y.-H. Zhong, J.-R. Li, L.-H. Chung, W.-M. Liao, J. He, Flexible side arms of ditopic linker as effective tools to boost proton conductivity of Ni8-pyrazolate metal-organic framework, Chinese

Chem. Lett. (2021). https://doi.org/10.1016/j.cclet.2021.10.042.

[47] S. Shalini, S. Aggarwal, S.K. Singh, M. Dutt, T.G. Ajithkumar, R. Vaidhyanathan, 10000-Fold Enhancement in Proton Conduction by Doping of Cesium Ions in a Proton-Conducting Zwitterionic Metal-Organic Framework, Eur. J. Inorg. Chem. 2016 (2016) 4382–4386. https://doi.org/10.1002/ejic.201600364.

[48] X. Lai, Y. Liu, G. Yang, S.S. Liu, Z. Shi, Y. Lu, F. Luo, S.S. Liu, Controllable proton-conducting pathways via situating polyoxometalates in targeting pores of a metal–organic framework, J. Mater. Chem. A. 5 (2017) 9611–9617. https://doi.org/10.1039/C6TA10958F.

[49] Y.-B. Lu, Y.-Q. Liao, L. Dong, S.-D. Zhu, H.-R. Wen, J. Huang, X.-X. Dai, P. Lian, X.-M. Jiang, R. Li, Y.-R. Xie, Ultra-Stable Metal–Organic Framework with Concurrent High Proton Conductivity and Fluorescence Sensing for Nitrobenzene, Chem. Mater. (2021) acs.chemmater.1c02562. https://doi.org/10.1021/acs.chemmater.1c02562.

[50] F.-M. Zhang, L.-Z. Dong, J.-S. Qin, W. Guan, J. Liu, S.-L. Li, M. Lu, Y.-Q. Lan, Z.-M. Su, H.-C. Zhou, Effect of Imidazole Arrangements on Proton-Conductivity in Metal–Organic Frameworks, J. Am. Chem. Soc. 139 (2017) 6183–6189. https://doi.org/10.1021/jacs.7b01559.

[51] L. Qin, Y. Yu, P. Liao, W. Xue, Z. Zheng, X. Chen, Y. Zheng, A "Molecular Water Pipe": A Giant Tubular Cluster {Dy 72 } Exhibits Fast Proton Transport and Slow Magnetic Relaxation, Adv. Mater. 28 (2016) 10772–10779. https://doi.org/10.1002/adma.201603381.

[52] X. Zhao, C. Mao, X. Bu, P. Feng, Direct Observation of Two Types of Proton Conduction Tunnels Coexisting in a New Porous Indium–Organic Framework, Chem. Mater. 26 (2014) 2492–2495. https://doi.org/10.1021/cm500473f.

[53] M.-J. Wei, J.-Q. Fu, Y.-D. Wang, Y. Zhang, H.-Y. Zang, K.-Z. Shao, Y.-G. Li, Z.-M. Su, Highly tuneable proton-conducting coordination polymers derived from a sulfonate-based ligand, CrystEngComm. 19 (2017) 7050–7056. https://doi.org/10.1039/C7CE01589E.

[54] Q. Gao, X.-L. Wang, J. Xu, X.-H. Bu, The First Demonstration of the Gyroid in a Polyoxometalate-Based Open Framework with High Proton Conductivity, Chem. - A Eur. J. 22 (2016) 9082–9086. https://doi.org/10.1002/chem.201601233.

[55] Z. Hassanzadeh Fard, N.E. Wong, C.D. Malliakas, P. Ramaswamy, J.M. Taylor, K. Otsubo, G.K.H. Shimizu, Superprotonic Phase Change to a Robust Phosphonate Metal–Organic Framework, Chem. Mater. 30 (2018) 314–318. https://doi.org/10.1021/acs.chemmater.7b04467.

[56] H. Matsui, M. Tadokoro, Proton conduction through the nanochannel water in weak-acidic nanoporous crystals [Cu2(phen)2(AcO)2(H2O)2][Al(OH)6Mo6O18]M+(nH2O) (M+= H+, Li+, Na+, K+), Solid State Ionics. 285 (2016) 165–169. https://doi.org/10.1016/j.ssi.2015.09.020.

[57] X. Meng, M.-J. Wei, H.-N. Wang, H.-Y. Zang, Z.-Y. Zhou, Multifunctional luminescent Zn(II)-based metal– organic framework for high proton-conductivity and detection of Cr3+ ions in the presence of mixed metal ions, Dalt. Trans. 47 (2018) 1383–1387. https://doi.org/10.1039/C7DT03932H.

[58] L. Zou, S. Yao, J. Zhao, D.-S. Li, G. Li, Q. Huo, Y. Liu, Enhancing Proton Conductivity in a 3D Metal–Organic Framework by the Cooperation of Guest [Me 2 NH 2] + Cations, Water Molecules, and Host Carboxylates, Cryst. Growth Des. 17 (2017) 3556–3561. https://doi.org/10.1021/acs.cgd.7b00512.

[59] E.-X. Chen, G. Xu, Q. Lin, Robust Porphyrin-Spaced Zirconium Pyrogallate Frameworks with High Proton Conduction, Inorg. Chem. 58 (2019) 3569–3573. https://doi.org/10.1021/acs.inorgchem.8b03132.

[60] R.M.P. Colodrero, P. Olivera-Pastor, E.R. Losilla, M.A.G. Aranda, L. Leon-Reina, M. Papadaki, A.C. McKinlay, R.E. Morris, K.D. Demadis, A. Cabeza, Multifunctional lanthanum tetraphosphonates: Flexible, ultramicroporous and proton-conducting hybrid frameworks, Dalt. Trans. 41 (2012) 4045. https://doi.org/10.1039/c2dt11992g.

[61] M. Sadakiyo, T. Yamada, H. Kitagawa, Rational Designs for Highly Proton-Conductive Metal−Organic Frameworks, J. Am. Chem. Soc. 131 (2009) 9906–9907. https://doi.org/10.1021/ja9040016.

[62] K. Wang, X. Qi, Z. Wang, R. Wang, J. Sun, Q. Zhang, In Situ Encapsulation of Imidazolium Proton Carriers in Anionic Open Frameworks Leads the Way to Proton-Conducting Materials, Eur. J. Inorg. Chem. 2017 (2017) 2295–2300. https://doi.org/10.1002/ejic.201700157.

[63] H.-B. Bin Luo, M. Wang, S.-X.X. Liu, C. Xue, Z.-F.F. Tian, Y. Zou, X.-M.M. Ren, Proton Conductance of a Superior Water-Stable Metal–Organic Framework and Its Composite Membrane with Poly(vinylidene fluoride), Inorg. Chem. 56 (2017) 4169–4175. https://doi.org/10.1021/acs.inorgchem.7b00122.

[64] J.M. Taylor, S. Dekura, R. Ikeda, H. Kitagawa, Defect Control To Enhance Proton Conductivity in a Metal–Organic Framework, Chem. Mater. 27 (2015) 2286–2289. https://doi.org/10.1021/acs.chemmater.5b00665.

[65] M. Bazaga-García, R.M.P. Colodrero, M. Papadaki, P. Garczarek, J. Zoń, P. Olivera-Pastor, E.R. Losilla, L. León-Reina, M.A.G. Aranda, D. Choquesillo-Lazarte, K.D. Demadis, A. Cabeza, Guest Molecule-Responsive Functional Calcium Phosphonate Frameworks for Tuned Proton Conductivity, J. Am. Chem. Soc. 136 (2014) 5731–5739. https://doi.org/10.1021/ja500356z.

[66] J.M. Taylor, K.W. Dawson, G.K.H. Shimizu, A Water-Stable Metal–Organic Framework with Highly Acidic Pores for Proton-Conducting Applications, J. Am. Chem. Soc. 135 (2013) 1193–1196. https://doi.org/10.1021/ja310435e.

[67] N.E. Wong, P. Ramaswamy, A.S. Lee, B.S. Gelfand, K.J. Bladek, J.M. Taylor, D.M. Spasyuk, G.K.H. Shimizu, Tuning Intrinsic and Extrinsic Proton Conduction in Metal–Organic Frameworks by the Lanthanide Contraction, J. Am. Chem. Soc. 139 (2017) 14676–14683. https://doi.org/10.1021/jacs.7b07987.

[68] T.H.N. Lo, M. V. Nguyen, T.N. Tu, An anchoring strategy leads to enhanced proton conductivity in a new metal–organic framework, Inorg. Chem. Front. 4 (2017) 1509–1516. https://doi.org/10.1039/C7QI00350A.

[69] J.M. Taylor, T. Komatsu, S. Dekura, K. Otsubo, M. Takata, H. Kitagawa, The Role of a Three Dimensionally Ordered Defect Sublattice on the Acidity of a Sulfonated Metal–Organic Framework, J. Am. Chem. Soc. 137 (2015) 11498–11506. https://doi.org/10.1021/jacs.5b07267.

[70] M. Bazaga-García, M. Papadaki, R.M.P. Colodrero, P. Olivera-Pastor, E.R. Losilla, B. Nieto-Ortega, M.Á.G. Aranda, D. Choquesillo-Lazarte, A. Cabeza, K.D. Demadis, Tuning Proton Conductivity in Alkali Metal Phosphonocarboxylates by Cation Size-Induced and Water-Facilitated Proton Transfer Pathways, Chem. Mater. 27 (2015) 424–435. https://doi.org/10.1021/cm502716e.

[71] Y.-G. Huang, S.-Q. Wu, W.-H. Deng, G. Xu, F.-L. Hu, J.P. Hill, W. Wei, S.-Q. Su, L.K. Shrestha, O. Sato, M.-Y. Wu, M.-C. Hong, K. Ariga, Selective CO 2 Capture and High Proton Conductivity of a Functional Star-of-David Catenane Metal-Organic Framework, Adv. Mater. 29 (2017) 1703301. https://doi.org/10.1002/adma.201703301.

[72] S. Nakatsuka, Y. Watanabe, Y. Kamakura, S. Horike, D. Tanaka, T. Hatakeyama, Solvent-Vapor-Induced Reversible Single-Crystal-to-Single-Crystal Transformation of a Triphosphaazatriangulene-Based Metal–Organic Framework, Angew. Chemie Int. Ed. 59 (2020) 1435–1439. https://doi.org/10.1002/anie.201912195.

[73] Z.-Q. Shi, N.-N. Ji, M.-H. Wang, G. Li, A Comparative Study of Proton Conduction Between a 2D Zinc(II) MOF and Its Corresponding Organic Ligand, Inorg. Chem. 59 (2020) 4781–4789. https://doi.org/10.1021/acs.inorgchem.0c00053.

[74] S. Biswas, J. Chakraborty, V. Singh Parmar, S.P. Bera, N. Ganguli, S. Konar, Channel-Assisted Proton Conduction Behavior in Hydroxyl-Rich Lanthanide-Based Magnetic Metal–Organic Frameworks, Inorg. Chem. 56 (2017) 4956–4965. https://doi.org/10.1021/acs.inorgchem.6b03147.

[75] S. Liu, Y. Deng, F. Xu, An inorganic-organic hybrid MnIII{MnII62cluster consisting of rare Lindqvist-like Mn6subunits with high proton conductivity, Chem. Commun. 56 (2020) 6066–6069. https://doi.org/10.1039/d0cc01827a.

[76] S. Hwang, E.J. Lee, D. Song, N.C. Jeong, High Proton Mobility with High Directionality in Isolated Channels of MOF-74, ACS Appl. Mater. Interfaces. 10 (2018) 35354–35360. https://doi.org/10.1021/acsami.8b11816.

[77] L. Feng, J. Lan, F. Chen, H. Hou, H. Zhou, Strategically improving the intrinsic proton conductivity of UiO-66-NH 2 by post-synthesis modification, Dalt. Trans. 50 (2021) 5943–5950. https://doi.org/10.1039/D1DT00400J.

[78] R. Liu, L. Zhao, W. Dai, C. Yang, X. Liang, G. Li, A Comparative Investigation of Proton Conductivities for Two Metal−Organic Frameworks under Water and Aqua-Ammonia Vapors, Inorg. Chem. 57 (2018) 1474–1482. https://doi.org/10.1021/acs.inorgchem.7b02851.

[79] W.H. Ho, S.-C. Li, Y.-C. Wang, T.-E. Chang, Y.-T. Chiang, Y.-P. Li, C.-W. Kung, Proton-Conductive Cerium-Based Metal–Organic Frameworks, ACS Appl. Mater. Interfaces. 13 (2021) 55358–55366. https://doi.org/10.1021/acsami.1c17396.

[80] S. Uchida, R. Hosono, R. Eguchi, R. Kawahara, R. Osuga, J.N. Kondo, M. Hibino, N. Mizuno, Proton conduction in alkali metal ion-exchanged porous ionic crystals, Phys. Chem. Chem. Phys. 19 (2017) 29077–29083. https://doi.org/10.1039/C7CP04619G.

[81] Y.-S. Wei, X.-P. Hu, Z. Han, X.-Y. Dong, S.-Q. Zang, T.C.W. Mak, Unique Proton Dynamics in an Efficient MOF-Based Proton Conductor, J. Am. Chem. Soc. 139 (2017) 3505–3512. https://doi.org/10.1021/jacs.6b12847.

[82] L. Zhai, J.W. Yu, J. Zhang, W.W. Zhang, L. Wang, X.M. Ren, High quantum yield pure blue emission and fast proton conduction from an indium-metal-organic framework, Dalt. Trans. 48 (2019) 12088–12095. https://doi.org/10.1039/c9dt02472g.

[83] K. Zhang, X. Xie, H. Li, J. Gao, L. Nie, Y. Pan, J. Xie, D. Tian, W. Liu, Q. Fan, H. Su, L. Huang, W. Huang, Highly Water-Stable Lanthanide-Oxalate MOFs with Remarkable Proton Conductivity and Tunable Luminescence, Adv. Mater. 29 (2017) 1701804. https://doi.org/10.1002/adma.201701804.

[84] F. Yang, H. Huang, X. Wang, F. Li, Y. Gong, C. Zhong, J.-R. Li, Proton Conductivities in Functionalized UiO-66: Tuned Properties, Thermogravimetry Mass, and Molecular Simulation Analyses, Cryst. Growth Des. 15 (2015) 5827–5833. https://doi.org/10.1021/acs.cgd.5b01190.

[85] T. Panda, T. Kundu, R. Banerjee, Structural isomerism leading to variable proton conductivity in indium(iii) isophthalic acid based frameworks, Chem. Commun. 49 (2013) 6197. https://doi.org/10.1039/c3cc41939h.

[86] D.A. Levenson, J. Zhang, B.S. Gelfand, S.P. Kammampata, V. Thangadurai, G.K.H.H. Shimizu, Particle size dependence of proton conduction in a cationic lanthanum phosphonate MOF, Dalt. Trans. 49 (2020) 4022–4029. https://doi.org/10.1039/c9dt04229f.

[87] I. Huskić, N. Novendra, D.-W. Lim, F. Topić, H.M. Titi, I. V. Pekov, S. V. Krivovichev, A. Navrotsky, H. Kitagawa, T. Friščić, Functionality in metal–organic framework minerals: proton conductivity, stability and potential for polymorphism, Chem. Sci. 10 (2019) 4923–4929. https://doi.org/10.1039/C8SC05088K.

[88] P. Rought, C. Marsh, S. Pili, I.P. Silverwood, V.G. Sakai, M. Li, M.S. Brown, S.P. Argent, I. Vitorica-Yrezabal, G. Whitehead, M.R. Warren, S. Yang, M. Schröder, Modulating proton diffusion and conductivity in metal–organic frameworks by incorporation of accessible free carboxylic acid groups, Chem. Sci. 10 (2019) 1492–1499. https://doi.org/10.1039/C8SC03022G.

[89] S. Khatua, A. Kumar Bar, S. Konar, Tuning Proton Conductivity by Interstitial Guest Change in Size-Adjustable Nanopores of a Cu I -MOF: A Potential Platform for Versatile Proton Carriers, Chem. - A Eur. J. 22 (2016) 16277–16285. https://doi.org/10.1002/chem.201601964.

[90] M.-L. Wei, P.-F. Zhuang, H.-H. Li, Y.-H. Yang, Crystal Structures and Conductivities of Two Organic-Inorganic Hybrid Complexes Based on Poly-Keggin-Anion Chains, Eur. J. Inorg. Chem. 2011 (2011) 1473–1478. https://doi.org/10.1002/ejic.201001144.

[91] Y. Gao, R. Broersen, W. Hageman, N. Yan, M.C. Mittelmeijer-Hazeleger, G. Rothenberg, S. Tanase, High proton conductivity in cyanide-bridged metal–organic frameworks: understanding the role of water, J. Mater. Chem. A. 3 (2015) 22347–22352. https://doi.org/10.1039/C5TA05280G.

[92] X. Wang, T. Qin, S.-S. Bao, Y.-C. Zhang, X. Shen, L.-M. Zheng, D. Zhu, Facile synthesis of a water stable 3D Eu-MOF showing high proton conductivity and its application as a sensitive luminescent sensor for Cu 2+ ions, J. Mater. Chem. A. 4 (2016) 16484–16489. https://doi.org/10.1039/C6TA06792A.

[93] S. Ohkoshi, K. Nakagawa, K. Tomono, K. Imoto, Y. Tsunobuchi, H. Tokoro, High Proton Conductivity in Prussian Blue Analogues and the Interference Effect by Magnetic Ordering, J. Am. Chem. Soc. 132 (2010) 6620–6621. https://doi.org/10.1021/ja100385f.

[94] X. Wang, X. Duan, C. Kong, M. Wei, A complex based on a decorated Keggin-type cluster from Cu(II) and 4,4′-dimethyl-2,2′-bipyridine: synthesis, structure and proton conductivity, J. Coord. Chem. 69 (2016) 779–787. https://doi.org/10.1080/00958972.2016.1139105.

[95] F. Igoa, M. Romero, G. Peinado, J. Castiglioni, J. Gonzalez-Platas, R. Faccio, L. Suescun, C. Kremer, J. Torres, Ln(iii)–Ni(ii) heteropolynuclear metal organic frameworks of oxydiacetate with promising proton-conductive properties , CrystEngComm. (2020) 5638–5648. https://doi.org/10.1039/d0ce00900h.

[96] D.D. Borges, S. Devautour-Vinot, H. Jobic, J. Ollivier, F. Nouar, R. Semino, T. Devic, C. Serre, F. Paesani, G. Maurin, Proton Transport in a Highly Conductive Porous Zirconium-Based Metal-Organic Framework: Molecular Insight, Angew. Chemie - Int. Ed. 55 (2016) 3919–3924. https://doi.org/10.1002/anie.201510855.

[97] S. Sen, N.N. Nair, T. Yamada, H. Kitagawa, P.K. Bharadwaj, High Proton Conductivity by a Metal–Organic Framework Incorporating Zn 8 O Clusters with Aligned Imidazolium Groups Decorating the Channels, J. Am. Chem. Soc. 134 (2012) 19432–19437. https://doi.org/10.1021/ja3076378.

[98] T. He, Y.-Z. Zhang, H. Wu, X.-J. Kong, X.-M. Liu, L.-H. Xie, Y. Dou, J.-R. Li, Functionalized Base-Stable Metal-Organic Frameworks for Selective CO 2 Adsorption and Proton Conduction, ChemPhysChem. 18 (2017) 3245–3252.

https://doi.org/10.1002/cphc.201700650.

[99] H. Bunzen, A. Javed, D. Klawinski, A. Lamp, M. Grzywa, A. Kalytta-Mewes, M. Tiemann, H.-A.K. von Nidda, T. Wagner, D. Volkmer, Anisotropic Water-Mediated Proton Conductivity in Large Iron(II) Metal–Organic Framework Single Crystals for Proton-Exchange Membrane Fuel Cells, ACS Appl. Nano Mater. 2 (2019) 291–298. https://doi.org/10.1021/acsanm.8b01902.

[100] Y.-B. Lu, J. Huang, X.-R. Yuan, S.-J. Liu, R. Li, H. Liu, M.-P. Liu, H.-R. Wen, S.-D. Zhu, Y.-R. Xie, A Three-Dimensional Porous Mn(II)-Metal–Organic Framework Based on a Caged Structure Showing High Room-Temperature Proton Conductivity, Cryst. Growth Des. (2022). https://doi.org/10.1021/acs.cgd.1c00872.

[101] X.-Y. Dong, R. Wang, J.-B. Li, S.-Q. Zang, H.-W. Hou, T.C.W. Mak, A tetranuclear Cu4(μ3-OH)2-based metal–organic framework (MOF) with sulfonate–carboxylate ligands for proton conduction, Chem. Commun. 49 (2013) 10590. https://doi.org/10.1039/c3cc46226a.

[102] Y. Qin, M.H. Xue, B.H. Dou, Z.B. Sun, G. Li, High protonic conduction in two metal-organic frameworks containing high-density carboxylic groups, New J. Chem. 44 (2020) 2741–2748. https://doi.org/10.1039/c9nj05735h.

[103] W. Ma, B. Hu, J.-L. Li, Z.-Z. Zhang, X. Zeng, J. Jin, Z. Li, S.-T. Zheng, M.-L. Feng, X.-Y. Huang, The Uptake of Hazardous Metal Ions into a High-Nuclearity Cluster-Based Compound with Structural Transformation and Proton Conduction, ACS Appl. Mater. Interfaces. 12 (2020) 26222–26231. https://doi.org/10.1021/acsami.0c06082.

[104] J. Zhang, H.-J.J. Bai, Q. Ren, H.-B. Bin Luo, X.-M.M. Ren, Z.-F.F. Tian, S. Lu, Extra Water- and Acid-Stable MOF-801 with High Proton Conductivity and Its Composite Membrane for Proton-Exchange Membrane, ACS Appl. Mater. Interfaces. 10 (2018) 28656–28663. https://doi.org/10.1021/acsami.8b09070.

[105] M. Mon, J. Vallejo, J. Pasán, O. Fabelo, C. Train, M. Verdaguer, S. Ohkoshi, H. Tokoro, K. Nakagawa, E. Pardo, A novel oxalate-based three-dimensional coordination polymer showing magnetic ordering and high proton conductivity, Dalt. Trans. 46 (2017) 15130–15137. https://doi.org/10.1039/C7DT03415F.

[106] L. Zhao, R.-R. Zhu, S. Wang, L. He, L. Du, Q.-H. Zhao, Multiple Strategies to Fabricate a Highly Stable 2D Cu II Cu I – Organic Framework with High Proton Conductivity, Inorg. Chem. 60 (2021) 16474–16483. https://doi.org/10.1021/acs.inorgchem.1c02312.

[107] H.-R. Zhao, C. Xue, C.-P. Li, K.-M. Zhang, H.-B. Luo, S.-X. Liu, X.-M. Ren, A Two-Dimensional Inorganic–Organic Hybrid Solid of Manganese(II) Hydrogenophosphate Showing High Proton Conductivity at Room Temperature, Inorg. Chem. 55 (2016) 8971–8975. https://doi.org/10.1021/acs.inorgchem.6b01438.

[108] R.M.P. Colodrero, P. Olivera-Pastor, E.R. Losilla, D. Hernández-Alonso, M.A.G. Aranda, L. Leon-Reina, J. Rius, K.D. Demadis, B. Moreau, D. Villemin, M. Palomino, F. Rey, A. Cabeza, High Proton Conductivity in a Flexible, Cross-Linked, Ultramicroporous Magnesium Tetraphosphonate Hybrid Framework, Inorg. Chem. 51 (2012) 7689–7698. https://doi.org/10.1021/ic3007316.

[109] M. Wei, X. Wang, X. Duan, Crystal structures and proton conductivities of a MOF and Two POM-MOF composites based on CuII ions and 2,2′-bipyridyl-3,3′- dicarboxylic acid, Chem. - A Eur. J. 19 (2013) 1607–1616. https://doi.org/10.1002/chem.201203154.

[110] Z. Sun, S. Yu, L. Zhao, J. Wang, Z. Li, G. Li, A Highly Stable Two-Dimensional Copper(II) Organic Framework for Proton Conduction and Ammonia Impedance Sensing, Chem. - A Eur. J. 24 (2018) 10829–10839. https://doi.org/10.1002/chem.201801844.

[111] J. Li, X.-L. Cao, Y.-Y. Wang, S.-R. Zhang, D.-Y. Du, J.-S. Qin, S.-L. Li, Z.-M. Su, Y.-Q. Lan, The Enhancement on Proton Conductivity of Stable Polyoxometalate-Based Coordination Polymers by the Synergistic Effect of MultiProton Units, Chem. - A Eur. J. 22 (2016) 9299–9304. https://doi.org/10.1002/chem.201601250.

[112] R. Li, S.-H. Wang, X.-X. Chen, J. Lu, Z.-H. Fu, Y. Li, G. Xu, F.-K. Zheng, G.-C. Guo, Highly Anisotropic and Water Molecule-Dependent Proton Conductivity in a 2D Homochiral Copper(II) Metal–Organic Framework, Chem. Mater. 29 (2017) 2321–2331. https://doi.org/10.1021/acs.chemmater.6b05497.

[113] H. Xu, L. Feng, W. Huang, Q. Wang, H. Zhou, A water-stable Ni(<scp>ii</scp>) diphosphonate exhibiting water vapor adsorption and water-assisted high proton conductivity, New J. Chem. 43 (2019) 807–812. https://doi.org/10.1039/C8NJ04776F.

[114] T. Yamada, M. Sadakiyo, H. Kitagawa, High Proton Conductivity of One-Dimensional Ferrous Oxalate Dihydrate, J. Am. Chem. Soc. 131 (2009) 3144–3145. https://doi.org/10.1021/ja808681m.

[115] B. Joarder, J.-B. Bin Lin, Z. Romero, G.K.H.H. Shimizu, Single Crystal Proton Conduction Study of a Metal Organic Framework of Modest Water Stability, J. Am. Chem. Soc. 139 (2017) 7176–7179. https://doi.org/10.1021/jacs.7b03397.

[116] L. He, J.K. Nath, E.-X. Chen, H.-D. Lai, S.-L. Huang, Q. Lin, Dual-cubic-cage based lanthanide sulfate–carboxylpyrazolate frameworks with high hydrolytic stability and remarkable proton conduction, Chem. Commun. 55 (2019) 2497–2500. https://doi.org/10.1039/C8CC09474H.

[117] S.-J. Liu, C. Cao, F. Yang, M.-H. Yu, S.-L. Yao, T.-F. Zheng, W.-W. He, H.-X. Zhao, T.-L. Hu, X.-H. Bu, High Proton Conduction in Two Co II and Mn II Anionic Metal–Organic Frameworks Derived from 1,3,5-Benzenetricarboxylic Acid, Cryst. Growth Des. 16 (2016) 6776–6780. https://doi.org/10.1021/acs.cgd.6b00776.

[118] F.-D. Wang, W. Su, C. Zhang, Q. Wang, High Proton Conductivity of a Cadmium Metal–Organic Framework Constructed from Pyrazolecarboxylate and Its Hybrid Membrane, Inorg. Chem. (2021) acs.inorgchem.1c02165. https://doi.org/10.1021/acs.inorgchem.1c02165.

[119] F.-Q. Mi, F.-X. Ma, D.-S. Zhan, S.-X. Zou, T. Zhang, A Proton-Conductive Metal-Organic Framework Based on Imidazole and Sulphate Ligands, Dalt. Trans. (2022). https://doi.org/10.1039/d1dt04129k.

[120] H.-B. Luo, M. Wang, J. Zhang, Z.-F. Tian, Y. Zou, X.-M. Ren, Open-Framework Chalcogenide Showing Both Intrinsic Anhydrous and Water-Assisted High Proton Conductivity, ACS Appl. Mater. Interfaces. 10 (2018) 2619–2627. https://doi.org/10.1021/acsami.7b17189.

[121] L.-J. Zhou, W.-H. Deng, Y.-L. Wang, G. Xu, S.-G. Yin, Q.-Y. Liu, Lanthanide–Potassium Biphenyl-3,3′-disulfonyl-4,4′-dicarboxylate Frameworks: Gas Sorption, Proton Conductivity, and Luminescent Sensing of Metal Ions, Inorg. Chem. 55 (2016) 6271–6277. https://doi.org/10.1021/acs.inorgchem.6b00928.

[122] E. Pardo, C. Train, G. Gontard, K. Boubekeur, O. Fabelo, H. Liu, B. Dkhil, F. Lloret, K. Nakagawa, H. Tokoro, S. Ohkoshi, M. Verdaguer, High Proton Conduction in a Chiral Ferromagnetic Metal–Organic Quartz-like Framework, J. Am. Chem. Soc. 133 (2011) 15328–15331. https://doi.org/10.1021/ja206917z.

[123] B.-L. Liu, H.-Y. Zang, H.-Q. Tan, Y.-H. Wang, Y.-G. Li, Engineering the proton conductivity of metal–organic hybrid materials by varying the coordination mode of the ligand, CrystEngComm. 18 (2016) 3300–3305. https://doi.org/10.1039/C6CE00299D.

[124] R. Liu, Y. Liu, S. Yu, C. Yang, Z. Li, G. Li, A Highly Proton-Conductive 3D Ionic Cadmium–Organic Framework for Ammonia and Amines Impedance Sensing, ACS Appl. Mater. Interfaces. 11 (2019) 1713–1722. https://doi.org/10.1021/acsami.8b18891.

[125] S.-S. Bao, N.-Z. Li, J.M. Taylor, Y. Shen, H. Kitagawa, L.-M. Zheng, Co–Ca Phosphonate Showing Humidity-Sensitive Single Crystal to Single Crystal Structural Transformation and Tunable Proton Conduction Properties, Chem. Mater. 27 (2015) 8116–8125. https://doi.org/10.1021/acs.chemmater.5b03897.

[126] Y. Song, A.E. Khudozhitkov, J. Lee, H. Kang, D.I. Kolokolov, A.G. Stepanov, M. Yoon, Transformation of a proton insulator to a conductor: Via reversible amorphous to crystalline structure transformation of MOFs, Chem. Commun. 56 (2020) 4468–4471. https://doi.org/10.1039/d0cc00755b.

[127] M. Taddei, A. Donnadio, F. Costantino, R. Vivani, M. Casciola, Synthesis, Crystal Structure, and Proton Conductivity of One-Dimensional, Two-Dimensional, and Three-Dimensional Zirconium Phosphonates Based on Glyphosate and Glyphosine, Inorg. Chem. 52 (2013) 12131–12139. https://doi.org/10.1021/ic4019597.

[128] R. Moi, A. Ghorai, S. Banerjee, K. Biradha, Amino- and Sulfonate-Functionalized Metal–Organic Framework for Fabrication of Proton Exchange Membranes with Improved Proton Conductivity, Cryst. Growth Des. 20 (2020) 5557–5563. https://doi.org/10.1021/acs.cgd.0c00732.

[129] Q. Lin, Y. Ye, L. Liu, Z. Yao, Z. Li, L. Wang, C. Liu, Z. Zhang, S. Xiang, High proton conductivity in metalloring-cluster based metal-organic nanotubes, Nano Res. 14 (2021) 387–391. https://doi.org/10.1007/s12274-020-2785-x.

[130] C.F. Seidler, M. Wark, Proton Conductivity of Porous Zirconium-Organic Frameworks Filled with Protic Ionic Liquid, Chemie Ing. Tech. (2021) 1–8. https://doi.org/10.1002/cite.202100140.

[131] L. Liu, Z. Yao, Y. Ye, Q. Lin, S. Chen, Z. Zhang, S. Xiang, Enhanced Intrinsic Proton Conductivity of Metal–Organic Frameworks by Tuning the Degree of Interpenetration, Cryst. Growth Des. 18 (2018) 3724–3728. https://doi.org/10.1021/acs.cgd.8b00545.

[132] M. Inukai, S. Horike, T. Itakura, R. Shinozaki, N. Ogiwara, D. Umeyama, S. Nagarkar, Y. Nishiyama, M. Malon, A. Hayashi, T. Ohhara, R. Kiyanagi, S. Kitagawa, Encapsulating Mobile Proton Carriers into Structural Defects in

Coordination Polymer Crystals: High Anhydrous Proton Conduction and Fuel Cell Application, J. Am. Chem. Soc. 138 (2016) 8505–8511. https://doi.org/10.1021/jacs.6b03625.

[133] Q. Tang, Y. Liu, S. Liu, D. He, J. Miao, X. Wang, G. Yang, Z. Shi, Z. Zheng, High Proton Conduction at above 100 °C Mediated by Hydrogen Bonding in a Lanthanide Metal–Organic Framework, J. Am. Chem. Soc. 136 (2014) 12444–12449. https://doi.org/10.1021/ja5069855.

[134] H. Chen, S.-Y.Y. Han, R.-H.H. Liu, T.-F.F. Chen, K.-L.L. Bi, J.-B.B. Liang, Y.-H.H. Deng, C.-Q.Q. Wan, High conductive, long-term durable, anhydrous proton conductive solid-state electrolyte based on a metal-organic framework impregnated with binary ionic liquids: Synthesis, characteristic and effect of anion, J. Power Sources. 376 (2018) 168–176. https://doi.org/10.1016/j.jpowsour.2017.11.089.

[135] D. Umeyama, S. Horike, M. Inukai, Y. Hijikata, S. Kitagawa, Confinement of Mobile Histamine in Coordination Nanochannels for Fast Proton Transfer, Angew. Chemie. 50 (2011) 11706–11709. https://doi.org/10.1002/anie.201102997.

[136] L.H. Chen, B. Bin Wu, H.X. Zhao, L.S. Long, L.S. Zheng, High temperature ionic conduction mediated by ionic liquid incorporated within the metal-organic framework UiO-67(Zr), Inorg. Chem. Commun. 81 (2017) 1–4. https://doi.org/10.1016/j.inoche.2017.04.019.

[137] S. Liu, Z. Yue, Y. Liu, Incorporation of imidazole within the metal–organic framework UiO-67 for enhanced anhydrous proton conductivity, Dalt. Trans. 44 (2015) 12976–12980. https://doi.org/10.1039/c5dt01667c.

[138] D. Umeyama, S. Horike, M. Inukai, S. Kitagawa, Integration of Intrinsic Proton Conduction and Guest-Accessible Nanospace into a Coordination Polymer, J. Am. Chem. Soc. 135 (2013) 11345–11350. https://doi.org/10.1021/ja4051668.

[139] J. Cao, W. Ma, K. Lyu, L. Zhuang, H. Cong, H. Deng, Twist and sliding dynamics between interpenetrated frames in Ti-MOF revealing high proton conductivity, Chem. Sci. 11 (2020) 3978–3985. https://doi.org/10.1039/C9SC06500H.

[140] Z. Li, G. He, Y. Zhao, Y. Cao, H. Wu, Y. Li, Z. Jiang, Enhanced proton conductivity of proton exchange membranes by incorporating sulfonated metal-organic frameworks, J. Power Sources. 262 (2014) 372–379. https://doi.org/10.1016/j.jpowsour.2014.03.123.

[141] L. Yang, B. Tang, P. Wu, Metal–organic framework–graphene oxide composites: a facile method to highly improve the proton conductivity of PEMs operated under low humidity, J. Mater. Chem. A. 3 (2015) 15838–15842. https://doi.org/10.1039/C5TA03507D.

[142] B. Zhang, Y. Cao, Z. Li, H. Wu, Y. Yin, L. Cao, X. He, Z. Jiang, Proton exchange nanohybrid membranes with high phosphotungstic acid loading within metal-organic frameworks for PEMFC applications, Electrochim. Acta. 240 (2017) 186–194. https://doi.org/10.1016/j.electacta.2017.04.087.

[143] H. Sun, B. Tang, P. Wu, Rational Design of S-UiO-66@GO Hybrid Nanosheets for Proton Exchange Membranes with Significantly Enhanced Transport Performance, ACS Appl. Mater. Interfaces. 9 (2017) 26077–26087. https://doi.org/10.1021/acsami.7b07651.

[144] Y.Y. Cai, Q. Yang, Z.Y. Zhu, Q.H. Sun, A.M. Zhu, Q.G. Zhang, Q.L. Liu, Achieving efficient proton conduction in a MOF-based proton exchange membrane through an encapsulation strategy, J. Memb. Sci. 590 (2019) 1–8. https://doi.org/10.1016/j.memsci.2019.117277.

[145] B. Wu, X. Lin, L. Ge, L. Wu, T. Xu, A novel route for preparing highly proton conductive membrane materials with metal-organic frameworks, Chem. Commun. 49 (2013) 143–145. https://doi.org/10.1039/C2CC37045J.

[146] Z. Li, G. He, B. Zhang, Y. Cao, H. Wu, Z. Jiang, Z. Tiantian, Enhanced Proton Conductivity of Nafion Hybrid Membrane under Different Humidities by Incorporating Metal–Organic Frameworks With High Phytic Acid Loading, ACS Appl. Mater. Interfaces. 6 (2014) 9799–9807. https://doi.org/10.1021/am502236v.

[147] H. Sun, B. Tang, P. Wu, Two-Dimensional Zeolitic Imidazolate Framework/Carbon Nanotube Hybrid Networks Modified Proton Exchange Membranes for Improving Transport Properties, ACS Appl. Mater. Interfaces. 9 (2017) 35075–35085. https://doi.org/10.1021/acsami.7b13013.

[148] C. Ru, Z. Li, C. Zhao, Y. Duan, Z. Zhuang, F. Bu, H. Na, Enhanced Proton Conductivity of Sulfonated Hybrid Poly(arylene ether ketone) Membranes by Incorporating an Amino–Sulfo Bifunctionalized Metal–Organic Framework for Direct Methanol Fuel Cells, ACS Appl. Mater. Interfaces. 10 (2018) 7963–7973. https://doi.org/10.1021/acsami.7b17299.

[149] Y. Duan, C. Ru, J. Li, Y. Sun, X. Pu, B. Liu, B. Pang, C. Zhao, Enhancing proton conductivity and methanol resistance of SPAEK membrane by incorporating MOF with flexible alkyl sulfonic acid for DMFC, J. Memb. Sci. 641 (2022)

119906. https://doi.org/10.1016/j.memsci.2021.119906.

[150] A. Donnadio, R. Narducci, M. Casciola, F. Marmottini, R. D'Amato, M. Jazestani, H. Chiniforoshan, F. Costantino, Mixed Membrane Matrices Based on Nafion/UiO-66/SO3H-UiO-66 Nano-MOFs: Revealing the Effect of Crystal Size, Sulfonation, and Filler Loading on the Mechanical and Conductivity Properties, ACS Appl. Mater. Interfaces. 9 (2017) 42239–42246. https://doi.org/10.1021/acsami.7b14847.

[151] Y. Guo, Z. Jiang, W. Ying, L. Chen, Y. Liu, X. Wang, Z.-J. Jiang, B. Chen, X. Peng, A DNA-Threaded ZIF-8 Membrane with High Proton Conductivity and Low Methanol Permeability, Adv. Mater. 30 (2018) 1705155. https://doi.org/10.1002/adma.201705155.

[152] M. Erkartal, H. Usta, M. Citir, U. Sen, Proton conducting poly(vinyl alcohol) (PVA)/ poly(2-acrylamido-2-methylpropane sulfonic acid) (PAMPS)/ zeolitic imidazolate framework (ZIF) ternary composite membrane, J. Memb. Sci. 499 (2016) 156–163. https://doi.org/10.1016/j.memsci.2015.10.032.

[153] X.Y. Dong, J.J. Li, Z. Han, P.G. Duan, L.K. Li, S.Q. Zang, Tuning the functional substituent group and guest of metal-organic frameworks in hybrid membranes for improved interface compatibility and proton conduction, J. Mater. Chem. A. 5 (2017) 3464–3474. https://doi.org/10.1039/c6ta07761g.

[154] J. Escorihuela, Ó. Sahuquillo, A. García-Bernabé, E. Giménez, V. Compañ, Phosphoric Acid Doped Polybenzimidazole (PBI)/Zeolitic Imidazolate Framework Composite Membranes with Significantly Enhanced Proton Conductivity under Low Humidity Conditions, Nanomaterials. 8 (2018) 775. https://doi.org/10.3390/nano8100775.

[155] X.-Y. Dong, J.-H. Wang, S.-S. Liu, Z. Han, Q.-J. Tang, F.-F. Li, S.-Q. Zang, Synergy between Isomorphous Acid and Basic Metal–Organic Frameworks for Anhydrous Proton Conduction of Low-Cost Hybrid Membranes at High Temperatures, ACS Appl. Mater. Interfaces. 10 (2018) 38209–38216. https://doi.org/10.1021/acsami.8b12846.

[156] A. Barjola, J. Escorihuela, A. Andrio, E. Giménez, V. Compañ, Enhanced Conductivity of Composite Membranes Based on Sulfonated Poly(Ether Ether Ketone) (SPEEK) with Zeolitic Imidazolate Frameworks (ZIFs), Nanomaterials. 8 (2018) 1042. https://doi.org/10.3390/nano8121042.

[157] L. Ahmadian-Alam, H. Mahdavi, A novel polysulfone-based ternary nanocomposite membrane consisting of metal-organic framework and silica nanoparticles: As proton exchange membrane for polymer electrolyte fuel cells, Renew. Energy. 126 (2018) 630–639. https://doi.org/10.1016/j.renene.2018.03.075.

[158] H.J. Kim, K. Talukdar, S.-J. Choi, Tuning of Nafion® by HKUST-1 as coordination network to enhance proton conductivity for fuel cell applications, J. Nanoparticle Res. 18 (2016) 47. https://doi.org/10.1007/s11051-016-3346-9.

[159] C.-H. Tsai, C.-C. Wang, C.-Y. Chang, C.-H. Lin, Y.W. Chen-Yang, Enhancing performance of Nafion ® -based PEMFC by 1-D channel metal-organic frameworks as PEM filler, Int. J. Hydrogen Energy. 39 (2014) 15696–15705. https://doi.org/10.1016/j.ijhydene.2014.07.134.

[160] U. Sen, M. Erkartal, C.-W. Kung, V. Ramani, J.T. Hupp, O.K. Farha, Proton Conducting Self-Assembled Metal–Organic Framework/Polyelectrolyte Hollow Hybrid Nanostructures, ACS Appl. Mater. Interfaces. 8 (2016) 23015–23021. https://doi.org/10.1021/acsami.6b05901.

[161] Z. Rao, M. Lan, Z. Wang, H. Wan, G. Li, J. Zhu, B. Tang, H. Liu, Effectively facilitating the proton conduction of proton exchange membrane by polydopamine modified hollow metal−organic framework, J. Memb. Sci. (2021) 120098. https://doi.org/10.1016/j.memsci.2021.120098.

[162] J. Vega, A. Andrio, A.A. Lemus, L.F. del Castillo, V. Compañ, Conductivity study of Zeolitic Imidazolate Frameworks, Tetrabutylammonium hydroxide doped with Zeolitic Imidazolate Frameworks, and mixed matrix membranes of Polyetherimide/Tetrabutylammonium hydroxide doped with Zeolitic Imidazolate Frameworks for proton, Electrochim. Acta. 258 (2017) 153–166. https://doi.org/10.1016/j.electacta.2017.10.095.

[163] H.A. Patel, N. Mansor, S. Gadipelli, D.J.L. Brett, Z. Guo, Superacidity in Nafion/MOF Hybrid Membranes Retains Water at Low Humidity to Enhance Proton Conduction for Fuel Cells, ACS Appl. Mater. Interfaces. 8 (2016) 30687–30691. https://doi.org/10.1021/acsami.6b12240.

[164] F. Wang, C. Liang, J. Tang, F. Zhang, F. Qu, The promotion of proton conductivity by immobilizing molybdovanadophosphoric acids in metal–organic frameworks, New J. Chem. 44 (2020) 1912–1920. https://doi.org/10.1039/C9NJ05572J.

[165] T. Wen, Z. Shao, H. Wang, Y. Zhao, Y. Cui, H. Hou, Enhancement of Proton Conductivity in Fe-Metal–Organic Frameworks by Postsynthetic Oxidation and High-Performance Hybrid Membranes with Low Acidity, Inorg. Chem. (2021) acs.inorgchem.1c02671. https://doi.org/10.1021/acs.inorgchem.1c02671.

[166] K. Cai, F. Sun, X. Liang, C. Liu, N. Zhao, X. Zou, G. Zhu, An acid-stable hexaphosphate ester based metal–organic framework and its polymer composite as proton exchange membrane, J. Mater. Chem. A. 5 (2017) 12943–12950. https://doi.org/10.1039/C7TA00169J.

[167] X. Liang, F. Zhang, W. Feng, X. Zou, C. Zhao, H. Na, C. Liu, F. Sun, G. Zhu, From metal–organic framework (MOF) to MOF–polymer composite membrane: enhancement of low-humidity proton conductivity, Chem. Sci. 4 (2013) 983–992. https://doi.org/10.1039/C2SC21927A.

Abstract

The thesis is dedicated to the exploration of the conductivity performances of a new series of chemically stable proton conducting Metal Organic Frameworks (MOFs) as well as a superionic molecular crystal. Distinct effective approaches were employed to modulate the concentration of Brønsted acidic sites and charge carriers of MOFs, in order to further boost the conductivity properties. The resulting solids combine structural integrity with proton conductivity performances exceeding those ascribed to Nafion, the benchmark material solid state proton electrolyte under hydration. In addition, we demonstrated that a zirconium-formate molecular solid containing KCl ion pairs (ZF-3) switches from an insulator to a superionic conductor upon hydration, which makes this solid a promising candidate to be integrated in impedance-based humidity sensors.

Keywords: Metal Organic Framework, Protonic conductor, Sensor, Ionic Conductor.

Résumé

Cette thèse est dédiée à l'étude de nouveaux matériaux hybrides poreux MOFs conducteurs protoniques et d'un cristal moléculaire conducteur ionique pour des applications dans le domaine de l'énergie et de l'environnement. Nous avons développé diverses stratégies pour optimiser et contrôler la teneur en sites acides de Lewis et en porteurs de charges de MOFs afin de concevoir des matériaux aux propriétés de conduction protonique très prometteuses. Les meilleurs matériaux qui combinent stabilité structurale et conduction protonique élevée présentent des performances qui excèdent celles du Nafion, considéré comme le matériau de référence dans le domaine des électrolytes solides conducteurs protoniques sous hydratation. Nous avons également démontré que le cristal moléculaire Zr-3, à base de zirconium et contenant des paires ioniques, transite d'un comportement isolant à l'état anhydre vers un comportement super-conducteur ionique en présence d'eau, ce qui en fait un matériau de choix comme capteur d'humidité résistif.

Mots-Clés: Metal Organic Framework, Capteur, Protonique conductor, Ionic Conductor.